Statistical Modelling of Urban Heat Islands under Present and Future Climate

Sarah Berk

A thesis submitted to the School of Environmental Sciences of the University of East Anglia in partial fulfilment of the requirements for the degree of Doctor of Philosophy

September 2023

ABSTRACT

The urban heat island (UHI) is a well-observed phenomenon, where temperature in a city is usually warmer than the surrounding rural area. The properties of the UHI are influenced by both the climate and the morphology of the city. It follows therefore, that a changing climate is expected to result in consequences for characteristics of the UHI.

Modelling the future climate of cities remains a challenge as the resolution of global climate models is too coarse to capture the scale of a city, and regional climate models are computationally expensive. To address these limitations, statistical or machine learning models can prove effective. Focusing on cities in the tropics and subtropics and those with a population of less than 1 million, this research explores the relationship between the UHI effect and climate. Satellite data, with global coverage, is used to quantify the surface UHI (SUHI) of the chosen cities using a novel physics-based machine learning model fitted to the current observations, including predictive climate variables.

With use of this machine learning model and global climate model projections, changes in the SUHI under 2 °C global warming from preindustrial are examined. Based the 50th percentile of Earth System Model outputs, the model projects 81% of the selected cities will have an increase in the annual mean SUHI to varying extents up to 1.9 °C, with an increase of over 1 °C for 14% of cities. In the warmest 3 months of the year, SUHIs in the selected cities in China are shown to have increases in magnitude of 0.8 °C, further exacerbating uncomfortable temperatures for city residents during these months.

This new approach has potential to better inform adaptation and mitigation policies in vulnerable cities, especially in south and east Asia.

ACKNOWLEDGEMENTS

Completing this PhD would not have been possible without the support, guidance, and encouragement of numerous people.

First and foremost, I extend my deepest appreciation to my supervisors, Manoj Joshi, Peer Nowack and Clare Goodess for their guidence, insights and encouragement. Their support and constructive advice has contributed to both the growth of this thesis and myself as a researcher.

To many friends; my office mates in 01.04b for all the companionship through the ups and downs and countless teas and coffees, in particular to Emily who was there throughout. My incredible friends from the North, who undertook the long journey to Norwich to see me for weekend adventures, and my fellow ENV and BIO PhD students who always had time for a Friday evening pint; thank you for all the laughter and camaraderie.

And finally, I'd like to thank my parents for their unwavering support and kindness throughout, and for letting me move back in with them in the final months of writing and eat all their crumpets.

CONTENTS

List of Tables

List of Figures

Glossary

Acronym	Definition
ALE	Accumulated Local Effects
BSA	Black Sky Albedo
CFD	Computational Fluid Dynamics
CMIP	Coupled Model Intercomparison Project
CUHI	Canopy Urban Heat Island (Urban-Rural 2m air temperature difference)
EF	Evaporative Fraction
ESA	European Space Agency
ESM	Earth System Model
EVI	Enhanced Vegetation Index
GAM	Generalised Additive Model
GCM	Global Climate Model
GPR	Gaussian Process Regression
LAI	Leaf Area Index
LES	Large Eddy Simulation
LST	Land Surface Temperature
LULC	Land Use Land Cover
MLR	Multiple Linear Regression
MODIS	Moderate Resolution Imaging Spectroradiometer (satellite sensor)
NIR	Near Infrared Radiation
PDP	Partial Dependence Plot
RCM	Regional Climate Model
RCP	Representative Concentration Pathway (W/m^2)

RERF	Regression Enhanced Random Forest
RFR	Random Forest Regression
RH	Relative Humidity (%)
RMSE	Root Mean Squared Error
RR	Ridge Regression
SSP	Shared Socioeconomic Pathway
SSR	Net Surface Solar Radiation (W/m^2)
SUHI	Surface Urban Heat Island (Urban-Rural surface temperature difference)
TP	Total Precipitation (m/day)
UCI	Urban Cool Island
UHI	Urban Heat Island (Urban – Rural temperature difference)
WSA	White Sky Albedo

1 INTRODUCTION

Urbanisation represents one of the most extreme examples of anthropogenic land modification. Cities can be vast in size, with surfaces made up of an array of man-made materials such as concrete, brick, glass, metals and plastics. If someone were to stand in the same spot before anthropogenic influence, the area would be unrecognisable. It follows that this enormous alteration to the landscape should bring with it alterations to the local climate.

Figure 1.1 "The outward and upward growth of Panama City, Panama, 1930 – 2009" Figure 1.2 from Angel et al (Angel et al., 2016) (Skyscraper City, Brian Gratwicke).

An urban heat island (UHI) is a well observed phenomenon, where the temperature in a city is differs from the surrounding rural area, often being warmer. The name 'UHI' stems from the pattern on a heat map; these show an 'island' of a city surrounded by a 'sea' of surrounding cooler countryside (Oke, 1995). This pattern can be seen in Figure 1.2, showing the UHI of London in 1959.

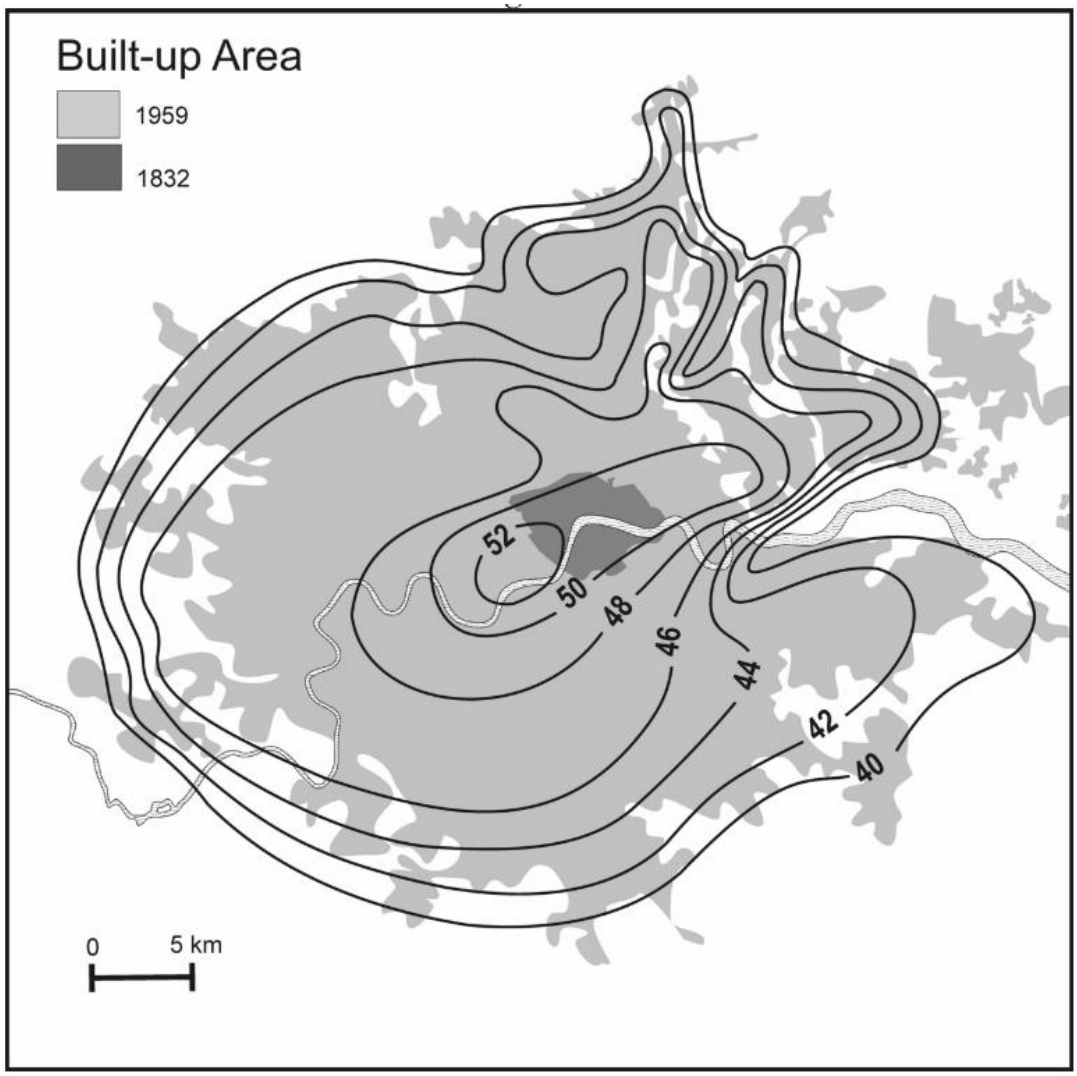

Figure 1.2: Distribution of minimum temperature in London, 14 May 1959. Isotherms numbered in °F. Figure 4 in the International Association of Urban Climate reprint of Howard (1833).

The UHI can be measured both by means of air temperature, known as the canopy urban heat island (CUHI) or by surface skin temperature, referred to as the surface urban heat island (SUHI). The benefits and limitations surrounding the two measures are discussed in section 2.3.

Understanding and predicting UHI behaviour is not simple, as it is very much dependent on the local climate, alongside properties relating to the city form. For example, in subtropical cities, UHI intensities are generally lower in comparison with cities in temperate regions, due to differences in anthropogenic heating and differences in surface water retention. Higher intensities are seen in dry seasons and lower in wet seasons, relating to moisture availability and cloud cover (Roth, 2007; Cui and de Foy, 2012). The peak intensity can occur in winter for a cold climate (Konstantinov *et al.*, 2018), and summer for a Mediterranean climate (Yague

et al., 1991). Based on these factors, it is difficult to say what the 'average' UHI magnitude is, as different values can be found conditional on the chosen region and time of year, but the CUHI has been known to reach up to 10 °C in certain locations and weather conditions (Chapman et al., 2017). Arid climates on the other hand, can experience negative heat islands (or urban cool islands), where cities experience cooler temperatures in comparison to the surrounding rural area due to higher moisture availability in the city, which has a cooling effect (Rasul *et al.*, 2017).

Given this strong dependence of the UHI on climate, a pressing question is how exactly will the UHI be affected by climate change. A deeper understanding of its drivers and potential future evolution can help city planners design cities in ways as to optimize for comfort and human health and mitigate the negative impacts that changes in climate can have on a city environment.

Assuming a continuation of the current mitigation measures only (emissions scenario SSP3-7.0, section 2.8.1), global mean surface air temperature is projected to have increased by between 1.95 and 4.38 °C by the period 2081–2100, relative to 1995– 2014 (Tebaldi *et al.*, 2021). In addition, extreme heat events are highly sensitive to this warming and studies have shown that anthropogenic climate change has led to current increases in the frequency of heat waves (Horton *et al.*, 2016). In global modelling studies of the UHI, warm nights with high heat stress increase more in urban areas than their rural counterparts, with the additional urban warming causing temperatures to be pushed above the threshold of human comfort (McCarthy *et al.*, 2010; Fischer *et al.*, 2012; Oleson, 2012). The effect of urbanisation is typically not resolved in global climate models, with urban land simply represented as a slab or rock cover (fraction of land type), as its scale is typically smaller than the horizontal resolution of the model itself. For regional climate models it is more important, and more detailed representations of the urban surface are often employed in these models (Daniel *et al.*, 2019). An increased understanding of the UHI will result in better representations of the urban surface in these models and lead to more accurate projections of how climate change induced temperature increases will affect and be distributed across urban areas.

Alongside an increasing global population, countries are seeing migration from rural areas to the cities as migrants seek to increase livelihood. Just over half the world's population currently lives in cities and this proportion is projected to increase to 68 percent in 2050 (Lerch, 2017; United Nations, Department of Economic and Social Affairs, 2019). Substantial urban population growth is projected to take place in cities of all sizes (Kii, 2021), yet despite this much of the current research focus of the UHI is on megacities. Typically, as cities expand

the intensity of their UHI also grows. However, detailed later in this thesis (section 2.5.3), it is observed that saturation of the UHI with city size occurs in very large cities (e.g., London). A complete picture of UHI must be therefore gained by examination of the medium sized cities, alongside the current body of research on larger cities.

Alongside an increasing number of people being affected by the impacts of the UHI, global health risks associated with extreme heat are increasing due to climate change (Kovats and Hajat, 2008). This means city inhabitants face the dual impact of both climate change and UHI related heat risks. The IPCC 5th assessment report states 'much of the key and emerging global climate risks are concentrated in urban areas'. Cities in low and middle income countries, which account for close to three-quarters of the world's urban population, contain highly vulnerable communities living in informal settlements, many of which are at high risk from extreme weather; one of these threats being heat stress (Revi *et al.*, 2014). These cities are often in the more southern parts of the world, yet in the current literature, the selection of cities tends to be in the more Northern parts of the world. Outlined in more detail later in this thesis (section 2.3.1), there is a lack of availability of suitable weather stations for cities in these areas, and, as local knowledge is beneficial when studying a city, many authors focus research on where the institute is located. Cities in different areas of the world have different forms and climates, and therefore it cannot be certain that knowledge gained from cities in one part of the world is transferrable to those in another. Therefore, it is essential this knowledge gap is addressed.

Additionally, even in high income countries, city dwellers are at increased risk of heat related health issues and discomfort, in particular the very young, the elderly and those with pre-existing illness (Maller and Strengers, 2011; Oudin Åström *et al.*, 2011; Taylor *et al.*, 2015; Heaviside *et al.*, 2017). Extreme heat leads to excess mortality and in many places, such as North America, is the largest weather related killer (Johnson and Wilson, 2009; Maller and Strengers, 2011). In these high-income cities, there are also compelling reasons to shift away from air conditioning as a solution. Not only does the high electricity use contribute to greenhouse gas emissions and dissipate heat outdoors, thereby exacerbating the problem it aims to combat, it also potentially creates a peak demand of electricity that exceeds supply, as has already been observed in Australia (Maller and Strengers, 2011). Clearly, other methods of cooling cities are needed. If the interaction of the UHI effect with climate change can be better understood, more effective solutions could be proposed to minimise it.

Aims and Objectives

The aim of this research is to examine to impact of climate change in the development of the surface Urban Heat Island (SUHI) in medium size (less than 1 million population) cities in a range of wet and dry climates.

In order to achieve this aim, the specific objectives are as follows:

1. To quantify the SUHI in terms of magnitude in cities of similar size (medium) and geographical characteristics (inland and in non-mountainous areas) in wet and dry climates.

2. To examine the relationship between these SUHI features and background climate by comparison of the results for different cities, building this knowledge into the development of a predictive model.

3. To use this predictive model to assess the importance of background climate as a predictor of SUHI behaviour and assess sensitivity of the SUHI to changes in the predictor variables.

4. To assess the potential impacts of climate change on the SUHI using the predictive model developed and CMIP6 climate change projections.

Thesis Overview

Section 2 of this thesis gives an overview of the key underlying concepts. The first of these is an explanation of the Urban Heat Island (UHI); why it exists, how it is measured and examined, and the various aspects of its behaviour, with a particular focus on its interaction with the local climate. The second concept is climate projections, outlining how future changes in climate can be quantified using physical models. Section 3 informs of the data used and the mechanisms of the statistical/ machine learning models it is to be used together with. In section 4, a machine learning model is created, with the ability to predict the SUHI magnitude for cities in a range of different climates. This model acts as a tool, allowing exploration of the influence of climate related factors on the magnitude of the SUHI. The focus of the next chapter, section 5 is on the future SUHI. Climate model projections are combined with the developed model to give a picture of future SUHI magnitudes for the selected cities. Finally, section 6 ties the chapters together with discussions and conclusions.

2 LITERATURE REVIEW

Some of the elements of this literature review has been published as my contribution in the paper Goodess et al (2021).

2.1 RATIONALE OF CONTENTS

In this literature review, there are seven sections that aim to provide a background for the motivation of the work in the later sections. Section 2.2 gives a physical explanation of why the UHI exists, so the contributing factors can be directly related to how they cause changes in the reasons for formation. In 2.3 we see how the UHI is currently studied, and the shortcomings and strengths of each approach. This is to give context to why statistical and machine learning approaches are used in this thesis. Section 2.4 examines the climate and how it affects the UHI, as climate is highly influential on the contributing factors outlined in 2.2. The focus of section 2.5 is to give an understanding of how the UHI varies in its diurnal cycle, within the city (e.g., locations of the warmest spots) and its long-term trends. Section 2.6 summarises the knowledge gaps, which the aims of this thesis addresses. Finally, sections 2.7 and 2.8 give the information needed for the non UHI specific aspects of this thesis, concerning the data used (how land surface properties are generated from satellite data) and climate projections.

2.2 FORMATION OF THE URBAN HEAT ISLAND (UHI)

The presence of an urban area modifies the lower atmosphere surrounding it through a number of mechanisms. The result of this modification, 'the urban boundary layer' and the processes which lead to its formation will be discussed in this section.

The urban boundary layer

The UHI can be split into two vertical layers. The lower layer is the *urban canopy* (seen in Figure 2.1), the layer at building level and caused by the roughness of the urban surface. This layer is dominated by the characteristics of urban surface itself and will be different depending on the materials and form of the surrounding environment, for example, an area dense with buildings versus a park. Buildings on the surface increase its roughness and turbulence dominates, leading to large variations in airflow speed and direction with height. For these reasons, this layer is controlled by urban *micro-scale* processes (see Figure 2.2 for scales of urban components).

The upper layer is the *urban boundary layer*, a local to mesoscale concept, depicted in Figure 2.1. The urban boundary layer is the area of the planetary boundary layer where the presence of the city has modified the climatic characteristics. Here the turbulence is more settled and more homogenous with height (Barlow, 2014), but increased drag and turbulence can lead to reduced wind speeds over the city in comparison to rural counterparts. This local slowing of wind causes convergence of air over the city, which can cause the boundary layer to 'dome' up over the city. For potentially tens of kilometres downwind of the city, an urban plume of rising air occurs. Another feature of the boundary layer is it tends to diminish at night as the bulk of the planetary boundary layer is stable and this supresses vertical transfer of heat (Oke, 1976, 1978).

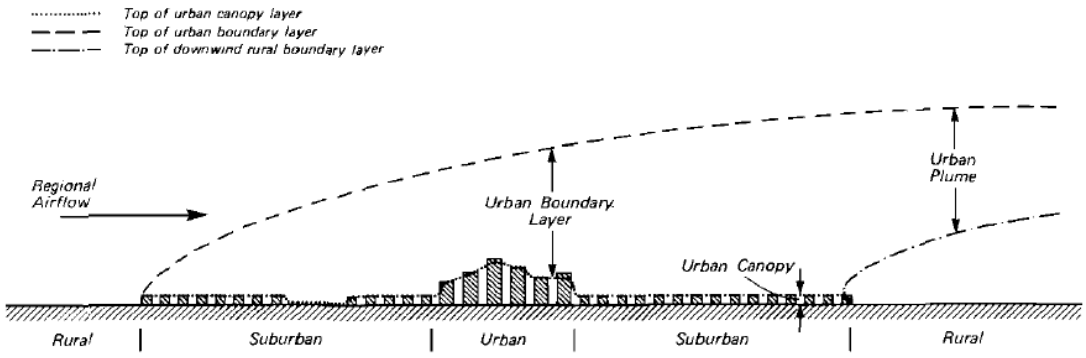

Figure 2.1 The urban boundary layer (Oke, 1976)

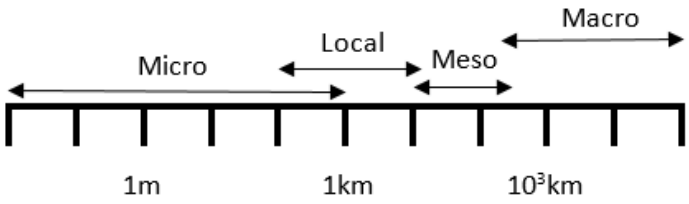

Figure 2.2 Scales of urban climate components, adapted (Oke, 2006). From the scale of a single building (micro) to a neighbourhood (local) to the entire city and large-scale thermal circulations such as country breezes (macro).

UHI studies are conducted at various spatial scales dependent on the objective of the study. An investigation into the impact of a park in improving pedestrian comfort, for example, requires a different scale to one examining urban-rural breezes (Mirzaei, 2015). Scales of UHI phenomena include the urban canopy layer at the microscale, the surface urban boundary layer at the local scale and the outer urban boundary layer at the mesoscale (Oke, 2006). At the urban canopy layer, the microscale, there are many different surface elements such as

buildings, greenspaces, trees or paved areas with a range of radiative, thermal, aerodynamic and moisture properties (Arnfield, 2003). At this scale, airflow can vary by large amounts due to perturbation, even by small objects. The local scale is that which climate stations are designed to monitor, including orography but aiming to exclude the microscale effects. The mesoscale is where the influence of the city on the climate will be seen, typically stretching tens of kilometres across the entire city (Oke, 2004).

The focus of this thesis is the local to mesoscale. At these scales, studies aim to understand the UHI across the entire urban area and how characteristics of a city such as its location, greenness or urban morphology can affect UHI magnitudes.

Contributing factors

In his pioneering work, Howard (1833) identified four causes for the UHI in London, with Oke (1981) later adding two further causes. These can be summarised as follows.

- Anthropogenic heat
- Impervious surfaces
- Thermal properties of the city fabric
- Surface geometry
- Urban roughness
- Air pollution

Anthropogenic heat, Q_F

The activity of a city itself acts as an internal heat source, which can be divided into three main causes. These are the heat produced by vehicle emissions, heat released from buildings and from the metabolic heat of people themselves (Allen *et al.*, 2011).

As it can be shown to account for less than 1% of the total anthropogenic heating of a city, most studies either ignore metabolic heat, or integrate it as a component of buildings (Sailor, 2011). The heat released by human activity is dependent on working patterns and public holidays, vehicle use and energy consumption of the particular city (Allen *et al.*, 2011). For example, on weekdays residential buildings peak in energy use in the early morning and evening, and heat from vehicle use reduces at the weekends as there is a dip in commuter travel (Figuerola and Mazzeo, 1998; Sailor, 2011).

A point to note, however, is that the UHI in temperate areas is often observed to be greatest in the warm season, rather than the cold when anthropogenic heat requirements are higher. The

implication of this is that anthropogenic heating alone is not the primary cause (Oke, 1982). The influence of anthropogenic heat is found to depend largely on the city and season in question; more developed cities carry out a higher volume of heat emitting processes, and seasonal temperature differences lead to varying heating and cooling requirements (Ichinose *et al.*, 1999; Zhou *et al.*, 2014). For some it is a key factor (Ichinose *et al.*, 1999), whereas for others it is not so prominent in comparison to other key drivers of the urban heat island (Zhao *et al.*, 2014).

Impervious surfaces / Surface 'waterproofing'

A key variable for the daytime radiant energy of an area is moisture availability, required for latent heat loss (Oke, 1982). City materials, such as concrete, asphalt or metals tend to be impervious, and city drainage systems remove excess water, whereas soil and vegetation retain moisture. This means there is very little cooling due to latent heat in highly built-up urban areas. Urban parks become cooler than the surrounding area due to the 'oasis' effect, as they are a source of moisture in an otherwise dry area. As with parks, the rural area acts as a source of moisture and evapotranspiration takes place, leading to more energy being dissipated in the latent form (Oke, 1978). Anthropogenic processes such as combustion in vehicle engines and industry also produce moisture, although this effect is often either not taken into account or simplified in studies of the urban climate (Sailor, 2011). The small role of latent energy in a city means sensible heating is the main energy release. A measure to consider here is the Bowen ratio, the ratio of sensible to latent heat fluxes. Urban areas characteristically will have a large value for the Bowen ratio (Oke *et al.*, 1992).

Thermal properties of city fabric

The thermal properties of the city fabric drive the heat stored in the city. Typically, the heat stored in a city is larger than the surrounding areas due to the city materials having greater thermal conductivity (k, in J K^{-1}) and heat capacity (C, in J K^{-1}). Thermal conductivity represents the ability of the material to conduct heat. For a given temperature difference, a material with a higher thermal conductivity will transmit larger amounts of heat to the environment than one with a lower value. Heat capacity indicates the ability to store heat, giving the amount of sensible heat taken up or released by a material based on its change in temperature. A high heat capacity means a smaller temperature change (Oke, 1982; Oke *et al.*, 2017). The combination of these properties (which make up thermal admittance, μ, in W m^{-2} K^{-1}), means the city materials release and store heat relatively easily, playing a large role in the nocturnal heat island. This is because heat storage is particularly important for maintaining temperatures in the absence of solar energy (Oke, 1982). However, it is important to note that heat capacity may not always be higher in the city in comparison to its surrounding rural area,

for example the greater values can be found in rural environments when soils are wet (Oke *et al.*, 2017).

Surface geometry

Surface geometry contributes towards the heat island by trapping radiation within the city, which in a rural (flatter) area would be released to the sky. Figure 2.3 shows an example of a rural surface and an urban street canyon. In the rural area, heat can be radiated back to the sky in all directions, whereas in the urban area, the heat from the surface is absorbed by the building walls with some escaping to the sky. The canyon walls also radiate heat back to the surface (Oke *et al.*, 1991). As the height to width ratio of the canyon increases, the nocturnal cool sky is replaced by the sides of warmer buildings; dense cities with tall buildings cool much slower than rural counterparts at night (Oke, 1981).

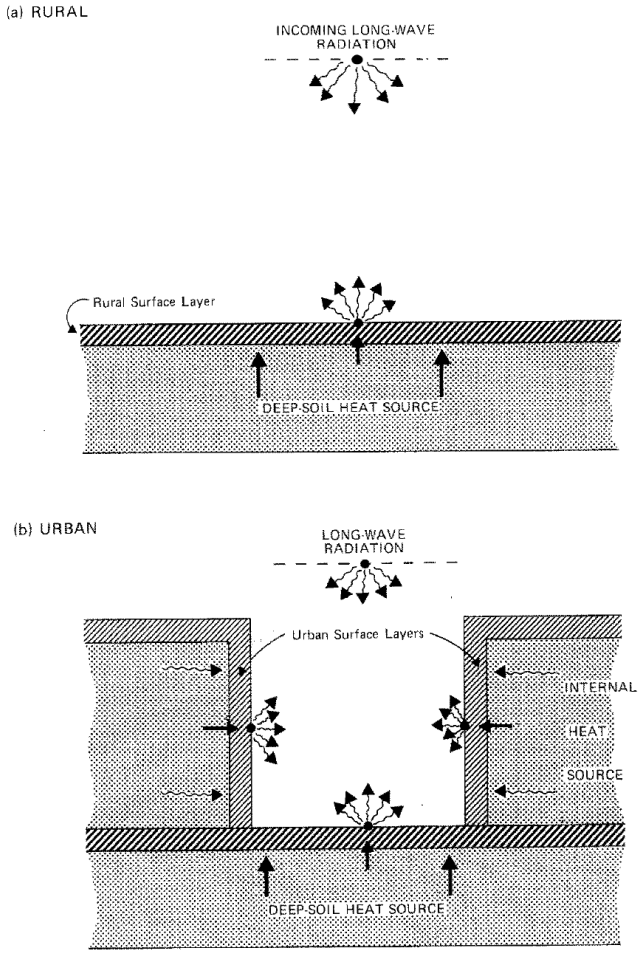

Figure 2.3: Schematic of a rural versus urban area with representation of the processes involved in nocturnal cooling of a) rural and b) urban canyon surfaces under 'ideal' (calm and cloudless) weather conditions. Taken from Johnson et al (1991).

Oke (1991) constructed physical models to show that the geometry of a city does indeed cool slower than a flat rural surface. This was done by building two wooden models, one with

similar geometry to a city and one completely flat, both made from the same mass of wood. The 'city' model cooled at a slower rate; with the only changing variable between the two simulations being the geometry, supportive of the hypothesis.

Urban roughness

The presence of high roughness parameters in urban areas results in restricted air circulation, and air decelerates as it flows over the area, limiting the dispersal of the heat and pollution generated by the urban form (Bornstein and Johnson, 1977; Barlag and Kuttler, 1990). This urban roughness is attributable to the numerous levels of tall, inflexible buildings of varying heights. This element of the urban surface results in the formation of a roughness sublayer, a layer of air closest to the urban surface, consisting of interacting waves and plumes of heat, humidity and pollutants, which can be up to several times the average building height in depth. This roughness sublayer behaves differently to the surface layer found in a rural area. While the surface layer characteristics are determined by height and vertical temperature gradient, the roughness sublayer characteristics depend on the horizontal distance and spacing of the elements within it (Rotach, 1999; Roth, 2000; Arnfield, 2003).

Air pollution and albedo

Pollution leads to an increased level of aerosols in the urban atmosphere, which can impact the radiation received by an urban area in two ways, depending on the type of aerosol. The first impact is that aerosols can absorb incoming and outgoing short-wave radiation and emit it as long-wave radiation. In this case, an urban area will receive additional longwave radiation (Oke, 1978; Li *et al.*, 2018). During the night, these aerosols cause urban radiation to be absorbed and re-emitted, contributing further to the difference in cooling rates between the urban and rural environments. The second way aerosols can impact the UHI is to scatter and reflect short-wave radiation, leading to a reduction in the amount of this energy reaching the city surface. Table 2.1 gives the example of two cities, where the differences in incoming solar and atmospheric longwave are quantified.

Table 2.1 Differences in incoming solar and atmospheric longwave radiation in urban and rural areas, due to the presence of aerosols.

City	Urban – Rural Difference Incoming Solar	Urban – Rural Difference Atmospheric Longwave	Reference
Toulouse, France	−30 W/m^2	15 to 25 W/m^2	(Estournel *et al.*, 1983)
Berlin, Germany	−30.07 and − 48.06 W/m^2	13.26 and 20.38 W/m^2	(Li *et al.*, 2018)

The albedo of city surfaces tends to be lower than rural counterparts, with the exception of forests and areas with dark soils (Oke, 1978). Oke (1978) calculates an average urban albedo for a mid-latitude city to be about 0.15, which is lower than most rural landscapes. The albedo of Sapporo and Tokyo, Japan is measured to be 0.12, lower than the surrounding forest of albedo 0.16. This is attributed to the sparse vegetation in city areas, and radiation undergoing multiple reflections in the urban canopy (Sugawara and Takamura, 2014). Basel, Switzerland as a mean albedo of around 0.1, in comparison with a rural average value of 0.2 (Christen and Vogt, 2004). In most cases the radiation imbalance due to pollution is partially offset by this lower urban albedo during the day (Oke, 1978), although at night the effect is stronger and found to enhance the UHI by 12% for a clear night in Berlin (Li *et al.*, 2018).

2.3 METHODS OF STUDYING UHI

2.3.1 Observations

As with many anthropogenic climate influences, the true size of any urban effect on its micro-climate is difficult to estimate without measurements of the same area pre-urbanisation. In the absence of this pre-urban baseline, temperatures of the surrounding rural area are taken to be a good approximation, although it should be noted that the rural land itself has often undergone human alteration, for example due to agriculture (Oke, 1978).

The Canopy UHI: using 2m air temperature

The earliest approach to examining the UHI uses urban-rural station pairs, taking the difference between urban and rural station temperatures as the UHI magnitude (Howard, 1833; Ackerman, 1985; Karl *et al.*, 1988; Moreno-Garcia, 1994; Figuerola and Mazzeo, 1998; Morris and Simmonds, 2001). These air temperatures are a measure of the urban canopy layer

(Figure 2.1), an important aspect of the UHI, and the UHI quantified by air temperature is sometimes referred to as the canopy urban heat island (CUHI). For clarity, the term CUHI when used in this thesis will refer to the increase in urban air temperatures in comparison to rural surroundings. The UHI refers to the difference in temperature created by the presence of a city and will refer to this phenomenon overall rather than for a specific measurement methodology. The 2 m air temperature is that which is experienced by the people in the city, and therefore an indication of the human discomfort experienced due to higher temperatures.

The long-standing nature of some weather stations means that the CUHI can be studied over a large temporal span using this method. For example, warming trends have been studied starting from 1900 and 1910 in London and Vienna, respectively (Jones *et al.*, 2008; Jones and Lister, 2009).

The limitation of this station pairing method is that it implicitly assumes that the urban surface is homogeneous and does not consider variations within the city. The city-atmosphere system is complex, and exchanges of energy, mass and momentum take place over a wide range of space and time scales. Understanding this from just one fixed point is not possible (Oke, 1982). Finding a rural site without some form of urban influence can also prove problematic. Jones et al (2008) overcome the lack of rurally located weather stations in China by using reanalyses[1], and in order to obtain accurate temperature data Kidder and Essenwanger (1995) use small cities as the rural temperature measurement. Small cities and even villages do, however, exhibit CUHI characteristics (Oke, 1973; Karl *et al.*, 1988; Lindén *et al.*, 2015). Stewart (2007) highlights the ambiguity of the term "rural" and the variation of these sites between studies, pointing out that a common source for temperature records, airports, have been used as both urban and rural sites in different studies. An additional limitation in using weather station data is cities which lack appropriately positioned weather stations cannot be studied. This limits research to certain areas, and in a study by Du et al (2021) after filtering cities for appropriate weather station data, 355 cities in the Northern hemisphere and 11 cities in the Southern Hemisphere remained. Figure 2.4 is taken from this paper and shows the locations by climate zone. Here, using this method strongly limits the climate types for which the CUHI may be studied.

[1] *Reanalyses are datasets which are created using both observations and models, in a process named data assimilation (Parker, 2016).*

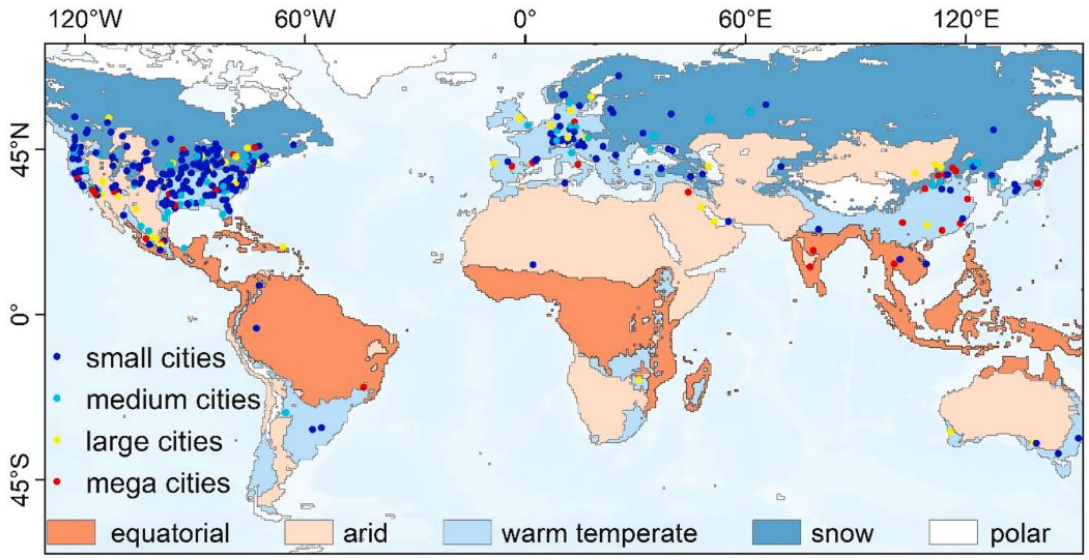

Figure 2.4 Figure 1 from Du et al (2021), showing the global distributions of the 366 cities where weather station data is available to study the CUHI.

To address the issue of urban heterogeneity, some studies use data taken from vehicles with temperature sensors attached. This gives a more detailed representation of the spatial characteristics of the urban heat island (Oke, 1973, 1976; Wong and Yu, 2005; Hart and Sailor, 2009; B. Zhou *et al.*, 2019). However, this traverse data is only a snapshot in time, and does not give information beyond the timeframe in which vehicles are deployed. This makes it difficult to compare with other data sources. The spatial extent of the data is also limited to the road network, so will not take into account areas such as parks when the cooling effect does not reach the road (B. Zhou *et al.*, 2019). Another method of studying the spatial extent of the CUHI is to use a network of sensors across a city. This can be temporary, to assess the CUHI over a short period of time (Chow and Roth, 2006; Kolokotroni and Giridharan, 2008), or permanent sensors to examine seasonal behaviour and the impact of different weather conditions (Schatz and Kucharik, 2014; Azevedo *et al.*, 2016). These sensor networks allow the analysis of different types of urban form across the city, with a longer temporal aspect than traverse data. A limiting factor of such studies is there are few cities that contain the dense sensor networks required, due to equipment cost and upkeep (Chapman *et al.*, 2015). A method of reducing such upkeep costs is for members of the public to maintain the sensors. For example, in Hong Kong a sensor network is run by citizen scientists in schools and local communities (Hung and Wo, 2012). Additionally, personal weather stations are gaining increasing attention as a method for increasing spatial resolution of urban air temperature observations, an approach known as crowdsourcing (Chapman *et al.*, 2023). This crowdsourcing approach has also been utilised using personal car thermometers to give CUHI spatial patterns at 200m resolution (Marquès *et al.*, 2022).

The effects of the UHI can also be measured in the boundary layer. Measuring this is often time consuming and costly, requiring tall towers, radiosondes and aircraft, and has been done in only a few large cities worldwide (D. Zhou *et al.*, 2019).

The surface UHI: using land surface temperature

The introduction of satellite remote sensing, used to generate land surface temperature (LST) datasets, led to explorations of the spatial extent of the heat island. Early studies are qualitative in type, describing the thermal patterns and simple correlations (Roth and Oke, 1989; Voogt and Oke, 2003). In recent years, as satellite data has become more freely and widely available, remote sensing has become a popular method of study due to its consideration of both spatial and temporal characteristics of the urban heat island (Weng *et al.*, 2004; Tiangco *et al.*, 2008; Li *et al.*, 2011; Clinton and Gong, 2013; Zhou *et al.*, 2014; Mallick *et al.*, 2013; Zhou *et al.*, 2013; Rasul *et al.*, 2015; Estoque *et al.*, 2017; Singh *et al.*, 2017; Equere *et al.*, 2020). The two commonly used satellite sensors are Landsat Thematic Mapper/ Enhanced Thematic Mapper/ Thermal Infrared Sensor and MODIS, which account for 78% of the publications in a 2019 review of satellite remote sensing for UHI studies. Other satellite sensors such as ASTER, AVHRR, SEVERI, GOES and more make up the rest (D. Zhou *et al.*, 2019).

Remote sensing methods compute the land surface temperature (LST) rather than air, and this technique brought with it a new measurement for examining the UHI, the surface UHI (*SUHI*). As with use of air temperatures to calculate the CUHI, there is not set formula for the calculation of a SUHI, and therefore different quantification methods are used to determine its magnitude. An idealised definition of the UHI is the temperature increase of an area that has resulted from the presence of a city. However, in order to know this, it must be possible to measure the temperature of an area with and without a city, in the same period of time. As this is impossible, a few different methods have been developed in order to quantify the magnitude of the SUHI. All methods require identifying the urban (city) area and a rural reference area, which is to act as a proxy for what the temperature in the city area would be if there did not exist a city. The urban area is relatively simple to define as it is the area marked as urban in landcover data. The rural area can be defined in numerous ways, however. The rural area can be defined as a 'buffer zone', a ring of rural area at a set distance around the urban outline (Clinton and Gong, 2013; Lai *et al.*, 2021) or a box (Anniballe *et al.*, 2014) a set distance from the city centre. Commonly, once these areas have been defined, the SUHI magnitude is taken to be the average urban temperature minus the average rural temperature. Some methods, however, aim to examine the peak SUHI intensity, where the temperature difference is at its greatest. This include using quantiles (Flores R. *et al.*, 2016), and fitting Gaussian surfaces to the city temperature difference (Streutker, 2002). More detail on these methodologies can be seen in section 4.2 and in the appendix section A.4. Schwarz et al (2011)

explores numerous methods of quantifying the SUHI, 11 in total, finding different quantification methods can show different characteristics of the SUHI. Based on this, the authors recommend consultation of multiple methods when examining SUHI magnitude.

Whilst the two measures are linked, studies show that both the magnitude and the temporal and spatial patterns of urban LST and air temperatures are different, meaning studies looking at the SUHI should not be directly compared to the CUHI. This must be taken into consideration when making conclusions from SUHI studies, particularly if they are related to human health and comfort, as here air temperature is most significant.

The issue with using remotely sensed LST (and therefore the SUHI) is that the observation from the sensor is two dimensional, whereas an urban area is in three dimensions. The area seen is limited by viewing angle, and vertical surfaces such as building walls and well shaded ground are hidden from view (Voogt and Oke, 2003). The sensor will capture the top of a tree canopy, for example, rather than the cool surface below, which is closer to the temperature felt by the city inhabitants. The structure of the surface itself (i.e., building heights and density) alters the city climate through advection and absorption or reflection of radiation (this can be seen later in this thesis in Figure 2.5) which two dimensional LST cannot capture (Stewart and Oke, 2012). Satellite measurements are also limited in their ability to study the full diurnal cycle (section 2.5.1), as satellites are over a given region for a limited time each revolution. If there happen to be clouds at this time, information of the SUHI below will not be captured (Mirzaei and Haghighat, 2010). This can lead to less data being generated in polluted and chronically cloudy areas, which if seasonal can introduce bias (Clinton and Gong, 2013). It also means it is not possible to gain a continuous record at short time intervals throughout a diurnal cycle, as the time of day that measurements are acquired at is limited to the overpass time. Avoiding cloud contamination, along with that the SUHI often being at its peak during this time, means summer daytime is a common time period of study in the northern hemisphere (B. Zhou *et al.*, 2019; D. Zhou *et al.*, 2019).

In studies, it is found that urban LSTs have a larger amplitude of diurnal cycle, tending to be larger during the day and smaller during the night in comparison to air temperatures (Jin and Dickinson, 2010; Amorim *et al.*, 2021). SUHI intensities tend to be largest in the day, whereas CUHI intensity is greatest at night, although this is climate dependent (Roth and Oke, 1989; Eliasson, 1996; Arnfield, 2003). Spatial patterns differ as the CUHI is altered by winds and advection, while the SUHI is more controlled by land cover types (Azevedo *et al.*, 2016). While both surface and air temperatures are dependent on surface energy balance, this additional effect of advection processes on air temperature leads to a lack of simple coupling between the two (Roth and Oke, 1989).

Studies have delved further into this complex relationship by examining both the CUHI and SUHI together for the same city or cities. As mentioned previously in this section, there are a number of methods used to define both the CUHI and SUHI, which results in a mix of methodologies to determine differences between CUHI and SUHI. Table A.1.1 in the appendix gives an overview of studies that compare the CUHI and SUHI, and this difference of methods is highlighted in the methods column of the table.

Using a dense sensor network of air temperature measurements and comparing with satellite LST is used to study a single city (e.g., Azevedo *et al.*, 2016; Feng *et al.*, 2019; Amorim, 2020) and allows for direct CUHI-SUHI comparisons at multiple locations. Using weather station pairs (e.g., Gawuc *et al.*, 2020; Sun *et al.*, 2020; Wang *et al.*, 2020) allows for a large number of cities to be studied at the same time (although it should be noted these are restricted by the availability of suitably positioned weather stations), but means that the location of the weather station must be used for both air and LST measurements for a direct comparison. The studies examined find SUHI magnitude is generally greater than CUHI (although for arid cities SUHI is lower than CUHI during the day). For a study of 342 cities in Europe using crowdsourced citizen weather station data, the SUHI is greater than the CUHI for 91% of cities during the day and 81% during the night (Venter *et al.*, 2021). Variance in both SUHI and CUHI could be explained by differences in evapotranspiration between rural and urban areas, but albedo was more influential on the SUHI and surface roughness more important for explaining the CUHI. Due to the influence of advection on the CUHI, windspeed and direction strongly influence its magnitude and spatial patterns. Wind direction can cause CUHI hotspots and SUHI hotspots within the city to lie in different areas, as the CUHI peak intensity shifts downwind (Azevedo *et al.*, 2016; Cao *et al.*, 2021). Multiple studies observe the CUHI-SUHI correlation is greater during the night (Azevedo *et al.*, 2016; Yao *et al.*, 2021; Berg and Kucharik, 2022), where different mechanisms control the formation of the UHI. During the day, it is attributed to differences between evaporative cooling, and at night, radiative cooling rates dominate (see section 2.5.1). The strength of the CUHI-SUHI correlation also can differ based on season (Ma *et al.*, 2016; Hu *et al.*, 2019), as seasonal weather patterns such as wind speed will impact the strength of the relationship.

These differences are problematic if SUHI is to be used to recommend CUHI mitigation measures, as given their relationship is not linear, it is hard to understand whether the impact on the CUHI will be the same. A quantifiable decrease in LST cannot be translated into a known impact for air temperature. This limits the applications of SUHI studies, as they cannot be used directly by policymakers or city planners who are aiming to reduce city air temperatures by set targets. It also can make deciding between two mitigation options tricky, as the impact on the CUHI may differ from the SUHI.

Although the relationship between LST and air temperatures in relation to the UHI is not simple, LST is nevertheless an important aspect of the phenomena. It plays a part in human comfort within an urban area by controlling the temperatures at the lower layers of the urban atmosphere and those inside buildings (Voogt and Oke, 2003), and a strong correlation between the two measures does exist. Surface temperatures can also give information for applications outside of human health. For example, to determine what temperatures building materials may be exposed to for civil engineering applications, or whether city surfaces will require gritting at the same time as surrounding rural area (Chapman and Thornes, 2006).

2.3.2 Modelling

In this section, the different approaches used to model the CUHI/SUHI are outlined. This gives context to why in this thesis, a statistical modelling or machine learning approach to modelling the SUHI is taken over other approaches.

Statistical Modelling and Machine Learning

Statistical analysis is an important tool in analysing the remotely sensed SUHI, and studies can be grouped into two categories. They tend to either focus on an individual or few cities (Weng *et al.*, 2004; Tiangco *et al.*, 2008; Xiong *et al.*, 2012; Mallick *et al.*, 2013; Rasul *et al.*, 2015; Geletič *et al.*, 2016; Equere *et al.*, 2020), or on large numbers of urban areas within a global or regional span (Tran *et al.*, 2006; Imhoff *et al.*, 2010; Clinton and Gong, 2013; Zhou *et al.*, 2013, 2014; Peng *et al.*, 2018).

Studies focusing on one or a few cities most often are interested in the spatial features of the SUHI. They analyse the LST and how it is related to the variations of land cover, giving a detailed picture of the SUHI within a city. Some studies look at cities over different years to investigate the impact of urban development and expansion (Xiong *et al.*, 2012; Mallick *et al.*, 2013). These aspects make these studies advantageous for city planning and for understanding the potential for mitigation measures. As outlined in section 2.3.1, there is not set methodology for how a SUHI or CUHI is quantified, making direct city-to-city comparisons of studies difficult. To address this lack of consistent and compatible observation data in standalone city studies, characteristics of large groups of cities have in other cases been analysed together, with the same SUHI quantification methods being used for all cities in question (e.g. Tran *et al.*, 2006). The relationships of these sets of SUHIs and their influencing factors are then explored, and statistical or machine learning techniques can be used to predict SUHI magnitudes. A summary of these studies (12 in total) can be found in the appendix, Table A.1.2, which outlines the different techniques used and the range of input variables explored. Not all studies examine climate variables (e.g., precipitation, relative humidity) as potential influencing factors on the SUHI, and climate variables feature in half of the studies. Measures

of vegetation, however, are included in the majority of studies, and this is related to climate indirectly as the abundance and type of vegetation in an area is a product of the climate.

The most popular method of study is linear regression, an approach is widely used in many fields of research and easy to interpret and understand. This makes it ideal for understanding relationships between influencing factors and the SUHI magnitude by examining the fitted coefficients (section 3.5). Comparison of the values of the fitted coefficients also can give an indication of the influence of each variable, with the most influential having the highest magnitude. It is used both to combine all influencing factors together to predict the SUHI magnitude (Zhou *et al.*, 2014; Schwarz and Manceur, 2015; Zhou *et al.*, 2017; Peng *et al.*, 2018; Y. Li *et al.*, 2021; Liu *et al.*, 2021), or as separate single variable models looking at the impact of an influencing factor in isolation (Imhoff *et al.*, 2010; Li, Zha and Zhang, 2020). However, a downside of this model is it lacks the flexibility to capture any nonlinear relationships, and assumes variables are independent. This means if correlated variables are used in the same linear regression model, the interpretation of coefficients will be distorted. The model also has a tendency to overfit, although this can be reduced by regularisation (section 3.5) and is sensitive to outliers. The other modelling technique used is random forest regression (section 3.5) (Clinton and Gong, 2013; Wang *et al.*, 2015; Ma *et al.*, 2021). Unlike linear regression, random forest regression is more flexible and can capture non-linear relationships, generally having a better predictive accuracy. As with interpreting the coefficients of linear regression, an understanding of the most influential variables on the SUHI are given using a method known as feature importance (a caveat being if correlated variables are included the importance of the related variables will be reduced). Of all the studies assessed, using both these modelling techniques, of note is that over half (7) of the studies fit and test the models on the entire dataset, meaning there is no assessment of overfitting. Additionally, none of the fitted models have been used for prediction, with the focus on statistical inference, aiming to understand relationships between the influencing variables and SUHI magnitude.

Aside from these studies, the more popular use for machine learning techniques relating to the CUHI/SUHI is in studies which aim to predict urban air temperatures based on urban LST measurements (Wang *et al.*, 2023). Established previously in this section (2.3.1), the ability to generate urban air temperature measurements at the resolution of satellite LST would be highly beneficial for UHI research. As the relationship between SUHI and CUHI is complex and nonlinear, these studies utilise a wider range of models (15 different methods are found in a recent review by Wang et al (2023)), such as random forests and neural networks, which can capture more flexible relationships. Often these studies also employ linear regression

models as a type of yardstick model, by which comparisons to the chosen nonlinear model can be made (dos Santos, 2020; Wang *et al.*, 2023).

Circulation models

An alternative approach used to examine the UHI is to use physics-based circulation models, to directly represent the processes involved with its formation via these climate, or circulation, models. With climate models, the overarching narrative for use in studying the UHI is a trade-off between computational expensive, which limits studies to a single city, and resolution, which if too coarse fails to capture the UHI. These models have the benefit of generating both air temperature projections, which can be used to assess the CUHI, and LST projections, which can be used with observations to validate the models.

Urban areas make up a small fraction of the Earth and are small in comparison to the grid size of most global climate models (GCMs), however, urban areas are of particular significance as such a high percentage of the world's population is concentrated in these areas. A more detailed picture of the physical processes can be given using regional climate models (RCMs), which have higher spatial resolutions. Scales of these models are coarser than the detailed Computational Fluid Dynamics models (see appendix section A.1), therefore some representation of the urban surface must be made by means of parameterisations, representing the city area by a simplified version of its true form. Information on urban parameterisations can be found in the appendix, section A.1.

The grid resolution of GCMs means they are not often used as a standalone tool to examine the UHI, although there are some exceptions. GCMs with embedded urban surface models have been used to simulate the impact of climate change on cities at a coarse (0.9375° x 1.25° resolution) scale (Fischer *et al.*, 2012; Oleson, 2012). These models focus on the impact of the CUHI and climate change on cities, analysing what climate change means for an urban area as opposed to a rural one. For example, Fischer et al (2012) studied heat stress across Europe and Africa, and found nights with extremely high heat stress occur more in cities than in the surrounding rural areas. However, these models do not have the capability to model the UHI on a finer scale to give intra-urban patterns or examine smaller cities (which are the focus of this thesis). The coarse scale does not allow for important features and feedbacks to be accounted for, for example urban expansion (Lauwaet *et al.*, 2016), and anthropogenic heat and moisture (Fischer *et al.*, 2012). The resolution also does not allow for temperatures at rural and urban reference locations to be extracted and compared to quantify the UHI in the same way as it is done for observations (Hamdi *et al.*, 2014). These drawbacks mean these models are not commonly used in UHI studies.

RCMs dynamically downscale projections from a GCM, or weather forecasting model to give results at a high spatial resolution. Some examples of these models used in UHI studies can be found in appendix Table A.1.3. These models are commonly initially developed for weather prediction, but often used to make projections of future climate. RCMs are useful both for examining how the UHI might change under future climate change scenarios (McCarthy *et al.*, 2011; Kusaka and Takane, 2012; Argüeso *et al.*, 2014; Hamdi *et al.*, 2014; Tewari *et al.*, 2017) and to explore understanding of the processes and highlight how it can be mitigated (Miao *et al.*, 2009; Sarkar and de Ridder, 2011; Wouters *et al.*, 2013; Salamanca and Mahalov, 2019). As to be expected for models providing detailed outputs (in comparison to a GCM), the downsides of using RCMs to simulate the UHI is they take a long time to run for an individual city, which can be limiting if a goal is to study large numbers of different cities, or to simulate the UHI over a large number of years (Lauwaet *et al.*, 2015). For these reasons RCM studies are mostly limited to a single city, and some of the higher resolution models are only used to model the present CUHI.

A fairly recent development in models used to study the UHI is the boundary layer climate model UrbClim (B. Zhou *et al.*, 2016; Garciá-Diéz *et al.*, 2016; Lauwaet *et al.*, 2016; Sharma *et al.*, 2016). This model was developed to address the computationally intensive nature of other urbanised mesoscale climate models such as RCMs, with the purpose to be used for urban climate projections. The model uses the simplest parameterisation scheme and simple 3-D model of the lower atmosphere rather than an RCM to ensure a simple scheme, designed to be fast to run. In validation exercises UrbClim was found to fulfil this purpose and ran two orders of magnitude faster than high resolution mesoscale climate models such as comparison model ARPS, in Table A.1.3 (De Ridder *et al.*, 2015). Its low computational cost also gives UrbClim the possibility of reaching resolutions of 250m (Lauwaet *et al.*, 2016). In accordance with its development purpose, the strengths of the model lie in urban climate projections, and it does not replace the need for the mesoscale atmospheric models when the focus of the study is on more complex urban interactions between the city and the atmosphere (Garciá-Diéz *et al.*, 2016). Typically, studies using this model focus on its validation against present UHIs (B. Zhou *et al.*, 2016; Sharma *et al.*, 2016) or other models (Garciá-Diéz *et al.*, 2016) due to its relatively recent development. Despite this model having a faster run time than an RCM, it is still relatively slow in comparison to a statistical or machine learning model, and therefore is suited to the study of an individual city.

Other modelling approaches

Other modelling approaches examine processes in the microscale, focusing on a building or single street, which is not the objective of this thesis. These include Computational Fluid Dynamics (CFD), which directly compute processes such as the temperature and velocity of

air based on the laws of fluid flow (Gagliano *et al.*, 2017), and lab based models, which are experimental physically constructed models representing a city. They are used in conjunction with heating chambers or wind tunnels to examine microscale processes. More details on both these modelling approaches can be found in the appendix section A.1.

2.4 INFLUENCE OF WEATHER AND CLIMATE

The contributing factors which result in the formation of the CUHI/SUHI (section 2.2) are related to climatic and meteorological conditions. By comparison of the CUHI and SUHI in section 2.3.1, it was seen that windspeed has a large influence on CUHI – SUHI differences. Therefore, in order to make connections or comparison between the two, any assessment of how windspeed impacts both is made. Cloud cover is important for the context of examination of the SUHI, due to the potential influence of cloud contamination on satellite sensed LST measurements. This means an understanding of the likely consequences of this cloud bias can be gained by reviewing how cloud cover impacts the UHI.

The second part of this section reviews how the UHI is influenced by climate. This is key, as an understanding how current climates interact with the UHI is the basis for understanding how changes in climate may impact its behaviour in the future.

2.4.1 Windspeed and Cloud

Calm, clear weather conditions are shown to result in stronger development of the UHI, and cloudy conditions weakening its intensity (Unwin, 1980; Yague *et al.*, 1991; Mihalakakou *et al.*, 2002; Santamouris, 2015). This phenomenon has been measured both for the daytime (Schatz and Kucharik, 2014) and night-time CUHI (Santamouris, 2015; Feng *et al.*, 2019; Q. Huang *et al.*, 2020). During the night, the CUHI is at its greatest and this is where the effect is seen the most (Schatz and Kucharik, 2014). The reason for these observed effects is that these weather conditions affect the mechanisms resulting the formation of the urban heat island in two ways. Cloud cover impacts the radiation exchanges, limiting the amount of solar radiation reaching the Earth's surface and trapping terrestrial radiation. Therefore, the rate of evaporative (relating to the solar radiation) and radiative (relating to the terrestrial radiation) cooling is impacted by the cloud cover. At night, this difference in the rate of radiative cooling between urban and rural areas (section 2.2) is an important factor for the formation of the heat island. Therefore, it follows that when this is dampened the CUHI intensity also decreases. Winds impact the turbulent and convective fluxes and advection, moving heat away from the urban surfaces, and cooler air from rural areas enters the urban boundary layer and mixes with warm urban air. Downwind, rural areas experience the opposite, with warmer urban air mixing with the cooler rural air (Wang *et al.*, 2020). High wind speeds have been found to prevent the

development of the night-time CUHI (Alonso *et al.*, 2007). In a study of Buenos Aires, strong winds were found to result in the formation of an inverse CUHI (or urban cool island, UCI) during the daytime, where the city was cooler than the surrounding rural area (Figuerola and Mazzeo, 1998). In order to remove these complex effects of wind and cloud, most CUHI studies are limited to the calm, clear conditions optimal for its development (Ackerman, 1985; Morris and Simmonds, 2001).

The impact of these conditions on the SUHI is harder to quantify, as the satellite sensed LST cannot be generated when cloud cover is present (see section 2.3.1). A higher relative humidity, which is associated with more cloudy conditions, is found to weaken the intensity of the night-time SUHI (Lai *et al.*, 2021). This is the same mechanism as described for the night-time CUHI, where the cloud cover limits the radiative cooling in the rural area to a greater extent than in the urban, and the nocturnal cooling rates of the two areas become more equal. The night-time SUHI also is found to decrease with increasing windspeeds (Feng *et al.*, 2019; Lai *et al.*, 2021), although Lai et al (2021) finds the windspeeds must be strong in order to do so, as here the mechanism is to cool urban surfaces through convection, in contrast to the movement of the cool and warm air in the CUHI.

Often cities are located in coastal areas, where sea breezes arise during the daytime due to land-sea temperature gradients. The presence of the CUHI intensifies the effect by increasing this gradient. The interaction of the CUHI with the daytime sea breeze is found to be significant and influence the city climate (Yoshikado, 1994; Acero *et al.*, 2013; Santamouris, 2015; Y. Zhou *et al.*, 2019; J. Yang *et al.*, 2022), with models showing the CUHI accelerates the sea breeze (Freitas *et al.*, 2007). Sea breezes decrease CUHI intensity by removing the warm urban air and replacing it with cool sea air, and therefore must be considered when studying the UHI of a coastal city (Kim and Baik, 2002). For example, an inland rural reference station compared to a coastal urban area would not reflect the true influence of urbanisation (Sakakibara and Owa, 2005). At night this sea breeze is reversed as the land cools rapidly in comparison to the sea. The urban area dampens this night-time breeze, due to both its friction and the CUHI, as its higher temperature now decreases the land sea temperature difference (Martilli, 2003). The topography of the surrounding area also influences the CUHI, with katabatic winds[2] distorting the nocturnal CUHI for cities located in areas surrounding by hills or mountains (Deosthali, 2000; Ohashi and Kida, 2002; Alcoforado and Andrade, 2006), or mountains even isolating the city from the cooling effect of the land-sea breeze (Charabi and Bakhit, 2011).

[2] *Katabatic winds are downslope winds, typically on a mountain, which are driven by temperature differences between the cooler air at the top of the slope versus that further down (Katabatic wind - AMS Glossary, 2012).*

The interaction between sea breezes and the SUHI have been less well studied, as it is related to the movement of air so the relationship with the UHI is more appropriate. Wang et al (2020) finds the CUHI-SUHI correlation is not as strong for cities with sea or mountain breeze effects, indicating the sea breeze effect on the SUHI is to a smaller extent.

In summary, two key points arise from the above. First, the CUHI tends to be of smaller magnitude in cloudy conditions, so SUHIs not calculated due to satellite images rendered unusable on days of high cloud cover are likely to have lower SUHI magnitudes than their counterparts on non-cloudy days. Secondly, CUHIs in coastal or mountainous/hilly areas are likely to have different behaviour to those that are not, due to the presence of localised wind phenomena, which is taken into consideration in the methods of this thesis by limiting cities to in-land and in relatively flat surroundings.

An additional point regarding the interaction of the UHI with the local climate is that the presence of the cities itself can impact other meteorological features in addition to temperature. This includes the formation of country breezes, alteration of precipitation patterns, and increases in cloud cover. More information on the mechanisms behind these urban influences can be found in the appendix, section A.1.

2.4.2 Climate

The factors that lead to the formation of the UHI are both related to the city morphology and the climate, as seen in section 2.2. Figure 2.5 shows a simplified schematic of some of these factors, split into whether they part of the urban or the rural form. In blue, the climate related properties can be seen. For example, the amount of precipitation in a region will impact the difference in moisture availability between urban and rural areas, and the solar radiation will determine how much evaporative cooling takes place. The vegetation abundance and type are also strongly linked to climatic factors; arid environments are likely to contain sparse shrubland or deserts, whereas warm, humid climates will have dense forests and grasslands or crops.

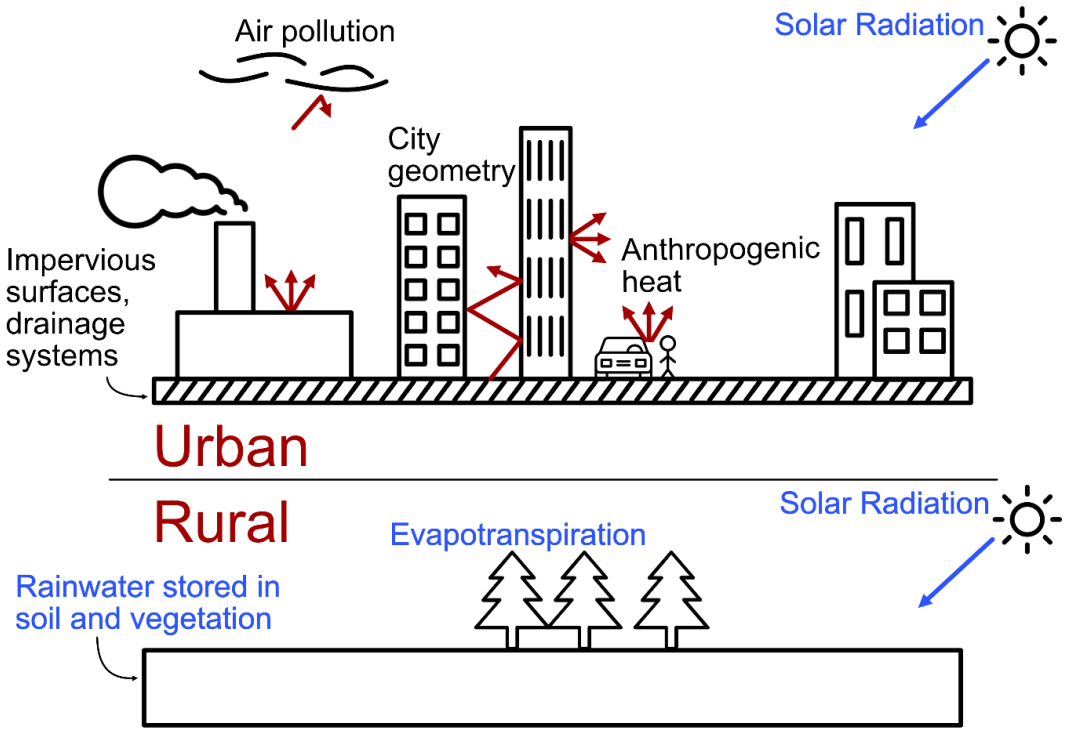

Figure 2.5 A comparison of the Urban and Rural form, showing how differences in the two lead to the formation of the UHI. Factors relating to the urban form are black and climate related properties are blue. Air pollution can be influenced by climate but is not considered in this thesis so is left in black.

A notable difference based on climate is the existence of a negative UHI, or urban cool island (UCI). Urban cooling can be seen in deep and narrow street canyons, where the street level is in continuous shade, limiting absorption of short-wave radiation (Oke, 1978). UCIs are most prominent in dry and arid climates (Bornstein *et al.*, 2012). This is driven by differences in convection and evapotranspiration due to the lack of vegetation and dry soils, desert or stone in rural areas. In these climates, when compared to rural areas, urban land is on average 20% more efficient at removing heat from the surface by convection. Urban trees and lawns contribute to this effect by evaporative cooling (Zhao *et al.*, 2014). This phenomenon exists for both the CUHI and SUHI (Rasul *et al.*, 2017).

The moisture content of rural soils has a big part to play in the formation of the UHI. Wet soils have high thermal admittance (μ, W/m^{2}K, see section 2.2), so heat up and cool down slowly, whereas the converse is true for dry soils. The properties of the urban materials such as concrete mean a city has a thermal admittance somewhere in the middle of a wet and dry soil (Bornstein *et al.*, 2012). Bornstein (2012) uses this information, along with seasonal distribution of regional precipitation to theorise CUHI behaviour for different climates, which are summarised in Table 2.2.

Table 2.2 Predicted behaviour of the CUHI in different climates (Bornstein et al., 2012).

City type	Köppen-Geiger Climate Classification	UHI maximum	UHI minimum
Warm/hot low latitude cities surrounded by wet rural soils	-Hot tropical climates at the equator (A) -Mediterranean climates with warm wet summers (Cfa)	Daytime and wet season	Nighttime and dry season urban cool island
Warm cities with dry rural soils	-Mid latitude dry climates on the Sahara and west side of the continents (B) -Marine Mediterranean climates with cool dry summers (Csb)	Nighttime	Daytime urban cool island
Cold cities	-Cold high-altitude climates in Tibet and the Andes (H) -High latitude cold snowy winter climates in Canada and Siberia (D) -High latitude cold polar climates in Antarctica, Greenland and Northern Canada and Asia (E)	Winter and night-time	Summer and daytime

In the table, the Köppen-Geiger climate classifications are listed. This classification system is a method of categorising climates based on long-term temperature and precipitation measurements and their cycles throughout the year, consisting of five main classes and 30 subgroups (Beck *et al.*, 2018). Table 2.3 shows the main climate categories based on two

letters. More detailed classifications based on additional criteria can add a third letter to the classification, to categorise further. The Köppen-Geiger climate classification locations can be seen in Figure 2.6. Linking this back to the areas where the UHI is understudied, this can be compared with Figure 2.4, mainly consisting of areas under around 40 ° N, which will be the focus of the thesis to address research gaps. Here, there exists large areas of A and B climate classifications (equatorial and arid), and additionally areas in the C classification (warm temperate).

Table 2.3 Köppen-Geiger main climate groups, first 2 letters of classification. Taken from Kottek et al (2006). T_{min} (Mean temperature of coldest month), T_{max} (Mean temperature of warmest month), P_{min} (Precipitation of driest month), P_{ann} (Annual precipitation), P_{smin} (lowest monthly precipitation in summer half-year), P_{wmin} (lowest monthly precipitation in winter half-year), P_{smax} (highest monthly precipitation in summer half-year), P_{wmax} (highest monthly precipitation in winter half-year), P_{th} (threshold precipitation, calculated dependent on annual temperature). Values given are per month.

Climate Type	**Description**	**Criterion**
A	**Equatorial climates**	$T_{min} \geq +18$ °C
Af	Equatorial Rainforest, fully humid	$P_{min} \geq 60$ mm
Am	Equatorial monsoon	$P_{ann} \geq 25$ mm $(100 - P_{min})$
As	Equatorial savannah with dry summer	$P_{min} < 60$ mm in summer
Aw	Equatorial savannah with dry winter	$P_{min} < 60$ mm in winter
B	**Arid climates**	$P_{ann} < 10\ P_{th}$
BS	Steppe	$P_{ann} > 5\ P_{th}$
BW	Desert	$P_{ann} \leq 5\ P_{th}$
C	**Warm temperate climates**	-3 °C $< T_{min} < +18$ °C
Cs	Warm temperate climate with dry summer	$P_{smin} < P_{wmin}$, $P_{wmax} > 3\ P_{smin}$ and $P_{smin} < 40$ mm
Cw	Warm temperate climate with dry winter	$P_{wmin} < P_{smin}$ and $P_{smax} > 10\ P_{wmin}$
Cf	Warm temperate climate, fully humid	neither Cs nor Cw
D	**Snow climates**	$T_{min} \leq -3$ °C
Ds	Snow climate with dry summer	$P_{smin} < P_{wmin}$, $P_{wmax} > 3\ P_{smin}$ and $P_{smin} < 40$ mm
Dw	Snow climate with dry winter	$P_{wmin} < P_{smin}$ and $P_{smax} > 10\ P_{wmin}$
Df	Snow climate, fully humid	neither Ds nor Dw
E	**Polar climates**	$T_{max} < +10$ ◦C
ET	Tundra climate	0 °C $\leq T_{max} < +10$ °C
EF	Frost climate	$T_{max} < 0$ °C

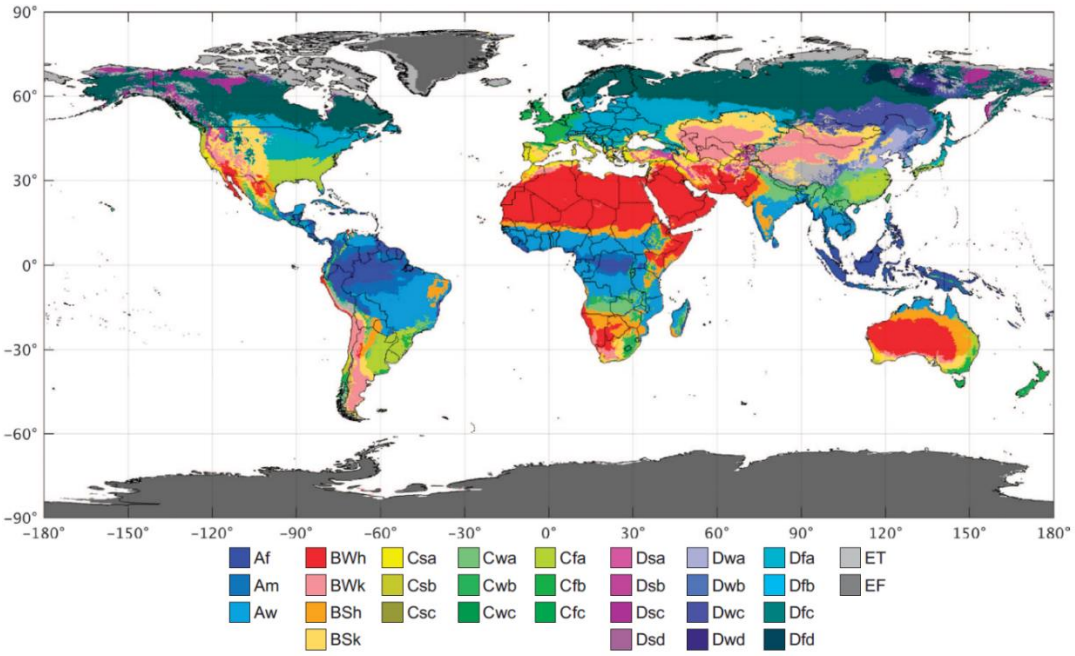

Figure 2.6 Köppen-Geiger classifications (1980-2016) (Beck *et al.*, 2018).

In reality for UHI studies generalising behaviour by climate zones is not so straightforward. Table 2.4 shows diurnal and seasonal patterns for some CUHI studies, grouped by climate. Comparison with Table 2.2 shows for climates in the A classification, the highest magnitudes would be expected to be during the daytime and the wet season, whereas in Table 2.4, these cities have the strongest CUHI at night and during the drier season. For climates in the dry (B) and marine Mediterranean (Csb) classifications, the behaviours are as expected for 2 out of 3 cities, with the maximum intensities of the CUHI occurring at night. The cold cities (H, D, E climates) show the expected behaviour, with the maximum CUHI occurring during the night, although some cities do not show a distinct diurnal cycle. Therefore, it can be seen that whilst climate is an important predictor of CUHI behaviour, it cannot alone determine the characteristics, and there are other variables that must be considered. For example, wintertime peaks in CUHI intensity for the coastal cities Lisbon and Bilbao are thought to be due to the sea breeze effect during summer (Alcoforado and Andrade, 2006; Acero *et al.*, 2013). This confirms coastal cities should be considered in a separate category to inland (section 2.4.1). An additional factor can be that grouping variables in any way, here done via Köppen-Geiger classifications, will lead to information being lost as a continuous variable is turned into a categorical.

Table 2.4 Diurnal and seasonal patterns of some CUHI studies.

Climate	Cities studied	Diurnal pattern	Seasonal pattern	References
-Hot tropical climates at the equator (A) -Mediterranean climates with warm wet summers (Cfa)	Singapore Bangkok, Chiang Mai, Songkhla (Thailand) Milan (Italy)	Strongest CUHI at night	Strongest during the drier season	(Chow and Roth, 2006; Jongtanom *et al.*, 2011; Pichierri *et al.*, 2012)
-Mid latitude dry climates on the Sahara and west side of the continents (B) -Marine Mediterranean climates with cool dry summers (Csb)	Muscat (Oman) Gaborone (Botswana) Eilat (Israel)	Strongest CUHI at night for Muscat, Gaborone, day for Eilat	Strongest during summer for Muscat and Eilat, winter for Gaborone	(Jonsson, 2004; Sofer and Potchter, 2006; Charabi and Bakhit, 2011)
-Cold high-altitude climates in Tibet and the Andes (H) -High latitude cold snowy winter climates in Canada and Siberia (D) -High latitude cold polar climates in Antarctica, Greenland and Northern Canada and Asia (E)	Fairbanks, Barrow (Alaska) Salekhard, Vorkuta, Nadym, Novy Urengoy (Russia) Seoul (Korea)	Strongest CUHI at night in Fairbanks, Seoul Some cities in Russia have no clear diurnal cycle in winter	Strongest during autumn and winter	(Magee *et al.*, 1999; Kim and Baik, 2002; Hinkel *et al.*, 2003; Lee and Baik, 2010; Konstantinov *et al.*, 2018)

-Temperate Oceanic Climates (Cfb)	Melbourne (Australia) Birmingham, London (UK) Bilbao (Spain)	Strongest CUHI at night	Weakest CUHI is in winter, strongest varies per city, autumn, summer and spring	(Unwin, 1980; Morris and Simmonds, 2001; Kolokotroni and Giridharan, 2008; Acero *et al.*, 2013)
-Mediterranean climates with dry summers and mild wet winters (Csb)	Barcelona, Madrid (Spain) Lisbon (Portugal) Adelaide (Australia)	Strongest CUHI at night	Strongest during summer for Madrid and Adelaide, winter and autumn for Barcelona and Lisbon	(Yague *et al.*, 1991; Moreno-Garcia, 1994; Alcoforado and Andrade, 2006; Erell and Williamson, 2007; Martin-Vide and Moreno-Garcia, 2020)
-Monsoon influenced humid climates (Cwa)	Delhi, Guwahati (India) Mexico City (Mexico)	Strongest VUHI at night	Strongest in summer for Guwahati, but found constant in Mexico City	(Cui and de Foy, 2012; Mohan *et al.*, 2012; Borbora and Das, 2014)

Background climate is a strong influencer on the seasonal patterns of the SUHI. In a global study, Chakraborty (2019) found arid regions to have distinct seasonal and diurnal patterns, with higher nocturnal SUHI intensities and seasonal two peaks in the year. Fu and Weng (2018) found the largest differences in seasonal temperature cycles in US cities were in tropical regions. As with CUHI studies, there are no clear rules to quantify the effect of background climate on a SUHI. The use of remote sensing is further complicated for tropical

cities, where cloud coverage problems can lead to SUHI data only being available for the dry season (Tran *et al.*, 2006).

To combat the loss of information by putting cities into climate groups, individual climate-related measures can be studied with relation to the UHI. As this requires a larger number of cities to sample a spread of different climates, these studies tend to look at the SUHI so they can utilise the global availability of satellite sensed LST data. The relationships with precipitation and relative humidity are discussed in the following for the SUHI mostly.

In the US, the annual mean midday SUHI intensity is found to be strongly positively correlated to precipitation (although night-time intensity was not), with cities in humid climates having higher intensities than those in dry regions (Zhao *et al.*, 2014; Gu and Li, 2018; Li *et al.*, 2019). This positive relationship between precipitation and SUHI intensity is also found in global studies, with saturation at high precipitation values (Manoli *et al.*, 2019) . Typically this is thought to be caused by a reduction in evaporative cooling in cities compared to rural areas (rural areas contain more vegetation and water is stored in soils) (Li *et al.*, 2019), although Zhao (2014) finds the main driver is convection. In humid climates rural land is densely vegetated and aerodynamically rough, which enhances convection by increasing the surface area available for this purpose, therefore dissipating more heat. In dry climates the urban land is rougher than rural, and the convection efficiency of the urban area is higher than the rural. This again illustrates the need to carefully consider comparisons of the SUHI and CUHI, as this mechanism will not have the same cooling effect on air temperatures.

A number of studies find a negative correlation between relative humidity and the CUHI (Kim and Baik, 2002, 2004; Santamouris, 2015; Hu *et al.*, 2019; Lai *et al.*, 2021) and SUHI (Hu *et al.*, 2019; Lai *et al.*, 2021), although it appears counterintuitive as lower relative humidity means there is drier soils and therefore less rural evaporation. There are numerous theories for why this relationship exists. High relative humidity occurs when there is higher cloud cover, and therefore less solar radiation reaching the city and rural areas to create strong differences in evaporative cooling rates. Due to its higher thermal admittance, mentioned earlier in this section, saturated wet soil absorbs more solar radiation and therefore stays warmer for longer. This means the wetter rural soils retain heat (Hu *et al.*, 2019). Roth (2007) and Kim and Baik (2002), who find the relationship in the CUHI, attribute the negative relationship to high water vapour content in the air, meaning there is less of a deficit for the evaporative cooling to take place. Lai et al (2021) (who study the SUHI) adds further to this that the high atmospheric water vapor also reduces the radiation load at the surface, meaning less solar radiation is going into heating the urban and rural surfaces.

A final important characteristic related to climate is the vegetation, as vegetation type, abundance and seasonal cycle is strongly linked to climate (Richardson *et al.*, 2013). Globally, the less vegetated cities have stronger SUHI intensities (Clinton and Gong, 2013), with the strongest SUHIs occurring when rural areas have large amounts of vegetation in comparison to urban, and negative SUHIs when urban areas contain more vegetation than their rural counterparts (Peng *et al.*, 2012). The CUHI/SUHI interacts with the vegetation itself, influencing the growing season of vegetation. In North America and in Northern Hemisphere cities (≥30° N) the CUHI was found to extend the growing season length (Zhang *et al.*, 2004; Wang *et al.*, 2019) and in a tropical city in Uganda, the growing season was shortened (Kabano *et al.*, 2021).

Understanding how climate can influence the CUHI is central to finding successful mitigation measures in city planning. Measures such as increasing green cover and albedo will be most effective in dry regions, whereas the cooling of tropical cities will not respond in the same way, and require different solutions to their counterparts in temperate regions (Manoli *et al.*, 2019).

2.5 VARIATIONS OF THE UHI IN TIME AND SPACE

2.5.1 Diurnal cycle

There is a need to understand the diurnal cycle of the UHI to contextualise the measurements taken at particular times (in the case of using satellite measures to determine the SUHI, these will be the overpass times). Are these measurements taken when the UHI is at its greatest magnitude, its smallest, or mid-range? In this section, the diurnal cycle of the CUHI will first be described, then the SUHI. As outlined in 2.3.1, studies making direct comparisons between the two have shown the peaks to occur at different times.

The CUHI intensity is in most cases greater at night then it is in the day, as shown in Table 2.4. This is well documented and found across many different climates, from temperate regions to semiarid areas (Sundborg, 1950; Vukovich, 1971; Roth and Oke, 1989; Oke *et al.*, 1992; Kim and Baik, 2002; Chow and Roth, 2006; B. Zhou *et al.*, 2019; Salamanca and Mahalov, 2019), although in some cases there is no change from day to night (Konstantinov *et al.*, 2018, Polar climate) or daytime CUHI intensity is greater (Sofer and Potchter, 2006, Arid coastal climate).

The peak in intensity seen at night is due to the difference in cooling rates between urban and rural areas. It can be explained by the reasons given for the formation of the CUHI given in section 2.2 (surface geometry, thermal properties of the urban fabric, anthropogenic heat and

air pollution). Geometry of the buildings leads to less thermal radiation escaping to the sky (urban surfaces are more closed off from the free atmosphere and sky), thermal properties of urban areas versus rural leads to more retention of heat in the urban environments, and finally anthropogenic heat from buildings act as internal heat sources (Johnson *et al.*, 1991). Figure 2.7 shows idealised features of a CUHI from Oke (1982). A rural area cools at a faster rate than its urban counterpart as solar radiation decreases in the evening, then heats at a faster rate as solar radiation increases again in the morning hours after sunrise. This pattern has been shown to exist for Vancouver, a temperate mid-latitude city and for Ouagadougou, Burkina Faso, an arid tropical city. Therefore, it can be theorised that the basic physics of the urban boundary layer remain the same for all urban areas, and the differences in boundary conditions such as surface cover, ground conditions and weather are drivers of any variations (Oke *et al.*, 2017). Oke (1999) speculates that urban areas around the world are actually climatically more similar to each other than to their rural surroundings, which include forests, fields, swamps, deserts, snow and more.

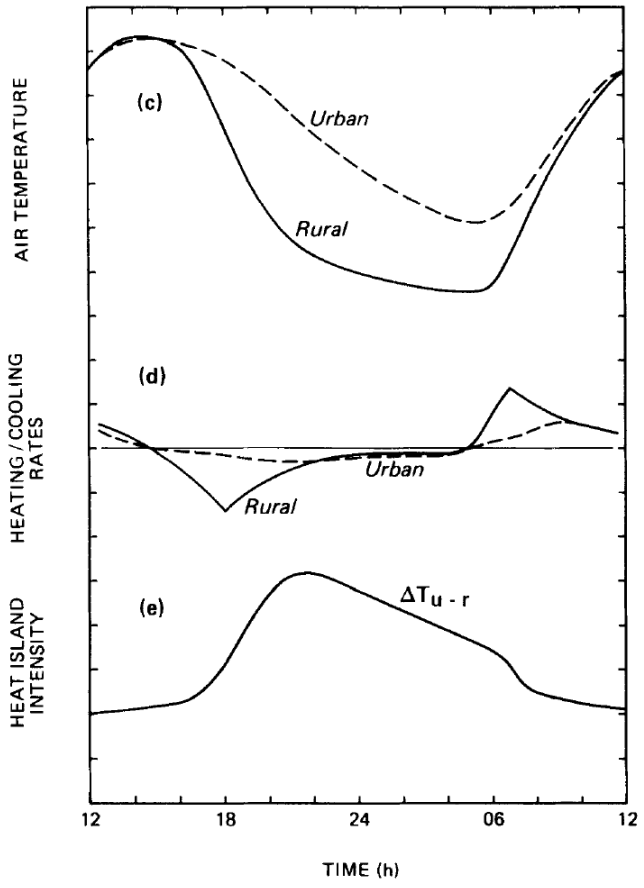

Figure 2.7 An idealised form of temporal features of the urban heat island. Showing air temperature, cooling and heat island intensity (Oke, 1982).

Due to weekday and weekend differences in anthropogenic energy use, weekly diurnal cycles also exist. Figure 2.8 taken from Sailor (2011) shows a typical diurnal cycle of anthropogenic heat on weekends and weekdays. Energy use on weekend and holidays are typically lower than those on workdays (Sailor, 2011). In Buenos Aires, where 60% urban movement was attributed to work (as a comparison in San Francisco, work was only 24%), Figuerola and Mazzeo (1998) found the maximum CUHI intensity fell 1°C on weekends in comparison to weekdays.

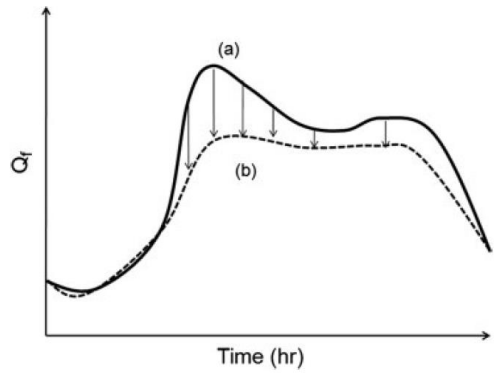

Figure 2.8 Typical shapes of diurnal profiles of anthropogenic heating for a) workdays and b) non-workdays (Sailor, 2011).

This diurnal cycle of anthropogenic emissions is rarely included in urban parameterisation schemes (appendix section A.1), as it is often considered to be small and difficult to estimate. In the case of London, anthropogenic heat output is believed likely to increase in the future, and evidence suggests that more accurate estimates should be considered in future research (Bohnenstengel *et al.*, 2014).

Satellite data has low temporal resolution, as there are limited overpasses over a region a day, and detailed diurnal cycles of the SUHI cannot be studied. The main comparison is made of nocturnal SUHIs versus daytime SUHIs. Generally, day-time SUHI is found to be higher than night-time (Schwarz *et al.*, 2011; Peng *et al.*, 2012, 2018), although the opposite is found for arid areas (Wu *et al.*, 2019). Ma et al (2021) finds the controlling factors of the night-time SUHI for cities in China to be due to variables relating to the urban from such as city area, as opposed to the daytime SUHI which is more connected to natural factors such as climate. Peng et al (2012) attributes albedo difference and night-time lights (a proxy for anthropogenic activity) to the formation of the SUHI at night, and differences vegetation activity to be an indicator for daytime SUHIs. Night-time SUHI shows less seasonal variations, which follows these observations, as natural factors such as climate and vegetation follow seasonal cycles but city-form related properties, such as size or building height, do not (Wu *et al.*, 2019).

2.5.2 Spatial variability within a city

The measurements used to quantify the SUHI (section 2.3.1) result in the phenomena being reduced to a single number, defining a difference between urban and rural temperature. However, in Figure 1.2, isotherms representing the CUHI of London are seen, showing the extent to which the CUHI impacts will be felt by a city inhabitant is conditional on where exactly in the city they are. The figure shows the characteristic spatial feature of the CUHI, represented by a 'thermal island'; a sharp incline at the urban perimeter, a rough plateau where most of the urban area is and a peak in the core of the city (Oke, 1981; Tiangco *et al.*, 2008). The internal pattern of a CUHI is controlled by the land use and building densities within (Karl *et al.*, 1988). Hot spots are in the urban core, industrial areas (Kumar *et al.*, 2023) and densely populated areas of the city (Cao *et al.*, 2021), whilst cool areas are found in the city parks and green spaces (Jonsson, 2004; Azevedo *et al.*, 2016). Based on current studies, an urban green space is on average 1°C cooler in air temperature than its non-green equivalent (Bowler *et al.*, 2010) during the day, and small wooded areas in cities had a cooling effect that was still apparent 100m away (Shashua-Bar and Hoffman, 2000). The cooling effect of city parks also exists at night, and can extend to over 1100m from a park border (Upmanis *et al.*, 1998),

The majority of studies examining spatial pattern utilise satellite sensed LST data to examine the SUHI, as air temperature measurements in uniform spatial distances are uncommon (just four cities have temperature sensor networks in review Table A.1.1). There is agreement with CUHI behaviour, with the warmest areas of cities found to be the highly built up industrial and commercial areas, and the coolest parks and vegetated areas, across a range of climates (Roth and Oke, 1989; Tran *et al.*, 2006; Tiangco *et al.*, 2008; Xiong *et al.*, 2012; Mallick *et al.*, 2013; Bokaie *et al.*, 2016; Geletič *et al.*, 2019; Equere *et al.*, 2020). Negative correlations have been found between vegetation abundance and surface temperature in urban areas (Tran *et al.*, 2006; Tiangco *et al.*, 2008; Li *et al.*, 2011; Bokaie *et al.*, 2016) and cities with less vegetation are found to have a large SUHI (Clinton and Gong, 2013). For dry, arid climates, where the SUHI/UHI is replaced by a UCI (section 2.4), there is a negative relationship between building density and surface temperature. Densely built up city centres and green spaces exhibit lower surface temperatures than the surrounding area, attributed to the increased availability of moisture for the SUHI (Rasul *et al.*, 2015; B. Zhou *et al.*, 2019).

The height of buildings are important factors in determining the spatial characteristics of the CUHI and SUHI. Areas of high-rise buildings can be found cooler than areas of low rise buildings in terms of LST (in San Francisco, Singapore, Shanghai) (Nichol, 1996; Li *et al.*, 2011; Equere *et al.*, 2020) and air temperature (in Portland) (Hart and Sailor, 2009) due to shading, a greater portion of horizontal surface for heating and a reduced sky view factor. Sky view factor is a measure of the radiation output from a point that is intercepted by the sky,

determining the fraction of a hemisphere over a point that is occupied by the sky (Oke, 1981). It should be noted that low sky view factors are also reasons for the nocturnal UHI, as mentioned in section 2.2, see Figure 2.3.

2.5.3 Long term trends

As explained in section 1, future pressures of climate change and increasing urban populations make this aspect of UHI research a vital issue. This section outlines how climate change and urban expansion have been shown to interact with the CUHI/SUHI in the past, and what the expected impact may be in the future.

More longstanding cities tend to show little change in the CUHI. The impact of urbanisation on the CUHIs of London and Vienna remain constant throughout the twentieth century, indicating the urban warming happened earlier than records began (Jones *et al.*, 2008; Jones and Lister, 2009; Bassett *et al.*, 2021). The relative strength of New York's CUHI only grew by approximately 0.5°C since 1900. It is noted that with areas of New York becoming more built up vertically, the expectation would be that this growth should be greater (Gaffin *et al.*, 2008).

However, in other cases there is a clear link between CUHI intensity and increasing urbanisation. Manchester CUHI increased in intensity from 2000 to 2009, as the urban site became more urban throughout the study period and lost green spaces (Levermore *et al.*, 2018). Beijing and Wuhan, Chinese cities which have experienced rapid urbanisation in the past 50 years, are found to have increased in temperature at a faster rate than rural reference stations (Ren *et al.*, 2007), as have Asian megacities between 1992-2012 (Lee *et al.*, 2020). A study of Fairbanks, Alaska, studies 49 years of temperature records, during which the population increases by 500%, and finds the highest increases in the UHI happened while the largest increase in population occurred (Magee *et al.*, 1999). The cases of London, Vienna and New York suggest saturation of the CUHI exists.

Remote sensing studies have found that SUHI intensity increases with size of the urban area, but the rate of increase tapers off amongst the larger cities. However conclusions are difficult to make, as there are many small cities but only a few large (Zhou *et al.*, 2013, 2017). Based on this, smaller cities are likely more at risk of large increases in UHI magnitudes with urban expansion, and representation of these in CUHI/SUHI future projections is of high importance (and in the objectives of this thesis). SUHI increases in recent years are also driven by climate change. Globally, trends from 2002 to 2021 show that surface warming in urban areas has been increasing at a faster rate than the rural counterparts, with the majority of this increase attributed to background climate change in all areas aside from India and China, where the majority of the increasing trend is due to urban expansion (Liu *et al.*, 2022).

Studies examining the impact of future climate change on the CUHI currently are limited to studies using models such as RCMs or UrbClim (section 2.3.2). In such studies examining the future CUHI, the impact of urban growth often is not considered, however a few studies account for this alongside the climate change scenarios. An assessment of 11 such studies (outlined in appendix Table A.1.4) finds three have included landcover changes due to urban expansion in the future scenario. These studies find that the landcover changes have more of an impact on the CUHI than those related to climate change. Argüeso (2014) finds the impact of urbanisation in Sydney, Australia will have a strong effect on minimum temperature (but little on the maximum) in an assessment of the 2040-2059 under a high emission scenario (SRES A2, Nakicenovic *et al.*, 2000). Tewari et al (2017) models the UHI of Phoenix and Tuscan, US in 2070 under the high emissions RCP8.5 scenario (Stocker *et al.*, 2013). The increased temperatures due to climate change are homogenous throughout the cities, but the temperature increase attributed to urban expansion is unevenly distributed, with higher increases in newly urbanised regions. Silva et al (2022) also uses the RCP8.5 scenario, in this case to examine the CUHI in Lisbon, and finds the largest increases in intensity in the period 2081 – 2100 are during the night, due to an increase in urban landcover combined with a decrease in greenspace.

Studies modelling the impact of the CUHI under climate change scenarios with no urban expansion find a range of different outcomes. In some studies the magnitude to be unaffected by the increase in global temperatures (e.g. McCarthy *et al.*, 2011; Lauwaet *et al.*, 2016; Keppas *et al.*, 2021), in others the CUHI will decrease in intensity (e.g. Oleson *et al.*, 2011; Hamdi *et al.*, 2014) and a couple find increases in summer-time intensity (van der Schriek *et al.*, 2020; Andrade *et al.*, 2023). As the CUHI is a relative measure, these decreases in its intensity can reflect more changes in the rural areas due to climate change. For example, Hamdi (2014) find the decrease in intensity is chiefly due to drier soils in the future. Studies additionally often examine the frequency of future heatwave events, and in Athens (Greece) and Brussels (Belgium), the formation of the CUHI results in an increased number of heatwave events in the city areas in comparison to rural, based on the definition of a heatwave as being days and nights where temperatures remain above a certain threshold (Hamdi *et al.*, 2014; van der Schriek *et al.*, 2020).

The balance between higher resolution and capturing a larger area described in section 2.3.2 can be seen in these examined studies (appendix Table A.1.4). For example, only two (of 11) studies examine more than two cities. In these studies, the resolution is coarse in comparison to those focusing on a single city. Oleson et al (2011) examines global cities with a resolution of 1.9 ° latitude x 2.5° longitude and McCarthy et al (2011) investigates the CUHI of UK cities with a 25 km resolution RCM. Whilst these resolutions are able to capture the CUHI of large

cities, they are much larger than the scale of a medium sized city. The current range of studies regarding the impact of future climate change give information on two types of cities, the first being large cities, and the second the select few cities for which RCM or UrbClim studies have been carried out. Also of note is that currently the majority of studies use emissions only based scenarios, with the most common the RCP8.5 (Stocker *et al.*, 2013), used by 7 of the studies. This does not take into account rural land use changes (which the most recent emissions pathways, the SSPs, do include, see section 2.8.1). The UHI is a product of both urban and rural areas, as increasing or reducing the vegetation in the surrounding area of a city will impact the CUHI (and SUHI), and potentially results may change with a different future scenario choice.

2.6 UNDERSTUDIED CITIES AND GEOGRAPHICAL REGIONS

In section 2.4.2, it was highlighted that the UHI is a product of both city form and climate. Therefore, it follows that to gain a full understanding of the UHI in both present and future climates, a range of city forms and geographical regions must be studied. However, in both these areas within the current literature, there exists research gaps, with a bias towards megacities or large cities and the global North.

Medium sized cities

The UHI is present in cities of all sizes, in fact, evidence of urban warming is not only limited to cities. Villages with just 1000 inhabitants are seen to exhibit a difference in temperature from the rural area (Oke, 1973; Lindén *et al.*, 2015) and urban effects on temperature are detectable for small towns with populations of around 10,000 (Karl *et al.*, 1988). Yet despite this, much of the current research focus of the UHI is on megacities, which represents just 12% of the urban population. Systematic reviews of urban climate studies highlight small and medium sized cities (population under 1 million) as key areas of focus (D. Zhou *et al.*, 2019; Lamb *et al.*, 2019).

Most future urban growth will take place in small cities, yet modelling of the UHI under the effects of climate change is limited to large, well-studied cities. Section 2.5.3 outlined how saturation in the UHI may occur for very large cities, which may lead to different behaviour of these cities under climate change. If climate change impacts are only studied in these large cities, the global impacts of climate change on the CUHI/SUHI may be underestimated. Basing policy in medium sized cities on studies of megacities could lead to ineffective UHI mitigation or adaption solutions being put in place.

The current tools to examine the impact of climate change on medium sized cities lack suitability. GCM studies of CUHI magnitudes based on future climate change have coarse

resolutions, due to the required trade-off between investigating a wider area versus more detail in a smaller area (Section 2.5.3). Whilst it is possible a grid cell may capture the resolution of a megacity, it cannot capture the scale of a medium sized city. RCMs do not provide a solution as smaller cities are more numerous than large cities or megacities. This means it is not possible to examine each one individually as a case study (as is the focus of RCMs due to computational expense, section 2.3.2), as can be done for megacities. An alternative methodology to assess the impacts of climate change on medium sized cities must therefore be developed.

Global South cities

In reviews of CUHI /SUHI studies, the lack of studies focusing on the global south is consistently highlighted (Wienert and Kuttler, 2005; Chapman *et al.*, 2017; Bai, 2018). Wienert and Kuttler (2005) find just 26 out of 150 cities examined were in the Southern Hemisphere. In a review of satellite based SUHI studies, out of a total 492 selected, under 37 included research in Africa, South and Central America and Oceania, and of these, most were as a global scale study rather than focusing on cities predominately in these areas (D. Zhou *et al.*, 2019). Rasul (2017) also highlights the need for the utilisation of remote sensing data to assess SUHI and SUCI of dry and semi dry environments on a large scale. An investigation into studies which assess large numbers of SUHIs, shown in appendix Table A.1.5 , shows a China and Europe in particular are favoured, alongside global studies with no particular regional focus. Of these 23 studies, seven investigate cities within China, six are global, five European, three look at cities within USA, one study looks at megacities in Asia and one study focuses on cities within South America.

Areas in the southern hemisphere are likely to be highly impacted by both the hazards of increased temperatures due to climate change and high levels of urbanisation. GCM projections show regions with potential for high CUHI intensities, such as Middle East, Indian sub-continent and East Africa are all also regions of high population growth (McCarthy *et al.*, 2010). In a global study, Manoli et al (2019) finds background climate is a strong contributor to the SUHI, and ‘one sizes fits all’ solutions will be inefficient in mitigating the SUHI, commenting tropical cities in Africa and South Asia will require different measures outside of increasing green space and albedo modification measures (e.g., white roofs). These are also areas of rapid urban expansion; more than two-thirds of the global urban expansion by 2050 is expected to occur in Asia and Africa (Huang *et al.*, 2019).

Medium sized cities in the global south

The two knowledge gaps of medium sized cities and the southern hemisphere have been highlighted. To give a complete and diverse picture of the UHI, these should be the focus of future studies.

The importance of addressing these knowledge gaps, together with climate change impacts, is highlighted in the IPCC 5th assessment report; "Urban centres in Africa, Asia, and Latin America with fewer than a million inhabitants are where most population growth is expected (UN DESA Population Division, 2012), but these smaller centres are "often institutionally weak and unable to promote effective mitigation and adaptation actions" (Romero-Lankao and Dodman, 2011)" (Revi *et al.*, 2014).

These research problems are to be addressed in this thesis by first of all, selecting cities to study with a focus on including those in the global south. Secondly, setting a population criterion of less than one million. And finally, use of a machine learning model which can take GCM projections and transform them into future SUHI projections for the chosen cities, bypassing the high computational expense of generating these using RCMs.

2.7 SATELLITE REMOTE SENSING PRINCIPLES

The land surface temperature and land cover data used in this analysis are taken from satellite sensor measurements. The following section gives a brief overview of how satellite remote sensing is used to generate land surface temperatures and land cover information.

Electromagnetic Radiation

The foundation of remote sensing is electromagnetic radiation. Satellite sensors detect and measure this electromagnetic energy above the Earth and the data is processed to derive information about the surface below. There are three types of interaction which are of importance for remote sensing. The first of these is transmission, where the radiation passes straight though. The second is absorption, where radiation is absorbed by the atmosphere. Finally scattering, where radiation is redirected in different directions by particles suspended in the atmosphere, or large molecules of atmospheric gases. Figure 2.9 shows the interactions of these processes with the atmosphere and satellite sensor (Tempfli *et al.*, 2009; Campbell and Randolph, 2011).

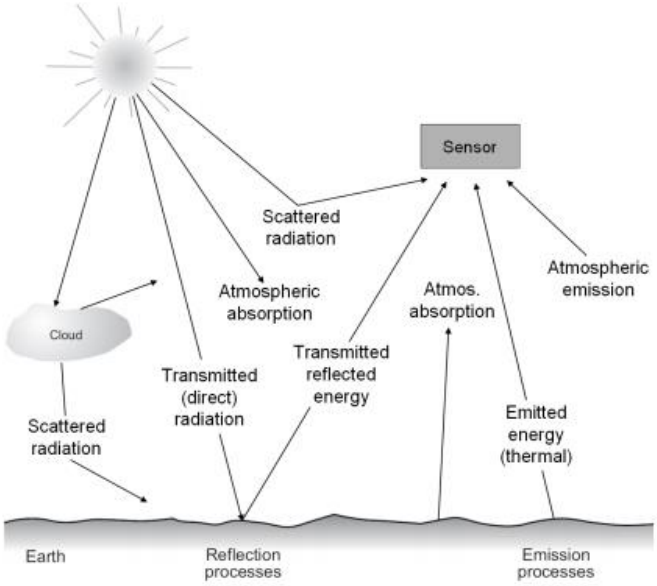

Figure 2.9 Energy interactions in the atmosphere, taken from Tempfli et al (2009).

Atmospheric Transmission Windows

Absorption and transmission are important processes to consider in satellite remote sensing, as radiation absorbed by the atmosphere will not reach the satellite sensors. Most solar radiation is absorbed by molecular oxygen, ozone, water vapour, or carbon dioxide. These gases absorb radiation at different bands, shown in Figure 2.10, resulting in ranges of wavelength able to pass through without absorption by the atmosphere, demonstrated in the figure by the white areas (Alavipanah *et al.*, 2010; Campbell and Randolph, 2011). These ranges are called the atmospheric transmission windows. Transmission windows determine the wavelengths that can be used for remote sensing of surface properties, where use of wavelengths outside of the atmospheric transmission windows will lead to an inaccurate image of the surface below.

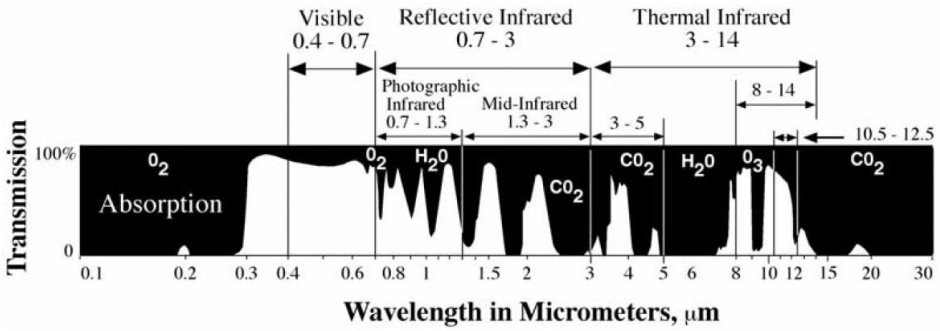

Figure 2.10 Atmospheric windows, figure from Alavipanah et al (2010).

The atmospheric windows used in satellite remote sensing are the 0.4 μm to 2 μm band, comprising mainly of reflected energy, and three windows in the thermal infrared range (two

in the 3 µm to 5 µm band and one from 8 µm to 14 µm) (Tempfli *et al.*, 2009). Infrared sensors typically operate around 3.5 µm to 11 µm (Dash *et al.*, 2002).

Measuring Temperature

Following on from these concepts, by choosing the correct band, the energy emitted by the Earth's surface can be measured using satellite sensors. The wavelength and energy emitted by an object is relative to its temperature, with higher temperatures leading to shorter wavelengths and more energy. Objects on Earth emit in the infra-red spectrum, so this wavelength range is used to determine their temperature.

Emitted energy flux (W m^{-3}) of a surface is measured by the satellite infrared sensor and using equations surrounding the wavelength and energy flux, the temperature of a 'blackbody' (an object which only absorbs and emits radiation, with none reflected) emitting the same energy fluxes is calculated (Campbell and Randolph, 2011). Most objects reflect radiation, and therefore only absorb and emit a certain fraction of radiation in comparison to a blackbody. This fraction is known as emissivity. Emissivity varies from surface to surface, and this aspect of measuring temperature can be calculated in different ways. The surface temperature dataset used in this thesis is generated (by the NASA science team) using a split window approach. This approach uses a classification scheme based on land cover type, by consulting a look up table containing emissivity for various classifications of surface types calculated using experimental data (Snyder *et al.*, 1998). Consequently, by measuring the energy flux at wavelengths in the infrared spectrum emitted by surfaces on Earth, it is possible to calculate temperature, given the emissivity for the surface type is known.

Measuring Surface Characteristics

Surface characteristics of the Earth can be measured by focusing on the visible and infrared energy reflected. The ratios of absorbed, reflected and transmitted energy are dependent on the wavelength and surface material. For materials of interest, the proportion of incident radiation reflected at different wavelengths can be measured experimentally using a field spectrometer, and a reflectance curve generated. Figure 2.11 shows an example of a reflectance curve for vegetation. A library of these reflective curves is then used to gather information on the surface materials, based on the satellite sensor measurements of the radiative energy reflected at each wavelength (Tempfli *et al.*, 2009).

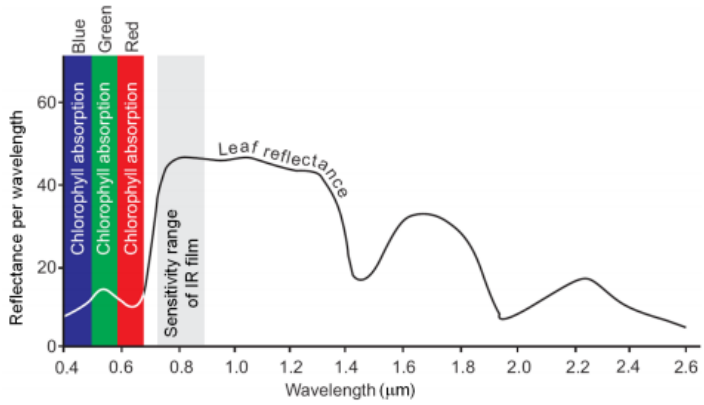

Figure 2.11 Idealised reflective curve for healthy vegetation, from Tempfli (2009).

2.8 Climate projections and the Coupled Model Intercomparison Project

Climate models are representations of the climate system based on equations of physical processes, parameterisations and observations (Goosse *et al.*, 2010). Parameterisations are used where the model processes cannot be resolved explicitly, due to for example the scale being less than the model resolution (e.g., cloud formation) and/or limited understanding of the exact equations determining the process (e.g., many biological processes). Different models have different parameterisation schemes and differing levels of complexity. For example, the atmospheric boundary layer, the area of the atmosphere which interacts with the surface of the Earth, which includes the urban boundary layer (section 2.2), must have some representation in terms of the behaviour of heat flux and wind stress in a model. This representation can be limited by computational power and the observations available to develop parameterisations. Climate projections are generated by models to understand the impact of differing levels of future external forcing to the climate systems (Katzav *et al.*, 2012). With models showing skill in different areas, the Coupled Model Intercomparison Project (CMIP) coordinates global model simulations, setting standardised outputs for analysis and experimental protocols, most recently in phase 6 of the project (CMIP6; Eyring *et al.*, 2016). The availability of the CMIP framework makes a direct intercomparison of a large range of model results possible (Lee *et al.*, 2021).

There is no standalone metric which can describe all aspects of model performance, even if the model used is to be highly specific, which makes selection of a single best performing model ultimately impossible (Eyring *et al.*, 2019). Outputs examined collectively give more of an understanding of how much uncertainty there may be in the projections and give an assessment of their robustness and reproducibility (Lee *et al.*, 2021). While the investigation of multiple model results for future projections is good practice, this is not without downsides,

because some models have the same components or parameterisations, so there will be a tendency for overall ensemble outputs are weighted towards these models (Sanderson *et al.*, 2015; Nowack *et al.*, 2020).

2.8.1 Shared Socioeconomic Pathways (SSPs)

CMIP6 consists of a number of experiments, upon which the model outputs are compared. These are known as Model Intercomparison Projects (MIPs). One of such MIPs is ScenarioMIP. Future climate projections are shaped by anthropogenic external forcings such as greenhouse gases (including chemically trace reactive gases), land use changes and aerosols. These forcings will be decided by future socioeconomic developments, and therefore a range of possible pathways are set out by ScenarioMIP, known as Shared Socioeconomic Pathways (SSPs) (O'Neill *et al.*, 2016). The SSPs are widely used in climate projections, for example in the IPCC chapter on future global climate (Lee *et al.*, 2021). There are five SSP narratives, which describe "future changes in demographics, human development, economy and lifestyle, policies and institutions, technology, and environment and natural resources" (O'Neill *et al.*, 2017).

These SSPs present varying levels of challenge for mitigation and adaption to climate change. Figure 2.12, taken from O'Neill et al. (2017) shows the extent to which each faces both.

Figure 2.12 SSPs and representations of the challenges they present for mitigation and adaption of climate change. Figure has been taken from (O'Neill et al., 2017).

In CMIP5, climate projections were based on Representative Concentration Pathways (RCPs), four pathways of radiative forcing (in W m^{-2}) based on emission, concentration and land use

trajectories ending in the year 2100 (van Vuuren *et al.*, 2011). For continuity with its predecessor, CMIP6 integrates RCP and SSP scenarios, combining the forcing pathway (the RCP) with the socioeconomic conditions of the SSP, so long as the two are consistent with each other. For example, a low emissions SSP could not be combined with a high emissions RCP (O'Neill *et al.*, 2016).

ScenarioMIP at the most basic level consists of four scenarios that are performed by all participating modelling groups, SSP1-2.6, SSP2-4.5, SSP3-7.0 and SSP5-8.5 (Lee *et al.*, 2021).

2.8.2 Vegetation projections

Vegetation can be expected to undergo changes in the future due to the impacts of climate change, carbon dioxide (CO_2) concentration and human influences. These are challenging to predict due to large numbers of interacting environmental variables (e.g., water availability, soil nutrients, surface energy) and land use change (e.g., irrigation, fertilisation, deforestation/ afforestation) (W. Yang *et al.*, 2022).

There are two main approaches to understand changes in vegetation. The first of these is to consult Earth System Models (ESMs), climate models which additionally encompass the movement of carbon through the earth as well as atmospheric and oceanic components. Vegetation-climate feedbacks are complex, with vegetation changes influencing aspects such as surface albedo and roughness, and fluxes of water, carbon dioxide and energy (Richardson *et al.*, 2013). As with representations of the urban surface (section 2.3.2), these complex and small-scale processes cannot be fully represented in models, so parameterisations must be used. One such parameterisation is a variable known as Leaf Area Index (LAI), used to represent the abundance of vegetation in an area. ESMs then use this to scale leaf level carbon and water fluxes to a regional or global scale. It is a dimensionless quantity, denoting the ratio of leaf area to ground area. For example, if an area had an LAI of 3, this means the area of leaves in that area placed flat on the ground would cover its area 3 times. This quantity is used in ESMs to describe changes in the vegetation canopy, so the impact can be translated into changes in the atmospheric component (Park and Jeong, 2021). Studies examining ESM projections under SSP scenarios show global LAI is expected to increase with changes in climate (Zhao *et al.*, 2020), but with a regionally diverse picture of increases and decreases (Chen *et al.*, 2022).

Future LAI projections can be uncertain. CMIP5 (predecessor to CMIP6) model agreement on LAI projections is weak, some models predict little change whereas others a significant amount (but generally an increase in the global mean). In the tropics, the models found to show the most skill when assessed with LAI observations tended to be those projecting smaller

changes (Mahowald *et al.*, 2016). This was confirmed to be the case for CMIP6 models in a study of vegetation in deciduous forests in the northern extratropics, where a positive bias was found in comparison to observations (Park and Jeong, 2021). Therefore, some model disagreement can be expected in the projections for vegetation changes, but this does not mean they cannot be useful to give potential future ranges of what the future vegetation changes may be. Additionally, the expectation is likely that vegetation changes could be on the lower end of the CMIP6 projections, due to the observed positive bias.

Satellite measurements of vegetation, known as vegetation indexes (section 3.2), measure the abundance and health of vegetation, and one such vegetation index is known as the Enhanced Vegetation Index (EVI). EVI and LAI are closely linked. In fact, one methodology of calculating LAI is to use satellite sensed vegetation indices and in situ LAI measurements and their empirical relationships (Fang *et al.*, 2019). Studies have examined the relationship between EVI and LAI and have found strong linear relationships from in situ measurements in a forest environment (Potithep *et al.*, 2010) and MODIS satellite measurements (the sensor used in this thesis) regardless of vegetation type or geographical area (Alexandridis *et al.*, 2020). Based on this, the percentage increase in LAI from ESMs can be used to give an idea of whether EVI will increase with future warming.

The second approach to project future changes in vegetation is to use climate variable outputs from GCMs, which are proven more reliable. Statistical models are built using observations of climate and vegetation variables, then projections made from model output climate variables (Ouyang *et al.*, 2020; Yuan *et al.*, 2021; Chen *et al.*, 2022). In this thesis, this approach to this is also taken, but to make SUHI projections rather than vegetation projections (sections 4 and 5).

3 DATA AND MODELS

The objective of this research is to select a dataset of cities meeting the requirements of medium size and including understudied regions and generate projections of the future SUHI based on observations. This is a novel approach for generating climate scenario-based projections of the SUHI, as the present literature methodologies focus on using RCMs or UrbClim to assess the future UHI (section 2.3.2).

Figure 3.1 gives an overview of the workflow involved with this thesis, with the section in which the component is described in labelled. The initial aspect of the workflow is identification of data suitable to meet the objectives of this research, and the chosen datasets are described in this section.

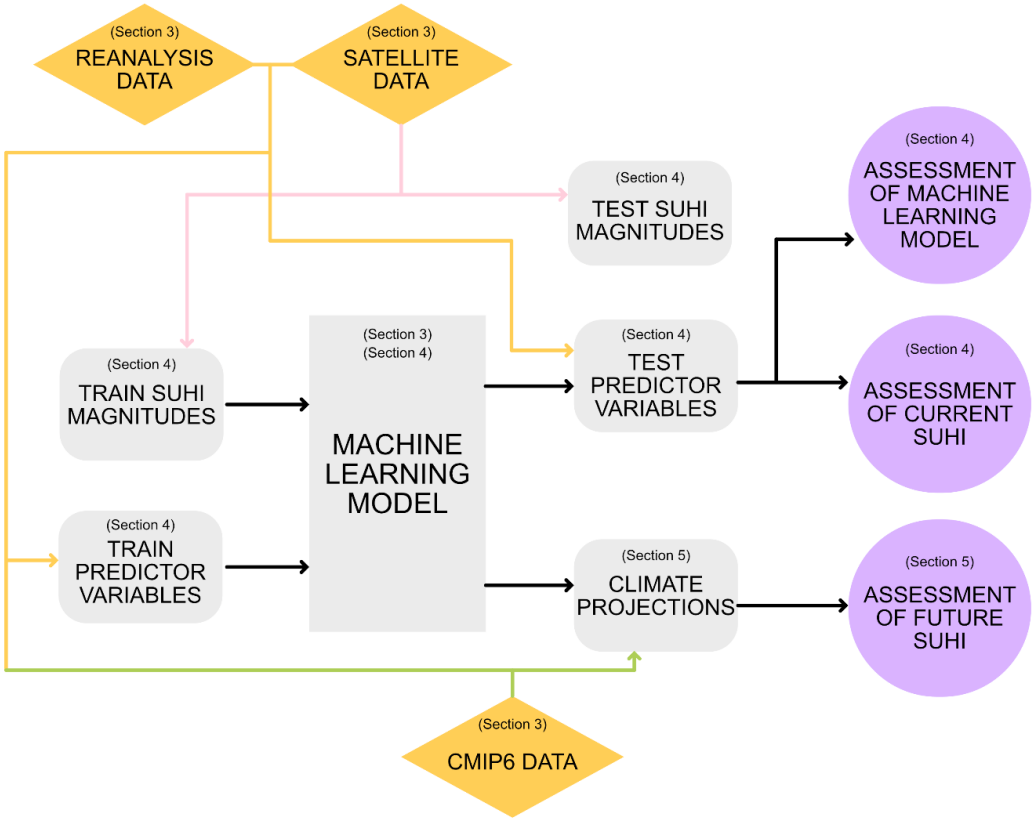

Figure 3.1 Workflow Diagram of the steps taken to create the machine learning model, assess its performance and use it examine the SUHI's for the current period (2002-2020). Yellow diamonds represent the data used and the grey rectangle with sharp corners the machine learning model, which are described in section 3. The grey squares with rounded corners are the processed data which is input into the models, and this is described in section 4. Descriptions of the machine learning model is in section 3.5 and the model build and evaluation in section 4. The assessment of the future SUHI, with use of CMIP6 data is carried out in section 5.

The first step of creating the dataset is to select cities to be included. This is done by starting from a wide pool of global cities and narrowing it down based on certain city selection criteria. As many datasets are used for this purpose, these are not shown on the workflow (Figure 3.1), but are fully described in section 3.1.

After the chosen cities are finalised, the next stage is to collect the city data which will be used to build the machine learning (ML) model. The target variable of the model is the SUHI magnitude, and the data used to generate this is outlined in section 3.2. The data used to generate predictor variables for the ML model are then outlined within the next sections, consisting of vegetation data, albedo data and landcover data information from satellite datasets (section 3.2) and climate variables from reanalysis data (section 3.3). Figure 3.1 shows how these datasets, represented as yellow diamonds, are used in the model building processes.

A final data source consulted was CMIP6 climate and vegetation projections (section 3.4), which provided, along with the current observations, the inputs predictor variables representing potential climate futures, to examine the potential impact of climate change on the SUHI. These are also shown as a yellow diamond on the workflow diagram (Figure 3.1).

The last aspect of this chapter, section 3.5 describes the ML model used.

Summary tables of the datasets (which this section goes on to describe in detail) used can be found in the appendix. The city selection data is in Table A.2.6, the SUHI quantification in Table A.2.7 and predictor variables in Table A.2.8.

3.1 CITY SELECTION DATA

The following datasets outlined in this section were used to select the cities used in the development of this model. The goal of the city selection stage is to define a set of comparable cities based on certain known characteristics (details in section 4.1). The required city characteristics are identified as;

- In understudied regions (below 40 ° latitude)
- Similar population (between 300, 000 and 1 million)
- Not coastal (due to sea breezes effects)
- Not near any very large water bodies (due to lake breeze effects)
- In a non-mountainous/hilly area (due to elevation/mountain breeze effects)

The datasets described below are used to quantify these chosen characteristics, to allow for the selection of the most suitable cities.

Urban Population

The population dataset is taken from the United Nations World Urbanisation Prospects 2018 report (United Nations, Department of Economic and Social Affairs, Population Division, 2018). This dataset contains estimates of current and projected populations produced from national information sources, most commonly censuses or population registers. Unless the urban definitions used by a particular country had changed over time, resulting in inconsistencies, the statistics reported in the dataset were not adjusted by the authors. The term Urban Agglomeration is defined as "the population contained within the contours of a continuous territory inhabited at urban levels of urban density" (United Nations, Department of Economic and Social Affairs, 2019). This definition of an urban area is applicable to this research, rather than administrative borders, as the heat island sprawl is urbanised or built-up land. This dataset also provides a global list of cities with population above 300 thousand inhabitants, which acts as a starting point for the city selection, where cities with a population of up to one million are selected to meet the objective of medium sized cities.

Distance to water bodies

Distance to the coast was taken from the NASA Goddard Space Flight centre Ocean Color Group distance to nearest coastline dataset, which contains distance to the coastline in kilometres calculated using the Generic Mapping Tools software with intermediate resolution coastline (Stumpf, 2012). Using this dataset, it is simple and straightforward to look up the distance of a coordinate point to a coastline. Some accuracy is lost due to the resolution of the coastline (the intermediate resolution coastline ignores features which are less than 20 km^2 in area). In this research, the distance to the coastline is used to ensure there is no influence of coastal breezes and is in the magnitude of tens of kilometres. Therefore, the resolution of the coastline is not needed to be extremely precise, and an increased resolution would be of negligible benefit, so the dataset resolution is acceptable for this purpose.

The distance to lakes is calculated using the GloboLakes: high- resolution global limnology dataset v1 (L. Carrea *et al.*, 2015). The dataset contains location and identification information for global water bodies at a resolution of 300m, generated from the Land Cover Climate Change Initiative dataset of the European Space Agency (Laura Carrea *et al.*, 2015). The dataset is highly useful for this purpose as it is specifically for identifying waterbodies, so land cover codes do not have to be interrogated and interpreted. The land use dataset (Landcover cci) used for the derivation of this dataset is also used in the land cover classification in this study and is discussed in section 3.2.

Elevation

Elevation data is taken from the Global Land One-kilometer Base Elevation (GLOBE) Digital Elevation Model dataset (Hastings *et al.*, 1999). GLOBE is a working dataset compiled from multiple broad sources of information from various organisations. The dataset is global in nature, developed in order to fill the gap of high-resolution digital elevation models (DEMs) which have global coverage and are not restricted by copyright. This is to ensure cities are not in valleys or in mountainous areas (the UHI is influenced by mountain breezes, and urban-rural elevation differences create temperature gradients unrelated to the UHI), via an upper threshold on the standard deviation of elevation.

3.2 SATELLITE DATA

Land Surface Temperature Data

The land surface skin temperature is taken from the Moderate Resolution Imaging Spectroradiometer (MODIS) sensor on Aqua and Terra, satellites with circular sun synchronous polar orbits. Both satellites have two overpasses a day over each location on Earth, Terra at 10.30 and 22.30 UTC and Aqua at 01.30 and 13.30 UTC, allowing the diurnal cycle of the SUHI to be examined. The Terra satellite has been active from 2000, with Aqua launching two years later in 2002, giving a number of years over which to examine seasonal cycle and change over this timeframe (*MODIS Web*, 2020).

The other satellite sensor most commonly used in SUHI studies is the Landsat Thematic Mapper/ Enhanced Thematic Mapper/ Thermal Infrared Sensor (Landsat series) (Deilami *et al.*, 2018; D. Zhou *et al.*, 2019). The Landsat satellite has a 16-day return period, which is reflected in its high spatial resolution in comparison to MODIS data, with Landsat at 30m versus MODIS at 1000m. This makes this dataset useful for examining spatial patterns and identifying hotspots within the city environment (e.g., Amani-Beni *et al.*, 2022; Berg and Kucharik, 2022). Due to its longer return period, Landsat will produce fewer images than MODIS over the same timeframe. As cloud contamination is a risk with satellite data, this may result in larger seasonal gaps in the data for Landsat data as more MODIS images results in a higher likelihood of capturing clear sky conditions. An advantage of using MODIS over Landsat series is the four daily overpasses of the MODIS sensors. With a single overpass every 16 days, the Landsat series gives a more limited view in terms of the SUHI temporal scales. The overpass of MODIS at 13:30 is also more suited to urban heat studies as this is the warmer part of day and therefore more relevant to human comfort, whereas the overpass for Landsat is around 10:00, when temperatures tend to be cooler. Similarly, for the study of nighttime temperatures, the MODIS overpass of 01:30 is preferable to Landsat's 22:00. To summarise, two different use cases can be made for the two satellite sensors. Detailed studies of spatial

characteristics are suited to Landsat, and monitoring of larger scale processes at a high temporal resolution are appropriate for MODIS. For the purposes of this thesis, prioritizing a high number of good quality images to avoid seasonal bias and a higher temporal resolution result in MODIS being the selected sensor.

The MODIS sensor has 36 bands, narrow ranges of wavelengths which the sensor measures (Tempfli *et al.*, 2009). Section 2.7 outlines how by using measuring the radiation emitted by a surface, its temperature can be calculated. The MODIS algorithm also corrects for the atmospheric effects on radiation by using adjacent infrared bands, calculating the differences in absorption between bands (Wan and Dozier, 1996). The final radiances can then be used to generate temperature. In comparisons with in situ values, the accuracy of this MODIS LST product is found to be better than 1 °C (Wan, 2008). It should also be noted that as the SUHI is quantified by a relative rather than absolute value (the difference between urban and rural LST), some systemic error will be removed by its calculation (Quan *et al.*, 2014).

The version of this product used is the 8-day average LST (MOD11A2), generated by averaging from two to eight days of the daily product (MOD11A1). Days where the LST cannot be calculated due to cloud contamination are removed, but the product will always contain at least two days of LST data in the average. The eight day compositing period was chosen as the exact ground track repeat of the satellite paths are 16 days, so choosing half of this reduces the influence of different viewing angles (Wan, 2013) (MODIS scans at ±55° from nadir (Wan and Dozier, 1996)). Measurements are sensitive to the viewing angle, as magnitude of radiation emitted by a surface can vary based on direction, known as anisotropy (Voogt and Oke, 2003), and the authors account for this when generating the MODIS LST datasets (Wan and Dozier, 1996).

Use of this 8-day product over the daily product is advantageous for a number of reasons, and this data product is commonly used in SUHI studies (Flores R. *et al.*, 2016; Sidiqui *et al.*, 2016; Keeratikasikorn and Bonafoni, 2018; Yang *et al.*, 2019; Peng *et al.*, 2020). One such benefit of using this composite product is an increased number of useable pixels, as gaps due to cloud contamination are reduced (Hu and Brunsell, 2013). The 8-day averaged product also results in less variation in the overpass local time, which fluctuates typically within a 2-hour window. For example, the 10.30am overpass time may actually be closer to 9.30am one day, and 11.30am another. This could lead to biases in LSTs, particularly during the daytime, as this is when the temperature is more variable (Hu *et al.*, 2014). By taking an average, this variability in time is mitigated. To assess any loss of accuracy due to this approach, Hu and Brunsell (2013) studied the impact of aggregation on LST by comparison of the MODIS daily and 8 day products for Houston, Texas. Results showed SUHI values were enhanced in terms

of intensity in the daytime and influences of aggregation seen most in spring and summer periods. However, for long term or global SUHI studies, as it the nature of this research, the authors concluded that aggregation is beneficial (Hu and Brunsell, 2013).

The main disadvantage of using thermal infrared satellite data for the purpose of measuring LST is that sensors cannot penetrate clouds. Overcast or rainy days where clouds are present therefore will not be included in analysis due to a large percentage of cloud contaminated pixels, resulting in bias towards certain seasons and conditions. With the use of a recently developed all weather LST product which spans Western China (TRIMS LST), Liao et al examines the SUHI intensities (based on urban- rural means) for clear sky conditions and finds the product has good agreement with MODIS LST for clear sky days (defined as images with less than 20% cloud contaminated pixels). Using the all-weather LST to examine the SUHI under different levels of cloud, it is found the SUHI generally decreases under cloudy conditions (as seen in section 2.4). This decrease is more apparent for the night-time SUHI than daytime. Seasonal bias will also exist when comparing variations in the city itself. Lai et al (2018) found for cities in China the extreme seasons, Summer and Winter, consisted of fewer clear sky days then the transitional seasons of Spring and Autumn. Additionally, algorithms that screen for cloud contamination are not always a hundred percent successful at detecting clouds. This means even products which are deemed cloud free can contain contaminated pixels (Hu *et al.*, 2014).

Despite the limitation of cloud contamination, thermal infrared satellite remains the dominant choice for SUHI studies. The use of microwave data, which is able to penetrate clouds (Ermida *et al.*, 2019) is not appropriate for SUHI studies. Microwave emissivity varies with land characteristics such as soil moisture, soil texture, surface roughness, land-cover type and vegetation optical depth, and assessment of the uncertainties involved is needed before these can be applied to wider applications (Prakash *et al.*, 2018), with the development of a general physical algorithm an ongoing area of research (Mao *et al.*, 2018). Microwave sensor resolutions also have coarse resolution, much larger than the area of a city and therefore must be ruled out for this study (Tomlinson *et al.*, 2011).

Land Cover Data

Landcover data is important in UHI studies as it allows for the identification of the city area. The MODIS landcover product MCD12Q1 is a popular choice for SUHI studies (Schwarz *et al.*, 2011; Zhou *et al.*, 2011; Anniballe *et al.*, 2014; Quan *et al.*, 2014; Bonafoni *et al.*, 2015; Sidiqui *et al.*, 2016; Keeratikasikorn and Bonafoni, 2018), with a global coverage and 500m resolution. Another MODIS product, MCD12C1 is also available at 5,600m resolution, but usage is not as common (Flores R. *et al.*, 2016). Other studies use local landcover datasets,

such as China's land use/cover datasets (CLUDs), which are found to have accuracy of over 90% (by comparison to 'ground truth' measurements such as GPS locations, photographs and google earth) (Yang *et al.*, 2019; Peng *et al.*, 2020). However, global span is required for the dataset used in this thesis, as cities in a wide range of locations are to be studied to address the research gaps of cities in the global south. This means regionally limited datasets are excluded, to allow for use of the same dataset for all cities.

The land cover information used in this study is taken from the European Space Agency (ESA) Land Cover Climate Change Initiative (Land_Cover_cci): Global Land Cover Maps dataset (ESA Land Cover CCI project team; Defourny, 2019). This dataset contains global land cover classifications at a 300m spatial resolution for each year from 1992 to 2015. The classifications are derived from three satellite time series; AVHRR (National Oceanic and Atmospheric Administration's Advanced Very High Resolution Radiometer) from 1992 to 1999, SPOT-VGT (SPOT satellite vegetation programme) from 1999-2013 and PROBA-V (ESA satellite) from 2014-2015.

The resolution of Land_cover_cci is slightly higher than MODIS MCD12Q1 at 300m. The annual temporal resolution of this dataset is beneficial, given the cities are to be studied over an extended period of time. In many studies, the change in urban extent is not widely considered, and the land cover information is used is taken from a single snapshot. However, it is advantageous to match land cover and LST data temporally. Zhao et al (2016) examined the effect of using outdated urban extent maps to quantify the SUHI, and finds "it is critical to use concurrent urban extent and LST maps to estimate UHI".

Vegetation Indices

A commonly used measure of vegetation activity, relevant to the SUHI due to its cooling effect (section 2.2), is vegetation indices (VI). These are generated by using at least two bands of wavelengths to measure the contribution of the vegetation to the reflected and absorbed light. This gives an indication of the photosynthetic activity and variations of the vegetation canopy (Huete *et al.*, 2002). This can therefore be used as a measure to quantify the extent and greenness of vegetation in an area.

The two MODIS VI products are the normalised difference vegetation index (NDVI) and the enhanced vegetation index (EVI). The NDVI was developed prior to the EVI, and is known as the 'continuity index', as it is often used so comparisons can be made with previous studies and datasets (Didan *et al.*, 2015). The NDVI is also more sensitive to chlorophyll than the EVI (Huete *et al.*, 2002). The chlorophyll in the vegetation absorbs light in the red band, whereas most near infrared radiation (NIR) is scattered. This results in the difference between the two

bands giving an indication of the 'greenness' of the vegetation. The NDVI is calculated using equation *(3.1)*.

$$NDVI = \frac{\rho_{NIR} - \rho_{Red}}{\rho_{NIR} + \rho_{Red}} \quad (3.1)$$

where ρ_{NIR} and ρ_{Red} are the surface bidirectional reflectance factors (a measure of the amount radiation reflected) for the NIR and Red bands.

The EVI was designed to improve upon the NDVI, using an additional blue band in the calculation to correct for atmospheric effects, resulting in a VI more sensitive to variations within the structure of the vegetation canopy (Huete *et al.*, 2002). EVI is calculated by *(3.2)*.

$$EVI = G\frac{\rho_{NIR} - \rho_{Red}}{\rho_{NIR} + C_1\rho_{Red} - C_2\rho_{Blue} + L} \quad (3.2)$$

where L, C_1, C_2 and G are constants, which for the MODIS EVI are set as L = 1, C_1=6, C_2=7.5 and G=2.5. $\rho_{NIR,}$ ρ_{Red} and ρ_{Blue} are the surface bidirectional reflectance factors for the NIR, Red and Blue bands.

Due the correction for atmospheric effects, the EVI is found to perform well in areas with high aerosol occurrences (Huete *et al.*, 2002). In cities and surrounding areas, there is likely to be pollution from urban activities, so this property is beneficial for this research.

The datasets used to calculate urban and rural EVI were MODIS MYD13A2 and MOD13A2 datasets. These datasets have a spatial resolution of 1000m, on the same grid as the MODIS LST data used, and the temporal resolution is 16 days. The algorithm generates the pixel output by taking the final value as the best available over the 16-day period (Didan *et al.*, 2015). The two datasets correspond to the aqua and terra satellites, with overpass times at 13:30 and 10:30, respectively. Both were used to improve the amount of data passing the quality checks. For the mean monthly values, a mean for each pixel was taken based on the ones of good quality.

Albedo

Albedo is a key property in land surface studies, representing the amount of surface reflected irradiance as a fraction of the total radiation incident on the surface. An increase in albedo will therefore lead to a decrease in the amount of latent and sensible heat at a surface, contributing factors in the formation of the UHI (section 2.2). Shortwave albedo is deemed the most important for surface energy budget studies as it is the band over which the majority of solar

radiation is distributed (Liang and Wang, 2020). There are two different measurements of albedo available for use, white sky albedo (WSA) and black sky albedo (BSA). WSA represents the albedo measurement with the angular dependency removed (i.e., illumination on the surface is from all directions), and BSA the albedo at local solar noon (directional hemispherical reflectance) (Schaaf *et al.*, 2015). For use in SUHI studies, there tends to be a preference for use of WSA (Zhao *et al.*, 2014; Zhou *et al.*, 2014; Yao *et al.*, 2018; Yang *et al.*, 2019; Du *et al.*, 2021), although BSA is used as well (Lai *et al.*, 2021). Peng et al (2012) assessed both WSA and BSA, and found the two have a linear relationship and show similar results.

The dataset used to calculate urban and rural albedo was the MODIS MCD43A3 dataset, consisting of 16-day averages weighted on the ninth day with a spatial resolution of 500m. The MODIS MCD43A2 dataset was also used to determine quality assessment flags for the albedo values. The shortwave band (0.3-5 µm) and WSA was used, as results with BSA would be expected to lead to similar results.

3.3 REANALYSIS DATA

Reanalysis datasets are widely used in climate monitoring applications, giving complete "maps without gaps" coverage of climate variables across the globe. Modelling tools are used to 'reanalyse' observations in order to produce spatially and temporally continuous datasets. The final product is a dataset made up of a combination of observations, forecast models, and data assimilation (Hersbach *et al.*, 2020).

The accuracy of reanalysis data is dependent on both observation error and model ability to correctly simulate physical processes, as any model bias or error will be passed on to the final product (Bližňák *et al.*, 2022; Gomis-Cebolla *et al.*, 2023). This is particularly relevant for processes which involved the simulation of clouds, e.g., precipitation and downwelling longwave radiation, which require parameterisations to capture the small-scale processes involved in the formation (Silber *et al.*, 2019).

Climate variables were taken from the ERA-5 Land reanalysis (Muñoz Sabater, 2019). This dataset was chosen as out of the global reanalyses considered (shown in appendix Table A.2.9), the horizontal resolution of this dataset is the highest. High resolution is beneficial for this study, where the focus is on the scale of a city. The ERA-5 reanalysis replaces the previous ERA-Interim reanalysis, benefitting from recent developments in model physics and data assimilation (including more satellite data) to provide higher levels of accuracy. Observational data consists of satellite data and in situ data, for example from weather stations, aircrafts, buoys or radar, and the forecasting model is the European Centre for Medium Range Weather

Forecasts (ECMWF) Integrated Forecasting System (IFS) Cy41r2, operational in 2016 (Hersbach *et al.*, 2020). The monthly product is used in this thesis, as the purpose is to examine the impact of these climatic variables on the monthly SUHI.

The variables total precipitation, air temperature at 2m and dew point temperature were taken from the ERA-5 dataset. Relative humidity (RH) was calculated from air and dew point temperature using the August-Roche-Magnus approximation (Thiis *et al.*, 2017).

$$RH = 100\frac{\exp\left(\frac{aT_d}{b+T_d}\right)}{\exp\left(\frac{aT}{b+T}\right)} \quad (3.3)$$

where T is the air temperature (in °C), a= 17.67, b = 243.5 and T_d is the dew point temperature (in °C).

3.4 CMIP6 DATA

Climate models (which will be referred to as GCMs (Global Climate Models) and ESMs (Earth System Models) from here on for clarity) are selected based on the criteria that they take part in the ScenarioMIP CMIP experiments (section 2.8) and have made available model output for the required variables (section 4.3) in both the historic and future projections. In addition, I paid attention to select models contributed by a range of different modelling centres (to ensure there is no particular selection bias towards specific modelling groups, e.g., if modelling centres submitted multiple versions of their climate models). Overall, this led to a selection of 14 GCMs listed in detail in appendix Table A.2.10.

The SSP3-7.0 scenario was chosen. This pathway assumes no additional mitigation takes place beyond the current measures, and acts to fill a gap between the lower and higher ends of the forcing pathways (Tebaldi *et al.*, 2021).

The GCM with the lowest horizontal resolution is the CanESM5 model, with a resolution of 2.8° x 2.8°. Therefore, all models are re-gridded to this resolution, to ensure an accurate comparison can be made. The variables taken from these models are near surface relative humidity (%) and precipitation flux (kg m^{-2} s^{-1}). Precipitation flux is multiplied by 24*60*60 to get the total rainfall in mm per day. These units and factorisations arise because 1kg (1 litre) of water spread over $1m^2$ is 1mm thick, then taken times the number of seconds in a day.

ESM projections are used to examine future vegetation (and climate) changes, using the projected changes in LAI to infer changes in EVI (see section 2.8.2). The ESMs used for this

are shown in appendix (Table A.2.11), consisting of five in total. Some of these models were also used as the GCMs to generate climate projections (see Table A.2.10), but because not all GCMs contain an earth system component, many of these could not be used. Again, the ESM with the lowest spatial resolution remains the CanESM5 model, so all ESMs were gridded to its resolution.

3.5 STATISTICAL AND MACHINE LEARNING MODELS

To assess the predictability of the SUHI magnitude based on environmental factors, a few different statistical or machine learning (ML) approaches were investigated. These are Multiple Linear Regression (MLR), Ridge Regression (RR), Generalised Additive Modelling (GAM), Random Forest Regression (RFR), Gaussian Process Regression (GPR) and Regression Enhanced Random Forest (RERF). This section outlines the statistical models and metrics that can be used to assess their performance.

The first part of this section outlines the performance metrics, which are used to determine how well the various models manage to predict the SUHI in comparison to the true values, the observations, and outlines other key metrics which are used. Then given are specifics of how the model fits are validated against overfitting, by splitting the data into training and test datasets. Aside from MLR, all the models have values which are not set by the fitting process itself and must be specified before the model fit, which are known as hyperparameters. These are set by a process known as cross validation, which is outlined in this section.

As the RERF model turned out to show the best performance, the focus of this and the result sections will be on this regression type. However, as the RERF is a hybrid of RR and RFR, all three approaches will be explained in detail. RR in turn builds upon the MLR, with MLR being a case of RR with nil regularization. Therefore, this section will follow the logic of increasing regression model complexity, starting with an explanation of MLR, followed by RR, RFR, and finally RERF.

The final aspect of the section tackles the 'black box' nature of machine learning models and how this is dealt with.

Performance Metrics

For many regression models R-squared (r^2, the coefficient of determination) is typically used to assess the most accurate model.

$$r^2 = 1 - \frac{\sum_{i=1}^{m}(y_i - \hat{y}_i)^2}{\sum_{i=1}^{m}(y_i - \bar{y})^2} \quad (3.4)$$

where m is the number of datapoints, $\hat{y}_i$ is the predicted value and $\bar{y}$ is the mean of samples y_i.

R-squared is the proportion of the variance in the data explained by the regression model (Wood, 2017). It gives an indication of how close the estimated results are to the observed, in reference to a model where simply the mean of the total observations is taken, essentially comparing a system which uses predictor variables to a system which simply uses the observed results (their mean). Figure 3.2 illustrates how this intuitively relates to equation (3.4).

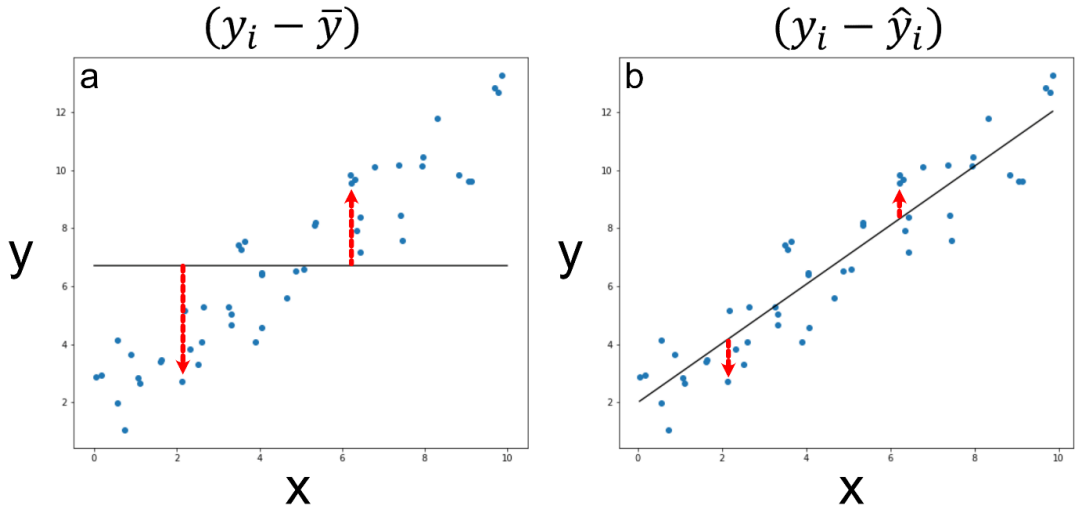

Figure 3.2 R-squared compares the fit of the regression model to taking the data mean. a) taking the difference of the observations from the mean. This is the denominator of equation (3.4). b) taking the difference of the observations from the regression model predictions. This is the numerator of equation (3.4). If using the regression model is no different to using the mean of the observations as the prediction for y, the sums for a) and b) will be equal and R-squared is 0.

Some caveats must be considered when using R-squared to compare models. Low R-squared does not necessarily mean the model is not useful, if R-squared is low but greater than zero (so the model is doing a better job than simply using the mean), the model can still give useful information on the relationship between variables. This is because R-squared is relative, so the model could explain a large fraction of the variance in absolute terms, but if the overall variance of the observations is very high, R-squared will be low.

Another typical metric to measure the performance of regression models is root mean square error (RMSE) (Geron, 2017b).

$$RMSE = \sqrt{\frac{1}{m}\sum_{i=1}^{m}(\hat{y}_i - y_i)^2} \quad (3.5)$$

where m is the number of datapoints, $\hat{y}_i$ is the predicted value and y_i the true value.

The more accurate the model, the smaller these error metrics will be. In general, RMSE is more commonly used in computer science (Geron, 2017b), but R-squared is found more commonly in SUHI modelling studies (for example, the studies outlined in Table A.1.2). Therefore, in order to avoid the potential pitfalls associated with using each performance metric in isolation, the combination of both RMSE and R-squared will be used to assess the models, as is also common in other studies comparing machine learning models, for example, Zhou et al (2011). RMSE gives an indication of how far the predicted values are from the observed in absolute terms, and R-squared how well the model explains the variance in the observations compared to just taking the sample mean.

Prediction Intervals

By choosing the best ML model and predictor variables, it is possible to minimise error in the prediction. However, there still will be some residual error, and this can be accounted for in the predictions made by means of prediction intervals. A prediction interval gives an upper and lower limit to the prediction and the probability of the true value falling within this range. One such method of generating prediction intervals is via the following formula.

$$\hat{y}_{p,upper}, \hat{y}_{p,lower} = \hat{y}_p \pm \sqrt{MSE \times (1 + \frac{1}{m} + \frac{(\hat{y}_p - \bar{y})}{\sum_i^m (\hat{y}_i - \bar{y})^2}} \quad (3.6)$$

where $\hat{y}_{p,upper}$, $\hat{y}_{p,lower}$ are the upper and lower prediction intervals, $\hat{y}_p$ is the prediction, MSE is the mean squared error ($RMSE^2$), m is the sample size, $\hat{y}$ are the predictions and $\bar{y}$ is the mean of the predictions.

These prediction intervals show where, for a new prediction made, the range that there is a 68% probability (i.e., ± the standard deviation) that the true value will fall within.

Predictor Variable Correlation

When building ML models, issues that can arise when predictor variables are correlated. Parameter estimates may be unstable, and the effect of predictor variables cannot be separated,

meaning it is hard to extrapolate. Dormann et al (2013) give the example of annual temperature and annual precipitation being used as predictor variables. The two variables are negatively linearly related, and one can be used to partly explain the effect of the other. So, if precipitation is the variable which is truly important and temperature is not, temperature may still be included in the model due to its correlation with precipitation. The model could incorrectly predict that the target variable will increase with temperature (and precipitation remaining constant) when in fact it will remain constant if precipitation remains so.

A common measure to measure correlation is Pearson's correlation coefficient, r, shown by equation (3.7).

$$r = \frac{1}{m-1}\sum_{i=1}^{m}\left(\frac{x_i - \bar{x}}{s_x}\right)\left(\frac{y_i - \bar{y}}{s_y}\right) \tag{3.7}$$

where x and y are the two variables and m is the number of observations. The formula represents the sum of the standardised products divided by the degrees of freedom of the sample (Boslaugh and Watters, 2008).

r ranges from -1 to 1, with 1 representing a perfect positive correlation and -1 a perfect negative correlation. Values close to zero show non-existent or very weak correlations.

Model Validation

Training test data split

The data was split into training and test samples at the start of model evaluation and analysis. Common practice is to use 80% of the data to train the model and 20% to generate test statistics quantifying its predictive power, although the 80:20 split is fairly arbitrary, and choices for test data percentage range from 20% to 50% (Joseph, 2022). The two options for how the data will be split are to generate test and training data based on city, or based on time.

Splitting the data by cities is useful as it answers the question, 'can we predict the SUHI of a city, given we know its climate?'. However, a drawback of this is that the success of the model may vary greatly depending on which city is in the test dataset, due to the issue of spatial autocorrelation. Spatial autocorrelation refers to the idea that areas which are geographically near each other will be more similar to those further away (Ploton *et al.*, 2020). In the cities selected for the analysis, outlined later in section 4.1, there ends up being more cities in Brazil, China, and India than in other countries. It is likely cities in the same countries share similar characteristics unrelated to climate, such as building types and materials. Therefore, if the test dataset is made up of cities in Brazil, China, or India, it may perform better than if the test

dataset consisted of cities outside of these three more represented countries. This can give an inflated level of confidence in the predictions made.

Splitting by time means taking the training data as certain years of data and testing this on the remaining years. The benefit of this is that it avoids any bias due to the cities selected to be part of the test set, as all are included. Additionally, using the early years as training data and later years as the test data evaluates the model's ability to predict future SUHI magnitudes based on past magnitudes, which is highly important for use in investigating future climates. On the other hand, this method does not measure the ability of the model to generalise to other cities outside of the dataset, as all the cities investigated are included in the model.

The train-test split is made using time, as this means the model can be evaluated for its intended purpose, using past climates to predict the future. Natural variability in the climate exists on an interannual basis due to factors such as ENSO (El Nino-Southern Oscillation) and including too few years in the test data could mean the range of climate related predictor variables the model is tested on is limited (for example, only being tested on years with lower precipitation). To ensure this is accounted for in the test data, the data was split evenly between the two (50:50), in contrast to the 80:20 percent split commonly used in statistical modelling applications (Joseph, 2022), as this would only give around 4 years of test data.

The split is made by putting odd years in the training dataset and even years in the test dataset. A test is also done using the earliest years (from 2002 to 2011) to predict the later years (2012 to 2020), to examine the model's ability to extrapolate.

Cross validation

To ensure a model is not overfitting, and will perform well on unseen data, model validation must be carried out. The approach was to use nested cross validation.

Nested cross validation first involves splitting the data into a training and test dataset, where the test dataset remained untouched throughout the model fitting process, which was done as described above. The ML models investigated in this thesis (RR, RFR, GAM and GPR) all contain values relating to the set-up of a model, that must be manually specified before the model is fit using the training data, known as *hyperparameters*. This are distinctly different to model parameters (e.g., the coefficients in MLR, see later in this section), which are calculated as part of the model fitting process using the training data.

There are a range of possible hyperparameters for each model, and these must be narrowed down to select the most appropriate. These must be determined using the training data, but also must be validated against overfitting. Yet, as the test data must remain untouched during the fitting process (it would not be a fair test of model skill if the model is tested based on data

used in the model development), the hyperparameters are identified using k-fold cross validation, where k is a predetermined number. The methodology takes the training dataset and divides it further into k datasets. One of these datasets is then removed (the validation dataset) and the model trained using the remaining k-1. Then the validation dataset is used to generate performance statistics based on the fitted model. This is repeated so each of the k datasets are removed from the data and used as the hold out validation dataset. Once performance statistics for all the validation datasets have been generated, they are averaged for each hyperparameter value and the hyperparameters from the model with the best skill is selected. The model is then refit on the entire training dataset with these selected hyperparameters. The value for k is chosen so datasets sufficient size to be representative of the overall data. Typically, either 5 or 10 is taken as the choice for k (James *et al.*, 2021). For this thesis, a validation dataset ideally contains a good spread of the different possible climate regimes, therefore, a choice of k = 5 is made to ensure the validation datasets are of a sufficient size.

Multiple Linear Regression (MLR)

As explained previously in this section, the ML model used is a hybrid model, which combines Ridge Regression and Random Forest Regression. Ridge Regression is an MLR with the addition of a regularisation parameter. Therefore, for a thorough explanation of the final model, an overview of MLR is given.

In quantitative research domains, MLR is often the first go-to model applied to identify relationships between predictor and target variables. It is easy to interpret and fit, which make it the most popular choice in SUHI studies (section 2.3.2).

It can be generally described with the equation,

$$y = \beta_0 + \beta_1 x_1 + \beta_2 x_2 + \cdots + \beta_k x_k \quad (3.8)$$

where y is the target variable, x_1, x_2, … x_k are the predictor variables, and β_1, β_2, … β_k, are the coefficients, which are fixed numbers determined by fits to the training data (the data samples upon which the model is built). The coefficients are chosen by minimising the sum of squared residuals i.e., R-squared (defined earlier) (Gujarati, 2020).

Within certain limitations, e.g., the assumption of linearity, assumptions about causality between the x_i and y, and collinearity, the method has the advantage to be easily interpretable. The sign and magnitude of coefficient values can be used to characterize the relative influence

of x_i on y so that predictor variables can be ranked in order of how important they are in predicting the model. A larger magnitude for the coefficient equates to a more important predictor variable.

A key limitation of this method is that it suffers from situations where input variables are correlated with each other (one can be described by a function of the other), known as multicollinearity. Multicollinearity causes both the estimates of coefficient and the accompanying statistics (the standard error, p-values and partial t-test results) to be unreliable, also affecting appropriateness for inference (Saleh *et al.*, 2019). However, if the goal of the model is to predict and not to infer this is, practically, less of an issue.

Another important factor to be wary of is the MLR potential to overfit if there are too many predictor variables. Variable selection processes, aiming to reduce predictor sets as to only keep variables with strong predictive power can be used to address overfitting. Holding back test data for independent verification of the model's ability to perform on unseen data is a standard way to examine whether overfitting has occurred, as previously outlined. In MLR, there is therefore no method-intrinsic way to address overfitting, or the 'curse of dimensionality', other than methods to reduce the number of predictors. In higher-dimensional predictions problems, e.g., for typical machine learning applications, this is a general issue when the regression model contains, by design, many predictor variables (the dimensions). Since the number of datapoints required increases exponentially with the number of dimensions, in many practical problems there is simply no way to avoid overfitting by means of collecting more data (Bishop, 2006). RR, described below, is a way to use regularization to address overfitting in MLR models with many predictors, even in underdetermined problems.

Other issues, not specific to but often encountered when using MLR, are (a) the assumption that the residuals have a normal distribution and constant variance (homoscedasticity), and (b) its sensitivity to outliers. This can be tested for by visually inspection of plots of the MLR residuals.

In the context of this present work, an issue is that the predictor variables in the dataset are correlated (for example, climate variables such as relative humidity and evaporative fraction). Earlier in this section, it was outlined how this is measured using Pearson correlation and this accounted for in the variable selection process (section 4.2). MLR is a common approach for SUHI studies (see Table A.1.2). As MLR is a case of Ridge Regression (RR) without regularization, outlined below, a MLR model does not need to be trained separately and is grouped in with RR for the purpose of this thesis.

Ridge Regression (RR)

Ridge Regression (RR) (Hoerl and Kennard, 1970) is described in this section as it is the 'base' used in the final hybrid model. Although there is a preference of past SUHI studies for using MLR (section 2.3.2), none have utilised RR at present, despite it having the same benefits without the downside of potential overfitting.

RR aims to improve upon a MLR by adding in a regularisation parameter, λ (sometimes referred to as a penalty value), in the optimisation process. This hyperparameter is added as a penalty term to reduce variance of the model and prevent overfitting. It was developed to overcome the problems of 'ill fitting' situations such as the multicollinearity issue of MLR explained previously (Draper and Smith, 1998).

In MLR, the fit is made by minimising the sum of squared residuals. In RR the fit is made by minimising the sum of squared residuals + λ multiplied by the gradient of the slope squared (i.e., the magnitudes of the coefficients squared). Doing so keeps the magnitudes of coefficients to a smaller range, but still aims to minimise the sum of square residuals. The aim of this is to penalise overfitting. The steeper the slope in MLR/ the larger the coefficient values, the more sensitive the prediction is to changes in the input variables, hence adding a penalty based on the steepness of the slope results in predictions less sensitive to small changes in input variables.

The hyperparameter λ is tuned via the outlined 5-fold cross validation process. One of the choices given as a potential value for λ is 0, which results in the fit being made by minimising the sum of squared residuals, with no consideration of the coefficient values. For this case, the RR is the same as the MLR model. This is how MLR is included in the model selection process for RR. As with the MLR model, when using RR caution must be taken when looking at the coefficient values, as they will be influenced by both any collinearity and the regularisation parameter (λ).

Random Forest Regression (RFR)

The second half of the hybrid model used is Random Forest Regression (RFR) (Breiman, 2001). Alongside MLR, RFR is also used in SUHI studies (section 2.3.2) due to its ability to capture nonlinear relationships.

RFR is a type of machine learning model that combines the outputs of multiple models in order to give one overall prediction, a technique known as ensemble learning. Specifically, RFR uses many decision trees to create multiple predictions and takes the mean as the final resultant prediction. An example of a decision tree can be seen Figure 3.3.

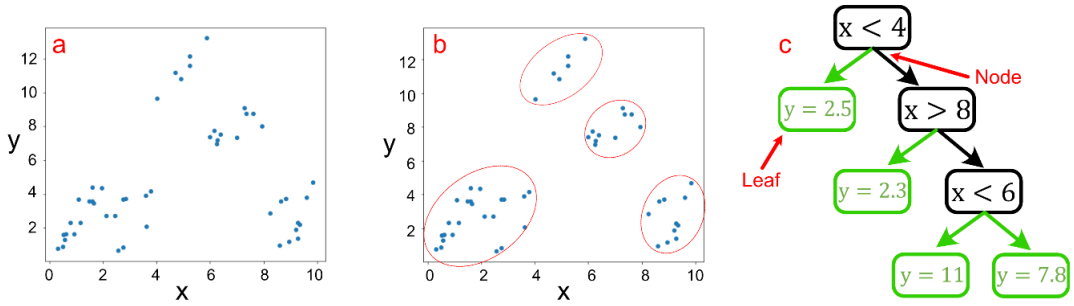

Figure 3.3 An example of a decision tree. The data has a nonlinear relationship, the decision tree gets around this by splitting the data at set points and using the mean result of the groups as the prediction. a) A simple two-dimensional example shows target variable y and input variable x. The relationship between the two is nonlinear. b) the data can be split into 4 groups based on x, which have similar values for y: $x < 4$, $4 < x < 6$, $6 < x < 8$ and $x > 8$. c) The decision tree is built by calculating which one of these groups an x value belongs to and outputting a prediction (shown in green). The output prediction is the mean value for the group. For example, the mean of the group $x < 4$ is $y = 2.5$, so this is given as the prediction if an x value of less than 4 is an input to the model.

The output prediction of the decision tree, shown in in Figure 3.3c by the green boxes and labelled in red, is known as a leaf. The point where the data is split into two paths is a node, also shown labelled in red. The value used to split the decision tree data points arriving at a given node (in Figure 3.3c the first value used to split the data is 4), is determined by the following.

1. Take a value for x, call this $x_{threshold}$.
2. Calculate the mean of the points greater and less than $x_{threshold}$, call these $y_{prediction\ over}$ and $y_{prediction\ under}$.
3. For all points work out the difference $y - y_{prediction\ over}$ or $y - y_{prediction\ under}$. These are the residuals.
4. Sum the square of the residuals, repeat for all x values and choose the $x_{threshold}$ which minimises the sum of squared residuals.

Decision trees have an advantage of being able to handle nonlinear relationships, but the drawback is a tendency to overfit. RFR maintains this ability to fit nonlinear relationships but reduces the risk of overfitting by using many different trees.

There are various methods to make each tree distinct (e.g., by using a slightly different subset of the overall dataset as the basis for the tree), of which two are used in the case of this thesis and described below.

Different subsets are typically created in a process called bootstrapping to generate a unique sample of the original training data. To do this a sample of the dataset is produced by taking training points at random with replacement, meaning that each sample contains some datapoints only once, some not at all, and some are duplicated. For example, take the original

dataset: p_1, p_2, p_3, p_4, p_5. A bootstrapped sample of this might be: p_1, p_2, p_2, p_4, p_4. Here the points p_2 and p_4 appear twice, p_1 once, and the other 2 points not at all. Multiple unique samples are generated using this method and each of these samples are used to build an individual tree.

A second step to introduce further randomness relates to the predictor variable used to split the data. In the one-dimensional example in Figure 3.3, there was only one predictor variable, x. However, in a model with multiple input variables, say A, B and C, the algorithm will repeat the 4 steps to determine $x_{threshold}$ for A, B and C, and choose the variable that minimises the sum of squared residuals. Figure 3.4 illustrates this choice made to split the data for three input variables. Removing one of these variables from the running at random could result in the variable chosen to split the node being a different one to that if all variables had been considered (Breiman, 2001; Geron, 2017a).

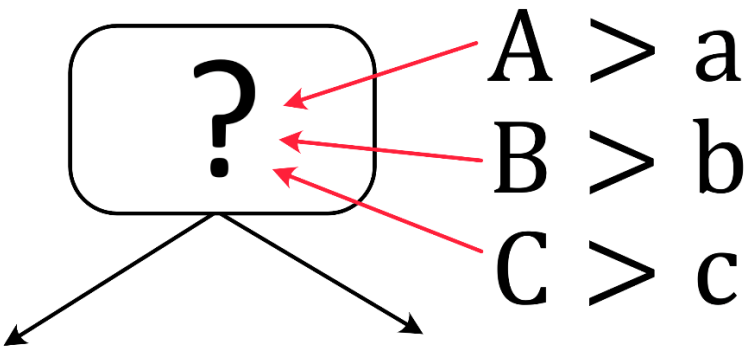

Figure 3.4 If the data has predictor variables A, B, C, there is a choice of these to split the data. If a subset of these is considered the data could be split only on A or C, for example.

There are several hyperparameters that can be tuned as part of the RFR optimisation process, also to address overfitting in combination with cross-validation. The most commonly tuned hyperparameters are:

- Tree depth.

  Tree depth is the number of steps the decision tree goes through before it reaches its final prediction. The tree depth should be large enough that the model can make an accurate prediction, but not so large that the model will overfit.

- Number of trees

  This is the number of trees which are included in the forest. Enough trees should be included so the predictions are stable, but after a certain number adding additional trees will have little impact on the prediction ability yet will require more computational power. Geron (2017a) likens this to a coin toss. For a small number of coin tosses, the heads to tails ratio will fluctuate, meaning it is difficult to determine an estimate of probably of

heads or tails. However, after a large number of coin tosses, the ratio will stabilise, and continuation of the exercise will have no benefit.

- Minimum number of samples per leaf

The minimum number of samples on a leaf indicates how many samples can be on the final point of a decision tree, where no further split occurs. This point is where the mean of the training data is taken and used as the prediction. In Figure 3.3b this refers to the minimum number of points enclosed by the red circles. If the minimum number of samples is too small the model can overfit and a value too large can result in underfitting.

- Minimum number of samples required to split a node.

This determines at what point the algorithm must stop trying to split the data further and turn the current group into a leaf. This point will also be influenced by the minimum number of samples per leaf, as the split at the node must result in the leaf having the required number of samples. As with the samples per leaf, this hyperparameter balances the model tendency towards overfitting versus underfitting.

- Max Features considered at each node

Randomness can further be introduced into the decision trees by only considering a subset of features when making decisions on how to split a node. The number of features considered can be determined using this hyperparameter.

An advantage of RFR is it is more flexible than models such as RR. Nonlinearity and interactions can be accounted for in the model, without having to explicitly define the relationship (Grömping, 2012). It can handle outliers better than a model fitting a function as their influence will be limited to the leaf the outlier datapoint falls on. Another major advantage is that RFR models are, relatively, interpretable non-linear models by means of intrinsically calculatable 'feature importances' (also known as relative importance). As these are not used in the main body of this thesis, these are outlined in appendix section A.3.

The main disadvantage of RFR in the context of the work presented here is that it does not have the ability to extrapolate outside the range of the training data. In the RFR, a datapoint will go through a decision tree and end up on a final leaf. The prediction at this leaf will be the mean of the training data outputs that are categorised into that leaf, and if a new datapoint was outside of the range of these datapoints, it would still be predicted as their mean. This contrasts to a linear model such as RR, which can be extended outside of the range, given the relationships between input and output remain linear (it should be noted these models will not be robust if the relationships are nonlinear). This is of particular significance for the results

discussed in section 5, as it is potentially to be used to make predictions based on variables that may change to outside of the current range under climate change. For example, if the driest area becomes even drier in the future.

Regression Enhanced Random Forest (REFR)

The chosen hybrid model used is the Regression Enhanced Random Forest (REFR) (Zhang *et al.*, 2019), which is a combination of RR and RFR, both of which were explained previously in this section. The purpose of these explanations was for an understanding of the RERF.

They aim to capitalise on the strengths of RR in its ability to extrapolate, and RFR, with its ability to fit nonlinear relationships. A 'base' estimator (RR in this case, although different base models can be used) is fitted to the observations. The residuals between the observations and this base model estimates are then calculated and a RFR is fit to these. When the RERF is used to make a new prediction, it creates a base model prediction and a prediction of the residuals, which are added together to create a final prediction. So the RERF has the advantage of the benefits of linear and nonlinear models, both of which have been used previously in the SUHI literature, but as separate models (section 2.3.2).

Care must still be taken when using REFR to extrapolate, as there is still the assumption that the underlying relationship between the variables does not change (as with RR) and that the distribution of residuals does not change beyond cases covered in the training domain.

Understanding the models

Many machine learning techniques are described as "black boxes". This refers to the concept that they take input data and output a prediction, but there is no explanation of how the model uses those input variables. Fox et al (2017) define three key reasons why these models should in fact be explainable.

The first of these is the need for **trust**. Understanding the relationship between target and predictors are important in assessing the reliability of the models; an unexpected relationship between a predictor and target variable could be an indication the model should not be trusted. In addition to the requirement for models to be accurate, they also should make intuitive sense, aligning with physical processes and laws.

Second is the need for **interaction.** There is a need for models not only to be used for prediction but also for inference. It is useful to understand how each predictor variable is interacting with the final prediction. For example, how adding vegetation to a city and therefore decreasing the urban – rural EVI difference might affect the predicted SUHI.

Finally, the need for **transparency**. Where the model is not making the correct predictions (i.e., not predicting the test data), why is this? If there is range of values for which the model is not accurate, we want to understand the data values where this is happening, which can indicate how to improve the model.

These aspects all apply to the models used in this thesis. The objective is to understand how the climate can influence the SUHI magnitude and to examine what may happen with climate changes. Therefore, it is important there is trust in the predictions and the underlying relationships are reliable and will not substantially change in the future. Inference is to be made from the models, as shown in the example given, to understand how each variable individually contributes to the SUHI magnitude. This in turn could lead to conclusions about mitigation measures, and which are the most effective – in which climates could albedo altering methods such as white roofs be more impactful than urban greening? Therefore, tools which can address the black box nature of machine learning models are used to identify how the models operate, and these are described below.

Partial Dependence and Accumulated Local Effects Plots

Partial dependence plots (PDPs) and Accumulated Local Effects (ALE) plots are useful tools in understanding how individual variables contribute to the overall outcome of a model, both aiming to show how a variable influences a model on average. PDPs show the marginal effect that each feature has on the model predictions (Molnar, 2022). For example, if the magnitude of the SUHI increases if there is a decrease in the surrounding vegetation (EVI). For the RR model, these relationships will always be linear, but for non-linear models the PDP can have a different shape. Figure 3.5 shows the process of creating a PDP for a set of dummy data. The x-axis on a PDP shows a variable, and the y-axis shows the average SUHI for that value of the variable.

1. A model is fit to the data in the table.

A	B	C	y
0.1	5	20	y_1
0.7	10	22	y_2
0.5	9	21	y_3
0.6	8	25	y_4

2. Variable A is artificially set to 0.1, keeping the values of other variables the same. The model is used to predict the value for y and a mean for the whole dataset (when A = 0.1) generated.

A	B	C	$\hat{y}$
0.1	5	20	$\hat{y}_{1\mid A=0.1}$
0.1	10	22	$\hat{y}_{2\mid A=0.1}$
0.1	9	21	$\hat{y}_{3\mid A=0.1}$
0.1	8	25	$\hat{y}_{4\mid A=0.1}$

$\hat{y}_{mean\mid A=0.1}$

3. The process is repeated for all values of A.

A	$\hat{y}$
0.1	$\hat{y}_{mean\mid A=0.1}$
0.7	$\hat{y}_{mean\mid A=0.7}$
0.5	$\hat{y}_{mean\mid A=0.5}$
0.6	$\hat{y}_{mean\mid A=0.6}$

4. These mean values are then plotted to give the PDP for variable A.

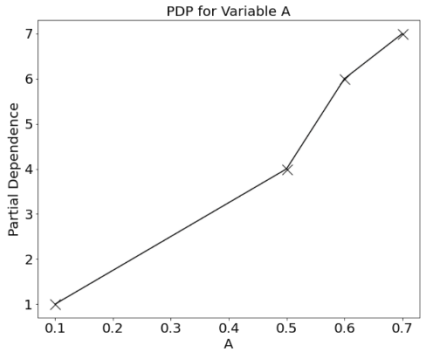

Figure 3.5 The process of creating a PDP. Step 1 shows a dummy dataset, created to give a simple example of the methods used to create the final plot, shown in step 4. PDPs are a way of understanding the individual impact of a variable on the model prediction. In step 4, as variable A increases (on the x-axis), the increase in the prediction is shown on the y-axis.

The biggest disadvantage of PDPs is that they assume the input variables are independent. This is because the mechanism behind calculating the values relies on artificially setting one feature to a certain value, and assuming this will not affect the others. This results in a PDP

that is calculated using points which in reality are not physically possible (Molnar, 2022). For example, a large amount of rainfall occurring in a month, but relative humidity being very low. As illustrated by this example, in this case the variables are not independent, so any analysis of these plots must take this into consideration. Even if the artificial datapoints used to create the PDP are physically sound, they could extrapolate significantly from the dataset used to build the model, which should be avoided. Another disadvantage can be seen in step 2 of Figure 3.5. The methodology takes means of the model predictions for a certain variable value but does not give any indication of the distribution of these predictions. A point marked on the PDP plot could have a high value for standard deviation that will not be visible to a reader of the plot.

ALE plots address the problems associated with PDPs' inability to handle correlated variables by examining the relationship between predictor and model prediction in a small window around the predictor variable observed value, examining the sensitivity of the target variable (the SUHI) to a chosen predictor. This is also less computationally expensive, as model predictions do not have to be generated for the entire dataset (Apley and Zhu, 2016). Figure 3.6 shows how an ALE plot would be calculated for the dummy dataset shown for a PDP in Figure 3.5. By only looking at an interval close to a true observation, the data points considered by the algorithm are realistic and not mixing the effect of correlated features. Accumulating the points and centering the plots on zero means that the y axis on the plot shows the difference from the mean prediction. The x-axis on the ALE plot shows a variable, and the y-axis shows the difference from the average prediction at that point (Molnar, 2022). For example, at A = 0.5 (see Figure 3.6), the value for the ALE plot is 0, and for A= 0.6 the ALE plot increases by 1. So, at A = 0.5 it can be expected you will have a y value around the mean of the dataset. If you increase variable A by 0.1 (from 0.5 to 0.6), this will increase y by 1.

1. A model is fit to the data in the table.

A	B	C	y
0.1	5	20	y_1
0.7	10	22	y_2
0.5	9	21	y_3
0.6	8	25	y_4

2. The first point where the ALE value is to be calculated is set to some interval above and below, leaving all other variable values unchanged. A prediction is generated for both and the difference taken. This is the 'local effect'.

A	B	C	$\hat{y}$
0.05	5	20	$\hat{y}_{1\mid A=0.05}$
0.15	5	20	$\hat{y}_{1\mid A=0.15}$

$$\hat{y}_{diff\mid A=0.1} = \hat{y}_{1\mid A=0.15} - \hat{y}_{1\mid A=0.05}$$

3. The process is repeated for all values of A. Values which are in the same interval window are averaged. The differences are then added together- this is the 'accumulation'.

A	ALE value
0.1	$\hat{y}_{diff\mid A=0.1}$
0.5	$\hat{y}_{diff\mid A=0.1} + \hat{y}_{diff\mid A=0.5}$
0.6	$\hat{y}_{diff\mid A=0.1} + \hat{y}_{diff\mid A=0.5} + \hat{y}_{diff\mid A=0.6}$
0.7	$\hat{y}_{diff\mid A=0.1} + \hat{y}_{diff\mid A=0.5} + \hat{y}_{diff\mid A=0.6} + \hat{y}_{diff\mid A=0.7}$

4. The accumulated effects are centred so that the mean effect lies on zero, then a plot is made.

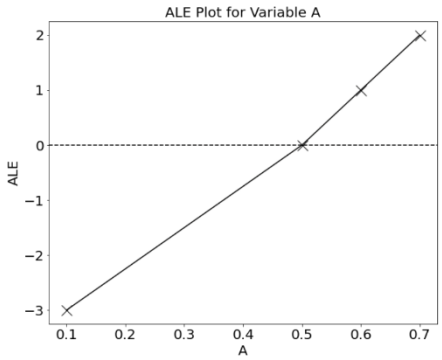

Figure 3.6 The figure shows the process of creating an ALE plot, based on a dummy dataset, shown in step 1. The final ALE plot is shown in step 4. ALE plots are a method of understanding how changes in a predictor variable can impact the prediction made by a model.

4 CREATING A STATISTICAL MODEL TO PREDICT THE SUHI

Creating a statistical model to predict the SUHI requires several steps, which are outlined in this chapter. The first is identification of the cities for which the SUHI will be examined. After these cities are selected, the SUHI magnitude (the target variable) and the variables used to predict it (the predictor variables) must be quantified. The target and predictor variables are then used to fit statistical/ machine learning models, with various methods employed to assess their accuracy and reliability and a choice of the best model is made. The model is then used to examine the current SUHI, through its relationships with the predictor variables. Each of these steps is discussed in this section.

4.1 SELECTION OF THE CITIES

In section 2.6, a need to address the gaps in the current literature with regards to both the locations of cities (to include cities in the Southern Hemisphere), and also the size of cities (medium sized cities). These are the cities projected to undergo increasing growth, resulting in urban hazards impacting increasingly higher numbers of people, yet the impacts of climate change on the city temperatures are uncertain. The selection of cities is made to include cities that satisfy both these criteria. Additionally, the surrounding features (lakes, hills, oceans) of cities are assessed, to control other variables and isolate the impact of climate. The cities are identified by starting with a large starting pool of cities, and narrowing this group down based on various criteria. A brief overview of the criteria can be seen in Table 4.1, with more descriptions given in this section.

Table 4.1 Brief Overview of the criteria for city selection and the number of cities remaining in the dataset after each step is performed.

Criteria	Threshold	Number cities remaining after criteria satisfied
Population	300,000 to 1,000,000	1,347
Location	< 40 °N Latitude	1,050
Not Coastal	> 100 km from shoreline	603
No lake breeze	> 50 km from large lakes (50 km diameter	600
No influence of water in rural reference	> 22 km from lakes greater than 1 km diameter	252
Topography	< 150 m standard deviation elevation in 55 km surrounding city	153
Nearby city influence	> 42 km to the nearest city with population over 300,000	120
City Area	> 5 km^2 city area in 2002	104

The starting dataset of cities was those with a population of between 300,000 and 1,000,000, taken from the United Nations population dataset (United Nations, Department of Economic and Social Affairs, 2019), discussed in section 3.1. These represent the medium sized cities, identified as a literature gap in section 2.6. This gave a total of 1,347 cities to explore. To meet the objective of studying cities of different climates and cities in the global south, cities were selected based on location being under 40°N latitude. Figure 4.1 shows the climate classification map detailed in section 2.4.2, with a line drawn to show the areas considered.

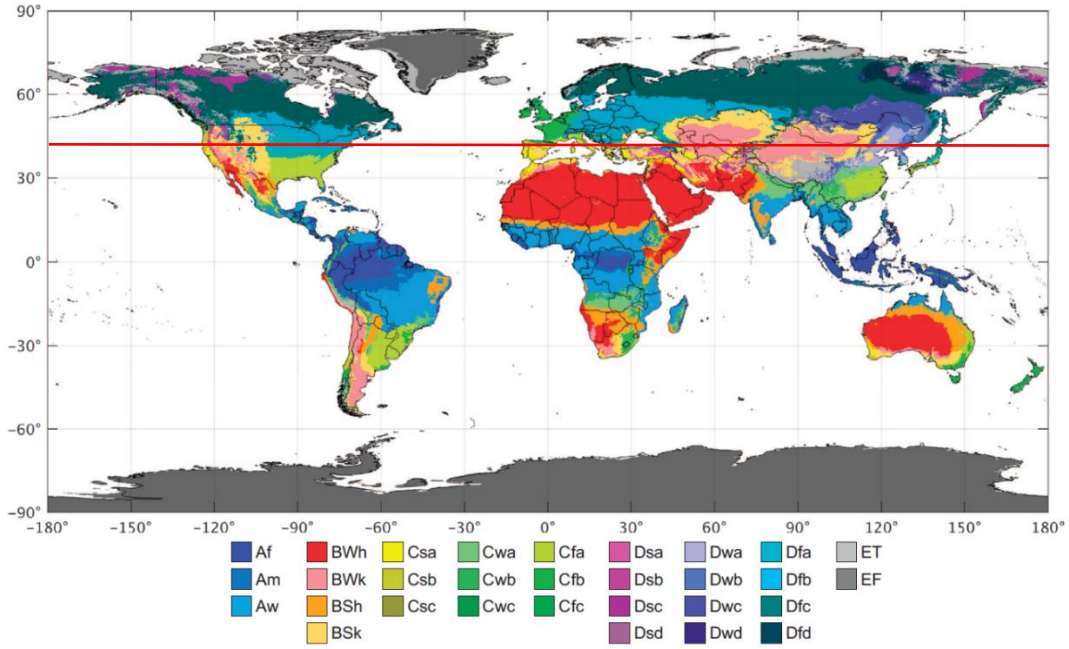

Figure 4.1 Koppen Geiger classification map, figure 1 from Beck et al (2018), areas under 40°N were considered in the selection criteria for final cities.

Sea breezes promote the dispersal of heat and are known to influence the UHI (section 2.4). The city selection process aims to remove any external influence aside from urbanisation hence coastal cities must be excluded. In a review of sea breeze observations, Abbs and Physick (1992) state whilst in mid latitudes the maximum sea breeze extent is 40 to 50 km, the tropical and subtropical sea breeze reaches up to 100 to 150 km inland. Therefore, in order to avoid the potential influence of a sea breeze on the SUHI, cities which were less than 100 km from the coastline are removed from the dataset (Figure 4.2).

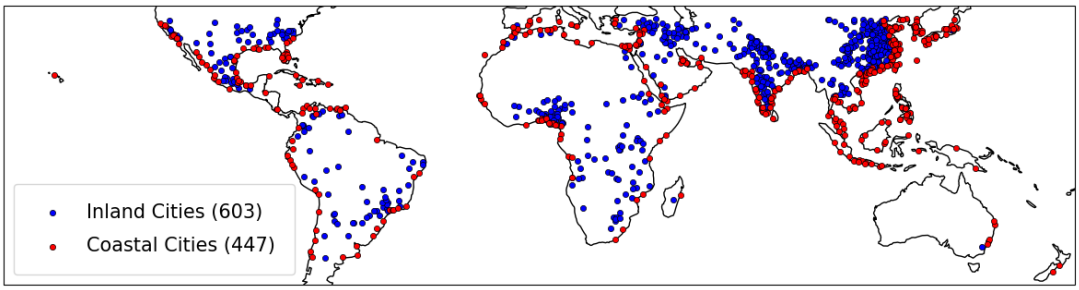

Figure 4.2 Cities less than 100km from the coast (red) are removed from the dataset.

For large lakes (diameter greater than 50 km), the lake breeze characteristics are similar to those of sea breezes (Segal *et al.*, 1997). The lake breeze is not as well studied as the sea breeze, but its inland penetration is shown to be less (Harris and Rao Kotamarthi, 2005). Based on this, a smaller distance to the large lake can be permitted, and cities within approximately 50 km (0.5° latitude/ longitude from the city centre) of a lake with diameter greater than 50

km were removed. Another important consideration is water bodies being in the rural area close to the city, as these have a cooling effect due to the heat capacity of water, and therefore must also be excluded. Therefore, cities with water bodies more than 1 km wide either in the city or the surrounding area (0.2° latitude/ longitude from the city centre) were also removed (Figure 4.3).

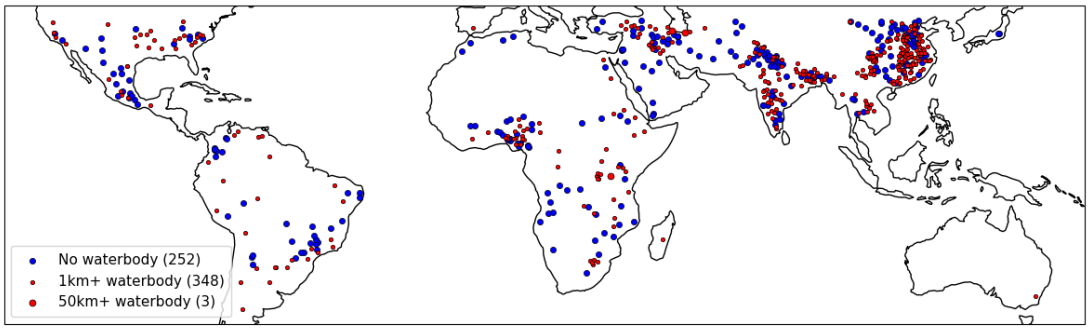

Figure 4.3 Cities where the influence of waterbodies could interfere with rural LSTs are removed (red).

Cities were also removed on the elevation of the area. In section 2.4, the UHI of cities surrounded by hills or mountains was influenced by this surrounding topography, so to mitigate this, cities where the city and surrounding area (55 km box around the city centre) have a standard deviation of elevation of more than 150 m are removed (Figure 4.4).

The 150 m figure was chosen based on limiting temperature differences due to elevation change. Experimentally, for the first 11 km of the atmosphere, the temperature difference is 1 °C for every 150 m change in altitude (Lente and Ősz, 2020). The accuracy of the LST data is found to be better than 1 °C (section 3.2), so an aim to keep the differences in the LST due to elevation to a minimum of 1 °C leads to keep elevation below 150 m.

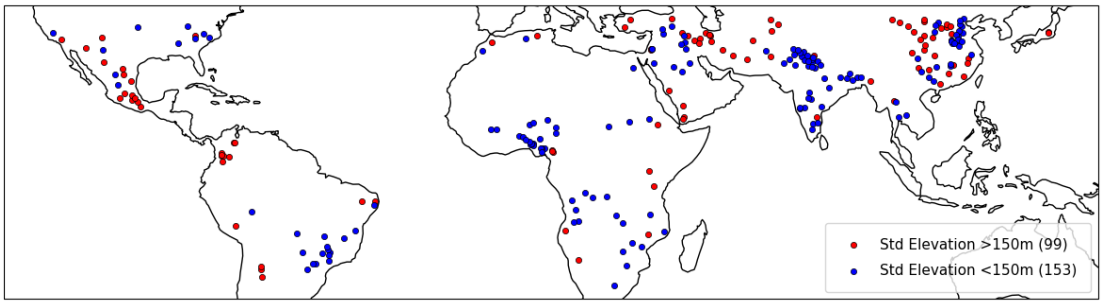

Figure 4.4 Cities in hilly areas are removed to reduce the influence of topography (red).

The distance to another city (with population greater than 300k) was considered. If another city is close by in the surrounding area, it will influence the LST of the surrounding rural pixels, leading to an inaccurate rural baseline LST. To avoid this occurrence, distances

between city centre coordinates and that of the nearest city were calculated, and those where the distance was less than 42 km were removed (Figure 4.5).

This distance was roughly calculated using the population density. According to the Organisation for Economic Co-operation and Development (OECD) (2020), population density of cities can range from 2,000 to 8,000 inhabitants per km^2 (in North America versus South Asia and Sub-Saharan Africa, respectively), so the midpoint of 5,000 inhabitants per km^2 is taken. The population range investigated in this study is from 300,000 to 1 million, so taking the upper end of the range gives a city area of 200 km^2 (1 million /5,000). It should be noted that the city areas found in this data will likely be smaller than this as they are calculate based on landcover data, and not administrative boundaries, so this is an estimate on the larger side to allow more room. The definition of the rural area to be used (outlined next in section 4.2) is three times the city height or width. Based on this, the rural extent considered for a square city of 200 km^2 area would be 42 km ($3 \times \sqrt{200\ km^2}$).

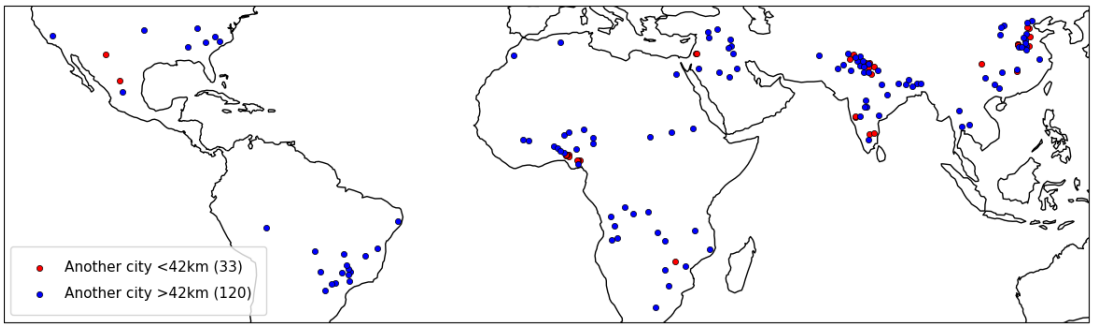

Figure 4.5 Cities with other cities in the surrounding area were removed to ensure a truly rural baseline (red).

After the cities were selected, land cover data (discussed in section 3.2) was used to determine the area of cities, and those with an area of less than 5 km^2 were removed, Figure 4.6. This was to ensure there was sufficient urban pixels in the LST dataset to not be too influenced by potential missing urban pixels (due to cloud contamination), as the resolution of this data is 1 km^2.

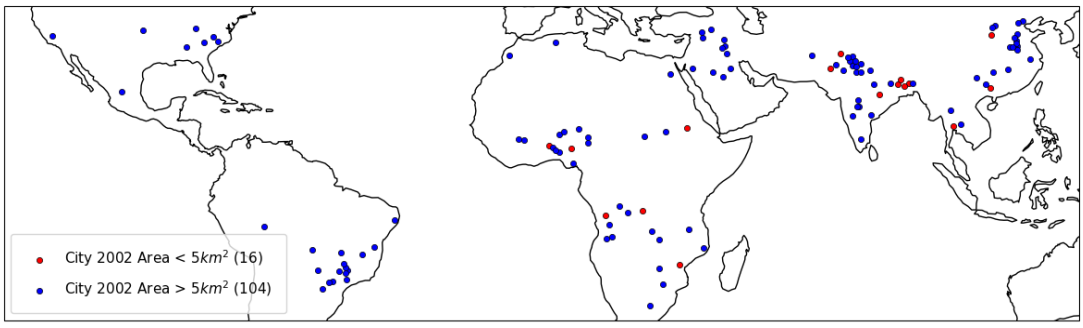

Figure 4.6 Cities which were smaller than 5km^2 in 2002 were removed to ensure the size is compatible with the LST dataset resolution.

The locations of the final selected cities can be seen in Figure 4.7, shown in blue, alongside those not selected in red.

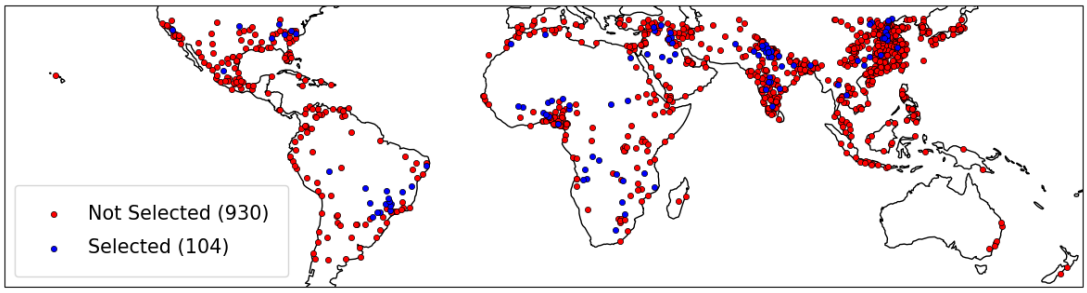

Figure 4.7 The final cities selected (blue) and those rejected (red) by the city selection process.

The final set of selected cities (104 in total) and are located in Afghanistan (1), Algeria (1), Angola (3), Bangladesh (1), Benin (1), Brazil (16), Burkina Faso (1), China (17), Democratic Republic of the Congo (DRC) (3), Egypt (1), India (18), Iraq (4), Mali (1), Mexico (1), Morocco (1), Mozambique (1), Niger (1), Nigeria (7), Pakistan (2), Saudi Arabia (4), South Africa (2), Sudan (2), Syria (1), Tanzania (1), Thailand (2), Turkey (2), United States of America (USA) (7), Zambia (1) and Zimbabwe (1).

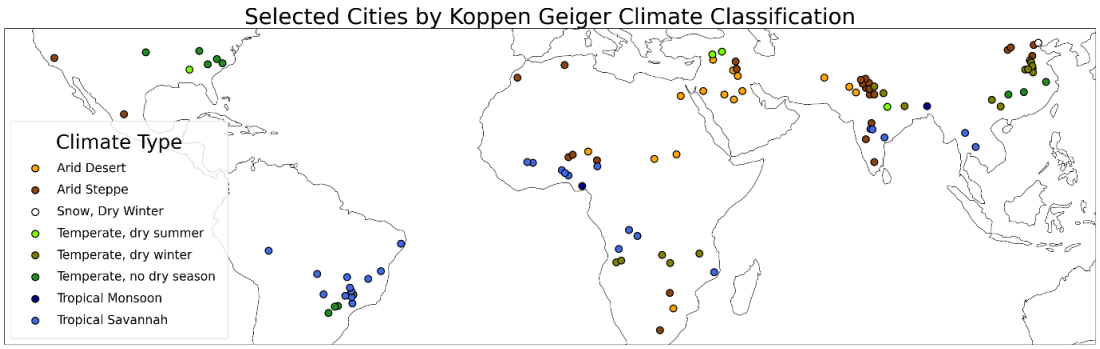

Figure 4.8 The final selected cities to be modelled and their Köppen Geiger Climate classifications.

Figure 4.8 shows the final selected cities by Köppen Geiger Climate classification. The cities encompass a range of different climates, ranging from arid to temperate to tropical. The plot also draws attention to some cities that are close in location but have different climate classifications, demonstrating the potential pitfalls of using categories for continuous data explained in section 2.4.

Figure 4.9, Figure 4.10, Figure 4.11, Figure 4.12, Figure 4.13 show photos of some of the selected cities.

Figure 4.9 Bikaner, India. View of the city from Jain temple before a sandstorm. Photo Credit: https://tinyurl.com/2rkhxey3.

Figure 4.10 Sokoto, Nigeria, Ariel View, Photo Credit: https://soluap.com/sokoto/.

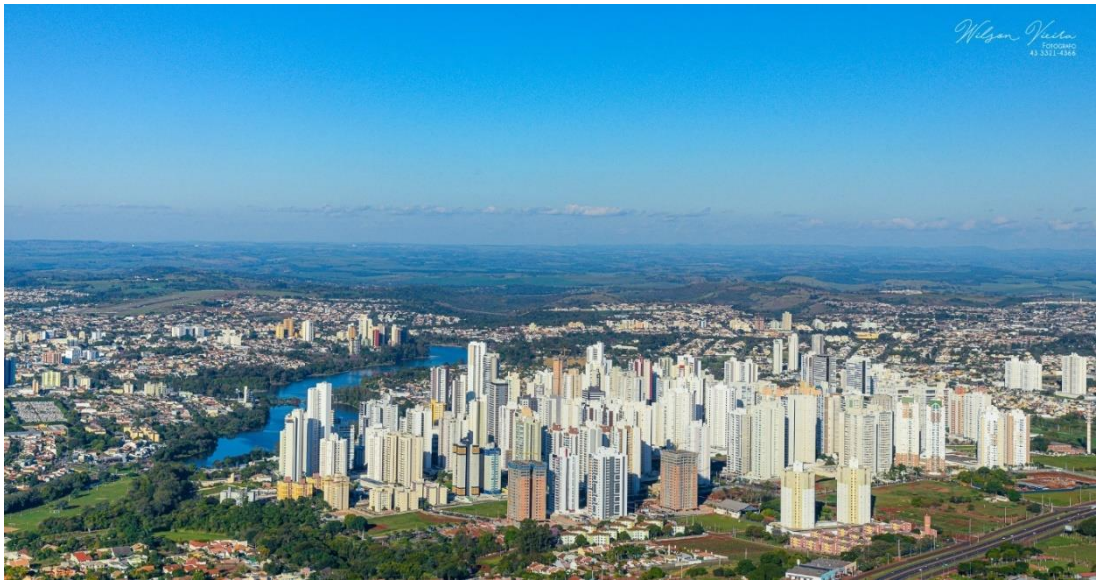

Figure 4.11 Londrina, Brazil, Photo Credit: Wilson Vieira, https://tinyurl.com/5fcswka9.

Figure 4.12 Visalia, USA. Photo Credit: Jacob Boomsma, https://tinyurl.com/rm3yetv7.

Figure 4.13 Heze, China. Photo Credit: https://tinyurl.com/ydceev3a.

4.2 GENERATING THE TARGET AND PREDICTOR VARIABLES

After city selection, the next step is to generate the target and predictor variables to be used as the data in the model. The target variable is the SUHI magnitude, as this is what the model should predict. The predictor variables are selected to be variables which are known to influence the SUHI magnitude. These variables are shown in Figure 3.1 as the grey boxes with rounded corners, where they are split into training and test data to build and assess the model, respectively. The target and predictor variables are generated using satellite and reanalysis data, described in section 3 and seen in Figure 3.1. An additional step for the satellite data was to ensure the images used were of sufficient quality, which is covered in this section first. The steps taken to process the data (satellite and reanalysis) and get it into the desired variables are then outlined.

Data Quality

One of the limitations of satellite data (section 3.2) is that it is possible for pixels to be unusable due to cloud contamination. If too many of the pixels are unusable on a given day, results generated from this dataset will be incomparable to days with more pixels and using these images will result in biased results. To ensure the satellite datasets used were accurate, a threshold for the number contaminated pixels was set at 30% for the LST, EVI and WSA data.

Any images with a number higher than this were discounted from the study, and for the images deemed acceptable, any poor-quality pixels were masked in the analysis to promote accuracy. This threshold for the number of pixels varies from study to study, ranging from 10% (Quan *et al.*, 2013) to 50% (Yang *et al.*, 2019; Li *et al.*, 2022). The 30% threshold was chosen as to strike a balance between selecting the most accurate LST images, but also aiming to reduce the inevitable bias towards certain weather conditions (if the threshold is chosen too strictly, images will be limited to completely cloud free days), discussed in section 3.2.

Another additional threshold was added for the percentage of high-quality urban pixels. In some cases, the cloud contamination may be high only over the city. This case could lead to an image passing the initial quality check based on overall pixels but have very few or no high-quality pixels within the city. Therefore, a threshold of 50% for the number of pixels within the city was set. This was set at 50% rather than 30% to reflect the fewer pixels in the city, as setting the criteria too strict could result in too many rejected images.

Figure 4.14 shows the total percentage of LST images which satisfy this selection criteria for each city.

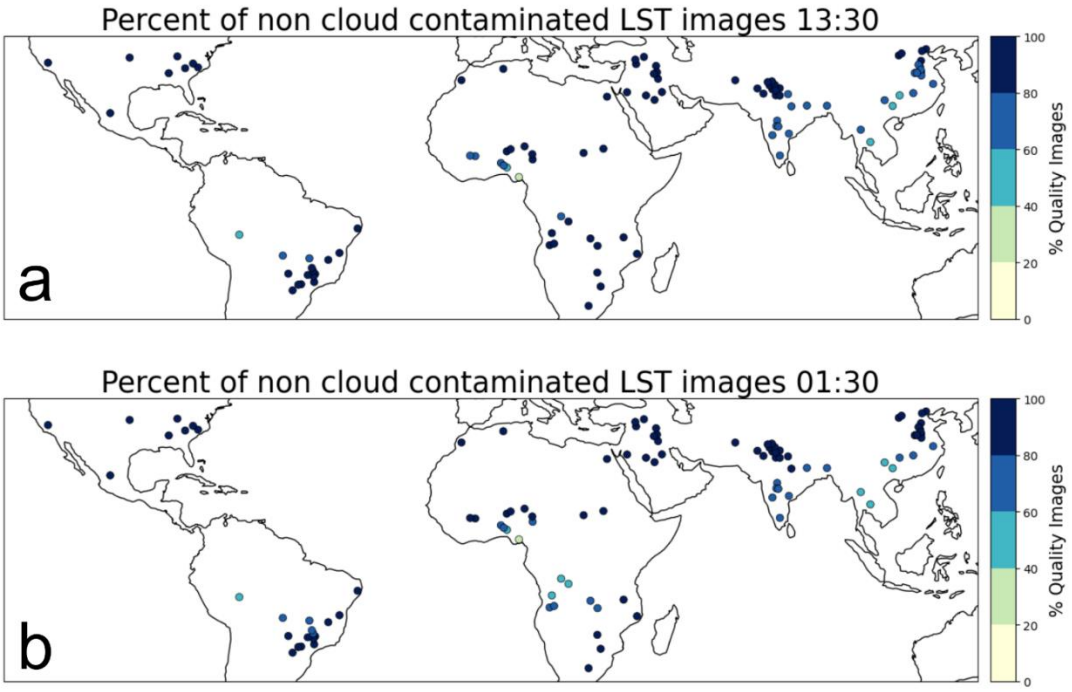

Figure 4.14 Map showing the locations of cities and the percentage of total images for which the city and its surrounding area has less than 30% cloud contamination and the city area has less than 50% contamination for a) the overpass at 13:30 and b) overpass at 01:30.

The majority of cities have a high percentage of LST image available for use, with the daytime and night-time city mean percentage of usable images at 85% and 84%, although some show a higher proportion of contamination. The city with the lowest number of available images is Umuahia, Nigeria, which has only 30% of those available showing good enough quality. Rio Branco, Brazil also shows a high percentage of contamination with 49% of images being available. A seasonal bias can be seen in the patterns of cloud contamination, shown in Figure 4.15 for the daytime (13:30) overpass and Figure 4.16 for the night-time (01:30) overpass. This reinforces the need to specify the analysis and model predictions made in this thesis are for the approximately cloud-free days only, and a large amount of extrapolation on precipitation volumes should not be done. The seasonal bias is expected, as during the wet seasons, there will be a high number of cloudy days. This is similar for both the daytime and night-time overpasses, as the cloud persists throughout the 24-hour period, although the night-time shows slightly fewer cloud contaminated images in some cases. JJA months (June, July, August) are when the highest number of cities have less than 10% of images available due to cloud contamination, consisting of four cities in total, Lampang and Nakhom Ratchasima (Thailand), Mymensingh (Bangladesh) and Umuahia (Nigeria). Figure 4.17 shows the seasonal precipitation patterns for the selected cities, which confirms the increase in cloud contamination during the rainy seasons. Comparison of the cloud contamination and

precipitation plots for the DJF months (December, January, February) also shows how the cities with more contamination are in the wet seasons during this time.

This bias is one of the main drawbacks of using satellite data (see section 3.2), and currently remains unavoidable. As useful information can be inferred about these cities from the data that is usable, they are kept in the analysis. However, when using the learned SUHI model to extrapolate, changes in precipitation are assessed to ensure they do not go too far beyond the model training input range.

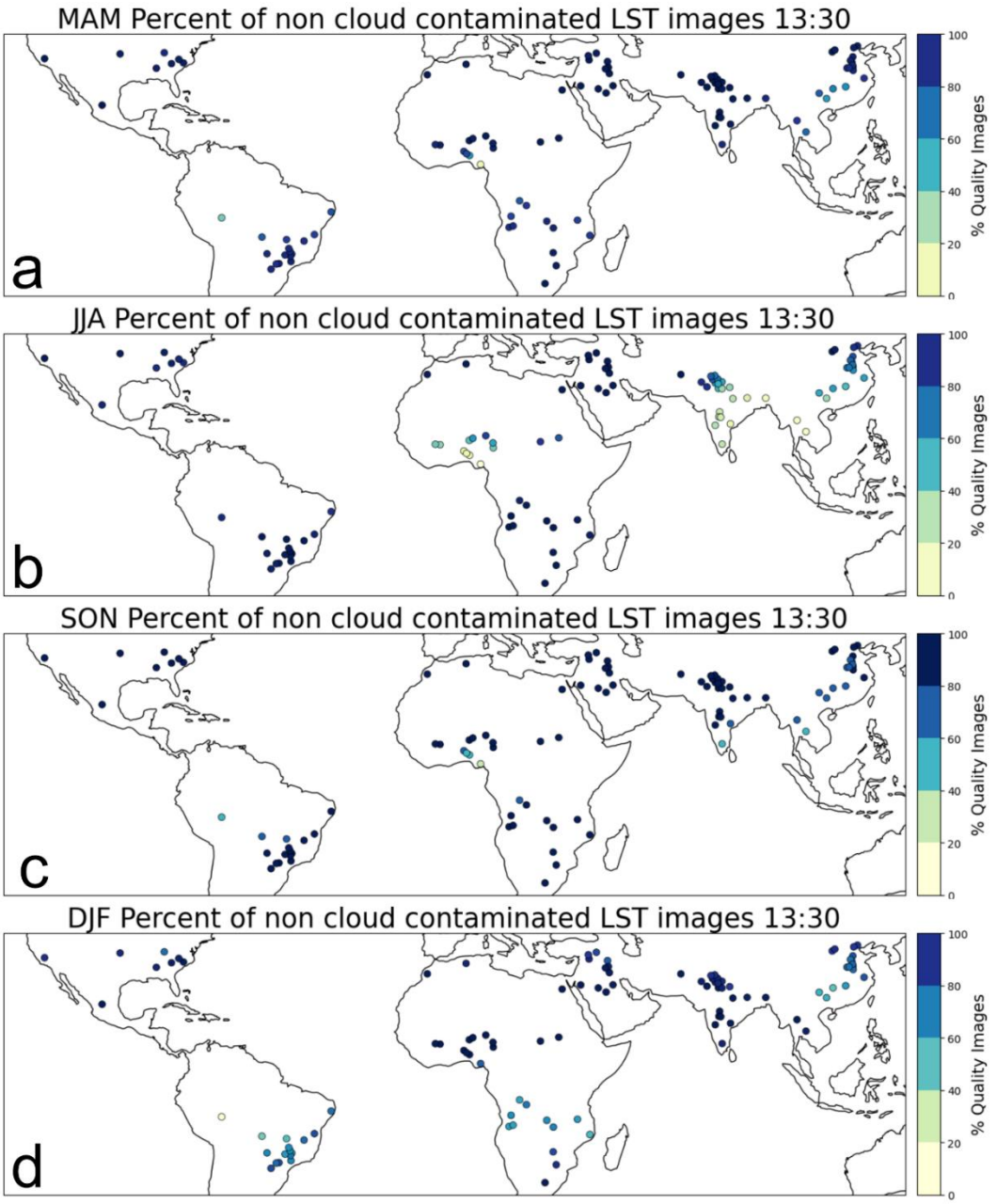

Figure 4.15 Map showing the locations of cities and the percentage of total LST images for which the city and its surrounding area has less than 30% cloud contamination and the city area has less than 50% contamination in the 13:30 overpass for a) MAM (March, April, May) b) JJA (June, July, August) c) SON (September, October, November) d) DJF (December, January, February).

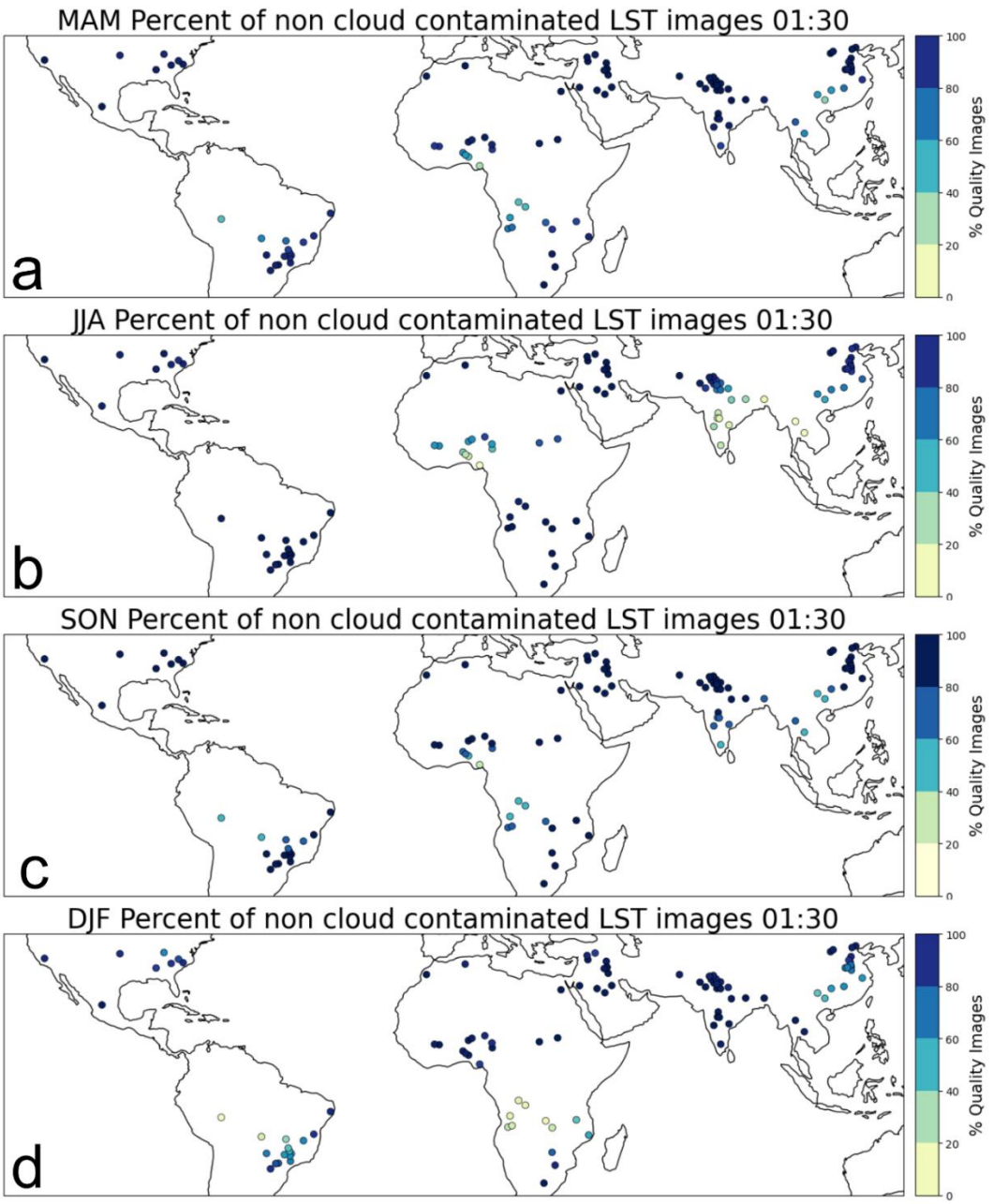

Figure 4.16 Map showing the locations of cities and the percentage of total LST images for which the city and its surrounding area has less than 30% cloud contamination and the city area has less than 50% contamination in the 01:30 overpass for a) MAM months (March, April, May) b) JJA Months (June, July, August) c) SON Months (September, October, November) d) DJF Months (December, January, February).

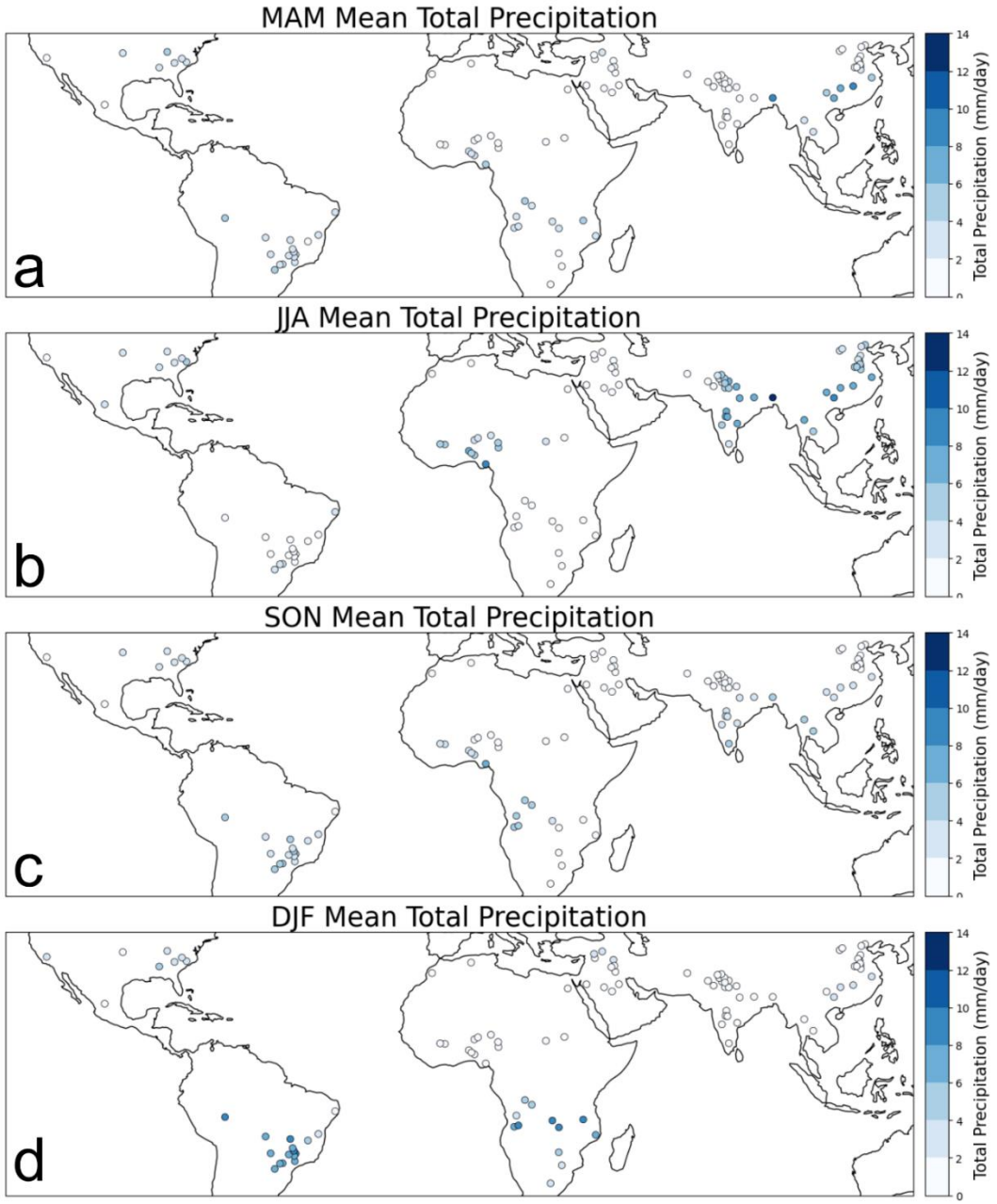

Figure 4.17 Total precipitation rate for a) MAM months (March, April, May) b) JJA Months (June, July, August) c) SON Months (September, October, November) d) DJF Months (December, January, February).

For EVI data, both the Aqua and Terra MODIS datasets were used, and the same quality thresholds applied. As the 16-day product was used, monthly means were calculated by combining images where the 8th day falls within that month. This is to ensure the timeframe where the EVI is calculated lines up with that of the LST data.

The annual mean percentage of quality images for a city was less than for the LST images at 76%. Figure 4.18 shows the spread of this percentage across the cities. Different measurements are used to calculate LST and EVI (EVI uses the red and blue in additional to

the near infrared bands, bands and LST the infrared bands) and the composition methods used to create the final products are different. LST in this thesis is only using the Aqua overpass in comparison to the additional use of the Terra (at 10:30) for EVI. Therefore, differences in the cloud contamination of the two measurements type can be expected. Table 4.2 shows a summary of the seasonal bias for each set of images.

As with the LST images, there are some cities that experience higher levels of cloud contamination than others. Ha'il (Saudi Arabia) and Gombe (Nigeria) have the lowest number of good quality images at 33% and 34% respectively.

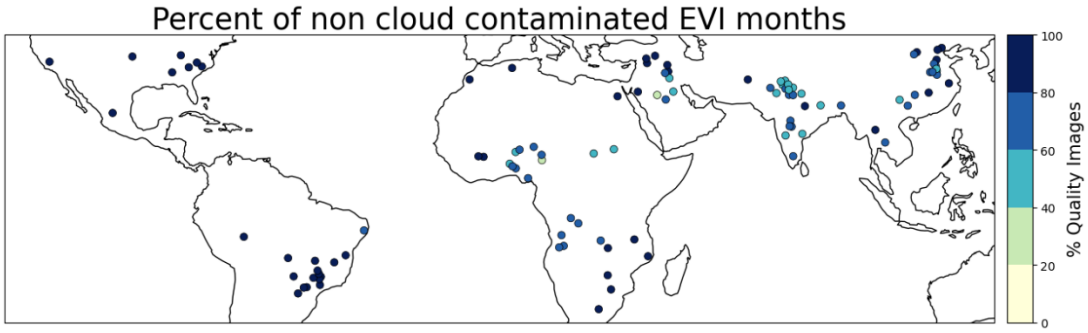

Figure 4.18 Map showing the locations of cities and the percentage of total EVI images for which the city and its surrounding area has less than 30% cloud contamination and the city area has less than 50% contamination.

Seasonal bias of the cloud contamination in EVI images can be seen in Figure 4.19.

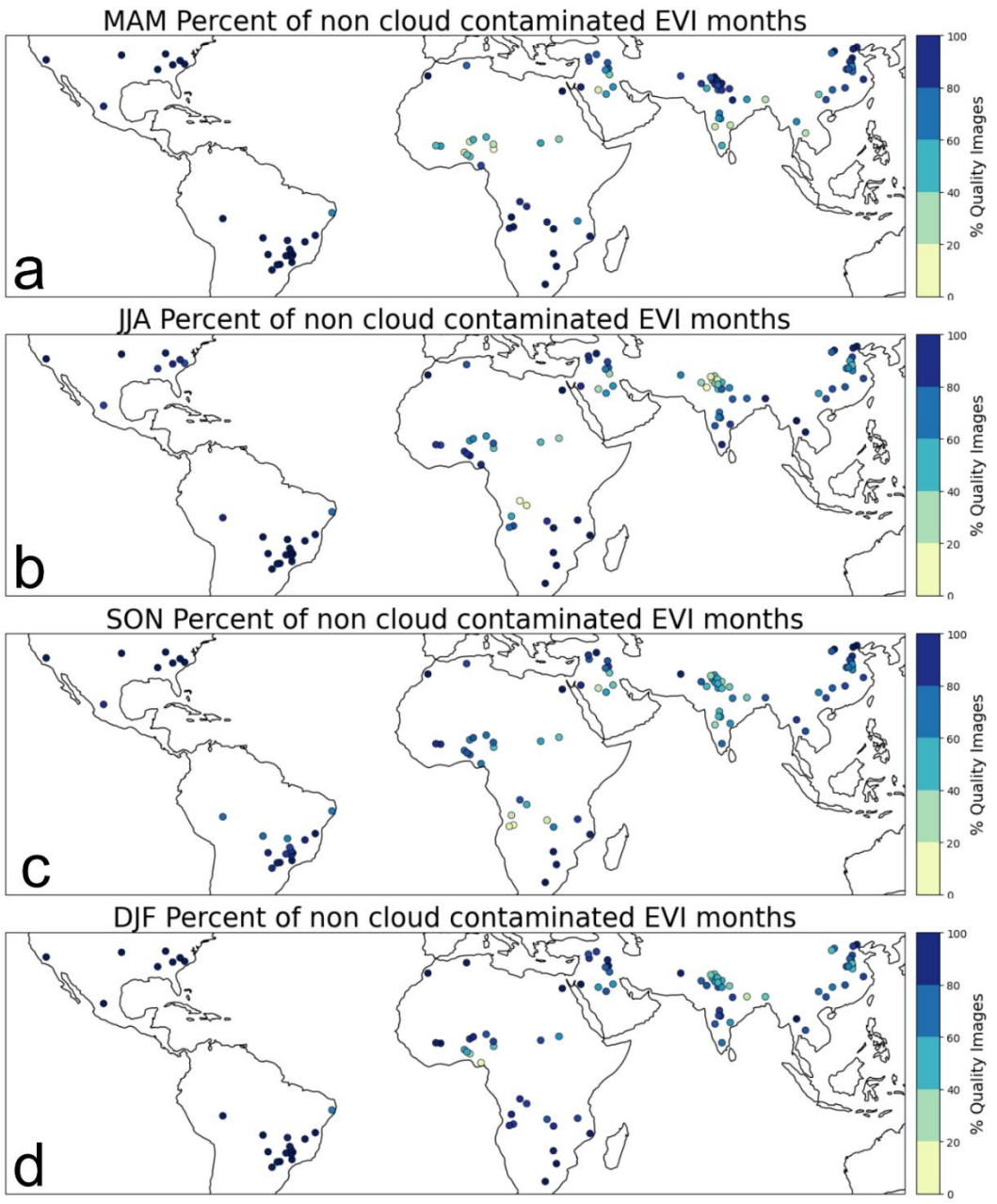

Figure 4.19 Map showing the locations of cities and the percentage of total EVI images for which the city and its surrounding area has less than 30% cloud contamination and the city area has less than 50% contamination a) MAM months (March, April, May) b) JJA Months (June, July, August) c) SON Months (September, October, November) d) DJF Months (December, January, February).

As with LST images, EVI images show the most contamination in the JJA months. Gombe (Nigeria) experiences the most contamination in MAM, Kikwit (DRC) and Bikaner (India) are seen to have the most during summer months, and Cuito (Angola) in SON months.

For the WSA data, quality flags were consulted, and a pixel was deemed of sufficient quality if there were at least two days out of the 16 for which the quality was good. The useable images

were grouped by the month of the 9th day (as the data is temporally weighted around this day) and the mean of these used as the final monthly value.

For WSA, 89% of the final monthly grouped images were useable. Figure 4.20 shows the distribution of the fits by city. As with the LST images, Umuahia (Nigeria) has the lowest percentages of usable months at 21% and Hechi (China) follows closely with only 26% of months usable.

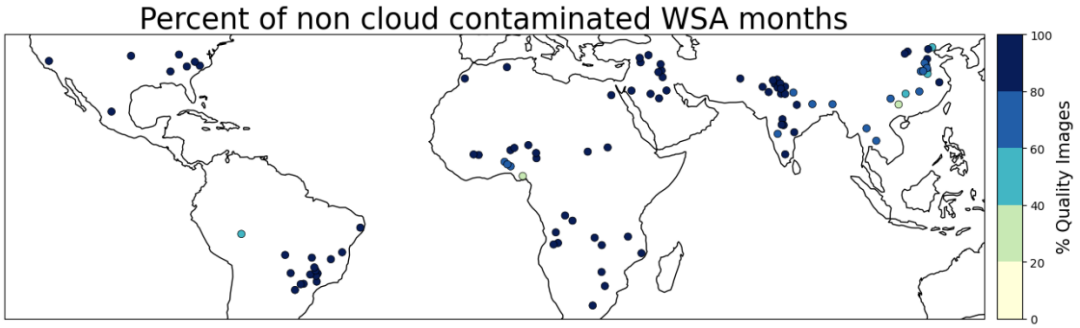

Figure 4.20 Map showing the locations of cities and the percentage of total WSA monthly images for which the city and its surrounding area has less than 30% cloud contamination and the city area has less than 50% contamination.

Table 4.2 Summary of the percentage of non-cloud contaminated images for LST 13:30, LST 01:30 and EVI data.

	Percentage of non-cloud contaminated images			
Season	**LST 13:30**	**LST 01:30**	**EVI**	**WSA**
MAM	92%	89%	77%	94%
JJA	75%	80%	75%	77%
SON	88%	87%	73%	92%
DJF	84%	80%	78%	92%
Annual	85%	84%	76%	89%

SUHI Quantification

The overpass times 13:30 and 01:30 are studied as these are closest to when the 2m air temperatures are at a maximum and minimum (and therefore encompass a wider diurnal range), in comparison with the 10:30 and 22:30 overpasses which are also available (Oke *et al.*, 2017; Du *et al.*, 2021).

Rural Extent

The first decision to be made when quantifying the SUHI is the area over which to examine. Whilst the area of the city can be clearly identified by land cover information, the extent of the rural area to use as a reference is less clear-cut. The choice of how the rural area is defined can have an impact on the values given for the SUHI. For example, an area too big can include too much topography and even other cities or urban areas (if the area is above 42 km in this case, as this was checked for in city selection, section 4.1), but an area too small can include too much influence from the city. Clinton and Gong (2013) find that using a 10 km ring around the city (known as the 'buffer', see section 2.3.1) results in a larger SUHI magnitude than the 5 km buffer, most likely due to the smaller area containing influence of suburban areas.

There are two types of approaches to defining the rural land. One approach would be to set the size of the whole area used, urban and rural, to a predetermined distance from the city centre and use this for all cities (Rajasekar and Weng, 2009; Anniballe *et al.*, 2014; Bechtel, 2015; Lai *et al.*, 2021). This is easy to implement, as the area stays the same for all cities so little processing is needed to determine the area. The second approach is to have the rural area proportional to the city size. For example, Yang et al (2019) set the rural area to be the same as that of the urban core. This means that in the larger cities, the number of rural pixels in comparison to the number of urban pixels will remain the same as in the smaller cities. Fewer rural pixels, and of these a high percentage nearer to city itself may lead to an apparent smaller SUHI in large cities due to this smaller heat differential in a smaller buffer (Clinton and Gong, 2013).

The rural area was therefore defined to follow the second approach, but rather than a circular buffer a rectangular shape was used. The area was chosen to be a box with width three times that of the city and height three times that of the city (so the city takes up roughly 10% of the entire area). To ensure the area was not too small for very small cities, if this ended up being less than 10 km, then a length of 10 km from edge of the city was used instead. The area in 2020 was used here for all the years in the study, to ensure a consistent rural landcover type throughout.

Mean SUHI (SUHI_MEAN)

The simplest way of quantifying the SUHI is to use a mean SUHI value (which will be referred to as SUHI_MEAN). The method takes the mean LST for the city pixels marked urban and subtracts the mean LST for the pixels marked rural, see equation (4.1). Any urban pixels in the area outside of the city were asked, and not included in either mean.

$$SUHI\_MEAN = \sum_{i}^{n_{urban}} LST_{urban} - \sum_{i}^{n_{rural}} LST_{rural} \quad (4.1)$$

where LST_{urban}, n_{urban}, LST_{rural}, n_{rural} represents the LST and number of urban and rural pixels, respectively.

A benefit of using the SUHI_MEAN is that it can be calculated for cities which have irregular shapes, or the warmest part of the city is not at the centre, which other methods do not deal well with (in particular the Gaussian Surface Approximation (GSA), outlined in the appendix, section A.4). Using the SUHI_MEAN definition therefore increases the range of cities for which the model can be applied.

The need to assess multiple methods of SUHI quantification is highlighted in section 2.3.1, as different quantification methods have been shown to result in different outcomes in terms of the impact of city or climate related properties. For this reason, other methods of SUHI quantification were also used, in particular the GSA Peak SUHI magnitude, to be referred to as SUHI_PEAK_GSA (appendix section A.4). The focus here will be on the method found to be captured best by the ML models, which is SUHI_MEAN (details comparing the SUHI quantification methods can be found in A.4).

Assessment of the SUHI

The SUHI_MEAN shows diurnal and seasonal variations. Figure 4.21 shows how the SUHI_MEAN varies on a seasonal basis at both 13:30 and 01:30. During the daytime, many cities show strong negative or positive SUHI_MEAN, which decrease in magnitude during the night, and for negative daytime SUHI_MEANs become positive. There are some cities however, which experience very small SUHI_MEAN magnitudes (less than 1 °C) during the day but encounter more nocturnal heating. The Pearson's correlation coefficient (section 3.5) for 13:30 versus 01:30 SUHI_MEAN, is -0.16. The slight negative coefficient could indicate a strong daytime SUHI is associated with weaker one at night, but the magnitude of the coefficient is low, so it is hard to draw firm conclusions. The lack of correlation found between the two is confirmed in other studies (Peng *et al.*, 2012) indicating the factors that contribute

to a high SUHI in the day are different to those that drive the SUHI during the night (section 2.5.1).

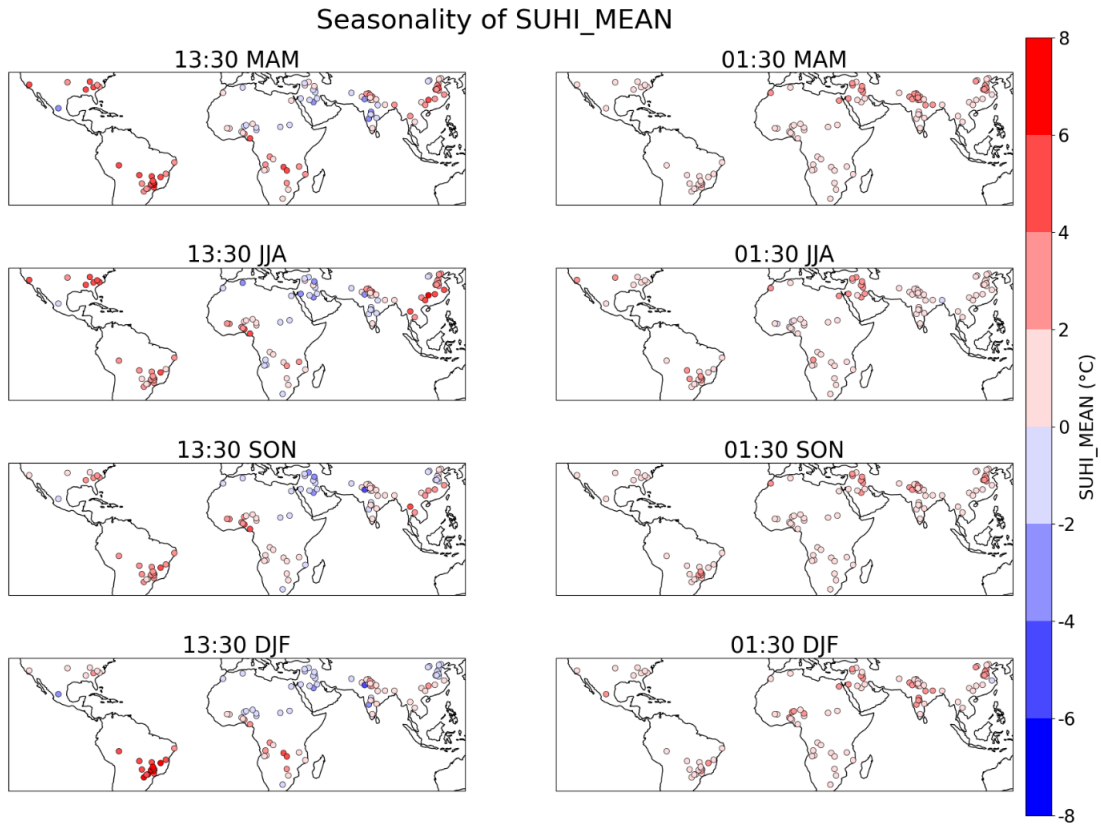

Figure 4.21 The seasonal and diurnal SUHI_MEANs for the selected cities. The seasonal SUHI_MEAN is shown for the 13:30 MAM (March, April, May), JJF (June, July, August), SON (September, October, November), and DJF (December, January, February) on the left-hand side, and the same for the 01:30 overpass on the right-hand side of the plot. Day (13:30) versus Night (01:30) differences can be seen by comparing the two sides.

Negative nocturnal SUHI_MEANs do not persist in any of the cities studied on average, although they have been observed for individual months, they are not a common feature for any of the cities studied. Table 4.3 gives a summary of the positive and negative annual SUHIs. The range of city annual SUHI_MEANs ranges from -4.0 °C to 5.4 °C for the 13:30 overpass and from 0.3 °C to 2.8 °C for the 01:30.

Table 4.3 Summary of the mean and standard deviations of SUHI_MEAN. These values were calculated by taking the annual means of the cities, then grouping them into two groups, those with a positive annual SUHI_MEAN and those with a negative annual SUHI_MEAN. The mean and standard deviation of these groups are then calculated and are seen in the table. The groupings are done separately for day and night. As outlined in the main text, there are not any cities with a negative SUHI_MEAN at night.

	Positive SUHI		Negative SUHI	
Metric	13:30	01:30	13:30	01:30
Mean SUHI	2.2 ± 1.3 °C	1.5 ± 0.6 °C	-1.1 ± 0.9 °C	-

Mean Enhanced Vegetation Index (EVI)

Mean EVI (section 3.2) was calculated for the urban and rural areas to give a measure of the greenness and vegetation activity in both areas. Both these urban and rural EVI values, and the difference between them are considered as predictor variables for the SUHI. The spatial averaging is done using the same method as for the mean SUHI outlined previously in this section (4.1), by simply calculating the mean result for the areas marked urban and rural. Figure 4.22 shows the annual mean values of rural and urban EVI (EVI_R and EVI_U) and the difference (urban minus rural) (EVI_D). For most cities, the rural EVI exceeds the urban, aside from 4 cities shown in blue in Figure 4.22c. Rural EVI also shows more variation between cities. Figure 4.22 shows the rural EVI split into 4 seasons. Rural EVI shows seasonal differences, increasing during the summer months (JJA or DJF, depending on the hemisphere of the city). The greatest rural EVI is in Cascavel (Brazil) in the DJF months at 0.56 and the lowest in Ha'il (Saudi Arabia) which persists at a mean of 0.06 year-round.

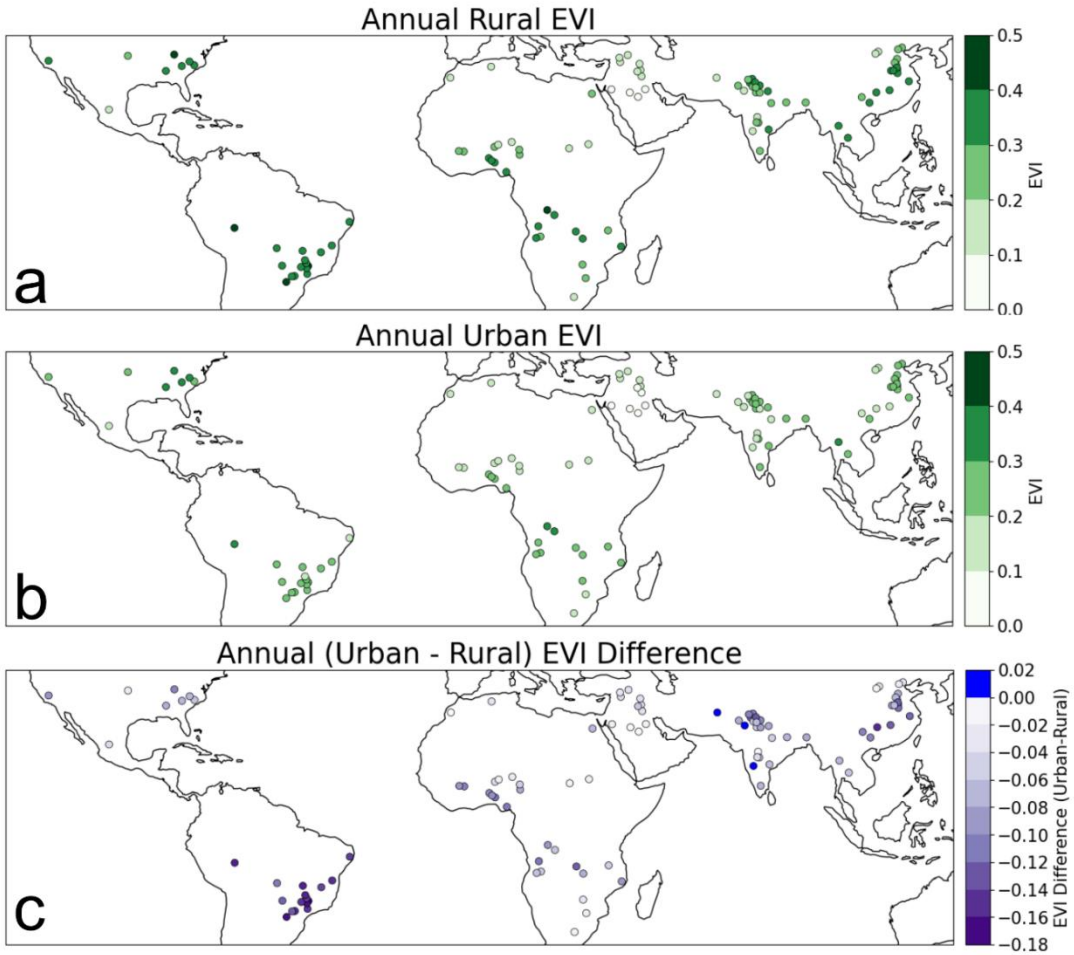

Figure 4.22 Map showing annual mean values of EVI averaged across 2002-2020 for a) rural area b) urban area and c) the urban minus rural difference. Cities with a positive EVI difference (urban area has a higher EVI than the rural area) are shown in blue.

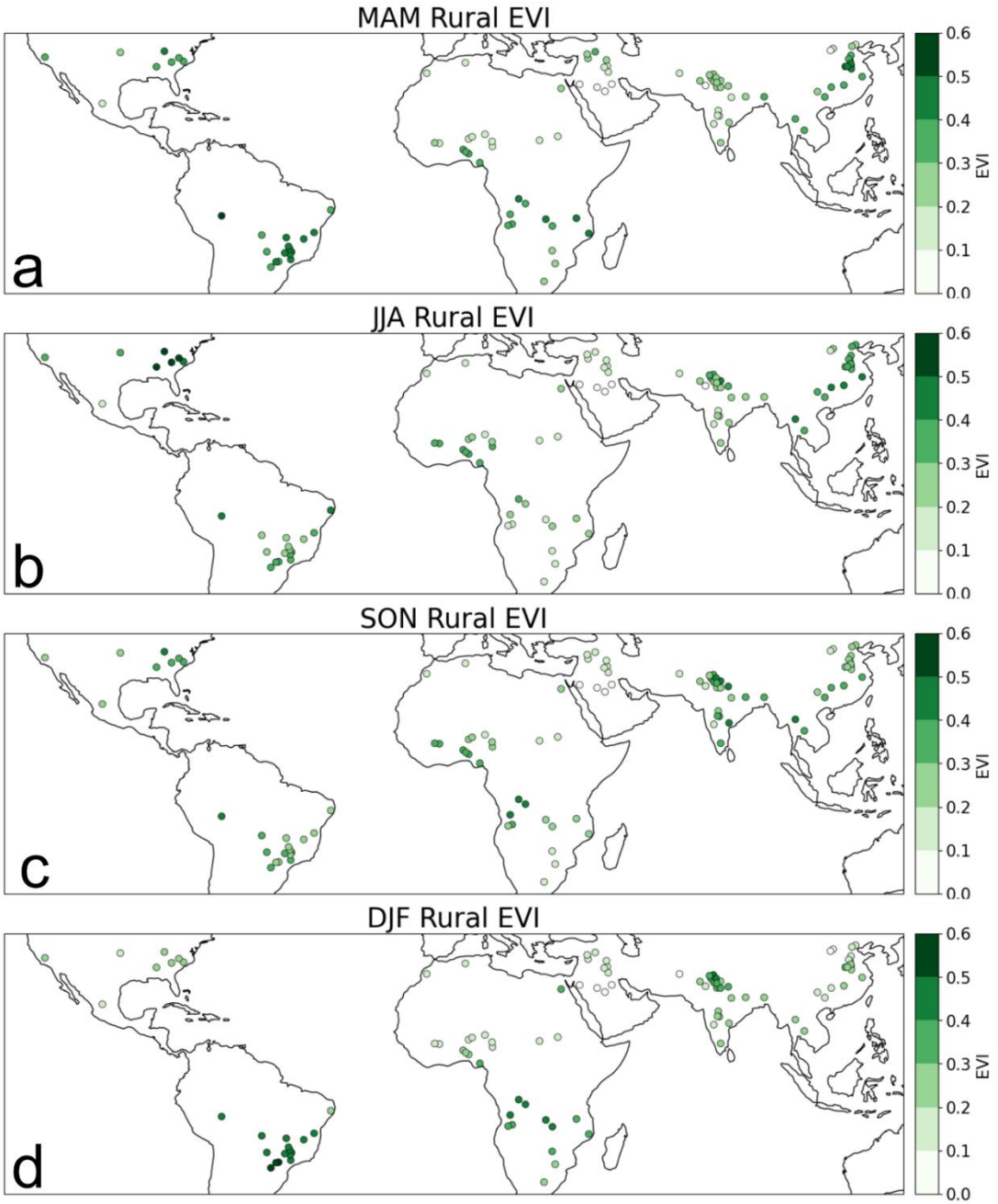

Figure 4.23 Seasonal Cycle of Rural EVI: the mean EVI of rural areas, averaged across 2002-2020 during a) Spring (March, April, May) b) Summer (June, July, August) c) Autumn (September, October, November) d) Winter (December, January, February)

Mean White Sky Albedo (WSA)

The mean WSA was calculated using the same spatial/pixel averaging method as for SUHI_MEAN and mean EVI values. Figure 4.24 shows the rural WSA (WSA_R) and the (urban – rural) WSA difference (WSA_D). The urban WSA is not included in the figure as the rural and urban WSA values are very similar, which can be seen by the scale of the WSA_D. Figure 4.24b shows the cities where there is a positive WSA_D in blue, where the WSA_U is greater than WSA_R, representing the cities where urban surfaces are more reflective than the surrounding rural area. This would be expected to lead to a decrease in the SUHI, as less solar radiation is reaching the city and warming its surfaces in comparison to the rural area. This is the theory behind SUHI mitigation measures such as white roofs. Areas with higher WSA_R are located in the arid environments, consisting of deserts, shrublands and bare soils, with comparatively higher albedos than forests and grasslands. The arid areas with high WSA_R also have the most negative WSA_D, so in these areas the urban materials are not as reflective as the rural surroundings.

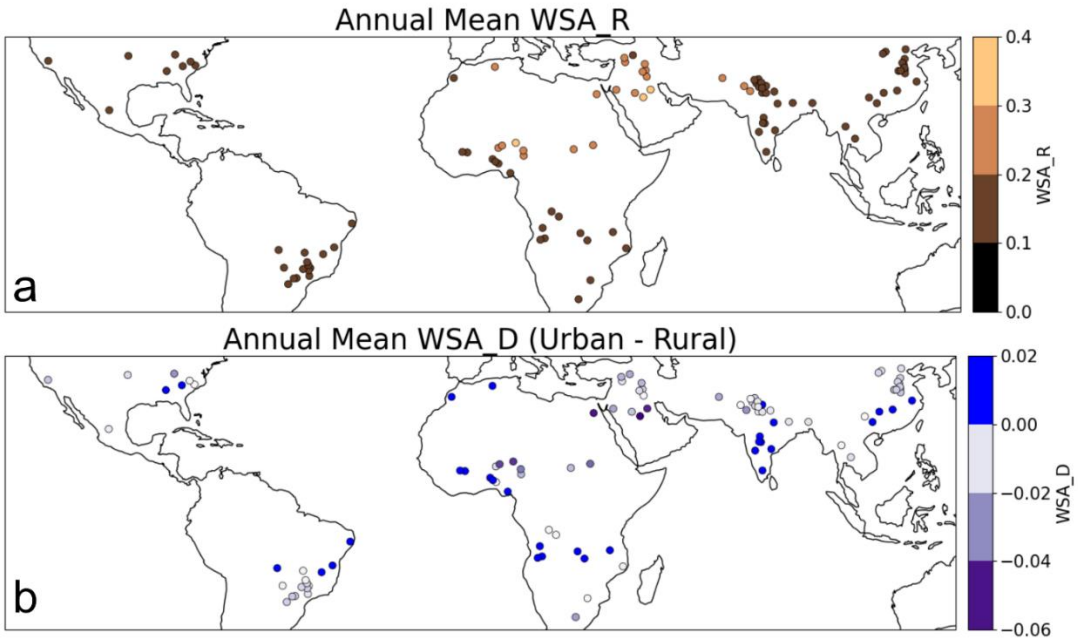

Figure 4.24 Map showing annual mean values of WSA averaged across 2002-2020 for a) rural area (WSA_R) and b) the urban minus rural difference. Cities with a positive WSA difference (urban area has a higher WSA than the rural area) are shown in blue. These are the cities which are brighter than the surrounding rural area.

City Size and Shape

The city predictor variables included in the model are the area and eccentricity of the city. Using the landcover dataset (section 3.2), the area of the city is calculated by summing the number of urban pixels within the bounds of the city area. Despite having population between 300 thousand and 1 million inhabitants, the areas of the selected cities show a wide range. Bahawalpur (Pakistan) and Mymensingh (Bangladesh) are the smallest two cities in any year, with areas of 5 km^2 in 2002, growing to 43 km^2 and 17 km^2 respectively in 2020. The largest city by 2020 is Birmingham, USA, spanning an area of 675 km^2. The methodology used to determine the city area means if a city is surrounded by a highly urbanised area (and therefore the whole area- city plus suburban surroundings- comes up as urban in the landcover data), these pixels will also be classed as urban and therefore part of the city. The city of Birmingham, USA has a large amount of suburban sprawl outside of the administrative borders of the city, which are classed as urban landcover. As the SUHI is driven by the urban landcover, it is important to still include these areas as belonging to the city.

Studies show as the city area increases, so does the magnitude of its SUHI (Zhou *et al.*, 2017; Gaur *et al.*, 2018; Dewan *et al.*, 2021). This relationship has been shown to be described by a logarithmic function (Imhoff *et al.*, 2010; Tan and Li, 2015; Li *et al.*, 2017). However, the focus in these past studies is on positive SUHI magnitudes. If the effect of the city area increasing is the amplify the SUHI, for a negative SUHI magnitude, the SUHI would be expected to become more negative as the area increases. The cities in this thesis show a similar relationship with $\log_{10}$(Area) as the current literature for cities with a positive SUHI_MEAN (averaged over the entire dataset, from 2002-2020) (Figure 4.25), and a relationship where the SUHI magnitude becomes more negative in cities with a negative SUHI_MEAN. As there are only positive annual SUHI_MEANs during the night-time (01:30), the relationship is positive here. Pearson's correlation coefficients show the strongest relationship is during the day (13:30) for positive SUHI_MEANs, at r = 0.39, followed by the negative correlation for negative SUHI_MEANs at r = -0.24. Finally, the night-time (01:30) SUHI_MEAN has a smaller positive correlation with the $\log_{10}$(Area) than during the day, at r = 0.22.

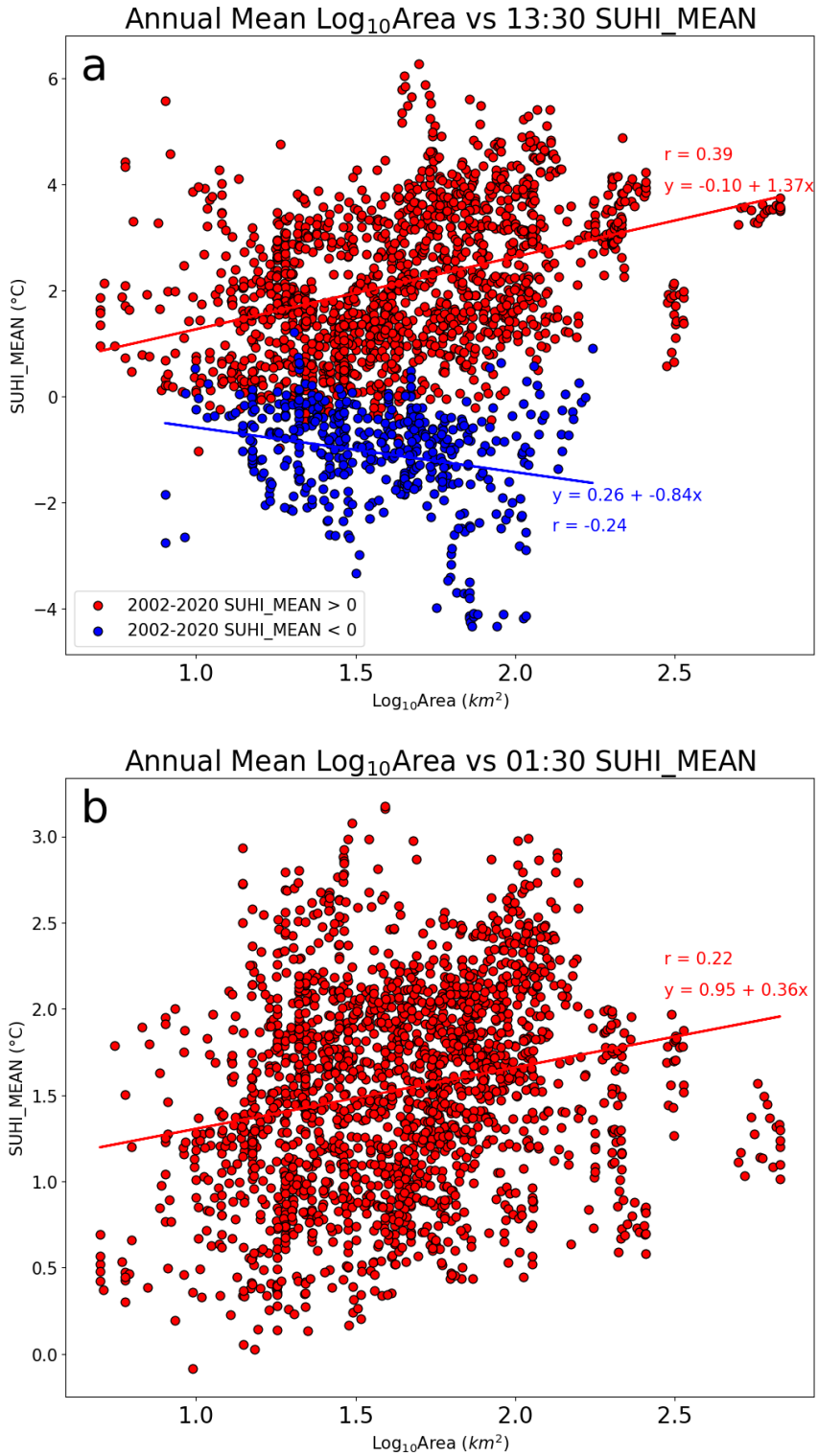

Figure 4.25 Log_{10}(Area) plotted against annually averaged SUHI_MEAN, with the type of SUHI_MEAN (positive or negative) shown by colour for a) 13:30 b) 01:30. The least squares optimised line of best fits and corresponding Pearson's correlation coefficients are shown for the Log_{10}(Area) versus positive (and negative if relevant) SUHI_MEANs.

The eccentricity is included as a measure of the city shape. It is calculated by fitting an ellipse representative of the city shape and calculating its eccentricity, defined by

$$ecc = \sqrt{\frac{a^2 - b^2}{a^2}} \tag{4.2}$$

where a^2 is the major axes and b^2 is the minor axes (a > b).

If the eccentricity is 0 the shape is a circle, and it becomes more elliptical as it moves closer to 1. This could reflect the change of a city shape over the years if it expands in one direction and reflect differences across cities. It is common for cities to have more of an elliptical shape, with few cities having an eccentricity of close to 0.

Zhou et al (2017) studied the urban form and its relation to the daytime mean SUHI for cities in Europe, finding its intensity decreases as the city becomes more elliptical. This could be due to an inner core less isolated from the surrounding rural areas. However, in the chosen cities, there does not appear to be an obvious trend between eccentricity and SUHI_MEAN. This suggests that for the cities considered here, other factors are more important and effectively overlay any possible effect of the city shape on the average SUHI_MEAN magnitude.

Climate Variables

The spatial resolution of the reanalysis climate data (section 3.3) used is relatively coarse in comparison to the satellite data (used for LST, EVI and WSA), with a spatial resolution of 9 km versus 1 km. This means it cannot capture values for the urban area and the rural area separately. Therefore, the climate variables (relative humidity, total precipitation, net surface solar radiation, evaporative fraction) were taken to be the mean of the entire area inspected for the analysis, including both the city and the rural area. To give an idea of the general climate characteristics, Figure 4.26 shows some of the climate characteristics of the selected cities (2m air temperature was additionally calculated to give a more detailed picture of the climate characteristics of the cities, but this is not used in the ML model).

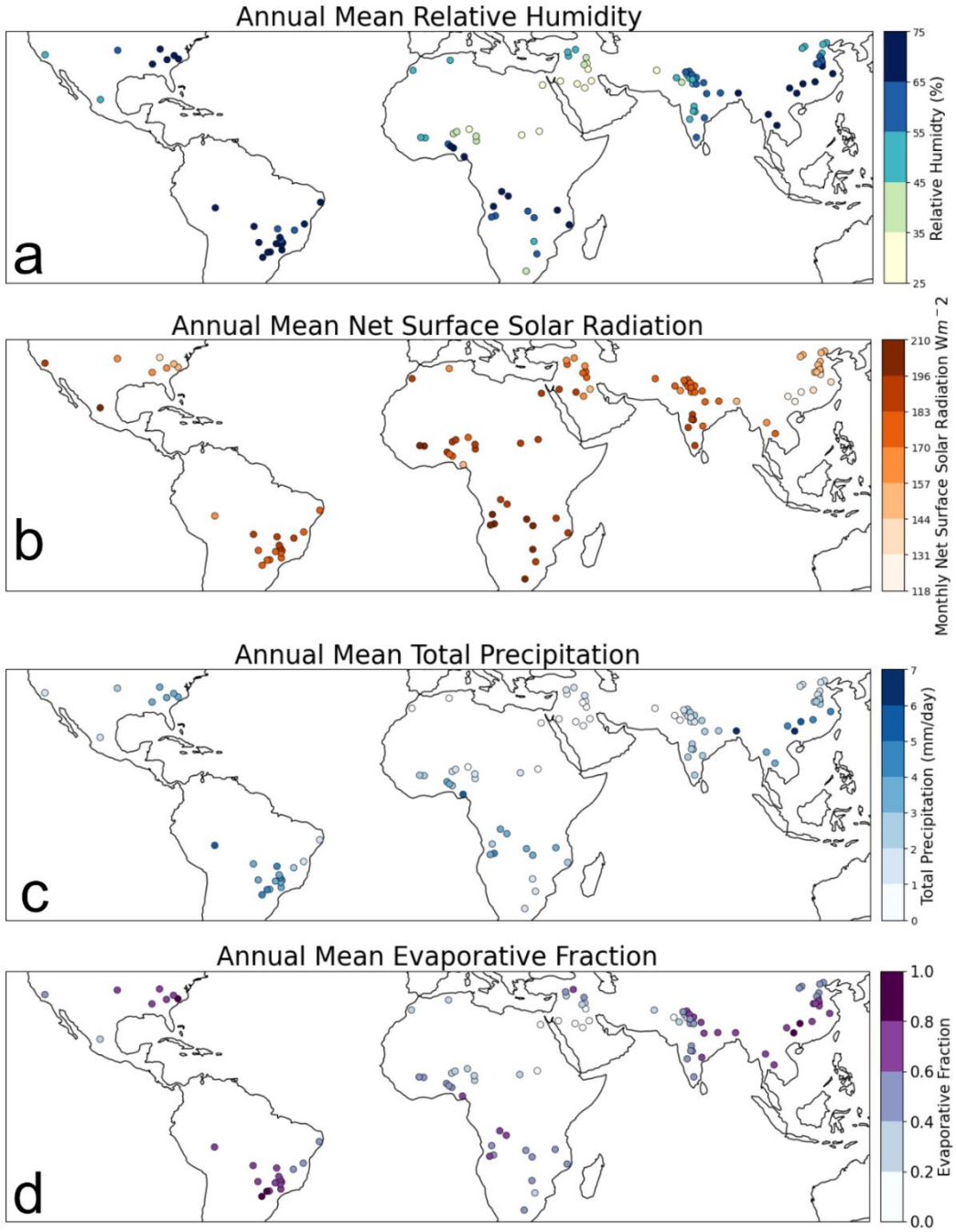

Figure 4.26 Annual mean climate characteristics averaged across 2002-2020 for the selected cities. Considered are a) relative humidity b) net surface solar radiation c) total precipitation per day d) evaporative fraction.

Seasonal cycles of total precipitation and 2m air temperature are shown in Figure 4.27. During certain seasons, heavy rainfall is experienced in some cities, in MAM and JJA months for those in Asia and during the DJF months for the cities in South America and southern Africa. For the rest of cities, there is less rainfall on average, and most cities (including those which do not experience a heavy wet season) have a total precipitation rate of less than 4mm/day. Generally, the cities with the highest annual mean 2m temperatures have smaller seasonal temperature cycles. For example, the cities in South America only slightly cool in SON

months and cities in South Asia are slightly cooler in the DJF months, but differences are not large in comparison to other cities. Cities in China, North America and the Middle East have the strongest seasonal temperature differences, with mean season 2m air temperatures ranging from below 10°C to above 25°C.

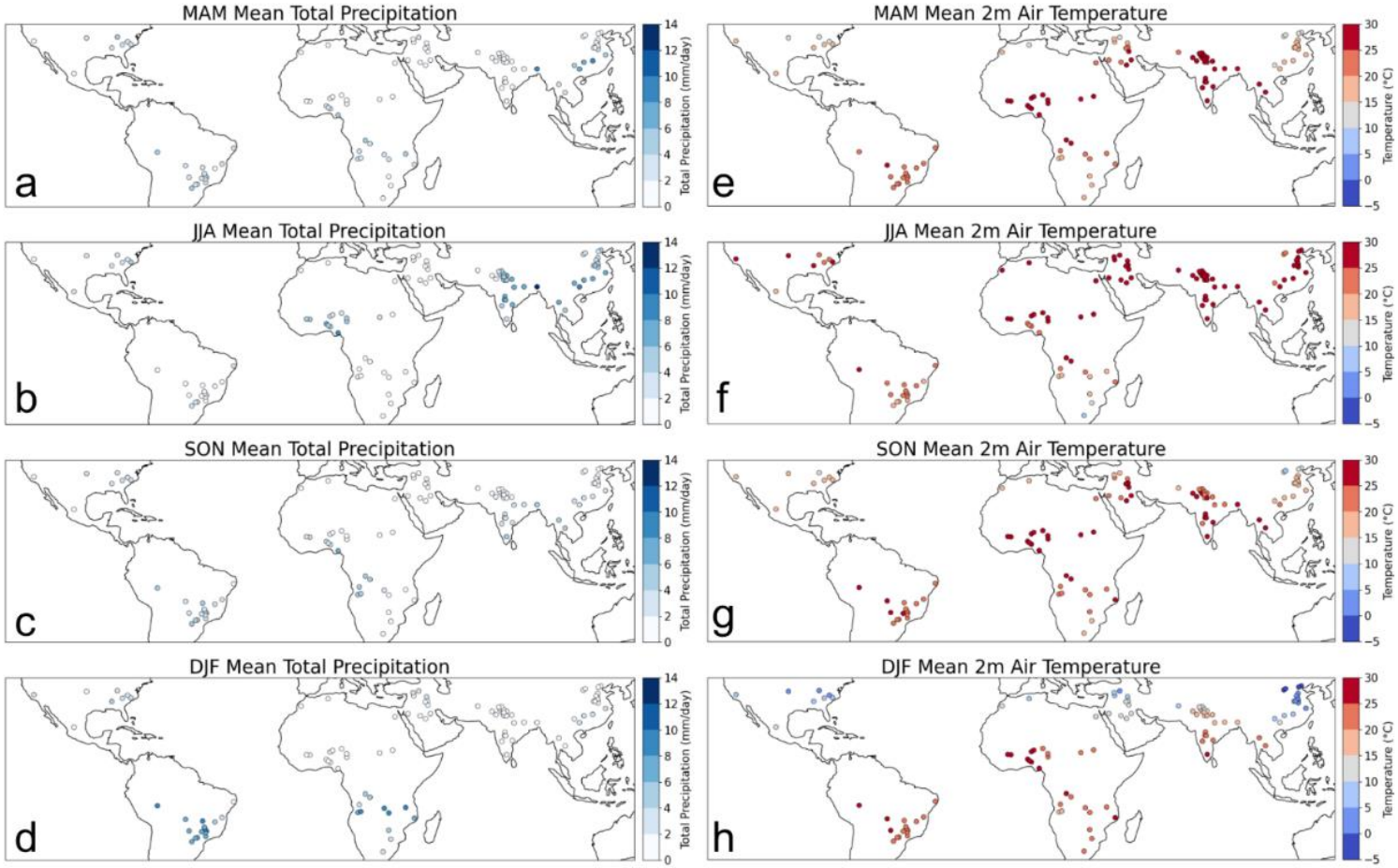

Figure 4.27 Seasonal Means of precipitation and 2m air temperature, averaged across 2002-2020. a) Precipitation MAM (March, April, May) b) Precipitation JJA (June, July, August) c) Precipitation SON (September, October, November) d) Precipitation DJF (December, January, February) e) 2m air temperature MAM (March, April, May) f) 2m air temperature JJA (June, July, August) g) 2m air temperature SON (September, October, November) h) 2m air temperature DJF (December, January, February).

4.3 OVERVIEW OF ALL PREDICTOR VARIABLES

A number of predictor variables are considered to be incorporated in the machine learning models for predicting the SUHI. These predictor variables summarised in Table 4.4. Here the short names for the variables are shown, and for the duration of the thesis, variables will be referred to by these. The physical meanings of the predictor variables are also included, to show how these variables related to the SUHI. Note that many of these variables are potentially a measure of the same impacts, and therefore are likely to be correlated, which is discussed in this section. Essentially the aim of this is to find the variables which most represent the factors that lead to the formation of the SUHI (section 2.2).

Table 4.4 Predictor variables considered for the machine learning predictive model for the SUHI.

Predictors	Short name	Units	Variable Physical Meaning
Rural Enhanced Vegetation Index	EVI_R	None	Measure of rural vegetation cooling
Urban Enhanced Vegetation Index	EVI_U	None	Measure of urban vegetation cooling
Urban - Rural Enhanced Vegetation Index	EVI_D	None	Measure of urban- rural differences in vegetation cooling
Evaporative Fraction	EF	None	Measure of latent heat cooling
Net Surface Solar Radiation with seasonal cycle removed	SSR_NO_SEASON	W/m^2	Measure of radiative heating
Relative Humidity	RH	None	Measure of latent heat cooling
Total Precipitation	TP	m	Measure of latent heat cooling and soil moisture
Log_{10}(City Area)	LOG_AREA	None	Measure of impervious surface lacking latent heat cooling
City Eccentricity	ECC	None	Measure of distance to the rural area from city points (further away means less benefit from green belt)
Rural White Sky Albedo	WSA_R	None	Measure of decreases of radiative heating in rural area
Urban White Sky Albedo	WSA_U	None	Measure of decreases of radiative heating in urban area
Urban - Rural White Sky Albedo	WSA_D	None	Measure of urban- rural differences in radiative heating
Urban – Rural Elevation	ELEVATION_D	m	Measure of elevation cooling differences
Rural Elevation Standard Deviation	STD_ELEVATION_R	m	Measure of rural elevation cooling
Urban Elevation Standard Deviation	STD_ELEVATION_U	m	Measure of urban elevation cooling
Urban – Rural Elevation Standard Deviation	STD_ELEVATION_D	m	Measure of elevation cooling differences

There is a high likelihood of the chosen variables being correlated, which can lead to complications and should be considered before fitting statistical and machine learning models (section 3.5). Dormann et al (2013) review various methods of dealing with collinearity, and contrast different predictive models in terms of their robustness to collinearity. They found correlation coefficients of $|r| > 0.7$ to be a threshold of where the model estimation will be severely distorted and therefore should be avoided. Figure 4.28 shows a matrix of the Pearson correlation coefficients for the potential input variables. There are 7 pairs of variables which, ideally, should not be used in a model together in order to meet the threshold of 0.7 for the magnitude of the correlation coefficient, listed in Table 4.5.

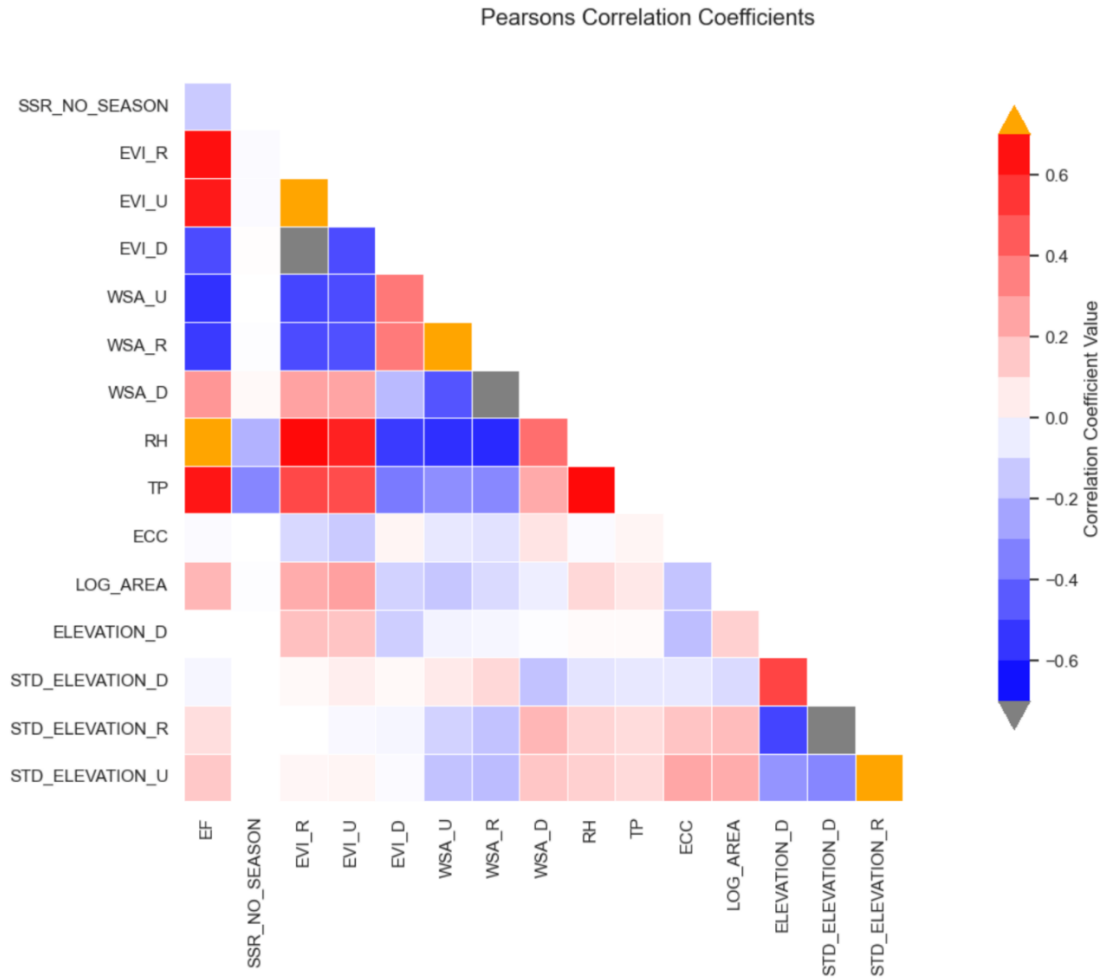

Figure 4.28 Pearson Correlation Coefficients for the input variable candidates. Variables with a correlation coefficient of greater than 0.7 are shown in orange and variables with a correlation coefficient of less than -0.7 are shown in grey.

Table 4.5 Highly correlated pairs of variables. The listed variables have Pearson correlation coefficients of above 0.7 or less than -0.7 and will not be used in any models together.

Variable 1	Variable 2	Pearson Correlation Coefficient
EF	RH	0.84
EVI_R	EVI_U	0.89
EVI_R	EVI_D	-0.83
WSA_R	WSA_U	0.94
WSA_R	WSA_D	-0.73
STD_ELEVATION_R	STD_ELEVATION_D	-0.89
STD_ELEVATION_R	STD_ELEVATION_U	0.73

A number of variables that can impact the SUHI are identified, but as only one of a pair of correlated variables can be included in the model, a variable selection process must be carried out. Therefore, all possible combinations of variables are investigated using the RR. This model is used as it is fast to run and thereby makes such a brute force method feasible. REFR (and other ML models considered) are very slow to fit when containing many variables, and do not have any variable ranking systems via which removal of non-contributing variables can be made. Performance statistics for each number of variables is generated, and the optimum variable combination is chosen.

4.4 MODELLING THE 13:30 SUHI

In this section, first the best ML model for prediction of the 13:30 SUHI_MEAN is identified and assessed for the case of extrapolation to warmer climates.

This (a) involved the optimization of the model considering different possible combinations of predictor variables and (b) the comparison of various linear and non-linear regression approaches for the predictive model in the form of MLR, RR, RFR, and RERF. Whilst the RERF was the chosen approach, it is important for the other models to be used as a comparison to demonstrate the more complex model is an improvement (needless complexity should be avoided). Secondly, the best model configuration is interpreted with respect to the predictive relationships it identified, which will also be important to inform any predicted changes under future climate scenarios.

Identifying the best set of predictor variables

Following this strategy, the first step is to identify which combination of predictor variables should be used. To do this, SUHI_MEAN is predicted as a function of all possible predictors.

For a fast optimisation and selection process, RR was used to fit the models. This results in multiple RR models, containing all possible combinations of predictor variables from single predictor variable models to a model with 16 predictor variables (the total number of predictor variables, see Table 4.4). The models which contain correlated variables are then discarded, and now the maximum number of possible variables is 12. For each number of variables, from 1 to 12, the best RR model was selected based on training data performance statistics. Figure 4.29 shows the performance statistics R-squared and RMSE for these RR models. In the plot, it can be seen that at 8 variables (on the x-axis), there is an 'elbow', marked with a red line. Before this elbow point, adding additional predictor variables to the model improves its performance statistics, but after this point, there is no additional gain by the inclusion of more predictors. Therefore, 8 variables are a good choice for the number of predictor variables to be used. The best performing RR model contained the predictor variables EVI_U, EVI_D, LOG_AREA, WSA_D, ELEVATION_D, RH, TP, and STD_ELEVATION_U.

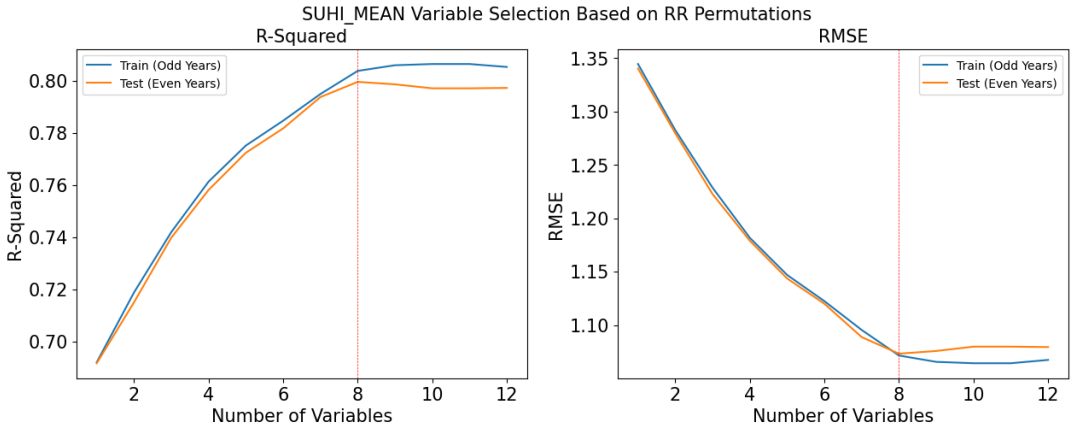

Figure 4.29 Performance statistics (R-squared and RMSE) for the best performing models for each number of predictor variables, with SUHI_MEAN as target variable. The red line marks the 'elbow' of the plot, taken to be where the addition of further variables will not improve model performance.

Identifying the best regression method

Multiple models are evaluated, and selection was made based on two criteria. The first of these was the performance statistics, R-squared and RMSE, and the second was the ability of the model to be used for potential extrapolation. Table 4.6 shows the training and test performance statistics for the RR, RFR and RERF models (further details on the model fittings such as hyperparameters and run times, and the other models examined can be found in the appendix section A.3).

Based the test data, the best performing model is the REFR, with a R-Squared of 0.87 and RMSE of 0.86 °C, although the performance of the RFR is around the same. Comparison of the training and test scores for the models also indicates if the models are doing a good job of

capturing the underlying relationships within the data or are overfitting to this particular dataset. Overfitting is most likely with the RFR (section 3.5), and this could be the case here to some extent as this model has the biggest decrease from training to test performance, although the test performance is still high. RR performance statistics show very little change from training to test datasets, which builds confidence in this model fitting the relationships between predictor variables and the SUHI_MEAN. The RERF, being a hybrid model of both the RR and RFR (see section 3.5), benefits from both the higher performance in terms of test statistics from the RFR and the better fit of the underlying relationships from the RR. To give a visual interpretation of the REFR performance, Figure 4.30 shows the REFR Predictions vs Observations scatter plots. Here it can be seen that the model is doing a good job at capturing both the positive and negative SUHI_MEAN magnitudes.

Table 4.6 Performance Statistics for the RR, RFR and RERF models.

Model	Train R-squared	Test R-squared	Train RMSE	Test RMSE
RR	0.78	0.77	1.14 °C	1.14 °C
RFR	0.90	0.85	0.77 °C	0.85 °C
REFR	0.90	0.87	0.77 °C	0.86 °C

The scatterplots in Figure 4.30 are used to assess if there is any model bias, by comparison of the line of best fit to the y = x line. This indicates the model predictions are relatively unbiased, with the intercept remaining the same for test and train data at -0.05, and the gradient close to 1, at 1.03 for the training data and 1.02 for the test.

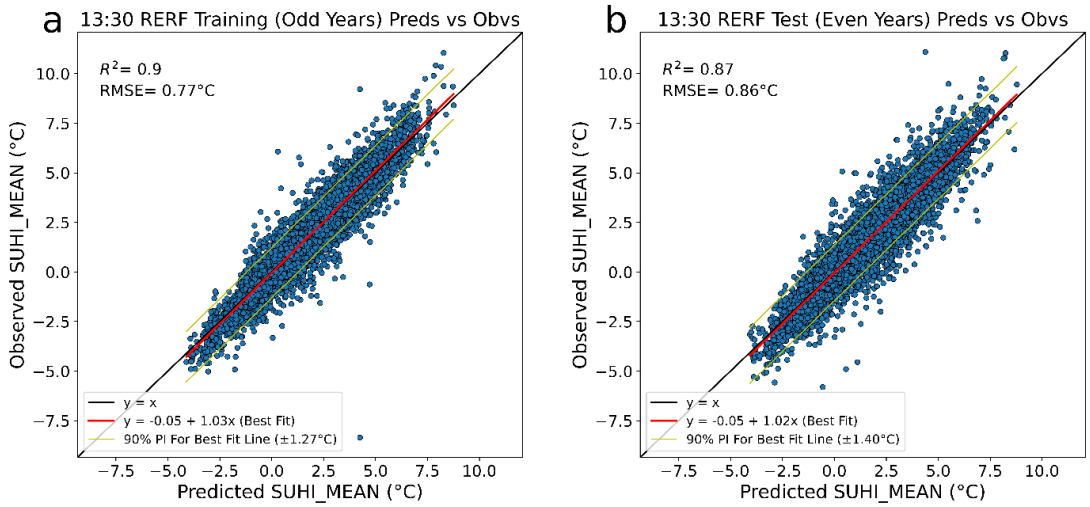

Figure 4.30 Predictions versus observations scatter plots for RERF a) train (odd years) and b) test (even years). The black line shows y = x, the red line a line of best fit (least squares fit), and the yellow line a 90% prediction confidence interval.

As discussed in 3.5, RERF is a hybrid of RR and RFR, using a 'base' model (RR is this case) to make a prediction and correcting this using a RFR prediction of the residuals. Figure 4.31 shows the predictions versus observations plots for this base model. The improvement can be seen clearly in the predictions for the negative SUHI_MEAN. In the RR base model, the model is not able to capture the SUHI_MEAN's below around -2.5 °C, whereas the RERF model is a marked improvement. The residuals are also smaller, as expected, with the prediction interval for the line of best fit 0.5 °C smaller for the test data.

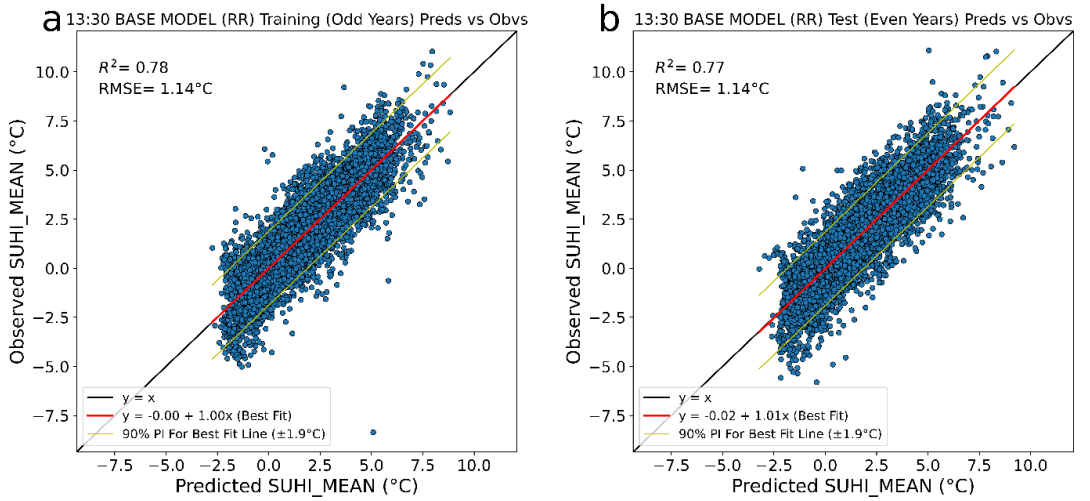

Figure 4.31 Predictions versus observations scatter plots for a RR fit, the base function which is used in the RERF a) train (odd years) and b) test (even years). The black line shows y = x, the red line a line of best fit (least squares fit), and the yellow line a 90% prediction confidence interval. The RERF is a significant improvement upon using the RR base model alone.

The second consideration of the model selection process was the model's ability to extrapolate. Both RR and REFR have been tested and found to perform well under extrapolation (Zhang *et al.*, 2019; Nowack *et al.*, 2021), whereas RFR does not.

The issue with extrapolation in RFR can be seen in the ALE plots (section 3.5) of the different models. Figure 4.32 shows and the ALE plot for the EVI_D variable, for both the REFR and RFR. For the lowest and highest values of EVI_D, the RFR predicts no change in the SUHI_MEAN for incremental increases or decrease at these values. This is due to the mechanisms of the model, explained in section 3.5. The RFR prediction of a new datapoint is determined by the mean value of all the observations on the 'leaf' the new datapoint is assigned to. So, if a new datapoints has an EVI_D value of 0.15, but the maximum EVI_D of the dataset is 0.08, the prediction for this datapoint would be the same if its EVI_D was 0.08 or 0.15.

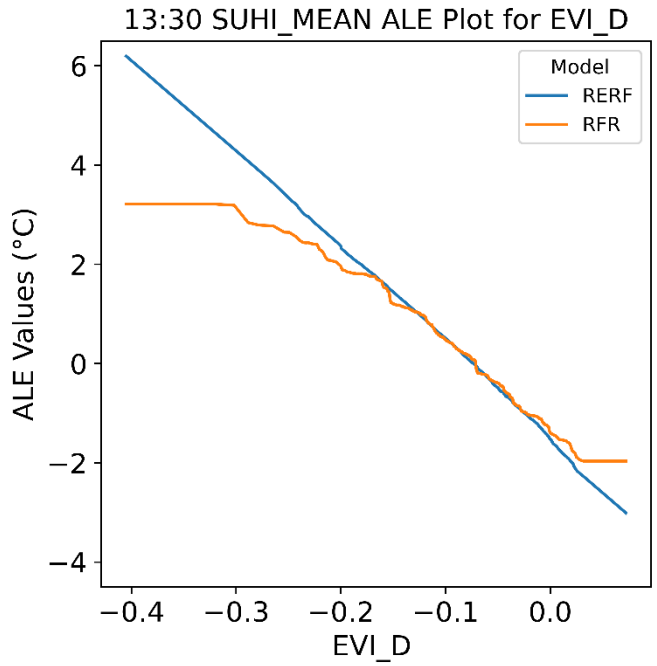

Figure 4.32 Accumulated Local Effects (ALE) plot for the predictor variable EVI_D. The ALE plot is a measure of how increasing (or decreasing) EVI_D impacts the prediction of SUHI_MEAN. The y-axis shows the change in the prediction. Shown in blue is the REFR and in orange is the RFR predicted effect on EVI_D. Further details on ALE plots can be found in section 3.5.

As the RERF has the RR as its base model (section 3.5), the ALE plot shows no saturation at either end, meaning the model is able to better predict outside of the training data range, with the assumption that the underlying relationships remain the same for values outside of the range.

To further examine the ability of the models to extrapolate, a training test data split using the early years to train and later years to test was fitted. Figure 4.33 shows the results for this split. The test data still shows similar performance, meaning reasonable confidence can be placed in the model ability to extrapolate to warmer climates due to climate change.

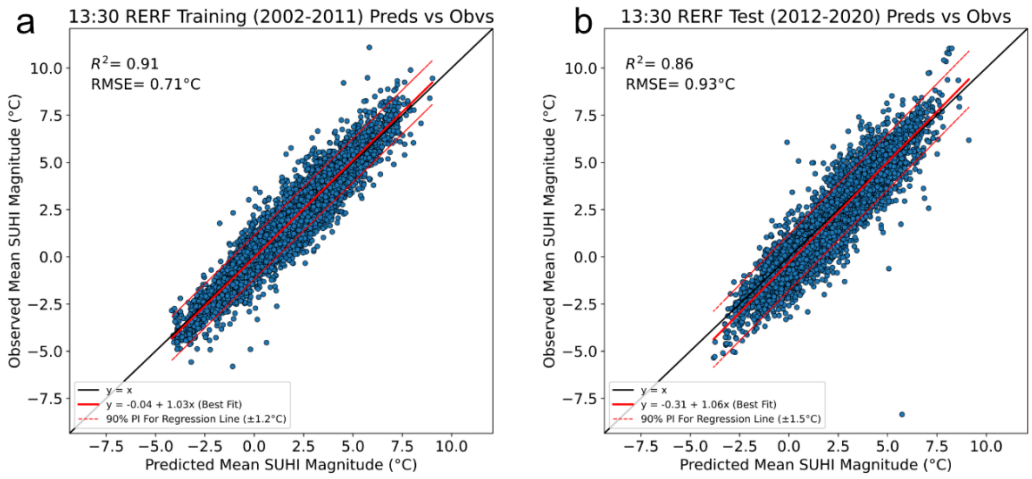

Figure 4.33 Predictions versus Observations Scatter Plots for 13:30 RERF a) train (2002-2011) and b) test (2012-2020) years. The black line shows y = x, the solid red line a line of best fit (least squares fit), and the dotted red line a 90% prediction confidence interval.

The ability of the RERF to extrapolate to MEAN_SUHI values outside of the training data range is also examined by taking the 10th percentile plus 90th percentile as the test data, and training on the middle 80%. This resulted in all data with SUHI_MEAN less than -1.4 °C and greater than 4.8 °C being in the test dataset, and data between the two values in the training. Figure 4.34 shows predictions versus observations scatterplots containing both test and train data for RERF, RR and RFR models fitted using this data split. Plots for the RERF (Figure 4.34a) and RR (Figure 4.34b) are similar. This similarity is anticipated, as the RERF uses the RR as its base model, and therefore maintains the same fit of the underlying relationships within the data.

The RERF and RR both have similar lines of best fit, with the intercept of -0.42 and gradient of 1.28 for the RERF and -0.45 and 1.27 as intercept and gradient for the RR. There is also a similar fit to between these RERF and RR scatterplots (Figure 4.34a and Figure 4.34b) and Figure 4.31 of the RR model fitted on the alternate years (odd - even) test train split. The RR (and RERF with RR as its base model) is therefore managing to capture the underlying relationship well, as it is performing similarly with and without the extremes. In all three of these cases (RERF, RR fit on the extrapolation test dataset and RR fit on alternate years dataset), the ML models capture the high extremes better than the low extremes. The RERF trained on alternate years (Figure 4.30) is able to capture these low extremes, indicating there

is some non-linearity or change in relationship for these strong negatively SUHI_MEANs, which is not captured in the data when the model is fit without these in the training data. Figure 4.34c shows the predictions versus observations scatterplot for the RFR. This demonstrates the pitfalls of RFR with regards to extrapolation, which are explained earlier with use of Figure 4.32. The training data for the extrapolation was capped between -1.4 ℃ and 4.8 °C, and this can be seen clearly in the scatterplots, with the predictions made using the model limited to between this training data range.

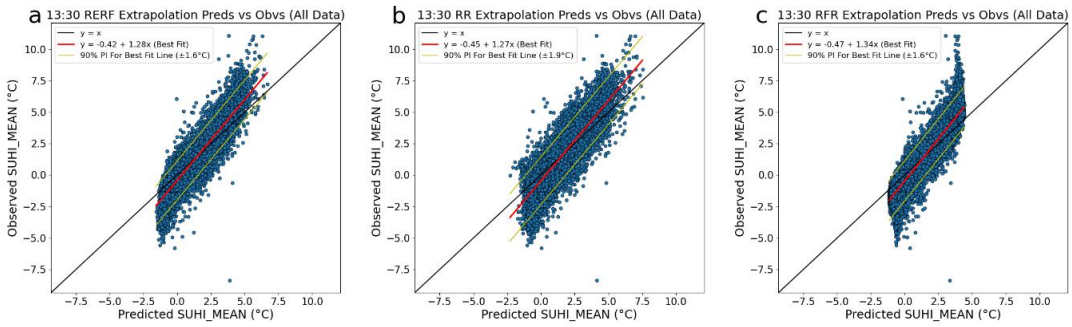

Figure 4.34 Predictions versus observations scatterplots for a) RERF, b) RR and c) RFR, trained on the middle 80% of the SUHI_MEAN values and tested on the 10% of lowest and 10% of highest values. The scatter plots here show 100% of the data.

Another assessment made on the RERF was to examine the ability to the ability to predict the SUHI_MEAN on an individual city level, to identify if there any cities for which the RERF significantly underperforms. There are 104 cities in the dataset, so one city for which the RERF performs poorly could potentially be masked in the dataset overall RMSE if the other cities are captured well. Figure 4.35 shows RMSE for the selected cities on an individual basis. Umuahia (Nigeria) has the highest RMSE, at 1.65°C. This is likely down to a limited amount of data for this city, as many images did not pass the quality assessment checks, highlighted in section 3.2. Another factor could be that Umuahia is only just over the threshold for cities not being near the coast, at a 100.4 km distance from the coastline. Penetration of sea breezes at 100 to 150 km can be found in the tropics and subtropics (section 4.1), so this could be driving the differences for this city.

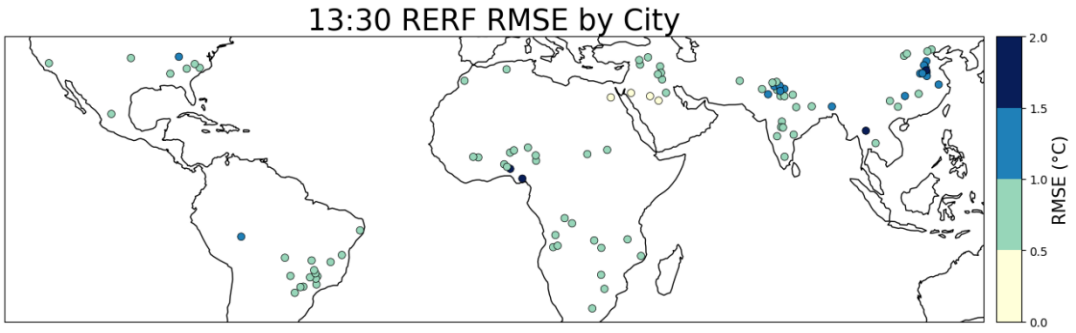

Figure 4.35 RERF RMSE for each individual city, calculated for the 13:30 SUHI_MEAN.

Interpretation of the predictive relationships found with RERF

Opening up the 'black box' and understanding the relationships within machine learning models is highlighted in section 3.5, motivated by the need for trust, interaction, and transparency of models. In Figure 4.36, the relationships identified by REFR are illustrated through the mean of ALE plots (section 3.5). The RR base model is also included, in yellow, to show how the model differs from its linear base. An assessment of the relationships based on these plots is as follows:

As EVI_U increases, the mean SUHI magnitude increases. At first, this appears to be contrary to expectations, because higher vegetation densities in cities would typically be associated with cooling effects. However, in a model based on correlations, this can be interpreted to be the result of the EVI_R and EVI_U being highly correlated (r = 0.89), as shown in Table 4.5, and the presence of the EVI_D variable as additional predictor (whose relationship in the ALE plots is negative). Cities in areas of abundant vegetation tend to have stronger positive SUHIs, and as EVI_U and EVI_R are correlated, so that a higher EVI_U implies statistically a higher EVI_R. As EVI_D becomes less negative the difference between urban and rural vegetation gets smaller, the mean SUHI magnitude decreases. In summary, the rural cooling aspect the vegetation is therefore captured via the EVI_U variable, whereas the extent to which the urban environment is cooled in comparison by vegetation is in this set-up represented by the EVI_D variable.

As LOG_AREA of the city increases, its mean SUHI magnitude increases. This follows expectation from current literature (section 4.2).

WSA_D (urban – rural) impact on the SUHI_MEAN shows a positive relationship between the two, with a higher urban (in comparison to rural) albedo leading to a higher SUHI_MEAN. The expected relationship would be a negative one, with a larger albedo difference meaning more solar radiation is reflected from the urban area than the rural, leading to a smaller (or more negative) SUHI_MEAN. The complex relationship could be due to seasonal effects,

with a study focusing on cities in China finding the SUHI- WSA_D relationship to be negative during the winter (Yao *et al.*, 2018), and a study with global cities finding a positive relationship during the day and a negative relationship at night (Peng *et al.*, 2012). It also may be the case that the albedo difference variable is picking up on landcover type. Surfaces such as forests have low albedos, and desert areas have high albedos (and cities in desert regions tend to have more vegetation than the rural area). The vegetative cooling effect overrides the low albedo during the day, but the increased solar radiation absorbed keeps more vegetated areas warmer during the night-time.

The ELEVATION_D (urban – rural) ALE plot shows as a negative relationship, although it is not completely linear. In areas where the city is higher than the surrounding rural area, the SUHI_MEAN will be smaller, and in areas where the rural area is higher than the city, the SUHI_MEAN is larger. This shows the cooling impact of elevation, as areas higher up experience lower temperatures.

As RH increases, mean SUHI decreases. This is in line with other studies, which find a negative correlation between the two, detailed in section 2.4, and is likely due to months with high RH being associated with cloudier conditions.

Increasing TP is shown to increase the SUHI_MEAN. This indicates that wet soils lead to more rural evaporative cooling (compared to its simultaneous cooling effect on the urban area). There will be some interaction between TP and RH, as the variables are connected. Where wet soils are combined with lower RH, the conditions would be ideal for evaporative cooling to take place.

STD_ELEVATION_U has a less clear effect on SUHI_MEAN in the ALE plots. For STD_ELEVATION_U of less around 60m, i.e., in relatively flat cities, there appears to be a minimal, noisy, effect, but after this a negative correlation occurs. In conclusion, hillier cities have a smaller (or more negative) SUHI_MEAN. This could be down to some impact of elevation, or potentially related to urban roughness. If the urban surface is rougher, there will be a larger area via which the surface can convect heat to the lower atmosphere.

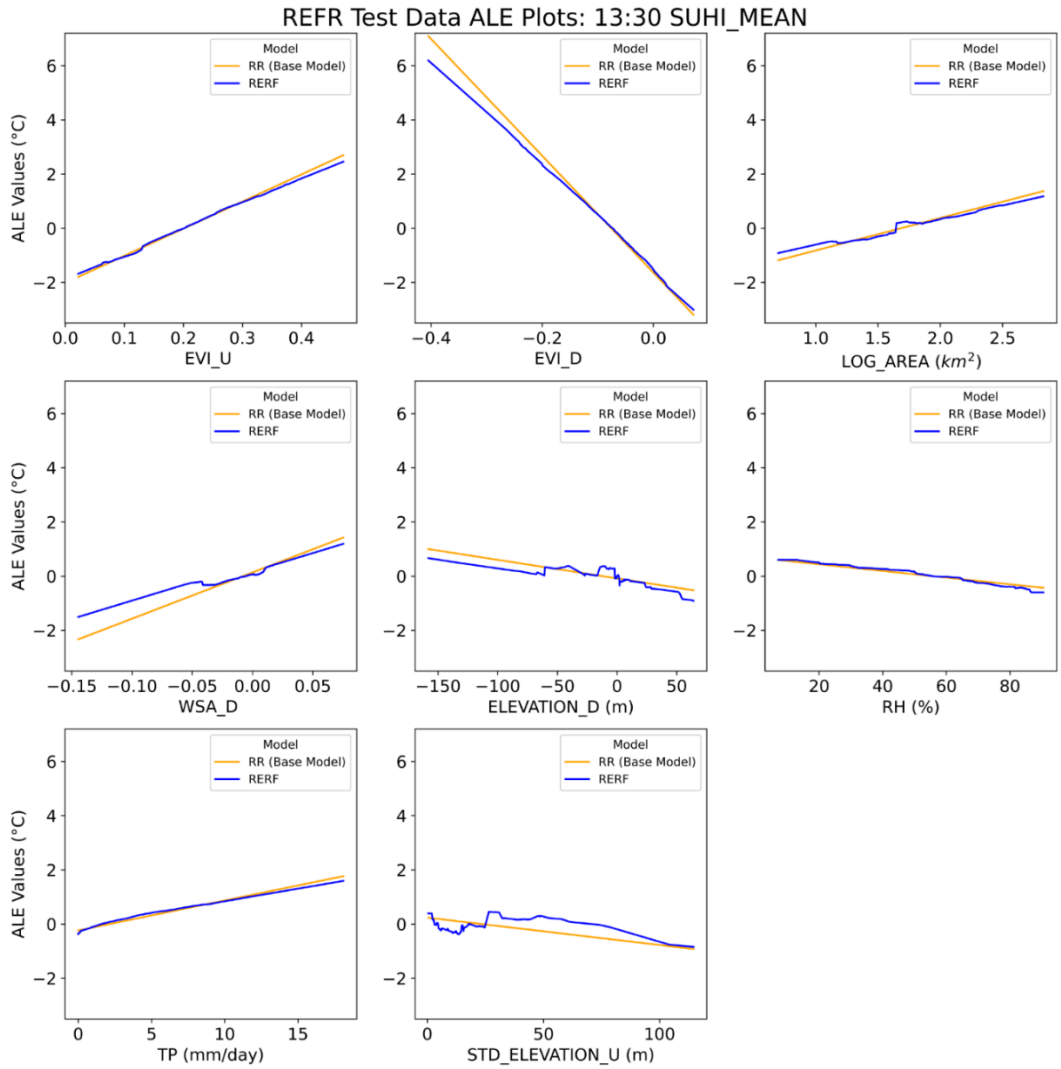

Figure 4.36 13:30 SUHI_MEAN ALE plots for the REFR (blue), with the base RR model included (in orange), to show the differences between the two. Details of ALE plots are given in section 3.5. The ALE plots were fit using test data. Training data ALE plots show the same relationships.

Inference made about the UHI through these ALE plots should be taken with some caveats, regarding the differences between the SUHI and CUHI during this time. In section 2.3.1, it was outlined how studies have shown during the daytime differences between the SUHI and CUHI are greatest. As the application of studying the UHI is the proposal of solutions to mitigate uncomfortable urban air temperatures, this limits the utility of daytime SUHI. The quantified impact on the SUHI_MEAN of decreasing EVI_D, for example, may not translate to the same change in the CUHI. During the nighttime, the SUHI-CUHI correlation is stronger and for this reason studies often focus on nighttime SUHIs (e.g., Feng *et al.*, 2019; Lai *et al.*, 2021). Additionally, the nighttime UHI is important as air temperatures during this time are important for human health and comfort. During the night, cool temperatures are required to recover from the heat of the day, and heatwave definitions include nighttime low thresholds in addition to daytime highs (Robinson, 2001).

4.5 MODELLING THE 01:30 SUHI

The variable selection and model fitting were carried out for the 01:30 overpass using the same methodologies as the 13:30. This allows for comparison of the different mechanisms driving the night-time SUHI as opposed to the SUHI during the day. Night-time SUHI is also of significance as it found to be more closely related to the CUHI (section 2.3.1), which is important for human health and comfort.

Identifying the best set of predictor variables

The same steps as for the 13:30 overpass were carried out for the 01:30 overpass to determine the best set of predictor variables. Figure 4.37 shows the performance of the first variable selection step for the 01:30 overpass. Something of note is that despite the R-squared performance statistic being much lower than the RR model for the 13:30 overpass, the RMSE is lower. This demonstrates one of the caveats with using R-square (section 3.5) in it being a relative rather than absolute value. The variance of the 01:30 overpass SUHI observations about the mean is relatively small, which means when the variance captured by the model is scaled by this, it gives a lower R-squared. However, a positive R-squared score still shows the model does a better job than simply using the mean of all observations. In fact, based on RMSE, the prediction error is small. A lower performance in terms of R-squared is found in other studies when predicting the night-time SUHI as opposed to the daytime (Peng *et al.*, 2012; Schwarz and Manceur, 2015). As can be seen in Figure 4.37, a set-up with 11 variables showed the best generalization performance. These variables are SSR_NO_SEASON, EVI_U, EVI_D, ECC, LOG_AREA, WSA_U, WSA_D, ELEVATION_D, RH, TP, STD_ELEVATION_R.

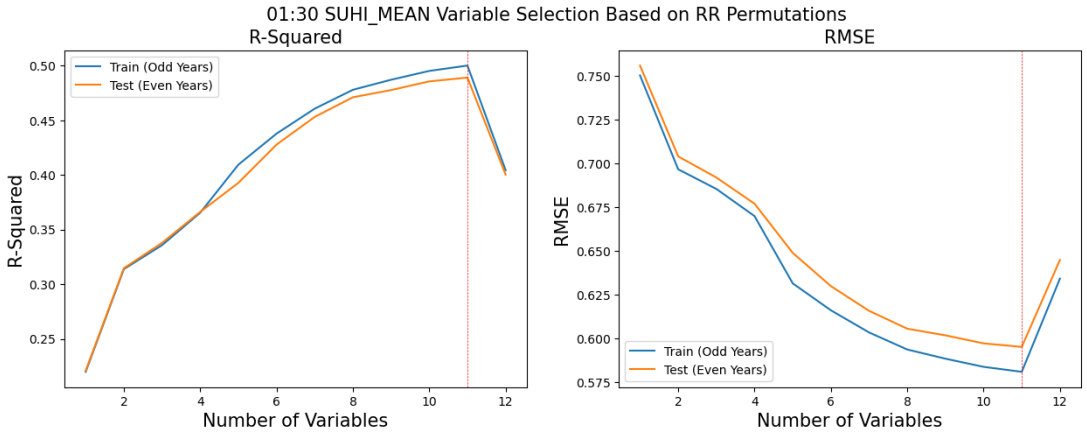

Figure 4.37 Performance statistics (R-squared and RMSE) for the best performing models for each number of variables for the 01:30 overpass. The red line marks the 'elbow' of the plot, taken to be where the addition of further variables will not improve model performance.

Identifying the best regression method

Evaluation of the same modelling techniques used for the 13:30 SUHI_MEAN gives the same model ranking, with the RERF performing the best on both train and test data. The difference between the performance statistics of the models in terms of R-squared is notable and can be seen for the RR, RFR and RERF in Table 4.7. Whilst the R-squared performance in predicting the 01:30 SUHI_MEAN is lower than the 13:30 (Table 4.6), RMSE of the 01:30 models is better. The 01:30 models are capturing less of the overall variance (as overall variance is lower), but the absolute error in the prediction is smaller.

Table 4.7 Performance Statistics for the 01:30 RR, RFR and RERF models.

Model	Train R-squared	Test R-squared	Train RMSE	Test RMSE
RR	0.33	0.33	0.67 °C	0.68 °C
RFR	0.63	0.58	0.50 °C	0.54 °C
REFR	0.73	0.67	0.43 °C	0.48 °C

Figure 4.38 show predictions vs observations scatterplots for the RERF predicted 01:30 SUHI_MEAN. The REFR is not able to capture the stronger negative SUHI_MEANs, which can be seen by the points which are below zero for the observations. There are relatively few points where this occurs, which makes it difficult for the model to capture this behaviour, and it also could be the case that these negative SUHIs are influenced by a variable which it not included in the model, for example, windspeed. As the model is better able to capture the SUHI at the higher end of the range, the line of best fit is not as close to the y = x line as the for the 13:30 SUHI.

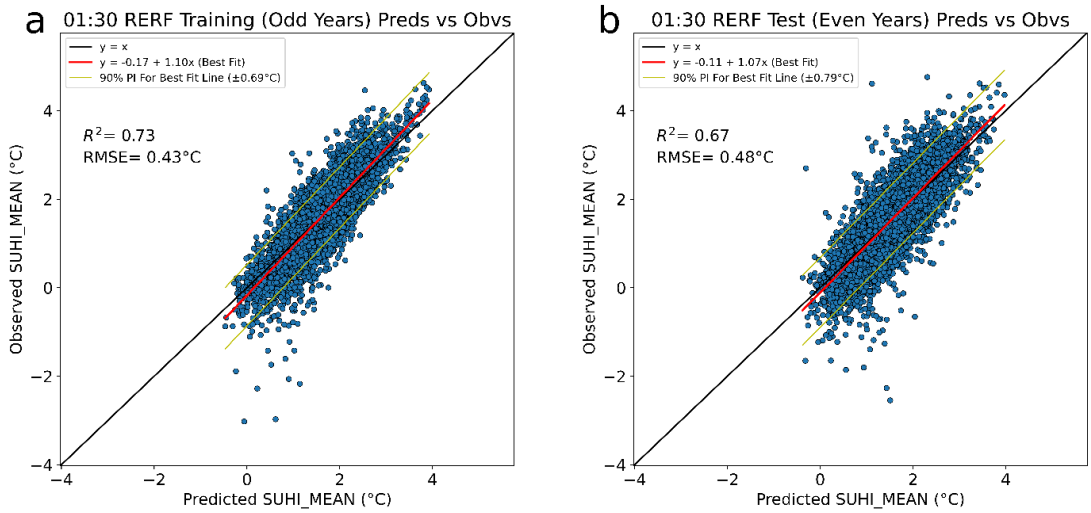

Figure 4.38 01:30 Predictions versus Observations Scatter Plots for RERF a) train (odd years) and b) test (even years). The black line shows y = x, the solid red line a line of best fit (least squares fit), and the dotted red line a 90% prediction confidence interval.

An assessment of the RERF prediction of 01:30 SUHI_MEAN for the individual cities is made, shown in Figure 4.39. For all cities, the RMSE is less than 1 °C. As expected from the overall RMSE, this is generally lower than the RMSE daytime RERF performance, where the maximum RMSE reached 1.65 °C. However, it is not the case that areas where the error in SUHI_MEAN is highest during the day is the same as those where the error during the night is high, indicating the features or mechanisms that lead to a city having a SUHI_MEAN that is difficult to capture during the day do not apply in the same way during the night. There is also no clear relationship between the climate type and the cities with higher RMSE, which points to the possibility of there being a city form related property, such as building height /density, missed that causes the prediction error.

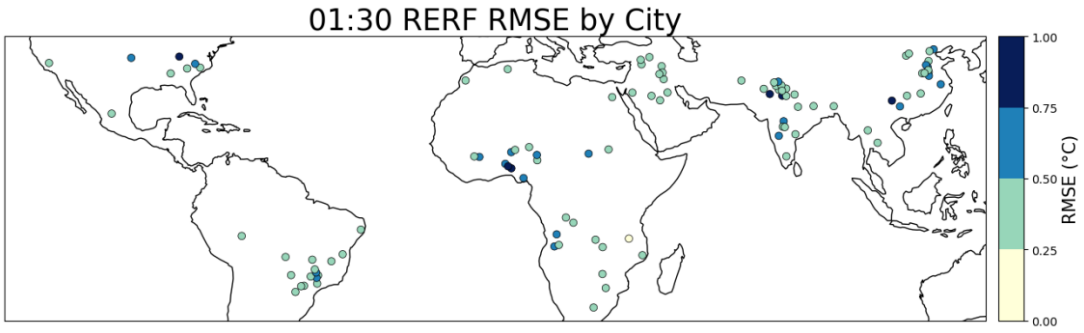

Figure 4.39 RERF RMSE for each individual city, calculated for the 01:30 SUHI_MEAN.

Interpretation of the predictive relationships found with RERF

Figure 4.40 shows ALE plots for the test data, where the REFR ALE is plotted in blue, with the RR base model in orange to show how the REFR differs from the linear base. Based on

the ALE plots, changes in RH have one of the larger impacts on the SUHI (spanning over 1.5°C), which agrees with the findings of Lai et al (2021) for the night-time SUHI. The SUHI_MEAN - RH relationship is the same for the 01:30 ALE plots as it is for the 13:30 ALE plots, with SUHI_MEAN decreasing as RH increases.

The relationship with EVI_D is also found to be the same for both overpass times. This is in agreement with other studies which find urban greening produces a cooling effect during both the day and night (Liu *et al.*, 2022), as increasing urban vegetation will decrease EVI_D in most cases. EVI_U, however, has less of a clear relationship for the nocturnal SUHI. For very small amounts of vegetation, there does not appear to be a clear relationship, then after this the relationship is weakly positive. However, taking into account the range of ALE values on the EVI_D plot, the variable influence is small. This confirms the theory that the SUHI during the day is known to be more influenced by land cover types, whereas the night-time SUHI does not have the same association.

The SSR_NO_SEASON variable has a negative relationship with the SUHI_MEAN. This represents a lagged relationship, and how solar radiation during the day can be stored in materials and released at night as the materials cool. When there is more solar radiation during the day, there is a decrease in the 01:30 SUHI_MEAN. If the rural area has wet soils, this relationship could be due to the higher thermal admittance of wet soils then urban materials (see section 2.4) meaning the soils take in more energy during the day, heating up slowly (so the 13:30 SUHI_MEAN would be smaller) and also cooling slowly during the night, giving a smaller urban- rural temperature difference.

The effect of ECC on the SUHI_MEAN is mixed, showing an increase in magnitude as the city shape becomes less circular, then have no impact until it reaches around 0.8, where the relationship is unclear. The impact of the changes in ECC are relatively small overall (less than 0.2°C), and it is likely this variable could be removed if the model was to be used for predictive purposes.

LOG_AREA shows the same relationship with SUHI_MEAN for 01:30 as 13:30, with the magnitude increasing as the city size increases.

WSA_U and WSA_D both have a negative relationship with SUHI_MEAN at 01:30. Again, this is likely a lagged relationship relating to the incoming solar radiation during the day. Increasing albedo of the city (in comparison to rural surroundings) leads to a smaller night-time MEAN_SUHI. If more solar radiation is reflected rather than absorbed in the urban area during the day, it will be quicker to cool and therefore urban – rural temperature differences will be smaller. Paired with SSR_NO_SEASON being found more influential at night than during the day, the WSA relationships show how the night-time SUHI is driven by differences

in rates of cooling, described in section 2.2, which then relates to the amount of heat stored in the city and rural materials during the day.

As with the 13:30 MEAN_SUHI, a negative relationship is found with the ELEVATION_D at 01:30.

The relationship between MEAN_SUHI and TP is negative at 01:30, in contrast to the relationship at 13:30 which is positive. This could be related to the higher thermal admittance of wet soils (section 2.4), which will cool slower than dry soils during the night.

Finally, the STD_ELEVATION_R variable shows no clear relationship with the SUHI_MEAN. Figure 4.41 shows the cities grouped into categories of STD_ELEVATION_R based on the changes in trend on the ALE plot. Here, there is some spatial clustering of cities which are close to each other (and therefore likely to be similar based on this rather than the variable STD_ELEVATION_R itself). This indicates overfitting for this predictor variable, and if using REFR to make predictions of the 01:30 SUHI_MEAN this predictor variable should be investigated further and likely should be removed.

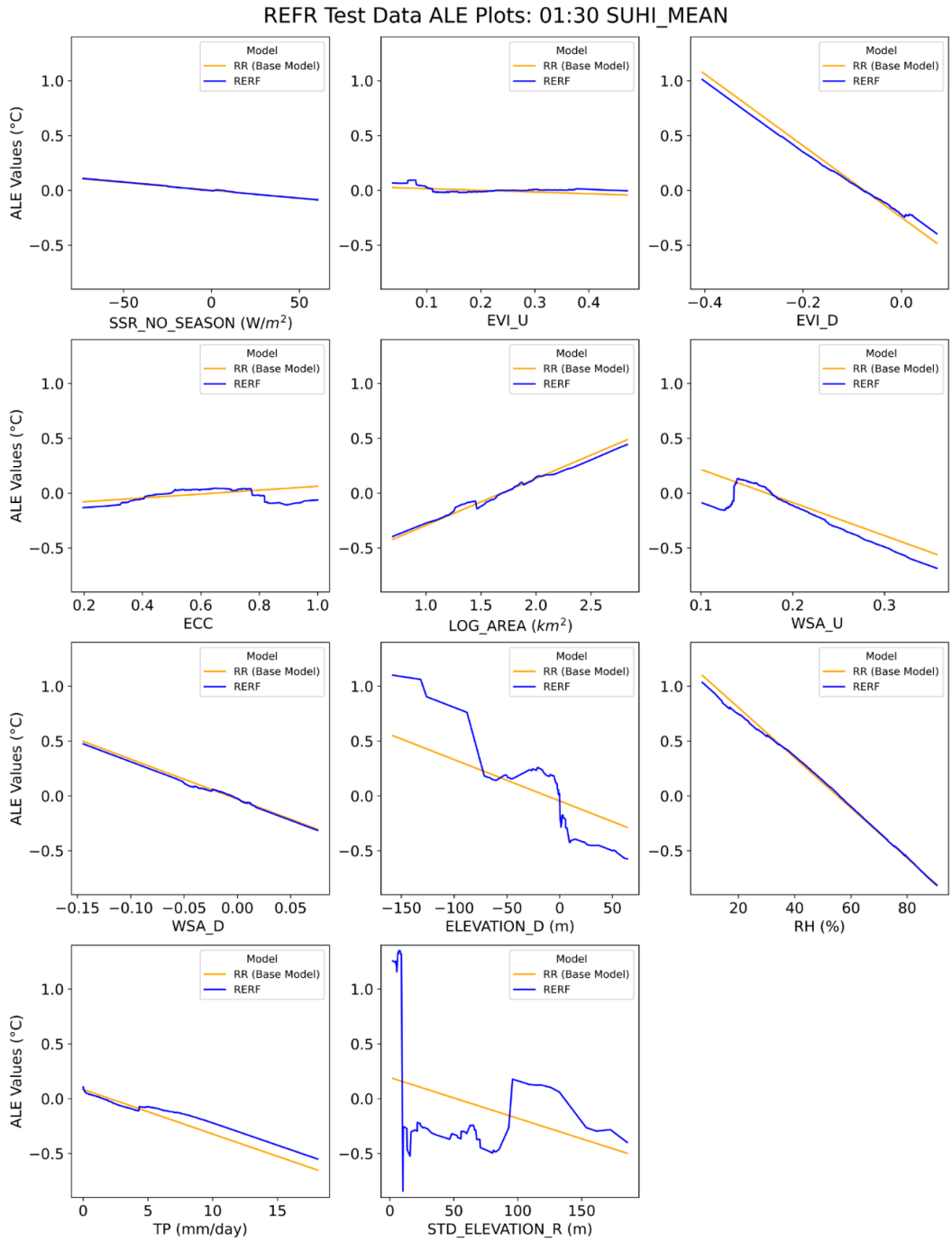

Figure 4.40 01:30 SUHI_MEAN ALE plots for the REFR (blue), with the RR base model included (in orange), to assess how the two models differ. Details of ALE plots are given in section 3.5. The ALE plots were fit using test data. Training data ALE plots show the same relationships.

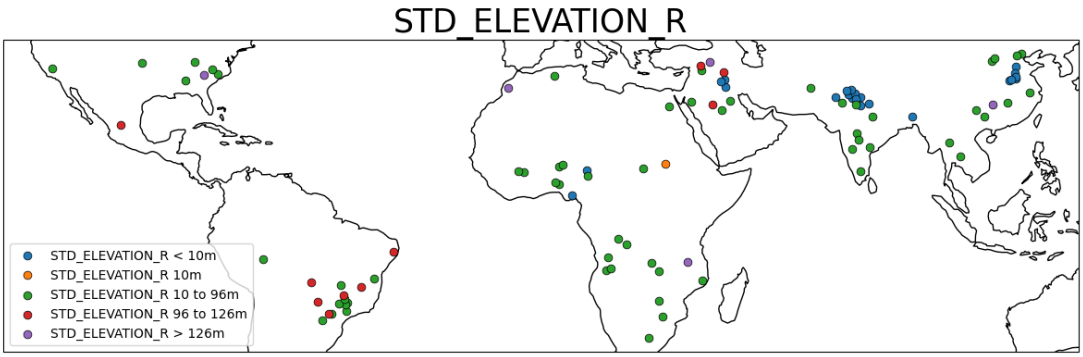

Figure 4.41 Cities grouped by STD_ELEVATION_R, based on the ALE plot for the 01:30 overpass. Here, the cities in blue represent the large values at the start of the ALE plot (where the contribution to SUHI_MEAN prediction is a large increase), and the city in orange where there is a sharp drop to negative ALE values. The cities in purple and green are where the ALE values are negative and around the same (although not completely flat), and the red values are at STD_ELEVATION_R 96 to 126, where the ALE values are positive. Here it can be seen there is some spatial grouping between the blue cities, seen in India and China, and the purple and green cities (which have the negative ALE values) are close together.

The results of the ALE plots and Figure 4.41 indicate the ECC and STD_ELEVATION_R variables in the RERF are overfit and therefore before using the model to make predictions they are removed. Table 4.8 shows a comparison of the performance statistics from the resulting RERF fit with 9 variables (RERF (9)), with the RERF performance statistics for the previous 11 variable model (RERF (11)). As would be expected, there is a decrease in the performance, but the removal of the variables potentially causing overfitting reduces the difference between the test and training performance statistics. The performance statistics for the RERF (9) still outperform the other models, as can be seen in Table 4.7.

Table 4.8 Performance statistics for the RERF fit with 11 variables – the initial fit, and with 9 variables – the fit with the 2 overfitting variables removed.

Model	Train R-squared	Test R-squared	Train RMSE	Test RMSE
REFR (11)	0.73	0.67	0.43 °C	0.48 °C
REFR (9)	0.68	0.65	0.46 °C	0.49 °C

The predictions vs observations scatter plots and performance statistics for this model can be seen in Figure 4.42. Comparison of this with Figure 4.38 shows the RERF (9) is not as effective as capturing the largest positive SUHI_MEAN magnitudes as the RERF (11). Based on this, it was likely these positive SUHI_MEANs were captured due to overfitting, rather than the model fitting the underlying relationships between SUHI_MEAN and the predictor variables at this extreme end.

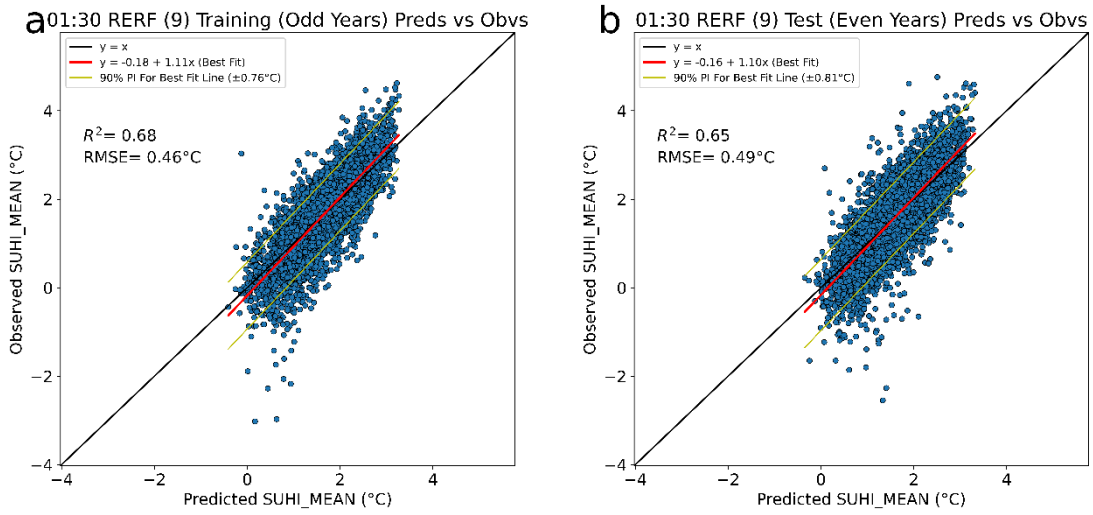

Figure 4.42 01:30 Predictions versus Observations Scatter Plots for RERF with 9 variables (ECC and STD_ELEVATION_R removed) a) train (odd years) and b) test (even years). The black line shows y = x, the solid red line a line of best fit (least squares fit), and the dotted red line a 90% prediction confidence interval.

The robustness of the RERF was further tested again for the 01:30, using a training test data split using the early years to train and later years to test. Figure 4.43 shows the results for this split. The test data still shows similar performance, meaning reasonable confidence can be placed in the model ability to extrapolate to warmer climates due to climate change.

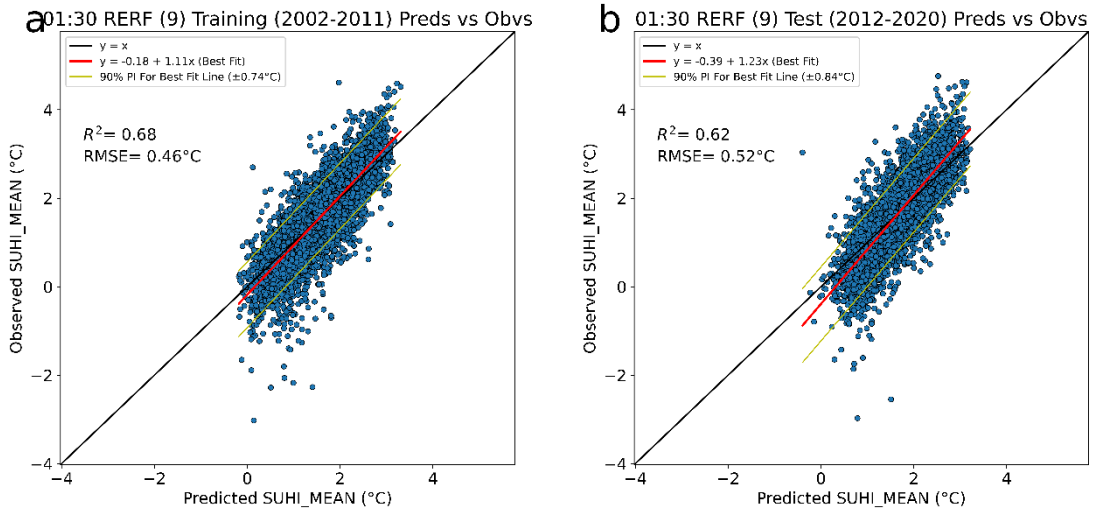

Figure 4.43 Predictions versus Observations Scatter Plots for 01:30 RERF (9) a) train (2002-2011) and b) test (2012-2020) years. The black line shows y = x, the solid red line a line of best fit (least squares fit), and the dotted red line a 90% prediction confidence interval.

Figure 4.44 shows the RMSE for the individual cities with the RERF (9). Comparison with Figure 4.39, the individual city performance for the RERF (11) shows the RMSE does not change greatly for the cities, which is to be expected. However, the maximum individual city RMSE is reduced. In the RERF (11), the highest RMSE was for Bikaner, India at 0.99 °C

and second largest Lexington-Fayette, USA at 0.91 °C. In the REFR (9) Bikaner has an RMSE of 0.72 °C and Lexington-Fayette is now 0.82 °C. Lexington-Fayette is now the largest RMSE, alongside Anshun, China which has increased on a RMSE of 0.77 °C to 0.82 °C. Overall, the RMSE reduces for 53% of cities and increases for 47% of cities. Based on the individual city assessment, despite the overall performance of the RERF (9) being slightly worsening in terms of overall performance statistics, it can be seen on an individual city basis, the tendency is to improve the prediction. Removing the variables that seem to cause overfitting has improved the model ability to generalise.

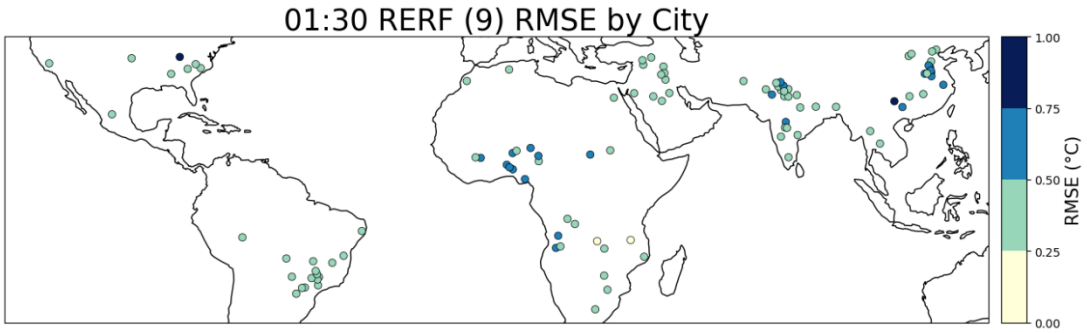

Figure 4.44 RERF (9) RMSE for each individual city, calculated for the 01:30 SUHI_MEAN.

5 USING A STATISTICAL MODEL TO EXAMINE THE FUTURE SUHI

In section 4, a machine learning model able to predict the SUHI_MEAN under a range of different climate regimes is developed. This section focuses on how this model can be utilised in examining how the SUHI_MEAN will respond to changes in climate.

It was seen in section 4 that there was the 01:30 SUHI_MEAN has less variability than the 13:30 SUHI_MEAN. Table 4.3 shows the annual 01:30 SUHI_MEAN is positive for all cities, and the standard deviation of the 01:30 SUHI_MEAN is 0.6 °C, opposed to the positive 13:30 SUHI_MEAN, which has a standard deviation of 1.3 °C. Based on this, it is apparent the same changes in climate and vegetation can be expected to produce a larger absolute change in SUHI_MEAN during the day in comparison to during the night.

The focus in this section is how the SUHI_MEAN changes in each city. For reference and context, Figure 5.1 shows the historical annual mean 13:30 SUHI_MEAN and Figure 5.2 the 01:30 SUHI_MEAN on top of which these changes are expected to occur.

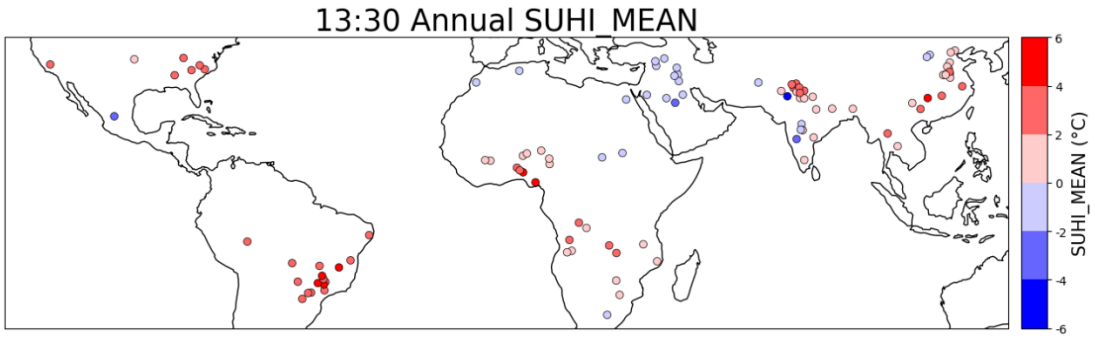

Figure 5.1 Annual mean SUHI_MEAN at 13:30 for the individual cities, based on the 2002-2020 dataset.

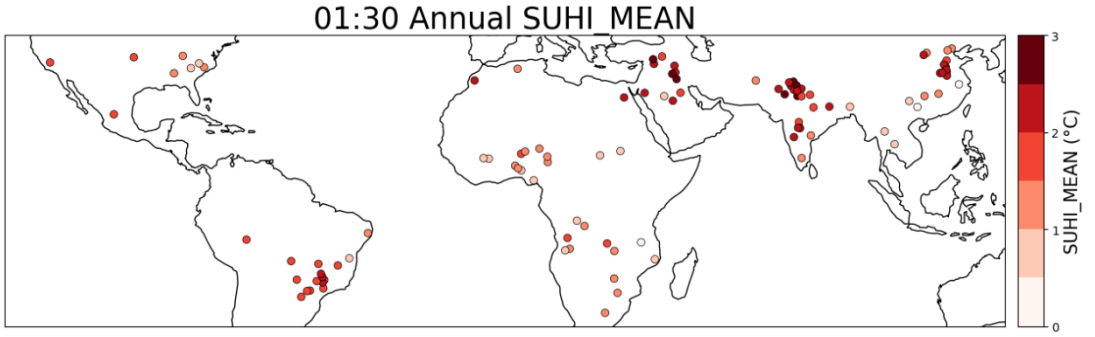

Figure 5.2 Annual mean SUHI_MEAN at 01:30 for the individual cities, based on the 2002-2020 dataset.

Before any analysis is carried out, the REFR model is refit on the entire dataset (with the same hyperparameters found using the training data) for both the 13:30 and 01:30 fits. This will

give the best constrained model on the largest possible training data range, still with the objectively best hyperparameter settings for the REFR fit.

The changes in SUHI_MEAN presented in this section are investigated by changing values of the predictor variables in the dataset, and examining how this alters the REFR prediction. This is done by subtracting the RERF prediction made on the unaltered dataset from the RERF prediction made on the dataset with changes in predictor variables. The difference between predictions is used, rather than difference between observations (the actual SUHI_MEAN values) and REFR predictions, to ensure that any changes are not simply due to the residual error in the predictions.

5.1 Sensitivity Analysis

To examine the extent to which changes in the predictor variables will impact each individual city, sensitivity tests are carried out. These involve changing one predictor variable at a time and assess the impact this has on the SUHI prediction. In these tests, all other predictor variables remain at 2002-2020 levels.

City Expansion

The extent of future urban expansion is uncertain, as it is conditional on various socioeconomic and practical factors (if there is space for the city to physically expand) (Huang *et al.*, 2019). Additionally, it varies geographically and with time (X. Li *et al.*, 2021), making it difficult to determine how expansion in the studied cities can be studied. As this is a sensitivity test rather than a projection, a simple approach is employed, and expansion is based on past trends.

To get an idea of how cities might expand in a 10-year period, the least squares line of best fit is used to predict the area of a city, for the most recent 10 years (2010 to 2020). This is then extrapolated to 2030 to get a quantification of city expansion, and the LOG_AREA for 2030 calculated. Figure 5.3 shows a map of how the selected cities will expand in a 10-year period if they were to continue the same expansion rate of area as for the years 2010 to 2020. The cities with the largest increases in LOG_AREA, with an increase of 0.22 log(km^2) are Gombe (Nigeria) and Mymensingh (Bangladesh), where the area increase is 33 km^2 and 11 km^2 respectively. Marrakech (Morocco) has the third largest increase in LOG_AREA (0.21 log(km^2)), and also the largest increase in area of 95 km^2. Birmingham (USA) also has a large increase in area, of 93 km^2, but as the city area is already very large (section 4.2 discusses the city size variable) this only translates to a 0.06 log(km^2) increase in LOG_AREA. This demonstrates the saturation of the SUHI_MEAN when city area becomes very large.

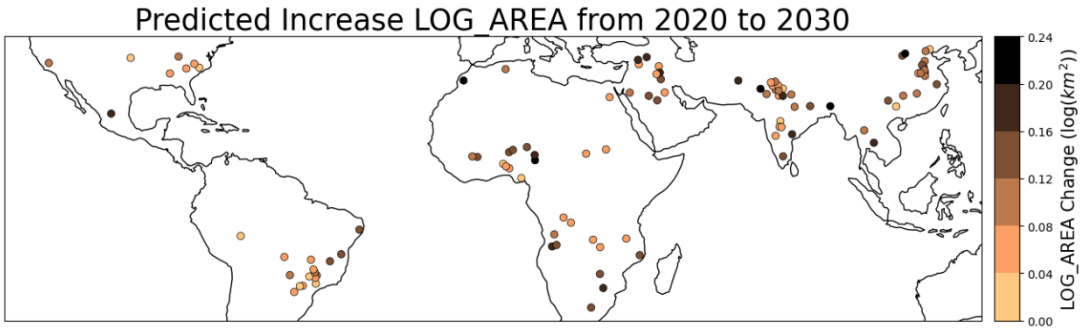

Figure 5.3 A projection of LOG_AREA in 10 years from 2020, based on the current trajectory from 2010 to 2020.

Changes in SUHI_MEAN based on these LOG_AREA trends were created by calculating the difference between a 'current' RERF prediction of SUHI_MEAN made based on the 2020 LOG_AREA, and a 'future' RERF prediction made on the estimated 2030 LOG_AREA.

The differences in the predictions made for the 13:30 overpass can be seen in Figure 5.4b. To give this context in terms of what this means for the overall 13:30 SUHI_MEAN, Figure 5.4a shows the RERF prediction for the annual mean based on the 2020 area. The largest decrease is in Kandahar (Afghanistan), where there exists a negative annual 13:30 SUHI_MEAN, so this becomes more negative, going from -1.45 °C to -1.95 °C (0.5 °C decrease). The largest increase is in Zacatecas (Mexico), where there is also a negative annual 13:30 SUHI_MEAN, so this becomes less negative, from -1.93 °C to -1.42°C (0.52 °C increase). Interestingly, these cities both have the same 2020 LOG_AREA value of 1.8 log(km^2) and the same increasing trend which leads to a 2030 LOG_AREA of 2.0 log(km^2) for both cities. This shows how the interactions of other predictor variables can determine how the increasing area impacts the predicted 13:30 SUHI_MEAN. For example, in Kandahar, the EVI_D is 0.01, whereas in Zacatecas it is -0.04. In Kandahar, an increase in area leads to an increase in vegetation cooling in the city, as there is more vegetation in the city than in the surrounding area, whereas this is not the case in Zacatecas. The assumption made here is that the urban area which is added to the city via its expansion has the same properties as the current city area (i.e., same amount of greenspace/ vegetation).

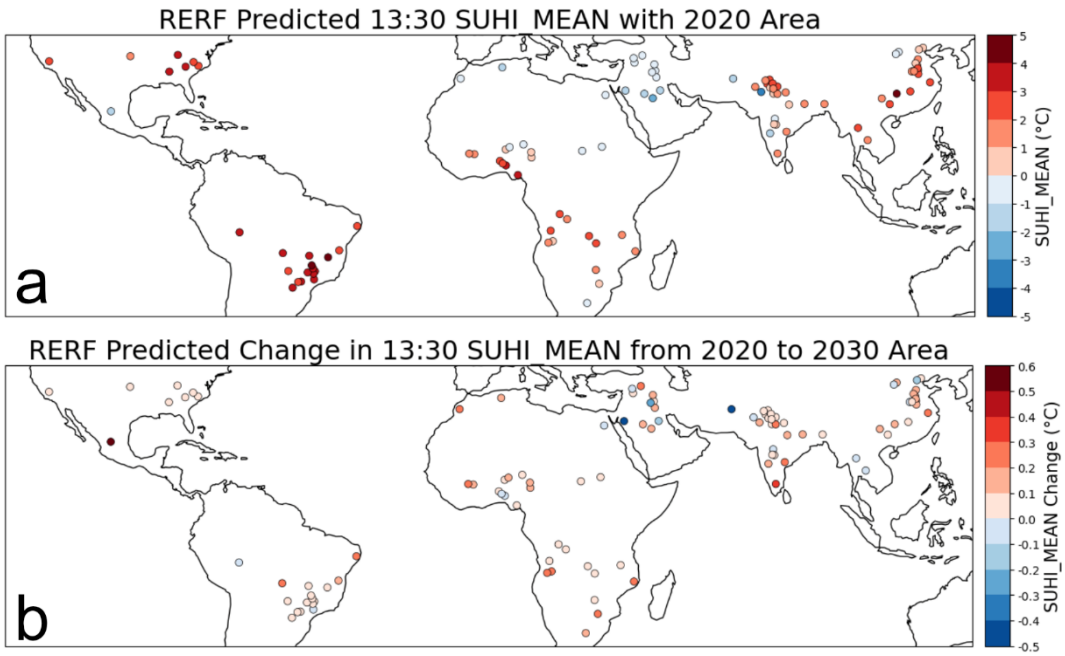

Figure 5.4 Investigation into how cities may expand and how this will impact the 13:30 SUHI_MEAN. The plots show a) The RERF projected 13:30 SUHI_MEAN based on the area in 2020 b) Based on the predictions of LOG_AREA in a), predicted changes in the 13:30 SUHI_MEAN from the LOG_AREA in 2020 to the LOG_AREA in 2030 are made using RERF.

An assessment of the sensitivity of the 01:30 SUHI_MEAN to the same urban expansion was made and can be seen in Figure 5.5. Here Figure 5.5a shows the projected SUHI_MEAN with the 2020 LOG_AREA, and Figure 5.5b shows the projected differences based on the expansion in Figure 5.3. The largest increase in the 01:30 SUHI_MEAN is in Kandahar (Afghanistan) going from 1.5 °C to 2.3 °C. Kandahar was also the largest change at 13:30, however at 13:30 this was a decrease. This is due to Kandahar having a negative SUHI_MEAN during the day, but a positive SUHI_MEAN at night. The city heats up slowly in comparison to rural surroundings during the day, then cools down slower than rural surroundings during the night. Overall, there is less change in the 01:30 SUHI_MEAN in comparison to the 13:30, as the SUHI_MEAN displays less variability during the night.

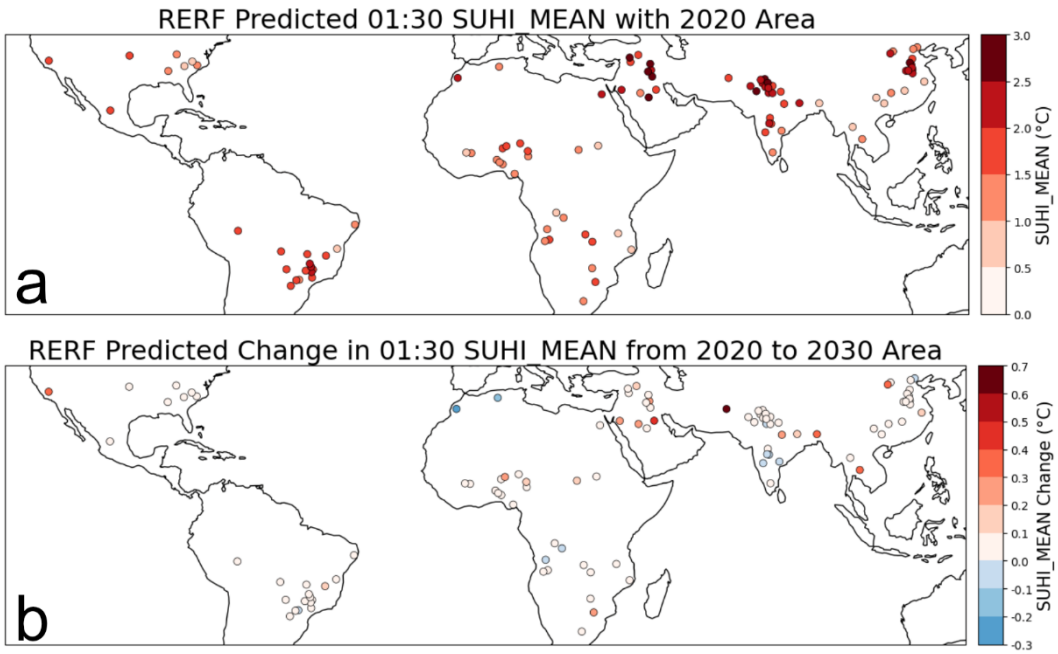

Figure 5.5 Investigation into how cities may expand and how this will impact the 01:30 SUHI_MEAN. The plots show a) The RERF projected 01:30 SUHI_MEAN based on the area in 2020 b) Based on the predictions of LOG_AREA in a), predicted changes in the 01:30 SUHI_MEAN from the LOG_AREA in 2020 to the LOG_AREA in 2030 are made using RERF.

There are some major limitations to this approach, as many of the cities experience a period of rapid growth which plateaus in recent years or have a steady area for earlier years and are currently experiencing a period of rapid growth. Based on this, it is unclear if the trends in either of these cases will continue as assumed here, and complex factors such as economic trends will play a large role. However, this approach does give a picture of how the urban growth in 10 years can impact the MEAN_SUHI of these cities, as it is based on past, plausible trends.

Decreasing Rural Vegetation

The impact of decreasing rural vegetation is examined by decreasing EVI_R. Future decreases in EVI_R may occur through deforestation, as forests are cleared for agriculture or logging, for example. Under a 'business as usual' scenario, Addae and Dragićević (2023) estimate global forest size to decrease by 10.5%. Therefore, the impact of a 10% decrease in rural vegetation is examined.

Figure 5.6 assesses the impact of EVI_R decreasing to 90% of the values from the period 2002 to 2020. Figure 5.6a shows this decrease represented by the absolute values, where for cities in more vegetated areas, the vegetation decrease translates as a large decrease in absolute terms. EVI_R is integrated into the model in the EVI_D variable, and a decrease in EVI_R leads to an increase in EVI_D. Based on the ALE plots (Figure 4.36and Figure 4.40), an

increase in EVI_D has the impact of decreasing the SUHI_MEAN, both at 13:30 and 01:30. Therefore, the changes shown in Figure 5.6b and Figure 5.6c are as expected, with a decrease in EVI_R reducing the SUHI_MEAN. This is driven by rural LST increases (as opposed to urban decreases), as less vegetation means less evaporative cooling.

Comparison with Figure 5.1, the annual 13:30 SUHI_MEANs, highlights the areas with the largest positive 13:30 SUHI_MEANs (all the 4 to 6 °C, some 2 to 4 °C) as those being the ones which are shown to decrease the most with the EVI_R decrease (0.7 to 0.9 °C). They are also the areas with the largest EVI_R decreases, seen in Figure 5.6a. In areas with very little vegetation (e.g., the middle east), which have negative 13:30 SUHI_MEANs, there is little change with the decrease in vegetation, as it translates to a very small absolute decrease. In nine cities (3 in India, 3 in Nigeria, 1 in Angola and 2 in China), the change in 13:30 SUHI_MEAN flips the sign of the annual SUHI_MEAN from positive to negative, as the rural area becomes warmer than the urban. The largest changes in annual 13:30 SUHI_MEAN were two cities in the USA, Fayetteville and Visalia (Figure 4.12), with decreases of 0.89 °C and 0.84 °C respectively (a 32% decrease for both).

Figure 5.6c shows the changes in the 01:30 SUHI_MEAN. Here the colour scale is different to represent the difference between the magnitude of the changes. The 13:30 SUHI_MEANs experience decreases of up to 0.9 °C, whereas at 01:30 the largest SUHI_MEAN change is a 0.15 °C decrease. Again, this is due to less variability in the 01:30 versus the 13:30 SUHI_MEAN. Comparable to 13:30, the largest reductions in the 01:30 SUHI are where the largest EVI_D decreases take place. The largest decreases in annual 01:30 SUHI_MEAN are in two US cities, Visalia (experiencing a 7% decrease) and Lexington, which reduces by 12%. Areas with little vegetation, mainly in the middle east, have the smallest changes in 01:30 SUHI_MEAN.

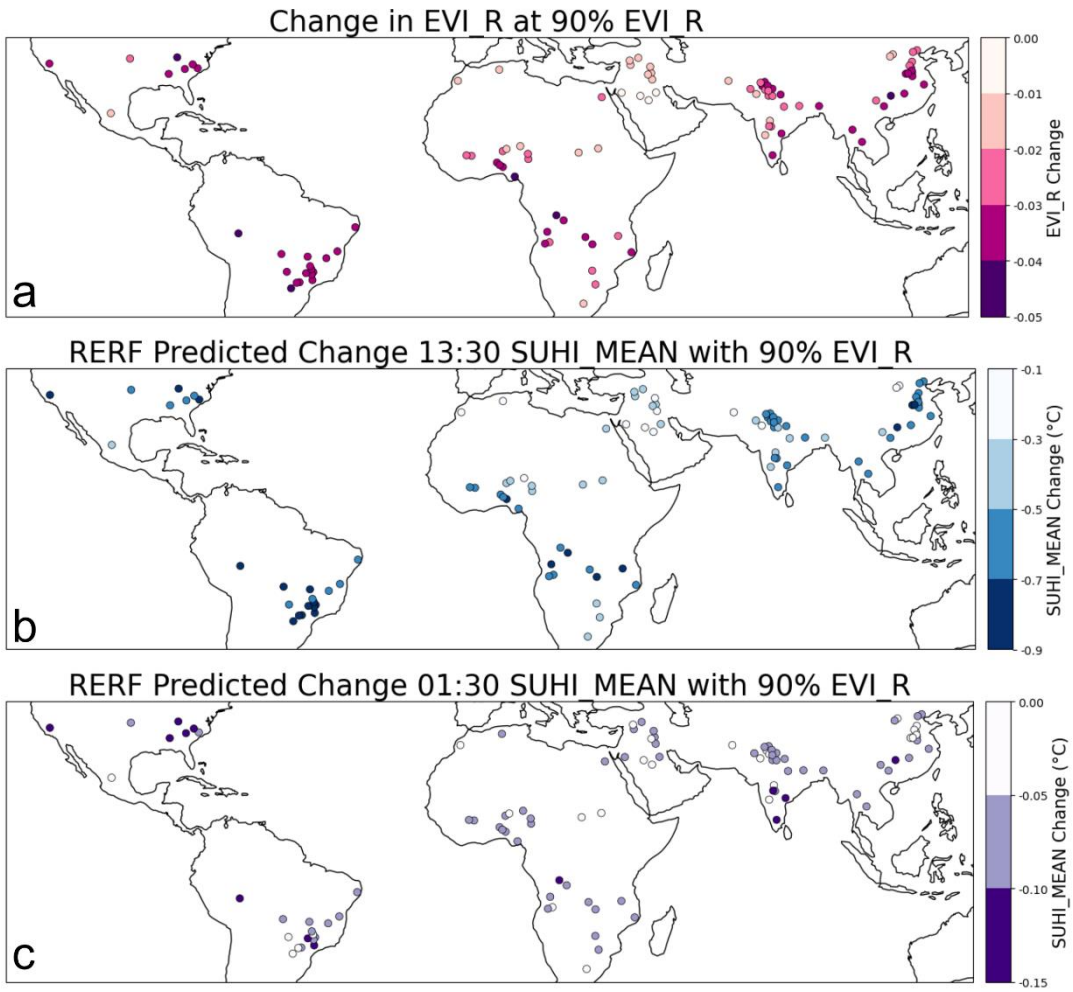

Figure 5.6 Investigation into how decreasing rural vegetation will impact the SUHI_MEAN. The plots show a) how a 10% decrease in EVI_R translates to the absolute value and b) based on this, predicted changes in the 13:30 SUHI_MEAN from RERF and c) predicted changes in the 01:30 SUHI_MEAN from RERF. Different colour scales are used for b) and c) to highlight the different magnitudes of the changes.

Urban Greening

The impact of increasing the vegetation in the city is examined by increasing EVI_U. The amount of green space in an urban area is a product of mostly climate, but also socioeconomic factors such as human development and population density (Bille *et al.*, 2023). Cities with high EVI_U values are those with climatic conditions such as precipitation favourable for the growth of vegetation, and urban greening strategies within these cities will need less management and irrigation in comparison to cities with small EVI_U, which tend to be in arid climates. Maintaining urban vegetation in these cities will be more challenging, as the climate conditions are not favourable for its growth.

This means, for a plausible increase in EVI_U, it follows a percentage increase on the current EVI_U is a good approach. Historical trends show mean global urban vegetation increased by

30% from 1990–2000, and 5.7% from 2000–2014, potentially driven by either changes in climate and carbon dioxide concentrations, urban greening policies, or a combination of the two (Corbane *et al.*, 2020). To examine the potential impact of city policies promoting urban greening (e.g., green roofs, tree lined streets), a 20% increase in EVI_U is examined, shown in Figure 5.7a. This was chosen to account for a continuation of the 5% increasing trend, plus a plausible increase of what might be possible under a policy of proactive urban greening.

As observed for EVI_R increases previously, the absolute value of the EVI_U decrease is city specific, and cities in greener areas experience a larger increase. Figure 5.4b shows how this increase in urban greening impacts the 13:30 SUHI_MEAN. For all cities, increased urban greening results in a smaller 13:30 SUHI_MEAN as urban vegetation driven cooling increases. Comparison of figure with Figure 5.1 with Figure 5.4b sees cities which have the largest decrease in 13:30 SUHI_MEAN also are those which have the large positive 13:30 SUHI_MEANs, although for the cities in India with negative 13:30 SUHI_MEANs (those on the western side, mostly south), the increase in EVI_U also has a strong cooling influence.

The impact of urban greening on the 01:30 SUHI_MEAN can be seen in Figure 5.4c. Change in the 01:30 SUHI_MEAN with urban greening is smaller than the 13:30 but has the same general trend. Cities which have the larger increases in EVI_U experience larger reductions in the 01:30 SUHI_MEAN, although there are some exceptions. For example, Zinder (Niger) has the largest reduction in 01:30 SUHI_MEAN, but not the largest EVI_D decrease. This indicates there are more non-linearities involved in the 01:30 RERF fit. This is reflected in the performance statistics (Table 4.7), as the linear base model, RR, captures little of the variance (measured by R-squared).

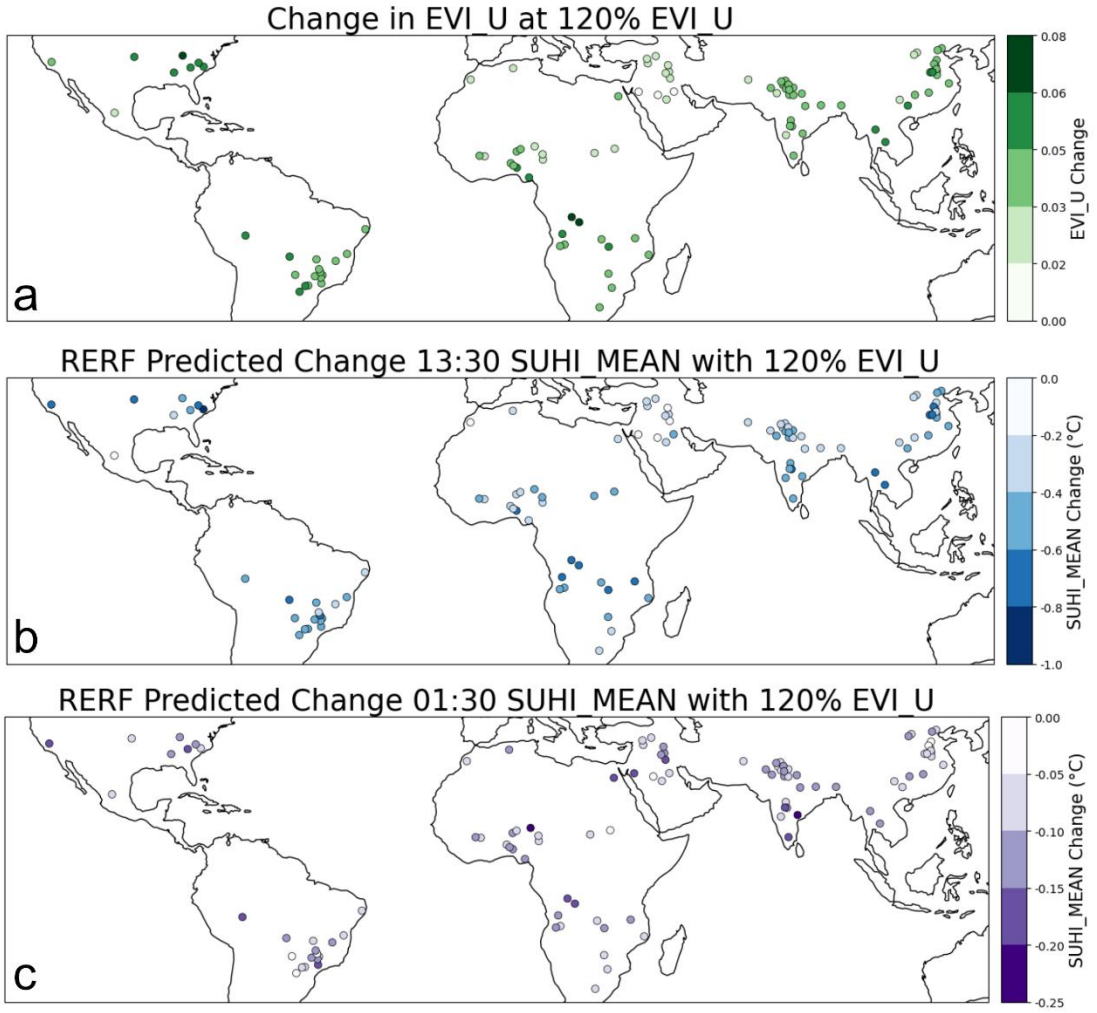

Figure 5.7 Investigation into how increasing urban vegetation will impact the SUHI_MEAN. The plots show a) how a 20% increase in EVI_U translates to the absolute value and b) based on this, predicted changes in the 13:30 SUHI_MEAN from RERF and c) predicted changes in the 01:30 SUHI_MEAN from RERF.

In this section, the sensitivity of the SUHI_MEAN to city related (city area) properties and vegetation related properties have been examined. The changes in SUHI_MEAN (at 13:30 and 01:30) for vegetation, in terms of EVI_R and EVI_U are both clear and intuitive in their impact. LOG_AREA, on the other hand, is not as clear-cut as it is dependent on the regional climate as to whether an increase enhances a negative 13:30 SUHI_MEAN/positive 13:30 SUHI_MEAN or causes a negative 13:30 SUHI_MEAN to decrease. This LOG_AREA relationship with SUHI_MEAN, where the same increase in LOG_AREA can result in a different increase in SUHI_MEAN in different cities highlights the need for region specific projections of changes in predictor variables. Figure 5.6 and Figure 5.7, showed how the same percentage increase in vegetation leads to varying magnitudes of change in the EVI values, as the regions themselves have varying levels of vegetation. The differing abundance of vegetation leads to differing potential impacts on the SUHI_MEAN due to vegetation changes.

For example, in Brazil, high EVI_R values mean deforestation can have a much larger impact on the SUHI_MEAN, whereas in the middle east, where EVI_R is very small, a reduction in this value will likely have little impact on the SUHI_MEAN, as the EVI_R change will be of a much smaller magnitude (16 cities in Brazil have an overall annual 13:30 SUHI_MEAN of 3.4 °C and decrease by 0.7 °C, the 12 cities in Syria, Egypt, Iraq, Saudi Arabia and Turkey have an overall annual 13:30 SUHI_MEAN of -0.9 °C and decrease by 0.3 °C).

5.2 CLIMATE PROJECTIONS

Generating the Predictor Variable Changes

A key question is how future changes in regional background climate will affect the SUHIs in cities of the type considered in this thesis. The impacts of climate change will not be the same in each region, and therefore, the changes in each city region, in terms of the predictor variables used in the model, will be different. In the following, this will be investigated by combining the RERF functions learned from observations with climate model projections for future regional changes (i.e., areas surrounding the cities considered) for the predictor variables. As outlined in section 2.8, the widest diversity and most consistent set of global climate change projections can be obtained from the CMIP6 archive, which is the most recent phase of the Coupled Model Intercomparison Project (CMIP). These climate model, or Global Climate Model (GCM), outputs - selected for a representative set of GCMs (section 3.4) – are used to quantify potential future changes in climate, so they can then be added into the dataset of predictor variables (see Figure 3.1).

In section 5.1, the impact of the potential direct human changes on vegetation (deforestation and urban greening) were examined via idealised percentage changes in EVI_R and EVI_U. Vegetation is expected to change in the future, due to changes in climate, atmospheric constituents (e.g., carbon dioxide concentrations) and other environmental variables, with climate change being the dominant factor (Teng *et al.*, 2023). As climatic changes vary from region to region, the same can be expected of the vegetation changes, so ESMs must be consulted for a realistic snapshot of future changes in the SUHI. These are used via the same approach as for the climate variables (projected using GCMs), by use of Earth System Models (ESMs).

As already discussed in section 2.8, a key challenge is that GCM (and ESM) climate projections show different rates of warming due to the forcings, feedbacks and parameterisations used (Eyring *et al.*, 2019). Looking at climate model projections at one point in time can therefore lead to a wide range of temperature increases. I will there pursue an alternative approach that looks at when a 2 °C global mean temperature from pre-industrial is

reached (Joshi *et al.*, 2011). Before being able to use the CMIP output as input to my statistical learning functions, variables are converted according to the following pre-processing steps:

1. Calculate a pre-industrial mean global temperature for each climate model, defined as the mean global temperature from 01/01/1850 to 01/01/1900.
2. Find the 20-year period where the mean global temperature is 2 °C higher than preindustrial baseline. This will be known as future period.
3. Re-grid the climate models so they are all on the same grid. This is the coarsest grid, CanESM5, which has spatial resolution 2.8 ° latitude x 2.8 ° longitude (see Table A.2.10 and Table A.2.11 for the resolutions of all models).
4. Use the climate model outputs from the pre-industrial period to get a baseline for the climate and vegetation variable outputs. These climate variables are (near surface) RH and TP from GCMs and vegetation variables are LAI from ESMs.
5. Use the climate model outputs from the future period (2 °C global mean warming from pre-industrial) to get a projection for the future climate and vegetation variables.
6. Calculate the change in the climate and vegetation variables using these two climate model outputs. This gives a change in RH and TP for each GCM (14 total) and a change in LAI, RH and TP for each ESM (5 total).

By looking at the difference between pre-industrial and 2 °C warming in the model rather than the absolute prediction for each predictor variable, bias correction is performed on the GCMs and ESMs. The changes in the predictor variables are then added to observations. This also means the resolution of the variables will remain that of the observations, and not those of the GCMs. This technique is known as the delta method (Navarro-Racines et al., 2020). This is of particular significance for the ESM LAI projections, where a positive bias has been found in the studied regions (section 2.8.2). An assumption of the approach is that the climate forcing will be the constant throughout the individual city study area (rural and urban). Essentially, that the change in a climate variable projected in a model grid box will be homogenous throughout the grid box area.

Figure 5.8 shows the median, 10^{th}, 90^{th} percentile of the GCM model changes in RH. The largest increases in RH can be seen in India, and even at the bottom end of the projections (10^{th} percentile), the changes are still positive, although fairly small. The largest increases, of 14% in the 90^{th} percentile, are seen in Mathura and Shahjahanpur (India). In Brazil, the largest decreases are seen, with GCMs predicting a decrease in RH, or a very little change in the 90^{th} percentile. The largest decrease in RH in the 10^{th} percentile is 9%, seen in Campo Grande and Cuiaba (Brazil). How cities experience these annual changes in RH are not the same throughout the annual cycle, illustrated by Figure 5.9, which shows the annual range of RH

changes. Two cities which experience the same change in RH could have this change as a consistent increase each month of the year, or as a large increase in couple of months and negligible change in the remaining. For example, Wichita (USA) experiences similar changes in RH in 10th, 50th and 90th quantiles to the other cities in the USA, yet the annual range is larger. In northern India, the changes in monthly RH are the most seasonal, and in the 50th percentile, the difference between the month with the smallest change and the largest change is 14%, indicating the strengthening of the Indian monsoon. This means the annual changes in SUHI_MEAN will likely be unevenly spread throughout the year, with some months experiencing larger changes in SUHI_MEANs than others. Therefore, although the focus of this section is mostly on the annual changes, some seasonal changes are also considered.

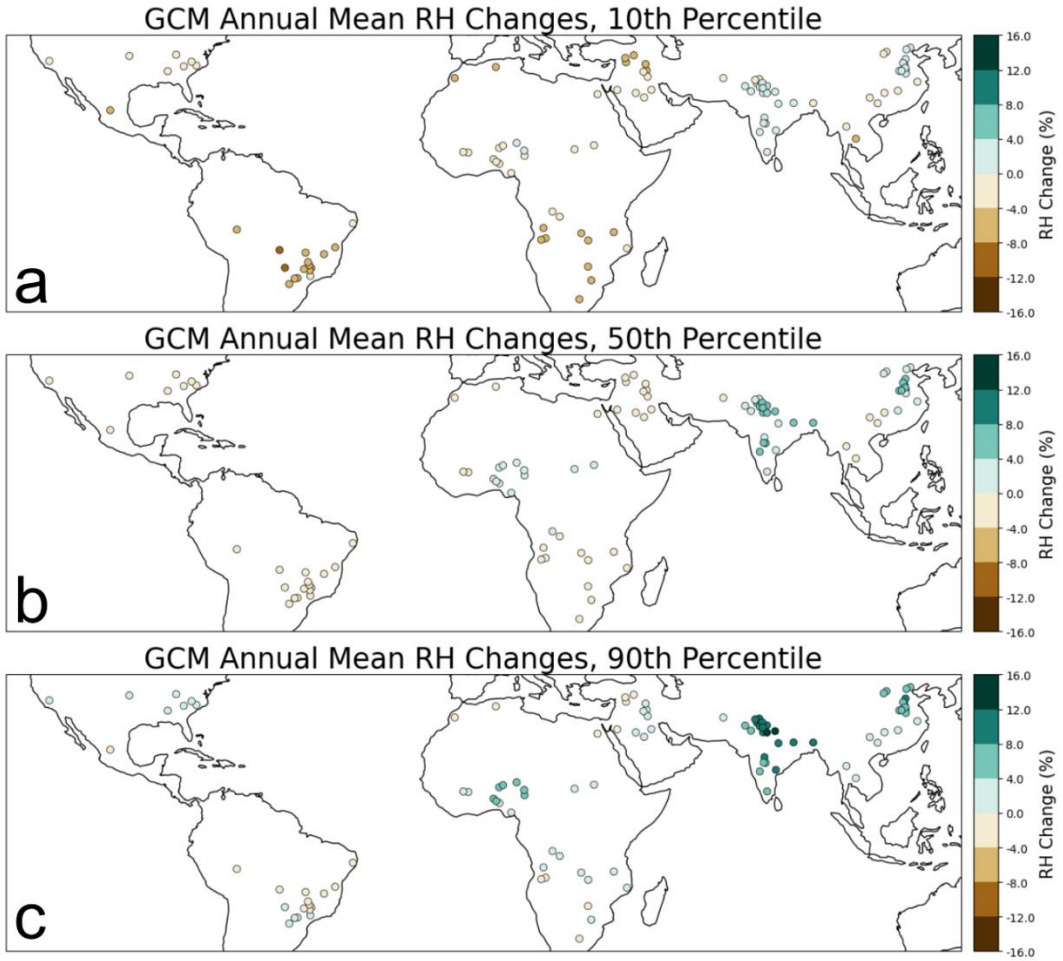

Figure 5.8 GCM RH change from historical pre-industrial RH to 2°C mean global temperature projected RH. The spread of the GCM projected changes is shown by a) the 10th Percentile, b) the 50th Percentile (Median), c) the 90th Percentile.

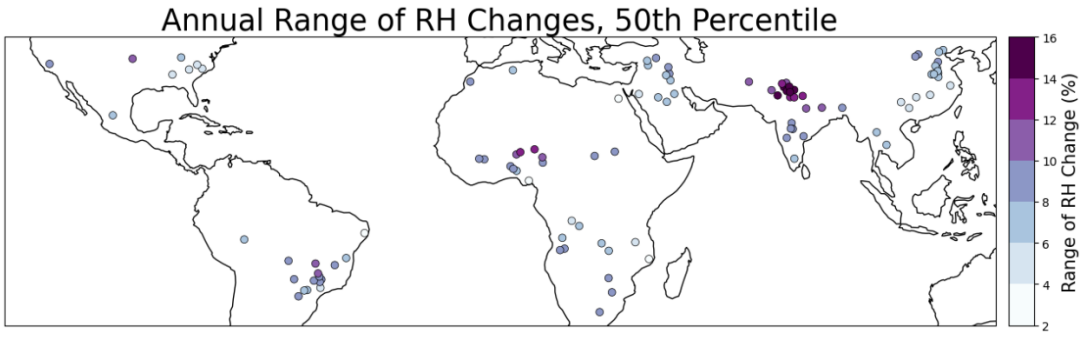

Figure 5.9 The median annual range of RH (the difference between the month with the smallest RH changes and the month with the largest RH changes). Cities which have similar annual changes in RH have different annual ranges.

Figure 5.10 shows the median, 10th, 90th percentile of GCM model in TP. Here, the spatial patterns can be connected to those of the RH changes. Areas where the RH show increases also show increases in TP, and areas of decrease in RH also show decreases in TP. Increased rainfall in an area leads to increased evaporation of surface water. This is of interest in relation to the RERF model, as the ALE plots show the SUHI_MEAN magnitude has a positive relationship with TP and negative relationship with RH. If this is the case, the contributions of changes in both variables may lead to less of a change in the SUHI_MEAN than if each are examined using the REFR separately. There is also a wide range in the percentiles of TP changes, with the majority of areas projected to have decreases in precipitation in the 10th percentile, and most areas increases in the 90th percentile.

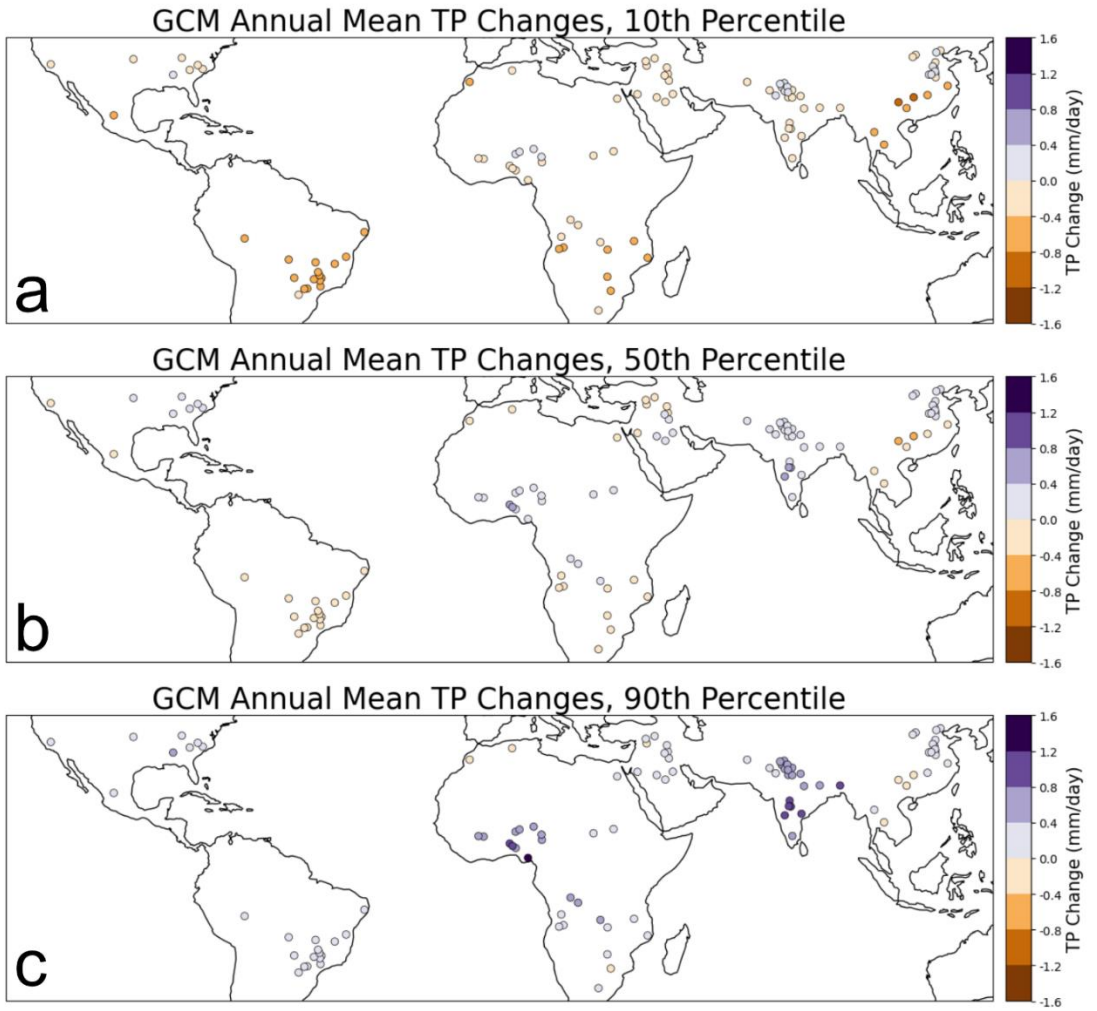

Figure 5.10 GCM TP change from historical pre-industrial TP to 2°C mean global temperature projected TP. The spread of the GCM projected changes is shown by a) the 10th Percentile, b) the 50th Percentile (Median), c) the 90th Percentile.

LAI projections from ESMs are used to examine changes in EVI, by means of the linear relationship between LAI and EVI (section 2.8). Due to this linear relationship, a percentage change in LAI can be expected to equate to a similar percentage change in EVI. Therefore, the change in LAI is scaled by dividing by the pre-industrial LAI, to give a fractional change which is translated to a change in EVI by multiplying by the monthly mean EVI over the 2002-2020 period. Figure 5.11 shows the changes in EVI_R. Plots showing the values for LAI changes can be seen in the appendix (Figure A.5.14). Again, the changes in vegetation mirror the changes in RH and TP. Where increases (decreases) in TP and RH are projected, the EVI_R also increases (decreases). This demonstrates how the variables interact and the importance of considering the impact of them together. The same changes are applied to the EVI_R and EVI_U variables to examine the projected future changes.

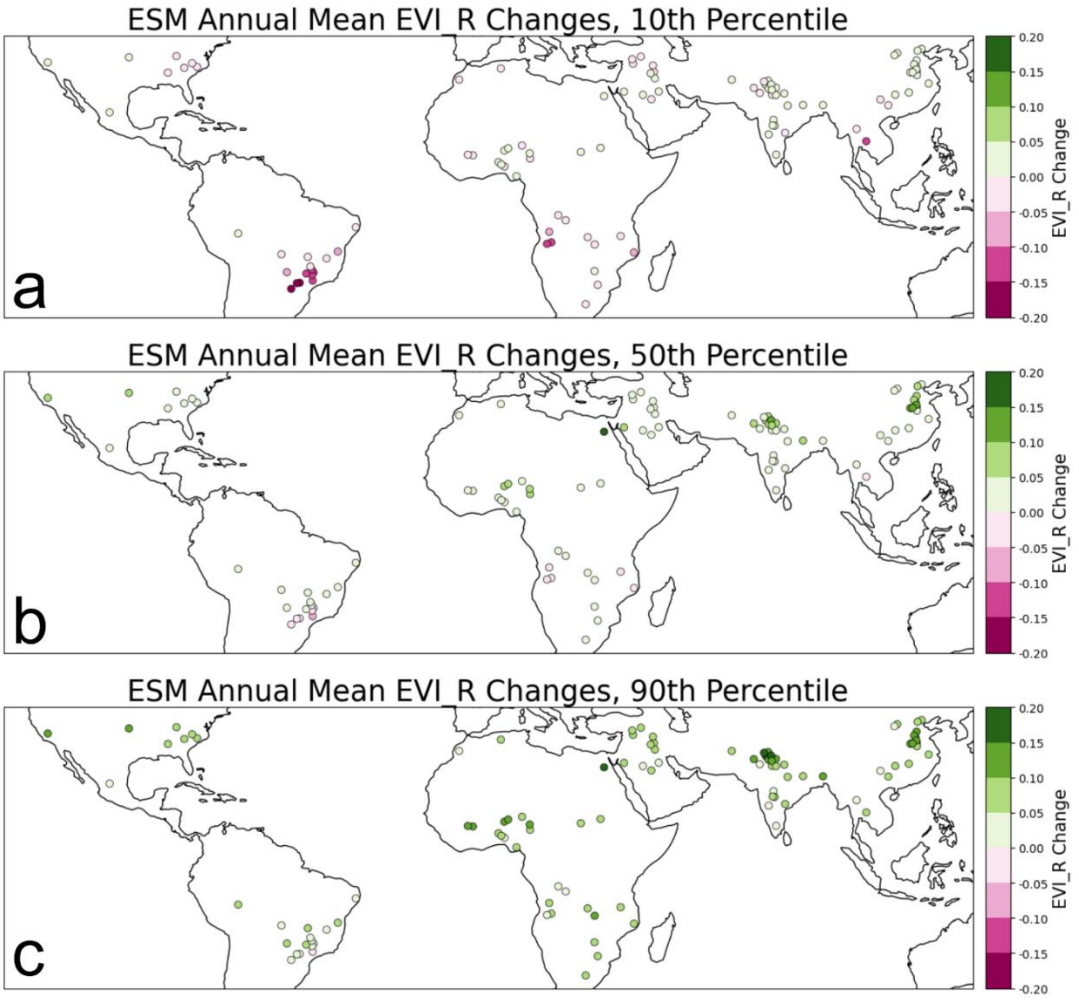

Figure 5.11 ESM EVI_R changes, based on LAI fractional change from historical pre-industrial LAI to 2°C mean global temperature projected LAI. The spread of the ESM projected changes is shown by a) the 10th Percentile, b) the 50th Percentile (Median), c) the 90th Percentile.

In addition to the LAI projections, RH and TP projections were taken for the ESM models, for use simultaneously to understand the overall impact of these interacting variables. As there are fewer ESM models, the range of the predictions for these are smaller than the GCM projections of RH and TP but general patterns are similar. Plots showing the 10th, 50th and 90th quantiles for the ESM TP and RH projections can be found in the appendix (Figure A.5.15 and Figure A.5.16).

Using Climate Projections in the Statistical Models

The impacts of the changing climate variables on the SUHI_MEAN is first examined individually. The changes in the SUHI_MEAN are generated using a dataset consisting of all the datapoints generated in section 4.2 (i.e., the monthly mean values for SUHI_MEAN and corresponding predictor variables from 2002 to 2020). A current RERF prediction of the SUHI_MEAN is made based on the dataset, which will be referred to as current prediction.

Then the monthly changes in the required climate variable, generated previously in this section, are added to the climate variable. For example, if the variable is RH, the new variable is RH + RH Change. A RERF SUHI_MEAN prediction is then made again, but now using the new climate variable with changes added, which will be known as future prediction. The difference between current prediction and future prediction is then calculated to determine the future change in SUHI_MEAN.

In GCMs and ESMs where the increase leads to changes in predictor variables which are not possible (for example RH outside of the range 0-100%). This a downside to the bias correction approach used, which involves looking at changes in the GCM or ECM variables rather than at the absolute prediction value, but must be balanced with using actual GCM values, which can have significant biases, especially in TP, for example (Tian and Dong, 2020). To ensure the predictor variables do not go beyond the realm of physical possibility, the ranges are capped to the maximum possible amount in that predictor variable (e.g., A RH of 110% will be input as 100%). For the EVI_D values, the EVI_R values were capped to between 0 and 1 (alongside the EVI_U values), and the difference recalculated. The values which have been capped are shown in brackets in Table 5.1.

Table 5.1 Table detailing how much extrapolation is taking place when the projections of the future SUHI_MEAN is made. The predictor variables altered (RH, TP, EVI_U, EVI_D) and their current and new ranges are shown. This is the range in the monthly values from 2002- 2020.

Variable	Current minimum value	Current maximum values	After projection minimum value	After projection maximum value
RH	7%	93%	0.2%	100% (116%)
TP	0.0004 mm/day	25 mm/day	0 mm/day (-3mm/day)	26 mm/day
EVI_U	0.01	0.54	0 (-0.29)	0.78
EVI_D	-0.41	0.08	-0.55	0.09

Figure 5.12 shows how the 13:30 SUHI_MEAN is predicted to change based on the potential future RH projections. In these annual mean plots, the changes in 13:30 SUHI_MEAN can be compared with the annual mean changes in RH, shown in Figure 5.8. Based on the RH plots, an expectation would be that the cities in Brazil will experience the largest 13:30 SUHI_MEAN increases in the 90th percentile (as the RH in these cities decreases the most in the 10th percentile), and cities in India experience the largest 13:30 SUHI_MEAN decreases

in the 10th percentile (due to largest RH increases in the 90th percentile), and this is seen in the 13:30 SUHI_MEAN predicted annual changes. In the 50th percentile (Figure 5.12b), areas where the RH increases (India, Bangladesh, China, Nigeria, and Sudan) show decreases in 13:30 SUHI_MEAN. These are all areas with positive annual 13:30 MEAN_SUHIs, apart from the two cities in Sudan, where the annual 13:30 SUHI_MEAN projection indicates it will become more negative. In some cases where a decrease in 13:30 SUHI_MEAN is found, the annual RH change decreases, and cities in the same regions have oppositive signs (positive/negative) of change. Here, changes in the seasonal means of RH could be influencing the predictions, as in Figure 5.9 shows how the range of changes in RH vary from month to month. Overall, the annual changes in 13:30 MEAN_SUHI from changes in RH only are small, ranging from a 0.27 °C decrease in the 10th percentile to a 0.29 °C increase. Half the cities (52) show a decrease in annual 13:30 SUHI_MEAN due to RH changes, and the other show an increase.

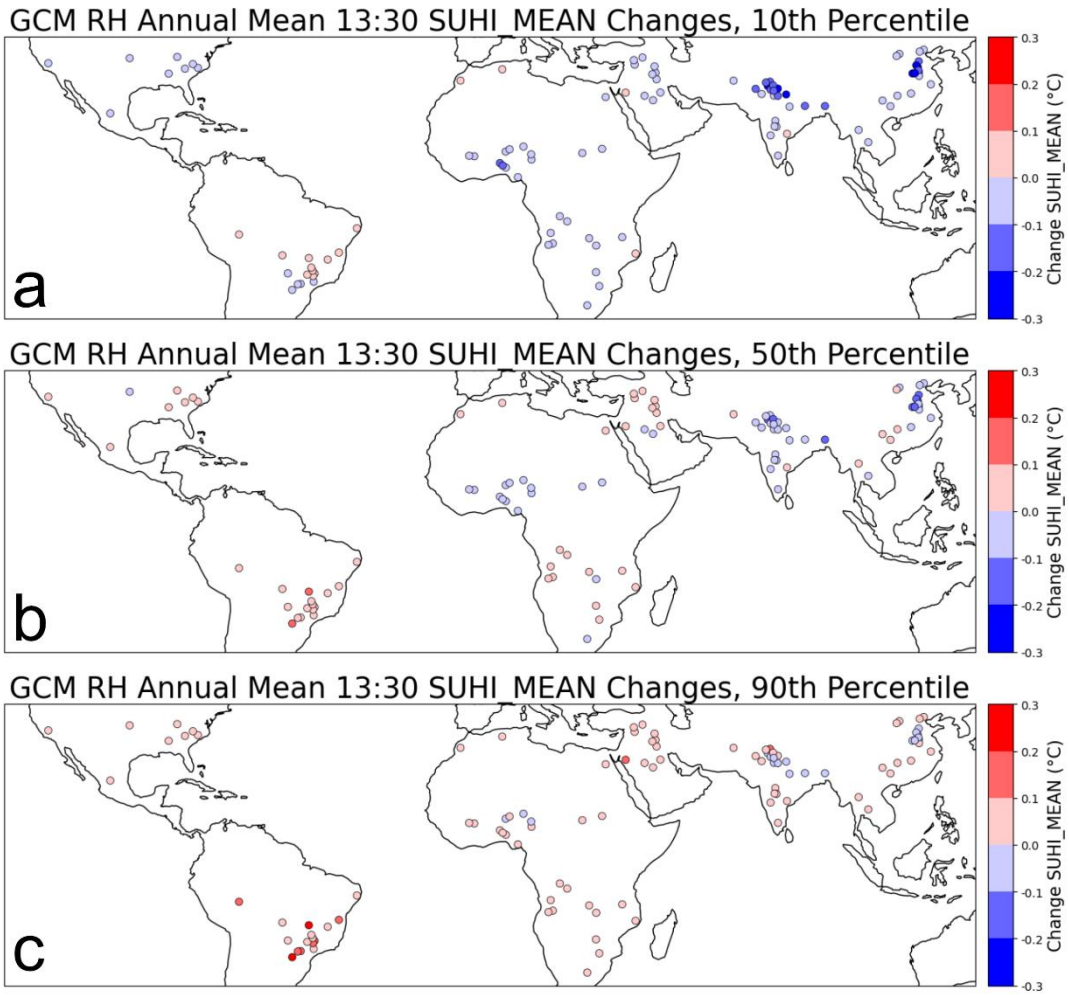

Figure 5.12 Plots showing how RERF predictions of 13:30 SUHI_MEAN change with the GCM projected changes in RH. The spread of the 13:30 SUHI_MEAN projected changes is shown by a) the 10th Percentile, b) the 50th Percentile (Median), c) the 90th Percentile.

Figure 5.13 describes the projected changes in the 01:30 SUHI_MEAN based on the future RH projections. The magnitude of change for the 01:30 SUHI_MEANs is similar to those seen at 13:30, despite the greater variation in the 13:30. This is to be expected based on the ALE plots (Figure 4.36 and Figure 4.40), which show RH to be the most influential variable on the 01:30 SUHI_MEAN, and therefore changes in this variable will have the greatest impact on the 01:30 SUHI_MEAN. Additionally, the ALE plots show increasing RH has a decreasing impact on 01:30 SUHI_MEAN. This can be seen by comparing Figure 5.13 to Figure 5.8; areas where RH decreases, such as Brazil, have a projected increase in 01:30 SUHI_MEAN and areas such as India and China where RH increases have decreases. The largest decreases in 01:30 SUHI_MEAN are all in India, with 12 cities decreasing by over 0.2 °C in the 10^{th} percentile. The largest increases in the 90^{th} percentile are for 5 cities in Brazil at over 0.15 °C. Overall, there is a roughly even split in SUHI_MEAN changes at 01:30, with 53% SUHI_MEANs increasing and the remaining 47% decreasing. All 01:30 SUHI_MEANs remain positive after the changes in RH.

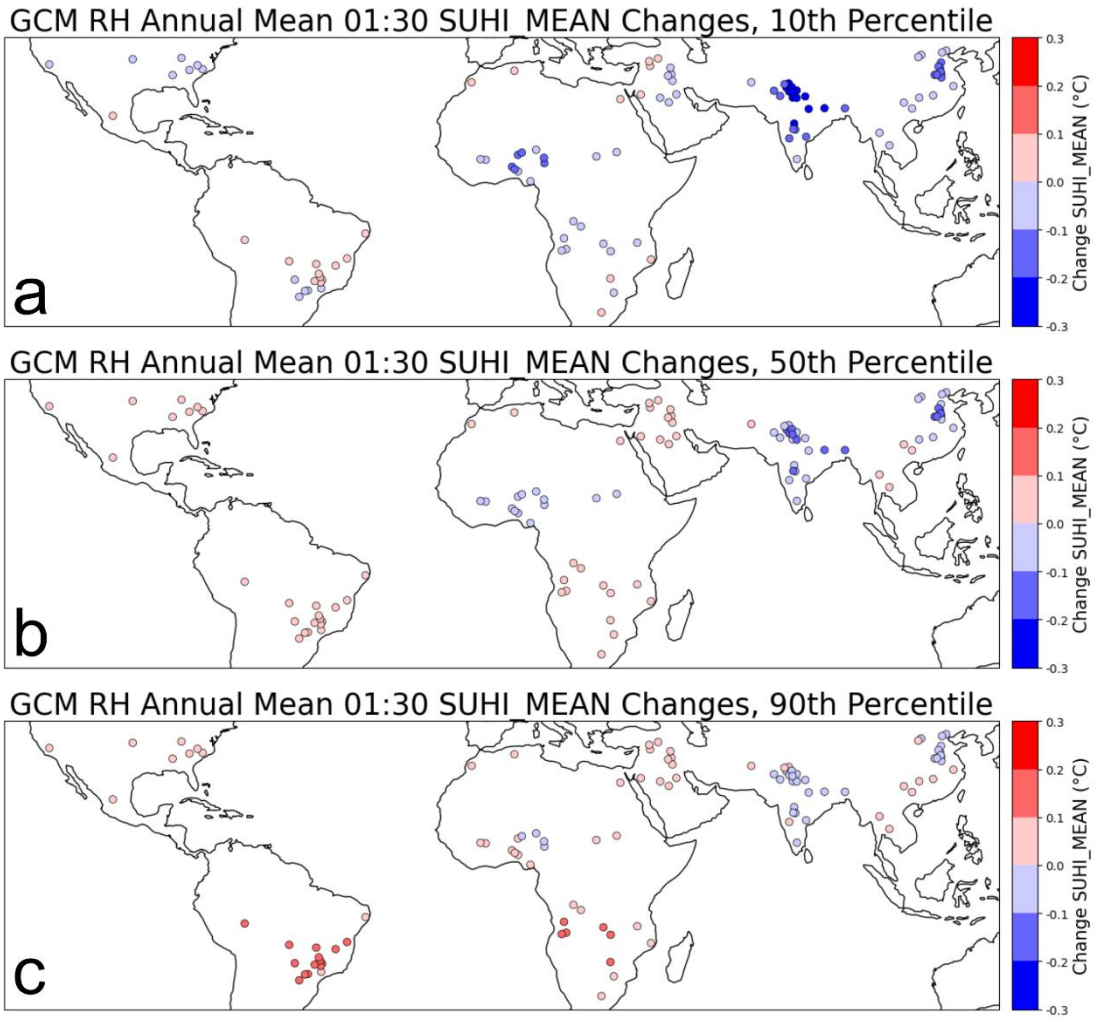

Figure 5.13 Plots showing how RERF predictions of 01:30 SUHI_MEAN change with the GCM projected changes in RH. The spread of the 01:30 SUHI_MEAN projected changes is shown by a) the 10th Percentile, b) the 50th Percentile (Median), c) the 90th Percentile.

The next climate variable examined was TP, changes for which can be seen in Figure 5.10. The impact of these changes on the 13:30 SUHI_MEAN can be seen in Figure 5.14. In agreement with the relationships observed in the ALE plots (Figure 4.36), in general when cities see an increase (decrease) in TP, the 13:30 SUHI_MEAN increases (decreases), although this is not always the case. Umuahia (Nigeria) and Caruaru (Brazil) city, show an increase in the 13:30 SUHI_MEAN in the 10th percentile, despite the TP decreasing. This could be related to both these cities only just meeting the coastal threshold as they are 100 km and 102 km from the coastline. The TP imposed changes in 13:30 SUHI_MEAN are of smaller magnitude than those from RH, with a maximum decrease of 0.13 °C in the 10th percentile and increase of 0.20 °C in the 90th percentile. 36% of annual 13:30 SUHI_MEANs decrease, and 64% show an increase. As mentioned previously, TP changes are connected to RH and EVI (by LAI), as it drives changes in both variables. Therefore, the actual changes due to TP

are likely to be larger, and changes of all these variables together are explored later in this section.

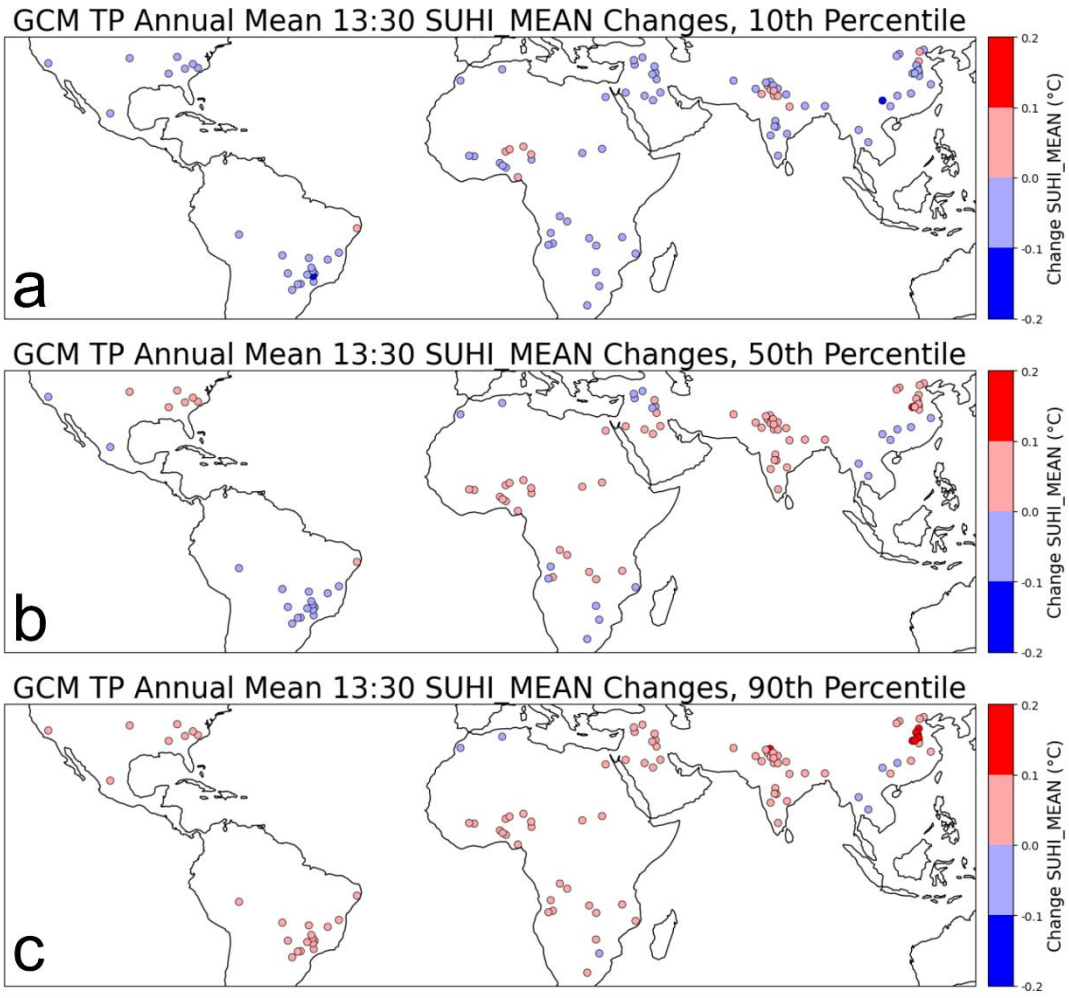

Figure 5.14 Plots showing how RERF predictions of 13:30 SUHI_MEAN change with the GCM projected changes in TP. The spread of the 13:30 SUHI_MEAN projected changes is shown by a) the 10th percentile, b) the 50th percentile (median), c) the 90th percentile.

The impact of the changing TP on the 01:30 SUHI_MEAN gives a different effect to the 13:30. Figure 5.15 shows projections of how the GCM changes in TP alter the SUHI_MEAN at 01:30. It is expected there will be day-night differences due to the output of the ALE plots. For the 13:30 SUHI_MEAN (Figure 4.36), an increase in TP results in an increased SUHI_MEAN, whereas in the case of the 01:30 SUHI_MEAN (Figure 4.40) it results in a decrease. During the day, wet soils take longer to heat up, causing rural areas to remain at a lower temperature and increasing the SUHI. At night, wet soils take longer to cool down, which keeps rural areas warmer, thereby reducing urban-rural differences in cooling rates (explained in section 2.4.2). Changes in 01:30 SUHI_MEAN remain below 0.1 °C magnitude for most cities in all GCM percentiles. Just one city, Gombe (Nigeria), has a decrease of just

over 0.1 °C in the 10th percentile of GCMs and Napula (Mozambique) has an increase of 0.18 °C in the 90th percentile. For 67% of 01:30 SUHI_MEANs, the TP changes lead to a projected increase.

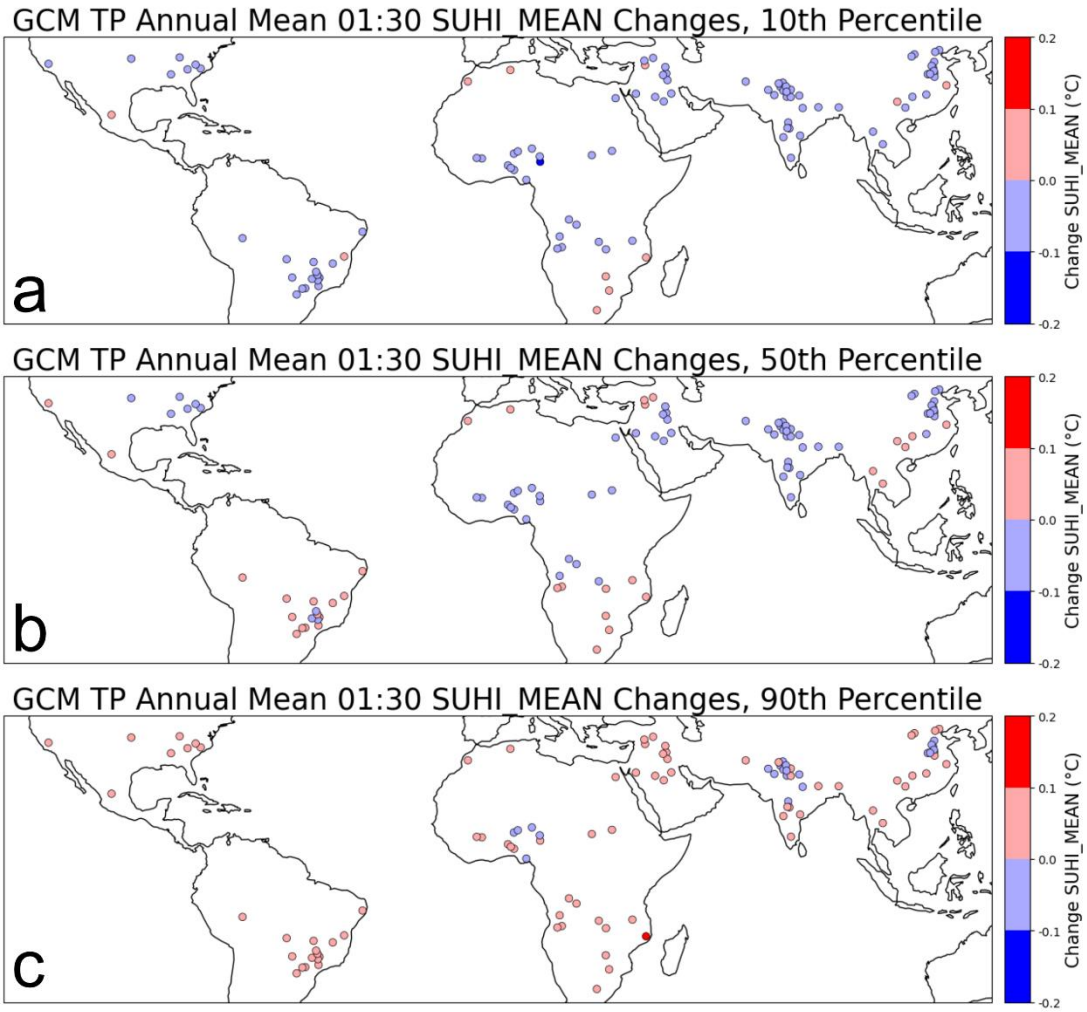

Figure 5.15 Plots showing how RERF predictions of 01:30 SUHI_MEAN change with the GCM projected changes in TP. The spread of the 01:30 SUHI_MEAN projected changes is shown by a) the 10th percentile, b) the 50th percentile (median), c) the 90th percentile.

The final predictor variables for which changes are examined in is the EVI variables, to give an understanding of how future changes in vegetation will affect the SUHI.

In section 4.3, it was shown that for the selected cities EVI_R and EVI_U are highly correlated, with a Pearson's correlation coefficient of 0.89. Climatic conditions favourable to vegetation growth promote more abundant vegetation both in the urban and rural areas, and the seasonal cycles of vegetation growth are generally the same across the city and its surroundings, although it has been shown the UHI can influence growing seasons by a few

days (Wang *et al.*, 2019). From this correlation, it follows that climate changes favourable (or unfavourable) to vegetation growth will impact both urban and rural vegetation.

Studies into urban greening the regions of cities in this thesis can be sparse (Lindley *et al.*, 2018) and there is no guarantee that urban greening policies in place today will remain the same in the future. The same urban greening in all cities cannot be assumed, as it can be limited by practical issues such as limited space in more compact cities. Urban greenspace can also decrease as city densification occurs to cater for increasing urban populations (Puplampu and Boafo, 2021). Therefore, no assumption either way is made and the percentage change in vegetation is taken to be the same for both the urban and rural areas.

The vegetation changes are applied to both EVI_U and EVI_R and changes in the RERF predictions of SUHI_MEAN are generated as previously. Figure 5.16 shows these changes in 13:30 SUHI_MEAN. Based on the 50th percentile plots (Figure 5.16b), it is somewhat likely the majority of cities will see an increase in the 13:30 SUHI_MEAN based on the projected vegetation changes (87% of cities have an increase in the 50th percentile scenario). This is in line with expectations as the median EVI projections show increases, although there is uncertainty here (see Figure 5.11); more vegetation leads to increased rural cooling. The cities with decreases in 13:30 SUHI_MEAN are those where there is a decrease in EVI, aside from one city, Bikaner, which is located near the Thar desert in northwest India. This city is one of few with a positive EVI_D (EVI_U > EVI_R, see Figure 4.22c), and therefore a proportional increase for both EVI_R and EVI_U will increase the EVI_D further, resulting in a more negative SUHI_MEAN. The other two cities with a positive EVI_D experience an increase in the SUHI_MEAN, or rather, the annual 13:30 SUHI_MEAN becomes less negative. Comparison of the 10th percentile of EVI_R changes (Figure 5.11a) to the 10th percentile of 13:30 SUHI_MEAN changes (Figure 5.16a) shows areas where there is the highest decrease in vegetation (the most southern cities in Brazil, cities in Angola, and a city in Thailand (Nakhon Ratchasima)) have the largest decreases in the 13:30 SUHI_MEAN.

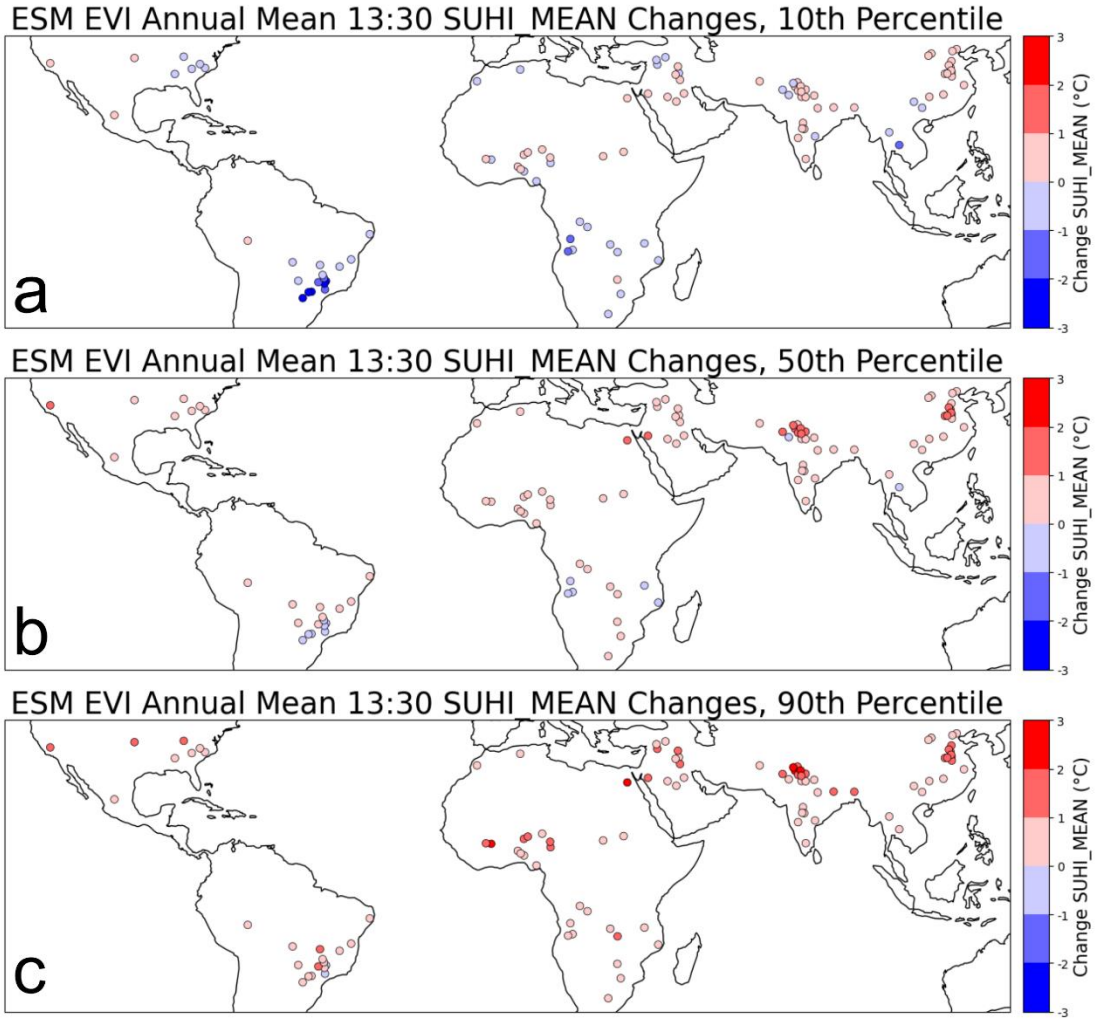

Figure 5.16 Plots showing how RERF predictions of 13:30 SUHI_MEAN change with the ESM projected changes in EVI. The spread of the 13:30 SUHI_MEAN projected changes is shown by a) the 10th percentile, b) the 50th percentile (median), c) the 90th percentile.

The impact of EVI changes on the 01:30 SUHI_MEAN is smaller (Figure 5.17). In the 10th percentile, 7 cities have decreases larger than 0.1 °C. Of these, 6 are in Brazil and one in Algeria. These are areas where the EVI is decreasing. In the 90th percentile, 12 cities have increases larger than 0.1 °C, the largest being a 0.16 °C increase in Bobo-Dioulasso (Burkina Faso). Comparison with the changes in EVI (Figure 5.11) show the changes in the 01:30 SUHI_MEAN show similar patterns of change in the 13:30 SUHI_MEAN, increasing (decreasing) where EVI decreases (increases). In the median outcome, in most cities (78%) there is an increase in 01:30 SUHI_MEAN.

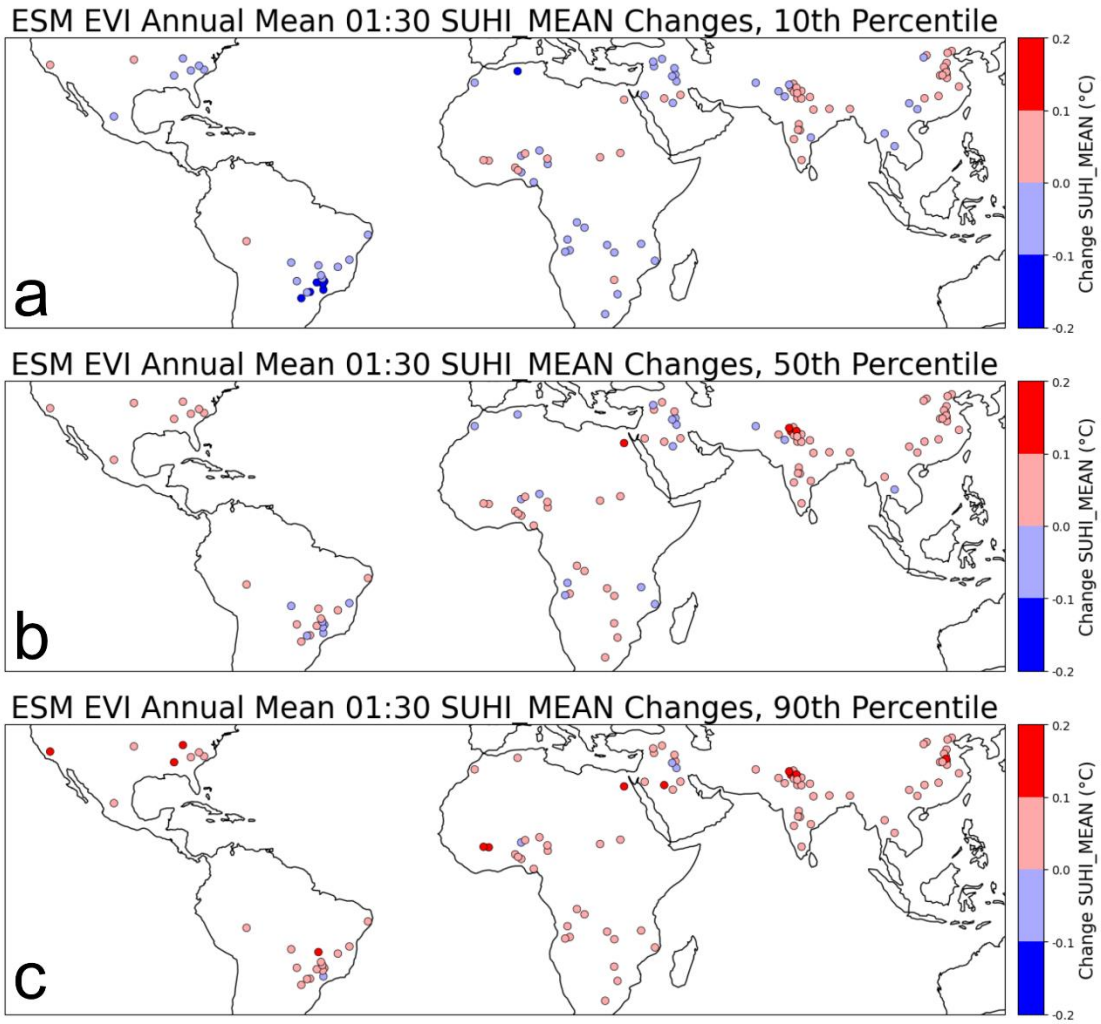

Figure 5.17 Plots showing how RERF predictions of 01:30 SUHI_MEAN change with the ESM projected changes in EVI. The spread of the 01:30 SUHI_MEAN projected changes is shown by a) the 10th percentile, b) the 50th percentile (median), c) the 90th percentile.

All three predictor variables for which projected climate changes have been examined are connected (RH, TP and EVI). As there will be interactions between the RH, TP and EVI within the ESMs, the changes in predictor variables fed into the RERF must all come from the same ESM or GCM. Therefore, as only the ESMs generate LAI projections, these are used to examine the combined changes.

Comparison of Figure 5.8, Figure 5.10 and Figure 5.11 shows how areas where RH is increasing also have increasing TP, and increases in EVI. The interactions between the three are clear; more precipitation leads to higher relative humidities, and also more soil water retention for vegetation growth. Therefore, via the means of the ESMs, the three are considered in unison (or four, as EVI_U and EVI_D are the predictor variables for EVI in the RERF model).

Figure 5.18 shows the RERF predicted increases in 13:30 SUHI_MEAN in the 10th, 50th and 90th percentile. Based on the 50th percentile, the expectation in the majority of cities is that the 13:30 SUHI_MEAN will increase (81% of cities have an increase in 13:30 SUHI_MEAN). This is mainly due to increases in rural vegetation. The addition of the ESM TP and RH changes into the model make a small difference to the 13:30 SUHI_MEAN changes, which is to be expected based on the relatively small changes shown in Figure 5.12 (the changes in 13:30 SUHI_MEAN due to RH) and Figure 5.14 (the changes in 13:30 SUHI_MEAN due to TP) compared with those in Figure 5.16 (the changes in 13:30 SUHI_MEAN due to EVI).

In Figure 5.18, it can be seen even in the 10th percentile, Chinese cities, along with a large proportion of cities in India and Nigeria, show increases in the 13:30 SUHI_MEAN. Over half (54%) of the selected cities in the middle east also show increases in the 13:30 SUHI_MEAN in the 10th percentile, and all in the 50th percentile, with the negative 13:30 SUHI_MEANs becoming less negative, or positive in some cases. The future of the 13:30 SUHI_MEAN for the cities in Brazil is more uncertain. The 10th percentile shows strong decreases in 13:30 SUHI_MEAN, whereas the 50th percentile shows both increase and decreases, and the 90th percentile all increases aside from a single city.

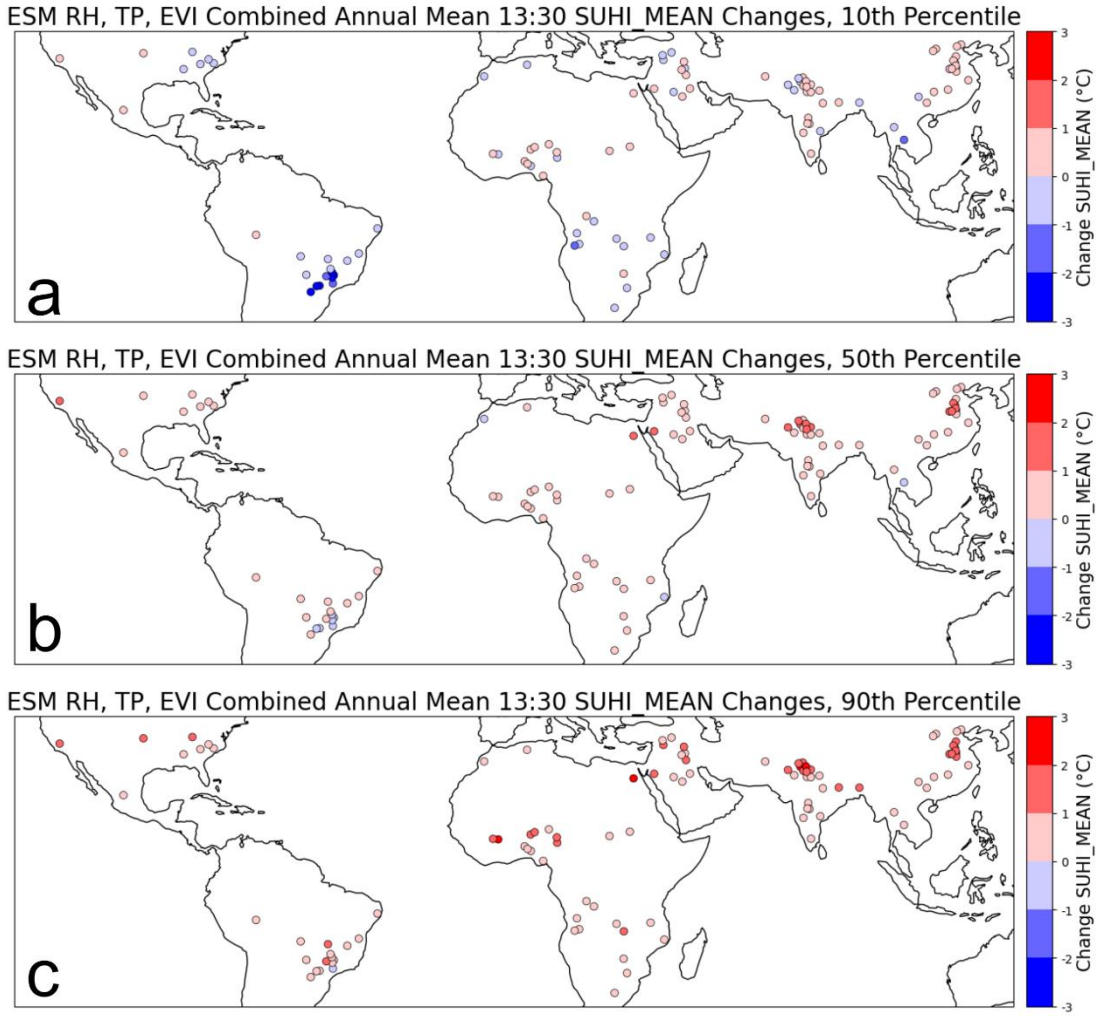

Figure 5.18 Plots showing how RERF predictions of 13:30 SUHI_MEAN change with the ESM projected changes in RH, TP and EVI (EVI_U and EVI_D). The spread of the 13:30 SUHI_MEAN projected changes is shown by a) the 10th percentile, b) the 50th percentile (median), c) the 90th percentile.

To contextualise the changes in the 13:30 SUHI_MEAN, Figure 5.19 shows points for the 13:30 SUHI_MEAN before and after the 2 °C warming, based on the median changes. A 68% prediction interval (section 3.5), based on the RERF error is shown on the after 2 °C warming points. This represents the interval which there is a 68% probability the true value lies within. Here it can be seen that the 2 °C warming pushes more of the 13:30 SUHI_MEANs above certain thresholds. For example, before, there are seven cities with an annual 13:30 SUHI_MEAN greater than 4 °C, but an additional five cities are added to this group by the climate change impacts. For three of the cities with negative 13:30 SUHI_MEANs, there is a change that flips this in sign to positive, with the largest change in Asyut (Egypt) (which is 1.9 ±0.2 °C). The magnitude of the increase is much larger than the prediction interval, so this change is significant. The changes in 13:30 SUHI_MEAN are not proportional to the current

13:30 SUHI_MEAN magnitudes, with cities with very similar 13:30 SUHI_MEANs at present showing different extents of changes.

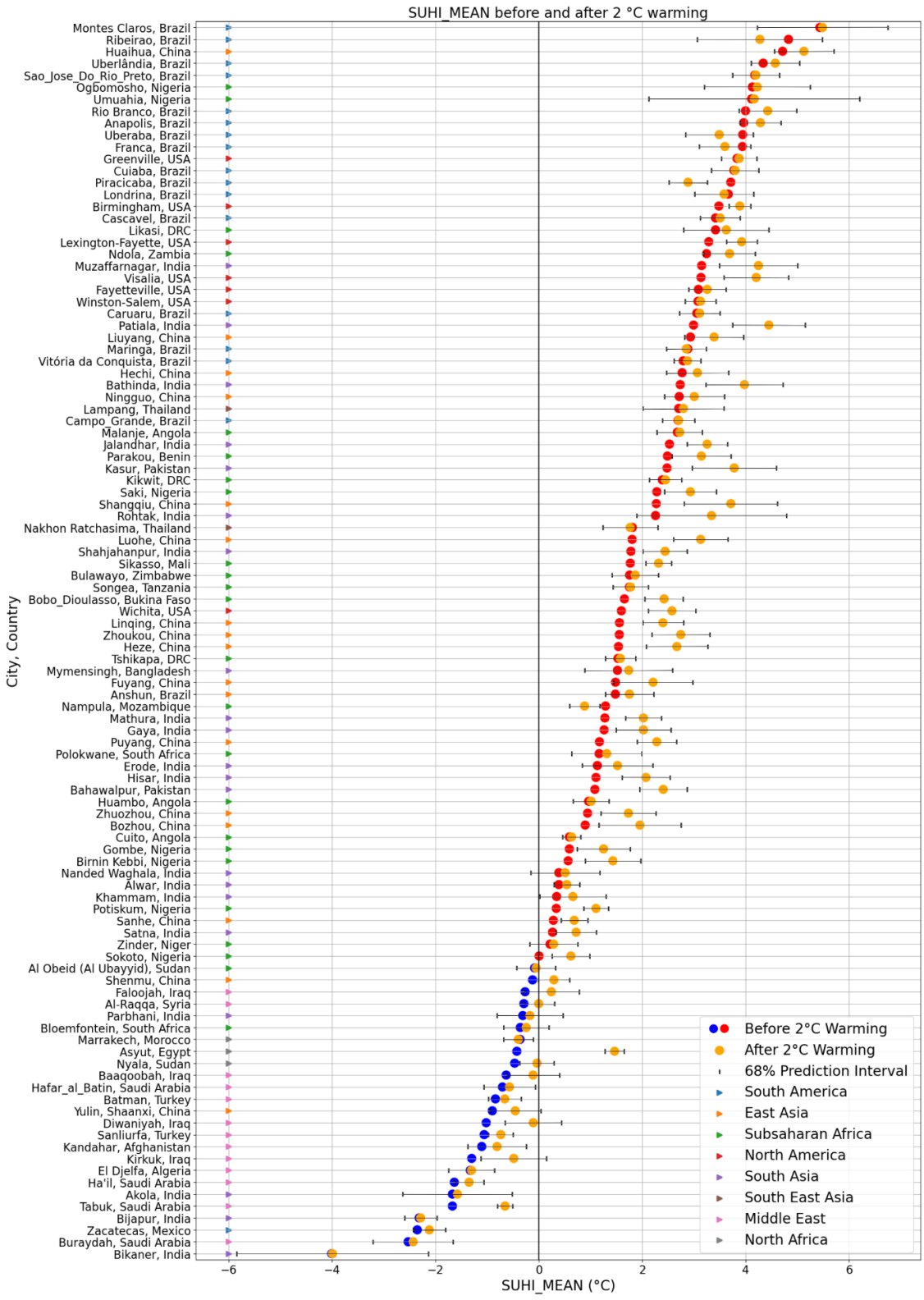

Figure 5.19 Comparison of the city annual 13:30 SUHI_MEANs current and with the RERF predicted changes. The orange dots show the median prediction for 13:30 SUHI with 2 °C warming, with a 68% prediction interval. The prediction interval was calculated for the annual values of each city individually to get city specific intervals. The blue and red dots show the current 13:30 SUHI_MEANs. Coloured arrows on the left-hand side of the plot denote the geographical regions the city is located.

When the same ESM RH, TP and EVI changes are applied to the 01:30 SUHI_MEAN, the projected changes are smaller than 13:30, reflecting its smaller magnitude in general (Figure 5.20). Percentage of cities increasing in 01:30 SUHI_MEAN is 58%, showing a less clear increase in comparison to the 13:30.

The most influential variable on the 01:30 SUHI_MEAN was RH (based on ALE plots, Figure A.3.4) and the impact of this variable can be seen by comparing the plots of all climate variables (Figure 5.20) to that where only changes in RH are investigate (Figure 5.13). The stronger decreases in the 01:30 SUHI_MEAN are seen in areas where the 13:30 SUHI_MEAN sees increase, for example India and China, and stronger increases seen in Brazil, which have decreases in the 13:30 SUHI_MEAN. The strongest decrease in 01:30 SUHI_MEANs are for 5 cities located in India (3 cities), Nigeria and Niger, where the decrease is over 0.2 °C in the 10^{th} percentile. The largest increase is seen in Rio Branco, Brazil, at 0.28 °C. These differences between the changes in SUHI_MEAN at 13:30 and 01:30 show how the formation of the UHI is driven by different factors during the day and night.

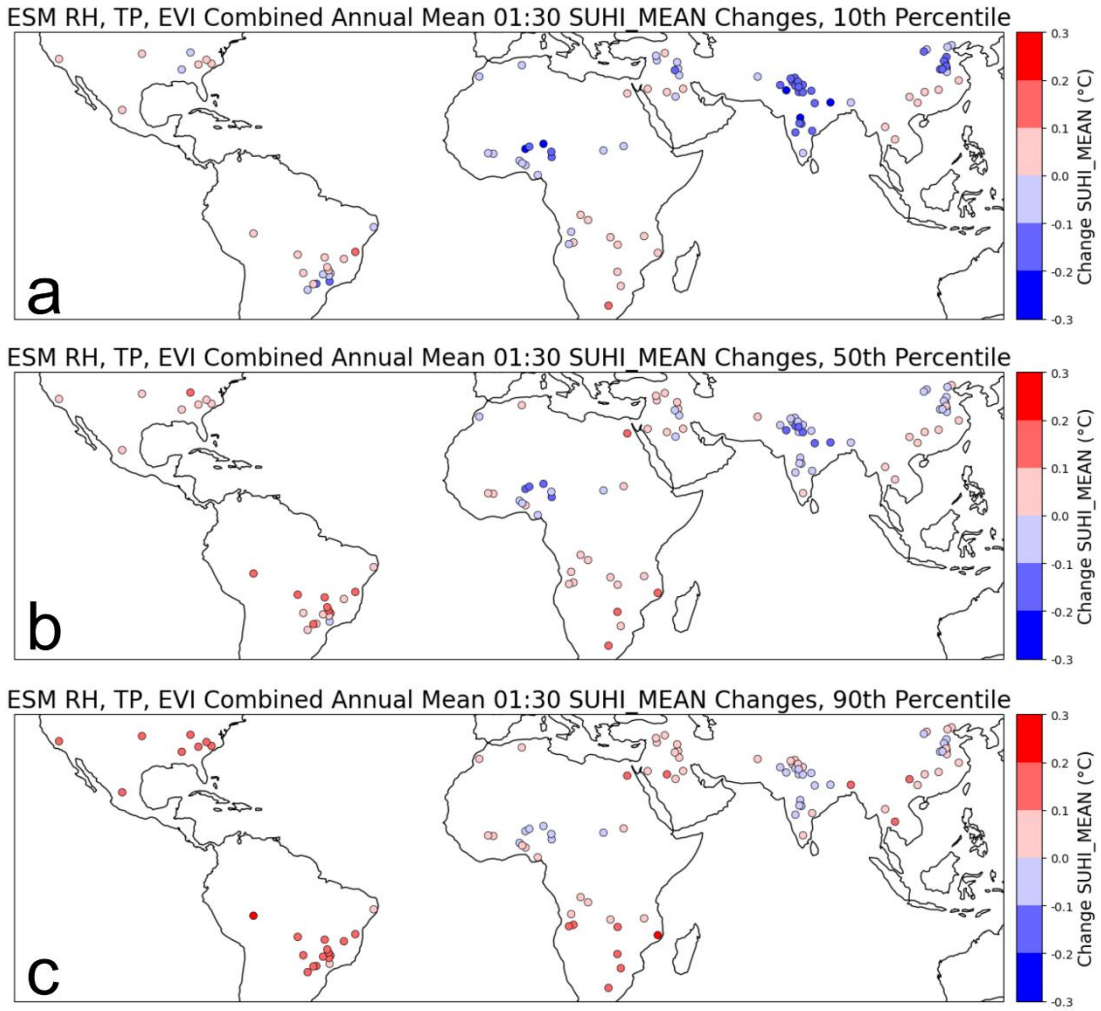

Figure 5.20 Plots showing how RERF predictions of 01:30 SUHI_MEAN change with the ESM projected changes in RH, TP and EVI (EVI_U and EVI_D). The spread of the 01:30 SUHI_MEAN projected changes is shown by a) the 10th percentile, b) the 50th percentile (median), c) the 90th percentile.

Figure 5.21 shows how changes in the 01:30 SUHI_MEAN have a small impact on its current annual mean value. Almost all the post 2 °C warming 01:30 SUHI_MEANs contain the pre-warming SUHI_MEAN within the 68% prediction interval. Two cities in Brazil, Vitória da Conquista, and Anápolis show increases and a city in India, Satna, has a decrease within the entire prediction band. None of the projected decreases in in 01:30 are large enough to make any of the SUHI_MEANs negative.

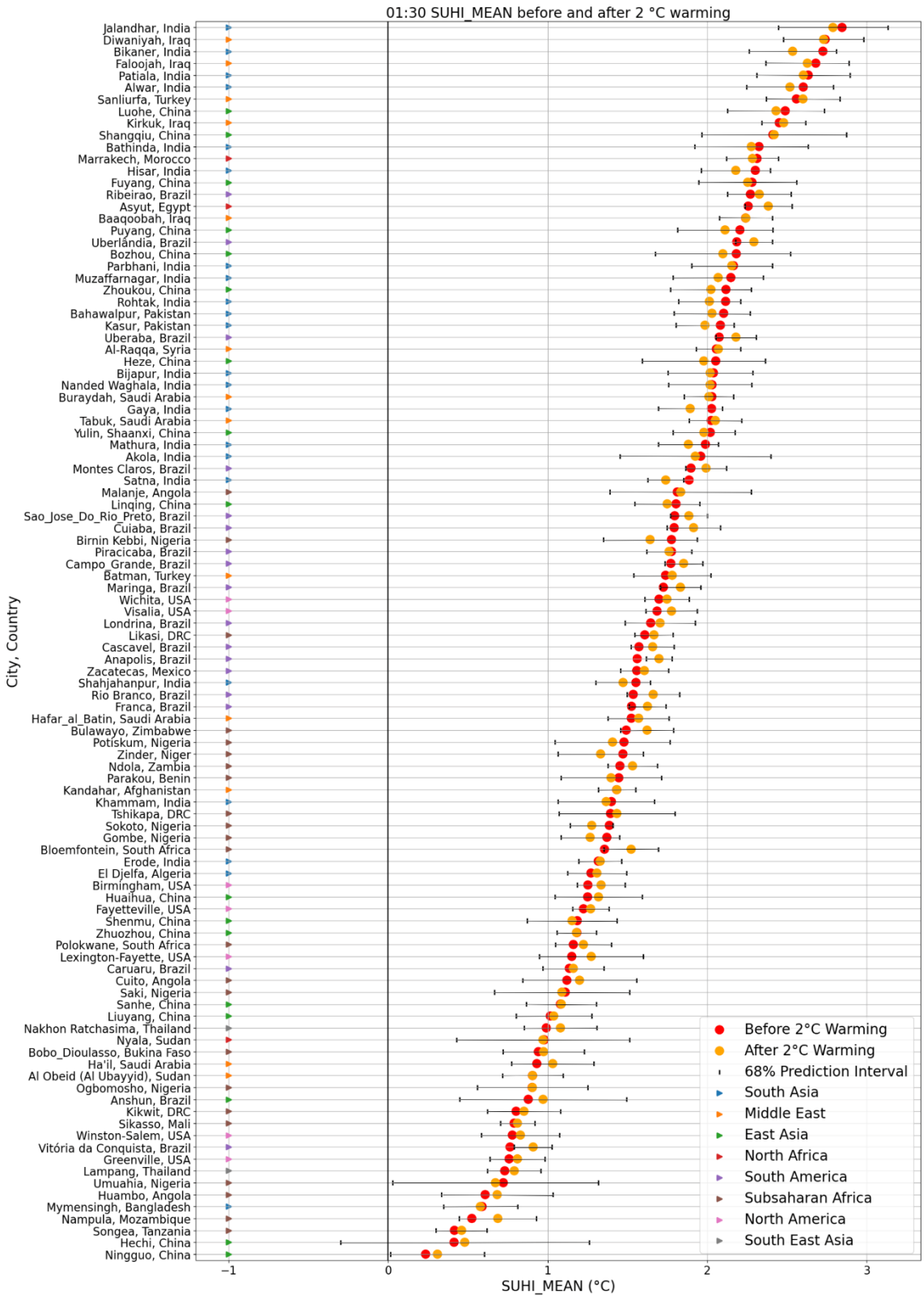

Figure 5.21 Comparison of the city annual 01:30 SUHI_MEANs current and with the RERF predicted changes. The orange dots show the median prediction for 01:30 SUHI with 2 °C warming, with a 68% prediction interval. The prediction interval was calculated for the annual values of each city individually to get city specific intervals. The red dots show the current 01:30 SUHI_MEANs. Coloured arrows on the left-hand side of the plot denote the geographical regions the city is located.

The discussion of this section so far has focused on the annual mean SUHI_MEAN, and how a 2 °C warming can lead to changes in its magnitude (Figure 5.18). As seen in Figure 4.27 (which shows seasonal means for 2m air temperature and TP), whilst some of the regions investigated have a relatively small seasonal cycle and therefore the SUHI_MEAN can be expected to be fairly consistent in magnitude and direction (positive or negative) throughout the year, some cities are located in regions with strong seasonal changes. Changes in the predictor variables could lead to small changes in one month and large changes in another, resulting in an apparent average annual change. There are stronger implications in terms of human impacts from higher SUHIs in the warmest months of the year, as the effect exacerbates warmer temperatures. Therefore, months where the 2 m air temperature is the highest are investigated. These months vary from city to city, as locations range from the north and south hemispheres. The months of monsoon also will be significant in shifts in the SUHI_MEAN, as it is highly influential on the climate and vegetations variables used in the machine learning model.

Figure 5.22a shows, when split into four seasons, when the warmest months occur for each city. In the highest north, this is during the JJA months, becoming more in the MAM months further down, and the DJF or SON months in the south. The mean 2 m air temperature and mean 13:30 SUHI_MEAN during these months are shown in Figure 5.22b and Figure 5.22c. During these warm months, where the mean air temperature across all the cities ranges from 18.8 °C to 37.8 °C, there does not appear to be any direct correlation between the warmest areas and the largest 13:30 SUHI_MEAN. Some of the hottest areas, located in the middle east, have negative 13:30 SUHI_MEANs and other similar temperatures experienced in northern India have positive 13:30 SUHI_MEANs, as other climate variables (such as TP and RH) and vegetation (EVI) are more influential.

Figure 5.22d gives the 50th percentile of the RERF projected changes, based on RH, TP and EVI ESM projections. Comparison with Figure 5.18b, which shows the annual mean 13:30 SUHI_MEAN change for the 50th percentile, shows during the warm season there are more cities with a reduction in the 13:30 SUHI_MEAN, although the number is still low at 22% of the total cities (versus 9% for the annual mean 13:30 SUHI_MEAN). This is most apparent in the east of the USA, where cities which have a projected annual increase in 13:30 SUHI_MEAN show a decrease in 13:30 SUHI_MEAN during the warmest three months. The other cities where the 13:30 SUHI_MEAN is negative in the warm season, but positive on an annual basis, mainly located in Africa, undergo small changes in the 13:30 SUHI_MEAN (less than 0.5°C). The overall range of 13:30 SUHI_MEAN changes is less than that on the annual basis, ranging from -1.7 °C to 1.7 °C. From the two aforementioned points, it can be concluded that the overall largest changes in 13:30 SUHI_MEAN occur outside of the warmest season.

Nevertheless, as the warm seasons are when the impacts of the SUHI_MEAN are felt the most, changes during this season are of significance. For cities which are relatively warm all year-round (the middle east) and where a negative daytime SUHI currently exists, the RERF and CMIP projected changes indicate this negative 13:30 SUHI_MEAN is likely to reduce in the future. This is of importance as heat in these areas is already at levels that can be uncomfortable for city inhabitants. The largest median change during the warm season is predicted for Asyut (Egypt), where the 13:30 SUHI_MEAN goes from being negative (although small at -0.04 °C) to a stronger positive 13:30 SUHI_MEAN of 1.66 °C. Some cities in China are predicted to experience strong increases in the 13:30 SUHI_MEAN, with a median change mean of 0.8 °C, although the strength of these changes vary based on the city location, with the more northern cities predicted to undergo larger changes (the median change mean rises to 0.9 °C when the four cities in China < 30 °N are excluded). Hechi, in the south, has a small projected change of 0.2 °C in the warm season, whereas the northern city Linqing is predicted to have an intensification of the 13:30 SUHI_MEAN by 1.4 °C, a 47% increase. Indian cities also are projected to have general increases in this season, with the median change overall 0.3 °C, rising to 0.4 °C if southern cities (< 21 °N) are excluded.

The same warm season changes are assessed for the 01:30 SUHI_MEAN. The current warm season 01:30 SUHI_MEAN is shown in Figure 5.23a. The strongest 01:30 SUHI_MEAN magnitudes are in some of the warmest cities studied (see Figure 5.22b), which is of concern. High temperatures at night are harmful for human heath as they do not allow the body to recover and sleep. Figure 5.23b gives the 50^{th} percentile of the RERF projected changes, based on RH, TP and EVI ESM projections. Overall, 63% of 01:30 SUHI_MEANs have an increase and 32% decrease (with 6 cities having no change at all during the warm season). As with the annual mean 01:30 SUHI_MEANs, the magnitude of changes are small in comparison to 13:30 changes. Visalia (USA) has the largest positive change at 0.1 °C and Zinder (Niger) has the largest decrease of 0.2 °C (this was also the decrease for Zinder on an annual basis). Other than Franca (Brazil), which has a decrease of 0.1 °C, all of the changes in 01:30 SUHI_MEAN are below 0.1 °C. The warm season 01:30 SUHI_MEAN has a range of 0.03 to 3.0 °C, compared to a range of -3.5 to 7.3 °C for the warm season 13:30 SUHI_MEAN. Therefore, to understand changes in this context, percentage increases in the 01:30 SUHI_MEAN are examined. For the majority of 01:30 SUHI_MEANs (64%), any change comes to less than 1% of the current 01:30 SUHI_MEAN. Cities with the larger proportional changes in warm season 01:30 SUHI_MEAN typically experience this due to having low current SUHI_MEANs, aside from Zinger (Niger), which has an 11% decrease.

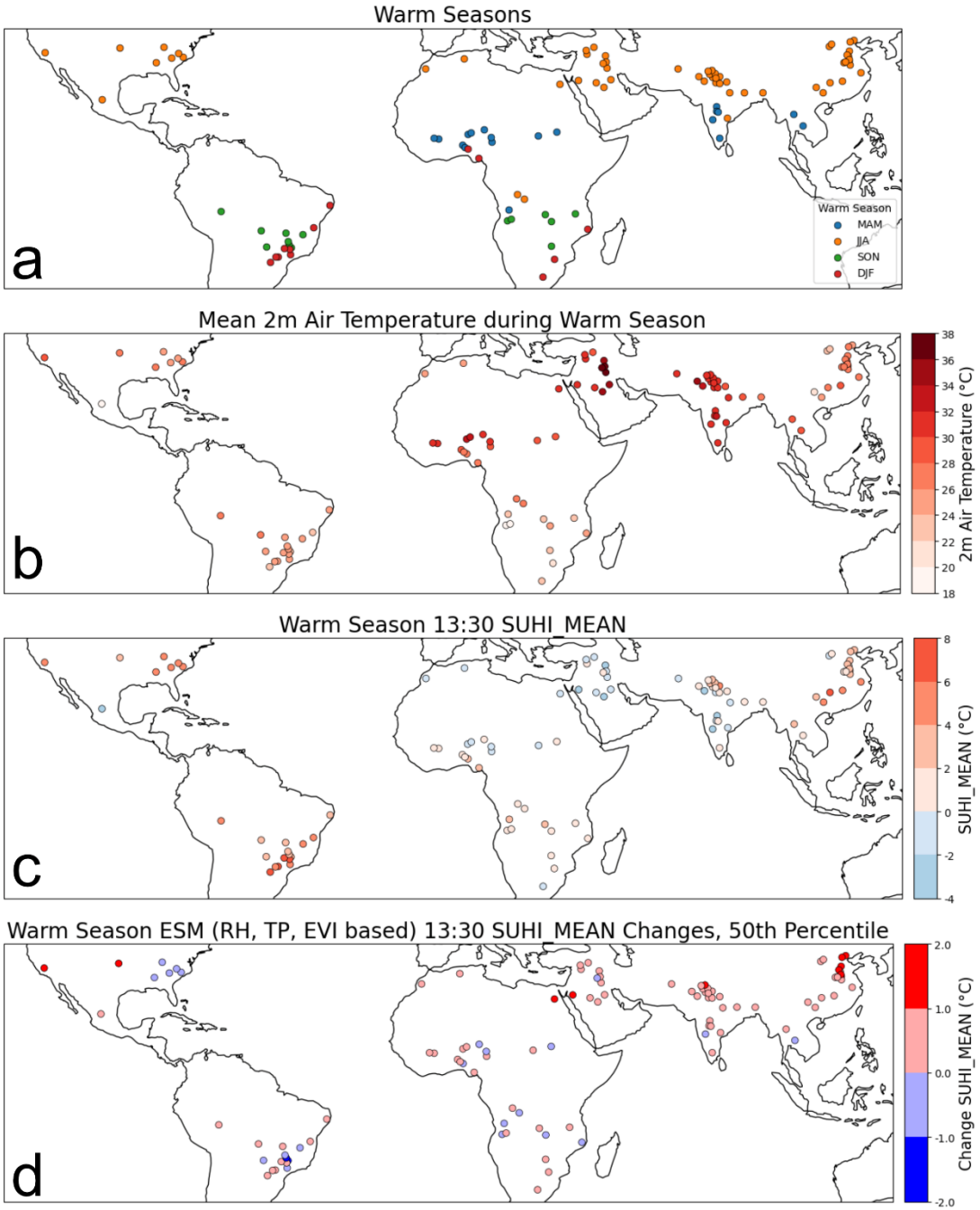

Figure 5.22 An assessment of 13:30 SUHI_MEAN during the warmest months. In a) the time of year which the warmest mean temperature occurs is shown, grouped into MAM (March, April, May), JJA (June, July, August), SON (September, October, November) and DJF (December, January, February). b) shows the mean 2m air temperature during the 3-month period denoted in a), where the mean 2 m air temperature is the highest. c) shows the mean 13:30 SUHI_MEAN during the 3-month period shown in a). this was calculated using observations. d) shows the 50th percentile change in the 13:30 SUHI_MEAN projected under 2 °C global mean warming, calculated using the RERF model and CMIP ESM model projections for EVI, RH and TP.

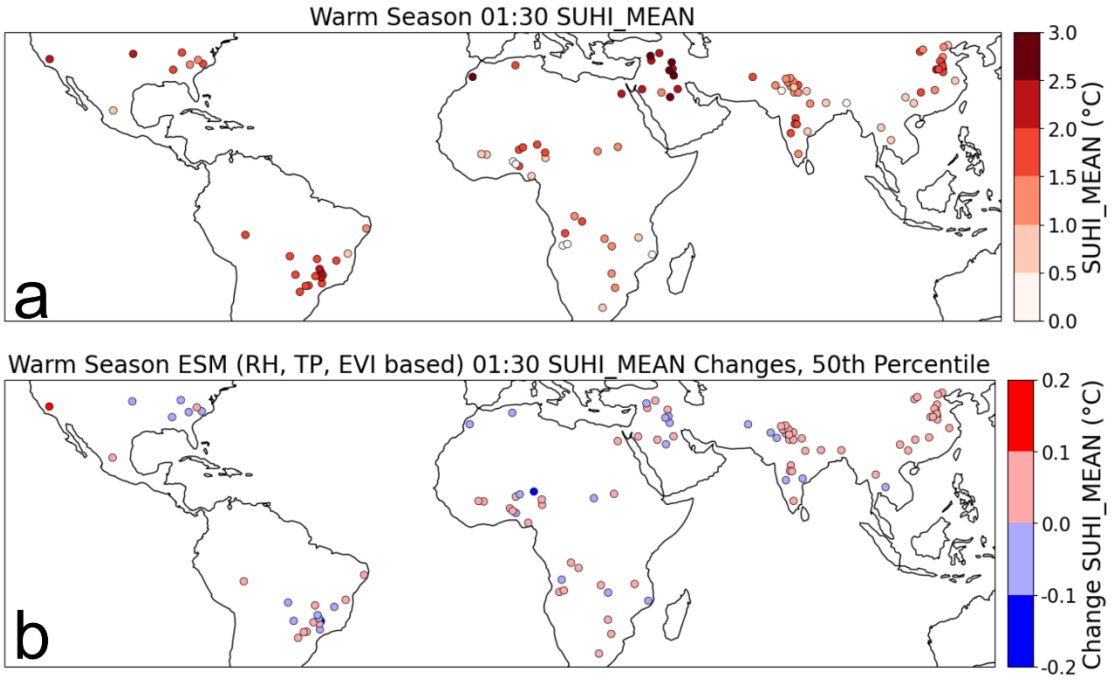

Figure 5.23 An assessment of 01:30 SUHI_MEAN during the warmest months. a) shows the mean 01:30 SUHI_MEAN during the 3-month period shown in a). this was calculated using observations. b) shows the 50th percentile change in the 01:30 SUHI_MEAN projected under 2 °C global mean warming, calculated using the RERF model and CMIP ESM model projections for EVI, RH and TP.

6 DISCUSSION AND CONCLUSIONS

6.1 DISCUSSION

The method developed has led to estimates of how the SUHI_MEAN magnitude in certain cities is likely to change with future changes in climate. Through the model fitting, it has been demonstrated how climate and vegetation variables, projected to change in the future, influence the SUHI_MEAN. Based on the ALE plots (Figure 4.36) most influential variable on the 13:30 SUHI_MEAN is the EVI_D, which shows a small difference between rural and urban vegetation leads to a small 13:30 SUHI_MEAN and when urban vegetation is greater than rural, a negative 13:30 SUHI_MEAN exists.

The ML models are combined with CMIP climate projections to determine how the annual 13:30 SUHI_MEAN may change in the future. With future changes in EVI, RH and TP, the results point to overall increases in the annual 13:30 SUHI_MEAN for 81% of cities (in cases where the 13:30 SUHI_MEAN is negative, it will become less negative).

This increase in 13:30 SUHI_MEAN has significance for climate change projections, as estimates of the future temperatures at a regional scale can be expected to be warmer in urbanised areas. This is minus the influence of urban expansion, which can have an additional increasing impact on the 13:30 SUHI_MEAN, although this is climate specific (negative 13:30 SUHI_MEANs become more negative, section 5.1). The results of this thesis show that additional to the projected regional increases in temperature due to climate change, most urbanised areas can expect a larger increase than their rural counterparts in the median (the annual median changes of all cities averages to 0.4 °C). This expected median annual change is as large as 1.9 °C (±0.2 °C for a 68% prediction interval) in Asyut, Egypt, where the 13:30 SUHI_MEAN goes from negative to positive (Figure 5.19), and over 1 °C for 14% of cities, which are mostly located in China and India. Interestingly, although this research set out with a focus on the southern hemisphere, the cities with positive latitudes are found to be those with some of the largest 13:30 SUHI_MEAN changes.

The cities that feature in this research are in the warmer parts of the world, which makes this increase even more significant. In India and China, the 13:30 SUHI_MEAN is increasing in the warmest months if the year (Figure 5.22), intensifying the impacts of rising temperatures for urban inhabitants in these areas. In India, heatwaves are projected to increase in frequency, duration and intensity (Murari *et al.*, 2015; Rohini *et al.*, 2019), and an increase in humid heatwaves (where high temperatures are combined with high humidity) is seen in the areas of eastern China where the 13:30 SUHI_MEAN increases the most, alongside India and Pakistan

(Domeisen *et al.*, 2023). The need for UHI mitigation in these regions is therefore all the more pressing.

The RERF was also used to examine the SUHI_MEAN during the night, for which the most influential variable was RH. When RH is low, the 01:30 SUHI_MEAN is larger. This is most likely due to the presence of more monthly cloud cover when RH is high, which dampens rural radiative cooling at night. Future changes in RH contribute to projected changes in the 01:30 SUHI_MEAN. At 01:30, in comparison to at 13:30, the SUHI_MEAN has a smaller variance (city annual values range from 0.3 °C to 2.8 °C as opposed to -4 °C to 5.4 °C for 13:30, also see Figure 4.21) for the predictor variables to capture. This leads to the 01:30 SUHI_MEAN having smaller absolute changes as a result of changes in input variables. However, small changes may still be important for city inhabitants in very hot parts of the world. Of note is that the 01:30 SUHI_MEAN changes can be positive when the 13:30 SUHI_MEAN changes are negative (for example, in Brazil, see Figure 5.20). It is important to be aware of this potential difference in future trajectories of SUHI magnitudes, to ensure the best adaption practices are made. Nighttime temperatures are important for human comfort. Prolonged high temperatures at night stop indoor spaces from cooling, cause lack of sleep and prevent the body from recovering after the heat of the day (Heaviside *et al.*, 2017).

The ML model used is based on variables with known physical relationships with the SUHI, and therefore through interpretation of how these variables interact with the SUHI_MEAN, conclusions relating to SUHI mitigation can be made.

The implications of these results are twofold. The first of these is that focus needs to be paid to SUHI mitigation (although the CUHI shall be the true target), as it can be expected to increase in the future, and the regions examined in this thesis should not be neglected. Due to climate change, there is expected to an increase in heat related mortality, with those living in the warmer parts of the world most at risk (Gasparrini *et al.*, 2017). LST and air temperature are closely correlated, and a larger SUHI leads to an increase in the CUHI (section 2.3.1). These rising urban temperatures are harmful to city workers and inhabitants. The most direct impact of the CUHI is relating to outdoor workers, such as those in construction (who additionally will be working with materials directly impacted by surface temperatures) or street venders, who are more vulnerable to the hazards of extreme heat. Outdoor workers face the negative impacts of heat exposure, such as heat stress, fatigue, dehydration, cardiovascular disease (when dehydrated, the heart has to work harder to pump blood round the body) and respiratory disease (as increased heat can lead to an increase in ground level pollution) (Moda *et al.*, 2019).

This is relevant to the cities in this thesis, as street venders are common in many of the regions. In India, seen in Figure 5.18 to experience daytime SUHI increases in most of the selected (medium sized) cities (even in the 10th percentile), countrywide there are 10 million street vendors and around 2.5% of the urban population is employed as such. There are also no employer regulations that protect these workers (as they are self-employed) and missing a day's work means they forgo a day's income. Many informal workers are women (Herrera *et al.*, 2012), and if pregnant face additional risks of poor pregnancy health and birth defects (Moda *et al.*, 2019). Additional to the economic need for the street vendors themselves, these street vendors are an important part of urban food networks. In sub–Saharan Africa (in Figure 5.18b, 24 out of 25 sub–Saharan 13:30 SUHI_MEANs increase in the median), these food sources are essential for the majority of households, with 70% regularly sourcing food from street vendors due to the spatial and financial accessibility (as they can offer credit) (Giroux *et al.*, 2021).

The impacts of heat are also felt by those inside city buildings. Studies show heat related mortality increases more in urban areas than in rural counterparts during heatwave events (Kovats and Hajat, 2008), and the existence of the CUHI during the night allows inhabitants little recovery from heat exposure during daytime hours. Based on CMIP model projections, Sherman et al (2022) calculate changes in simplified wet bulb temperatures (a unitless measure taking into account temperature and humidity). A simplified wet bulb temperature above 30 is determined to be outside the realm of human adaptability, and areas of the globe can be expected to go beyond this level are in critical need of air conditioning (AC) or alternative cooling systems. The authors find some of the largest increases in simplified wet bulb temperature are in Sub-Saharan Africa and the Middle East, both regions where the cities in this analysis see increase in 13:30 SUHI_MEAN, and it is highlighted that these areas already have simplified wet bulb temperatures that should require AC. India, where cities are also shown to have increasing 13:30 SUHI_MEANs, is projected to require large cooling demands in the future. This is problematic as the infrastructure may not be able to cope with this increased load, and the costs are prohibitive for many (Sherman *et al.*, 2022).

Although necessary, the solution of AC is not ideal as it heats the outside environment more by dispelling the hot air inside to outside the buildings, impacting on those in the urban outdoors or without access to AC. Additionally, growth in electricity demand can also lead to increased use of fossil fuels to meet this need, thereby contributing further to root cause of climate change. In addition to the health and emissions related impacts of rising temperatures, there is also an economic cost. Economic growth and heat are tied together, with hotter countries tending to be poorer. For countries in hot climates, hotter than average years are associated with lower per capita income (for cold climates, colder than average years result in

lower per capita income). This phenomenon is reduced by the use of AC, implying at least some of the reduction in income is due to human physiological impacts (other influential factors can be agricultural impacts, for example) (Heal and Park, 2013).

A key highlight of the warm season assessment (Figure 5.22) was that the Chinese cities, which do not have the overall highest 2m air temperatures, experience larger changes in the 13:30 SUHI_MEAN during the warmest months. During these months, which are when the SUHI is the most hazardous to city inhabitants, the 13:30 SUHI_MEAN is projected to increase by over 1 °C for 35% of the selected cities in China (and 65% increase by 0.5 °C).

RCM studies examining the impact of climate change scenarios on the UHI are limited in the cities examined (Table A.1.4) and do not include Chinese cities at present. Land use and population changes have been considered (Zhu *et al.*, 2021; Lan *et al.*, 2023), but the interaction of the UHI with climate and extent as to which the magnitude of the UHI is influenced by climate change is not currently assessed. This result signifies the current research could be underestimating the impact of climate change on the UHI in China, particularly in the north half of the country.

For the aforementioned reasons, mitigation of the SUHI (with the target of CUHI) and cooling cities should be a priority, as cities are faced with rising global temperatures and increasing frequency of extreme heat events. The regions in this thesis should also be a priority, as many of these are disproportionally affected by the heat related impacts of climate change (Mora *et al.*, 2017). This ties into the second aspect of the results, which is relating them directly to mitigation measures, to determine which methods could be the most effective for SUHI mitigation. The predictor variables used in the model offer exploration of two mitigation strategies, either creating green space (and therefore modifying EVI) or using white roofs or pavements to modify WSA. An important note is that these recommendations of mitigation measures are made using the SUHI, and examination in terms of the CUHI is essential to confirm it exists for this measure also, which is the true target for mitigation.

During the daytime, the most important influential variable on the SUHI_MEAN is the EVI_D variable (note the difference is urban - rural). This variable indicates that increasing EVI_U or decreasing EVI_R will lead to a smaller 13:30 SUHI_MEAN. As decreasing EVI_R results in a reduction in 13:30 SUHI_MEAN caused by rural warming rather than any change in urban LST, this is not a viable option for mitigation. It does indicate, however, that urbanisation in densely forested areas should be done with care, as these urban areas will have large SUHI magnitudes. It is well known that increasing urban vegetation (EVI_U), is an effective mitigation strategy for tackling the CUHI (Shao and Kim, 2022), and the results of this thesis are in line with other studies. Urban tree cover also offers shade for city dweller to take respite

from the heat and green spaces are known to improve mental health (Bratman *et al.*, 2019). In comparison to the impact of the EVI predictor variables, the WSA predictors have little influence on the 13:30 SUHI_MEAN, indicating solar radiation modification measures such as white roofs are not as effective as urban greening if the motivation is to reduce the SUHI during the day.

In a study of different mitigation measures across cities in the United States, Georgescu et al (2014) finds the most effective mitigation measure is dependent on geographical location. Findings here show there could also be a day versus night dependency. The night-time is when the CUHI is at its greatest (the SUHI is greatest during the day), so this finding is of significance where reducing nocturnal temperatures in cities is a concern. For the 01:30 SUHI_MEAN, the results of this thesis show there is a lagged effect of albedo, as WSA_U and WSA_D have decreasing effect on 01:30 SUHI_MEAN. This is in agreement with the findings of Peng et al (2012), where a negative correlation between albedo difference and night-time SUHI intensity was also found. Less solar radiation absorption by the city materials during the day results in less heat storage to radiatively cool during the night. In regions where night-time temperatures are a concern, white roofs should be recommended as mitigation measures.

A feature of the SUHI/CUHI is that it is not constant throughout the urban area; certain areas of the city are hotspots, and others cooler (e.g., parks) outlined in section 2.5. It is important to note that although the SUHI_MEAN was used as the quantification method in this thesis, alternative methods are explored. The SUHI_MEAN is more related to the vegetation properties (EVI), whereas the SUHI_PEAK_GSA (a SUHI quantification measure of the central hotspot of the SUHI, appendix A.4) is more a product of city related properties, which were not captured as well as the climate related factors in this thesis. This implies in future, the warmer parts of cities could be more influenced by city related properties, such as population density (Schwarz *et al.*, 2011), and the city in its entirety more influenced by factors such as vegetation differences. This may be related to the uneven distribution of vegetation within the city, where the city centre is likely the most densely build up area of the city, with little green space. Therefore, the cooling in this area of the city will be less than throughout the city overall, and rather than considering just the amount of green space overall, the placement of greenspace is significant for homogenous city cooling. Urban heat exposure throughout cities is unequal, with neighbourhoods with lower average incomes corresponding to higher SUHI intensities (Chakraborty *et al.*, 2019), and mitigation measures should also take this into account.

A final implication of the results of this thesis is the demonstrated ability of machine learning (ML) techniques for predicting SUHIs and their potential changes. The current main use of ML in UHI studies is aiming to predict the air temperature from LSTs, but here the results show that there is a wider range of applications for ML in SUHI studies, and the techniques used in this thesis can be applied to a wider range of cities, or cities in different locations. The use of cities in various climatic regions has allowed change in climate and vegetation that take variables outside of the regions current range to be examined, as this reduced the extrapolation. The identification and selection of a ML model which performs well in extrapolation circumstances has given confidence in the future projections.

The advantage of this statistical based model over RCM simulations is in the speed at which it can be run, allowing for the examination and comparison of a large number of cities (104 in this thesis), and that it can be trained directly on observations. RCMs can contain biases, inherited from GCMs (as GCMs are used to specify boundary conditions, section 2.3.2) (Kim *et al.*, 2021). GCM and ESM biases are corrected for in this methodology by looking at changes in the climate variables rather than the absolute projected values (the delta method, section 5). In this thesis, the selection criteria removed many cities, and relaxing these criteria with the addition of predictor variables to account for this (for example, distance to nearest water body, and its size) can make the model more general (section 6.3).

A limitation of the analyses in this thesis with regards to human health and comfort in cities is that the results are based on LST measurements. Air temperature would be a better variable to relate to these impacts, as it is what is felt by the city inhabitants. The relationships between SUHI and CUHI are by no means straightforward (see section 2.3.1), so it is difficult to directly relate the two, or quantify exactly what an increase of 1 °C, for example, of the SUHI means for the CUHI. Deriving urban air temperature measurements from LST is currently an active area of research (section 2.3.1) and with further developments in this area, the results of this thesis will become still more informative in the context of this understanding.

A further limitation, concerning the future projections of SUHI_MEAN, is that the changes in urban area are not considered (the LOG_AREA variable remains constant). Huang et al (2019) estimate the urban area of global cities will increase by 78%–171% compared to that in 2015 by 2050. In section 5.1 it was seen that increasing city area, based on continuation of the past 10-year trend of urban expansion continuing into the next 10 years, can result in considerable changes in the SUHI_MEAN (Figure 5.4). The dataset created by Huang et al (2019) is freely available, and the potential of inclusion of this is discussed in section 6.3.

Assumptions made in this thesis are that there are not city management schemes relating to vegetation or policies to increase urban greenspace. This could result in the EVI_U following

a different trend to EVI_R, as it was assumed the EVI_U would increase or decrease proportional to EVI_R. City expansion could also result in loss of urban green space, depending on city regulations for protecting city parks or on where new development may take place. Liu et al (2022) examine trends of urban EVI, and find that in South America and Africa there are trends of decreasing urban vegetation, indicating it is EVI_U changes have some regional dependence and a more sophisticated estimate for future EVI_U, perhaps additionally including the current trend in annual EVI_U could be included. Another limitation, with regards to SUHI mitigation recommendations, is that the influence of water bodies is not considered, as the resolution of the landcover data is not high enough to capture rivers or small lakes (the selection criteria removed larger lakes with a width of greater than 1 km) within the city and rural areas. It is common for cities, particularly in hotter climates, to be built on the banks of rivers. As these are not included as predictor variables in the ML model, it is not possible to assess the mitigation impact of water in the same way it has been done for green spaces, for example.

6.2 CONCLUSIONS

The aim of this thesis was to examine present and future SUHIs by means of satellite data, a ML model and CMIP6 climate projections. The first objective completed was to quantify the SUHI of medium sized cities in understudied geographical regions. This was done by development of a city selection process (section 4.1) to create a pool of cities for the basis of the thesis. Satellite data was then used to quantify the SUHI of these cities (section 4.2) to meet the remainder of objective 1.

The second objective was to examine the relationship between the quantified SUHIs and background climate, using the results to build a predictive model. To do this, influential predictor variables relating to background climate were quantified (section 4.2) and employed in a ML model able to predict the magnitude of the SUHI in the selected cities. Through selecting the best performing ML model, the most influential background climate variables (from those investigated, section 4.3) are identified. The ML model was then used to explore current relationships between predictor variables such as vegetation, precipitation, relative humidity and city area, and SUHI intensity (sections 4.4 and 4.5).

Objective 3 was to use the constructed ML model to assess the importance of background climate as a predictor of the SUHI and assess sensitivity to changes in predictor variables. Through assessment of the performance of this ML model (sections 4.4 and 4.5) and sensitivity tests (section 5.1), this objective was satisfied.

Finally, the last objective (4) was met by combining the ML model with CMIP6 climate change projections. This allowed an assessment of the future SUHIs, based on climate changes only.

The current use case for the statistics-based models in examining the SUHI for the purpose of inference, exploring the relationships between influencing factors and the SUHI, or for the prediction of urban air temperatures. The work in this thesis is novel in two ways.

The first is it utilises the constructed ML model for prediction, using it to examine how the future SUHI is likely to change based on changes in influencing variables. The second is, with use of scenario-based climate change projections, the ML model enables the examination of a large number of medium sized cities, benefiting from both high resolution and low computational expense. With the GCM and RCM based approaches, there is currently a trade-off between these two features (section 2.3.2), meaning the current focus is on a few individual cities. Thereby, the research gap of medium sized cities can be addressed, as the resolution is that of the satellite data (1 km). The satellite data used also has global coverage, allowing for a second research gap to be addressed; that of understudied regions of the world, for which a focus is on cities in the global south. Many of the cities examined in this thesis are highly vulnerable to the impacts of rising temperatures due to climate change.

The SUHI of a city can be predicted based on its background climate, and this thesis has demonstrated a physics-based ML model is able to do so. The ML model used has been shown to be appropriate for the use of predicting future SUHI_MEANs based on its ability to extrapolate. This model allows for assessment of a large number of future SUHIs, so certain areas can be highlighted as those most likely to have increases in SUHI magnitude due to changes in climate. Overall, the majority (81%) of selected cities show an increase in annual SUHI_MEAN in the 50^{th} percentile.

When examining the future climate in medium sized Chinese cities (particularly those in the eastern north/ central area) the magnitude of the SUHI (and therefore likely CUHI) should not be assumed constant. The results show the SUHI_MEAN in this area will increase annually and during the warm season when the repercussions of the SUHI with regards to human health and comfort are the greatest. Northern India is also highlighted as a key area where the climate change intensifies the annual SUHI_MEAN. Cities in arid areas, here mainly the middle east, can be expected to have less negative or even positive SUHI_MEANs in the future. In contrast, based on the CMIP models, it is uncertain whether cities in Brazil will undergo decreases or increases in the SUHI_MEAN.

Liu et al (2022) examine surface warming trends in global cities from 2002 to 2021 and find the warming trend in cities is greater than that in the rural areas, meaning the current behaviour

of SUHI magnitudes is of warming. The results of this thesis show these trends can be expected to continue with a continuation of changes in climate. The model assessment via ALE plots revealed the behaviour of the SUHI in the selected medium sized cities is in agreement with the current literature. The strong influence of EVI confirms the current theories on urban greening being an important mitigation measure (Shao and Kim, 2022), and that the daytime SUHI is largely driven by urban rural vegetation differences (Paschalis *et al.*, 2021). An additional finding to add to this is the day – night distinction of the best mitigation measures. During the day, it is clear attention should be given to urban greening, whereas for the night-time SUHI, urban greening combined with white roofs could be a more impactful strategy.

Due to the issues surrounding cloud contamination when using satellite data, the results of this thesis can only be applied to relatively cloud free days (section 3.2). Therefore, it is likely there is some overestimation in the mean values, as they do not include overcast days, where the UHI tends to be smaller. The use of reanalysis data means the model errors associated with the precipitation and solar radiation (section 3.2) within this source have been passed on.

A chief limitation of this thesis, highlighted in the discussion is that air temperature, and therefore the CUHI, is more important for human health applications. This should be considered when using the results for purposes such as CUHI mitigation measures.

Additionally, the influence of windspeed has been overlooked. In section 2.4.1 it was seen the UHI is largest during clear and calm days, with high windspeeds cooling the urban surface. As atmospheric stability increases, so does UHI magnitude (Tomlinson *et al.*, 2012). This means future changes in windspeed will have an impact on the SUHI_MEAN, and this has not been accounted for in the results of this thesis. GCMs project global decreases in near surface windspeed with climate change (Shen *et al.*, 2022), implying the projected SUHI changes in this thesis may have been underestimated.

In section 2.5.3, it was seen that climate model simulations show that the CUHI causes the number of urban heatwave events to increase in comparison to the rural surroundings, as UHIs push the city temperatures to above the threshold for heatwaves. When planning for the impacts of climate change in medium sized cities, it is likely the SUHI will not remain constant, and this must be considered. The future UHI magnitude is likely change with climate change, and urban adaptation measures must consider the impact of climate change alongside city expansion to protect a rapidly growing population of urban inhabitants.

6.3 FUTURE WORK

There are a few different avenues that could be explored to add additional value to the work done in this thesis. Some of these simply require more analysis based on the work currently done, whereas others will invite the use of additional data sources and processing. Starting with the most straightforward, this section outlines a few ideas for which the work in this thesis can be expanded.

The developed RERF model could be used with climate and vegetation projections from alternative SSPs, as in this these only one was examined, SSP3-7.0. Vegetation is highly influential for the SUHI_MEAN projections, and the SSPs factor in change in land use (O'Neill *et al.*, 2017). Different futures may result in varying levels of vegetation changes. Therefore, examining different pathways could give a wider range of the possible future SUHI_MEANs.

The issue of urban expansion could be addressed in the projections of future SUHI_MEANs by adding in projections for future urban expansion. In Huang *et al* (2019), the authors project future global urban expansion based on the SSPs, and have made the data freely available. This data is, however, looking at urban expansion by 2050 rather than with a 2 °C warming, as the CMIP data used in this thesis. Therefore, further investigation on this front is required.

Another aspect relating to climate projections, is to look at the impact of replacing EVI in the models with LAI, so they can be more directly linked to climate model outputs, without the conversion to EVI through the linear relationship. However, generating LAI satellite measurements can be complex (Zheng and Moskal, 2009).

Further future work could be to go back to the first step of the model creation, where the cities are selected (section 4.1) and relax the selection criteria. The criteria could then be included in the model as a predictor variable. One such criteria could be that of cities which have a waterbody greater than 1 km wide in the area. In the city selection process, 252 cities were excluded due to this criterion (Table 4.1), and therefore relaxing it, and including this as a potential predictor variable would increase the number of cities in the dataset. Another criterion would be to extend the population criteria. In section 4.2, it was noted that some cities can have a large suburban sprawl outside of the administrative boundaries, and cities with similar populations can have widely different areas depending on where in the world they are. This could be due to the city administrative area being smaller than the city area including its suburbs, or down to differences in city population density. As the REFR model has performed well for this range of city areas, there is an indication it is able to handle a larger range of city sizes, as having the LOG_AREA variable in the model takes city size into account. Other factors which cities were discounted based on was for the coastal influence, being near large

lakes, or in mountainous areas/ in a valley. By including these cities in the dataset with the selection criteria factored into the predictor variables instead, there is potential to quantify the influence of a large lake or the sea, for example, on the SUHI. Something of note regard the coastal aspect, however, was that the model did not perform as well for the city on the borderline of meeting the coastal criteria (Umuahia, Nigeria). It may be more appropriate to create a separate model for the coastal cities.

The RERF model itself also would benefit from being revisited and windspeed added as a predictor variable. This could improve the performance of the RERF and create more informed future projections of the SUHI with the impact of atmospheric stability included.

A final piece of future work, and the largest undertaking, would be to address one of the major issues with the use of LST for UHI studies, and investigate ways of examining and relating the CUHI to the results of the SUHI results. As there is a severe lack of suitable weather stations in the regions examined to obtain air temperature measures in both the rural and urban areas, and it is unfeasible to create a sensor network, there are highly limited options for how this could be done. A potential option is to use satellite remotely sensed atmospheric profiles to derive air temperature by vertically interpolating to surface pressure level, which has been shown to have good agreement with in situ measurements (Famiglietti *et al.*, 2018). This approach is relatively uncommon, but has been used in a couple of UHI studies (Hu and Brunsell, 2015; F. Huang *et al.*, 2020). The data is taken from MODIS sensor on the Aqua and Terra satellites, and as the Aqua MODIS sensor is used to derive the LST used in this thesis, direct comparison at the same times can be made. However, horizontal resolution of the atmospheric profiles is 5 km, so at a coarser scale than the LST data which has a resolution of 1 km. This approach is still in the early stages of being adopted, so validation would need to be done, and therefore cities with a sensor network would need to be examined at first to prove the approach is reliable.

7 REFERENCES

Abbs, D. J. and Physick, W. L. (1992) 'Sea-breeze observations and modelling: a review', *Aust. Met. Mag.*, (l).

Acero, J. A. *et al.* (2013) 'Urban heat island in a coastal urban area in northern Spain', *Theoretical and Applied Climatology*, 113(1–2), pp. 137–154. doi: 10.1007/s00704-012-0774-z.

Ackerman, B. (1985) 'Temporal march of the Chicago heat island', *Journal of climate and applied meteorology*, 24(6), pp. 547–554. doi: 10.1175/1520-0450(1985)0242.0.CO;2.

Addae, B. and Dragićević, S. (2023) 'Modelling Global Deforestation Using Spherical Geographic Automata Approach', *ISPRS International Journal of Geo-Information*, 12(8). doi: 10.3390/ijgi12080306.

Alavipanah, S. K. *et al.* (2010) 'Criteria of selecting satellite data for studying land resources', *Desert*, 15(2), pp. 83–102. doi: 10.22059/jdesert.2011.23005.

Alcoforado, M. J. and Andrade, H. (2006) 'Nocturnal urban heat island in Lisbon (Portugal): Main features and modelling attempts', *Theoretical and Applied Climatology*, 84(1–3), pp. 151–159. doi: 10.1007/s00704-005-0152-1.

Alexandridis, T. K., Ovakoglou, G. and Clevers, J. G. P. W. (2020) 'Relationship between MODIS EVI and LAI across time and space', *Geocarto International*, 35(13), pp. 1385–1399. doi: 10.1080/10106049.2019.1573928.

Allaga-Zsebeházi, G. (2021) 'Future temperature and urban heat island changes in Budapest: a comparative study based on the HMS-ALADIN and SURFEX models', *Idojaras: Quarterly Journal of the Hungarian Meteorological Service*, 125(4), pp. 675–692. doi: 10.28974/IDOJARAS.2021.4.7.

Allegrini, J. and Carmeliet, J. (2018) 'Simulations of local heat islands in Zürich with coupled CFD and building energy models', *Urban Climate*, 24, pp. 340–359. doi: 10.1016/J.UCLIM.2017.02.003.

Allen, L., Lindberg, F. and Grimmond, C. S. B. (2011) 'Global to city scale urban anthropogenic heat flux: Model and variability', *International Journal of Climatology*, 31(13), pp. 1990–2005. doi: 10.1002/joc.2210.

Alonso, M., Fidalgo, M. and Labajo, J. (2007) 'The urban heat island in Salamanca (Spain) and its relationship to meteorological parameters', *Climate Research*, 34, pp. 39–46. doi: 10.3354/cr034039.

Amani-Beni, M. *et al.* (2022) 'Quantitative-spatial relationships between air and surface temperature, a proxy for microclimate studies in fine-scale intra-urban areas?', *Sustainable Cities and Society*, 77(July 2021), p. 103584. doi: 10.1016/j.scs.2021.103584.

Amorim, M. C. de C. T. (2020) 'Daily evolution of urban heat islands in a Brazilian tropical continental climate during dry and rainy periods', *Urban Climate*, 34, p. 100715. doi: 10.1016/J.UCLIM.2020.100715.

Amorim, M. C. de C. T., Dubreuil, V. and Amorim, A. T. (2021) 'Day and night surface and atmospheric heat islands in a continental and temperate tropical environment', *Urban Climate*, 38(July), p. 100918. doi: 10.1016/j.uclim.2021.100918.

Andrade, C., Fonseca, A. and Santos, J. A. (2023) 'Climate Change Trends for the Urban Heat Island Intensities in Two Major Portuguese Cities', *Sustainability (Switzerland)*, 15(5).

doi: 10.3390/su15053970.

Angel, S. *et al.* (2016) *Atlas of Urban Expansion- 2016 Edition, Volume 1*.

Anniballe, R. and Bonafoni, S. (2015) 'A Stable Gaussian Fitting Procedure for the Parameterization of Remote Sensed Thermal Images', *Algorithms*, 8(2), pp. 82–91. doi: 10.3390/a8020082.

Anniballe, R., Bonafoni, S. and Pichierri, M. (2014) 'Spatial and temporal trends of the surface and air heat island over Milan using MODIS data', *Remote Sensing of Environment*, 150, pp. 163–171. doi: 10.1016/j.rse.2014.05.005.

Apley, D. W. and Zhu, J. (2016) 'Visualizing the Effects of Predictor Variables in Black Box Supervised Learning Models'. Available at: http://arxiv.org/abs/1612.08468.

Argüeso, D. *et al.* (2014) 'Temperature response to future urbanization and climate change', *Climate Dynamics*, 42(7–8), pp. 2183–2199. doi: 10.1007/s00382-013-1789-6.

Arnfield, A. J. (2003) 'Two decades of urban climate research: A review of turbulence, exchanges of energy and water, and the urban heat island', *International Journal of Climatology*, 23(1), pp. 1–26. doi: 10.1002/joc.859.

Azevedo, J. A., Chapman, L. and Muller, C. L. (2016) 'Quantifying the daytime and night-time urban heat Island in Birmingham, UK: A comparison of satellite derived land surface temperature and high resolution air temperature observations', *Remote Sensing*, 8(2), p. 153. doi: 10.3390/rs8020153.

Bai, X. (2018) 'Six research priorities for cities and climate change', *Nature*, 555(1 March), pp. 23–25.

Barlag, A. B. and Kuttler, W. (1990) 'The significance of country breezes for urban planning', *Energy and Buildings*, 15(3–4), pp. 291–297. doi: 10.1016/0378-7788(90)90001-Y.

Barlow, J. F. (2014) 'Progress in observing and modelling the urban boundary layer', *Urban Climate*, 10(P2), pp. 216–240. doi: 10.1016/j.uclim.2014.03.011.

Bassett, R. *et al.* (2021) 'Climate driven trends in London's urban heat island intensity reconstructed over 70 years using a generalized additive model', *Urban Climate*, 40, p. 100990. doi: 10.1016/J.UCLIM.2021.100990.

Bechtel, B. (2015) 'A new global climatology of annual land surface temperature', *Remote Sensing*, 7(3), pp. 2850–2870. doi: 10.3390/rs70302850.

Beck, H. E. *et al.* (2018) 'Present and future köppen-geiger climate classification maps at 1-km resolution', *Scientific Data*, 5, pp. 1–12. doi: 10.1038/sdata.2018.214.

Berg, E. and Kucharik, C. (2022) 'The Dynamic Relationship between Air and Land Surface Temperature within the Madison,Wisconsin Urban Heat Island', *Remote Sensing*, 14(1), pp. 1–19. doi: 10.3390/rs14010165.

Best, M. J. (2005) 'Representing urban areas within operational numerical weather prediction models', *Boundary-Layer Meteorology*, 114(1), pp. 91–109. doi: 10.1007/s10546-004-4834-5.

Best, M. J. and Grimmond, C. S. B. (2013) 'Analysis of the Seasonal Cycle Within the First International Urban Land-Surface Model Comparison', *Boundary-Layer Meteorology*, 146(3), pp. 421–446. doi: 10.1007/s10546-012-9769-7.

Bi, D. *et al.* (2020) 'Configuration and spin-up of ACCESS-CM2, the new generation Australian Community Climate and Earth System Simulator Coupled Model', *Journal of*

Southern Hemisphere Earth Systems Science, 70, pp. 225–251. doi: https://doi.org/10.1071/ES19040.

Bille, R. A., Jensen, K. E. and Buitenwerf, R. (2023) 'Global patterns in urban green space are strongly linked to human development and population density', *Urban Forestry and Urban Greening*, 86(September 2022), p. 127980. doi: 10.1016/j.ufug.2023.127980.

Bishop, C. M. (2006) *Pattern Recognition and Machine Learning*, *Springer Science+Business Media*.

Bližňák, V., Pokorná, L. and Rulfová, Z. (2022) 'Assessment of the capability of modern reanalyses to simulate precipitation in warm months using adjusted radar precipitation', *Journal of Hydrology: Regional Studies*, 42(June). doi: 10.1016/j.ejrh.2022.101121.

Bohnenstengel, S. I. *et al.* (2014) 'Impact of anthropogenic heat emissions on London's temperatures', *Quarterly Journal of the Royal Meteorological Society*, 140(679), pp. 687–698. doi: 10.1002/qj.2144.

Bokaie, M. *et al.* (2016) 'Assessment of Urban Heat Island based on the relationship between land surface temperature and Land Use/ Land Cover in Tehran', *Sustainable Cities and Society*, 23, pp. 94–104. doi: 10.1016/j.scs.2016.03.009.

Bonafoni, S., Anniballe, R. and Pichierri, M. (2015) 'Comparison between surface and canopy layer urban heat island using MODIS data', pp. 1–4. doi: 10.1109/jurse.2015.7120457.

Borbora, J. and Das, A. K. (2014) 'Summertime Urban Heat Island study for Guwahati City, India', *Sustainable Cities and Society*, 11, pp. 61–66. doi: 10.1016/j.scs.2013.12.001.

Bornstein, R. *et al.* (2012) 'Interactions of Global-Warming and Urban Heat Islands in Different Climate-Zones', *NATO Science for Peace and Security Series C: Environmental Security*, 125, pp. 49–60. doi: 10.1007/978-94-007-2430-3_5.

Bornstein, R. D. and Johnson, D. S. (1977) 'Urban-rural wind velocity differences', *Atmospheric Environment (1967)*, 11(7), pp. 597–604. doi: 10.1016/0004-6981(77)90112-3.

Boslaugh, S. and Watters, P. A. (2008) *Statistics in a nutshell*, *Scientific Computing*.

Boucher, O. *et al.* (2020) 'Presentation and Evaluation of the IPSL-CM6A-LR Climate Model', *Journal ofAdvances in Modeling Earth Systems*, 12, pp. 1–52. doi: 10.1029/2019MS002010.

Bowler, D. E. *et al.* (2010) 'Urban greening to cool towns and cities: A systematic review of the empirical evidence', *Landscape and Urban Planning*, pp. 147–155. doi: 10.1016/j.landurbplan.2010.05.006.

Bratman, G. N. *et al.* (2019) 'Nature and mental health: An ecosystem service perspective', *Science Advances*, 5(7). doi: 10.1126/sciadv.aax0903.

Breiman, L. (2001) 'Random Forests', 45, pp. 5–32.

Buja, A., Hastie, T. and Tibshirani, R. (1989) 'Linear Smoothers and Additive Models', *Annals of Statistics*, 17(2), pp. 453–555.

Campbell, J. B. and Randolph, W. H. (2011) 'Electromagnetic Radiation', in *Introduction to Remote Sensing*. 5th edn, pp. 31–58.

Cao, J. *et al.* (2021) 'Within-city spatial and temporal heterogeneity of air temperature and its relationship with land surface temperature', *Landscape and Urban Planning*, 206(June 2020), p. 103979. doi: 10.1016/j.landurbplan.2020.103979.

Carrea, Laura, Embury, O. and Merchant, C. (2015) 'Datasets related to in-land water for limnology and remote sensing applications: distance-to-land, distance-to-water, water-body identifier and lake-centre co-ordinates', *Geoscience Data Journal*, 2(2), pp. 83–97. doi: 10.1002/gdj3.32.

Carrea, L., Embury, O. and Merchant, C. J. (2015) 'GloboLakes: high-resolution global limnology dataset v1', *Centre for Environmental Data Analysis*, 21 July 20. doi: 10.5285/6be871bc-9572-4345-bb9a-2c42d9d85ceb.

Chakraborty, T. *et al.* (2019) 'Disproportionately higher exposure to urban heat in lower-income neighborhoods: a multi-city perspective', *Environmental Research Letters*, 14(10), p. 105003. doi: 10.1088/1748-9326/AB3B99.

Chakraborty, T. and Lee, X. (2019) 'A simplified urban-extent algorithm to characterize surface urban heat islands on a global scale and examine vegetation control on their spatiotemporal variability', *International Journal of Applied Earth Observation and Geoinformation*, 74, pp. 269–280. doi: 10.1016/j.jag.2018.09.015.

Chapman, L. *et al.* (2015) 'The birmingham urban climate laboratory: An open meteorological test bed and challenges of the Smart city', *Bulletin of the American Meteorological Society*, 96(9), pp. 1545–1560. doi: 10.1175/BAMS-D-13-00193.1.

Chapman, L., Bell, S. and Randall, S. (2023) 'Urban Climate Can crowdsourcing increase the durability of an urban meteorological network?', *Urban Climate*, 49, p. 101542. doi: 10.1016/j.uclim.2023.101542.

Chapman, L. and Thornes, J. E. (2006) 'A geomatics-based road surface temperature prediction model', *Science of the Total Environment*, 360(1–3), pp. 68–80. doi: 10.1016/j.scitotenv.2005.08.025.

Chapman, S. *et al.* (2017) 'The impact of urbanization and climate change on urban temperatures: a systematic review', *Landscape Ecology*, pp. 1921–1935. doi: 10.1007/s10980-017-0561-4.

Charabi, Y. and Bakhit, A. (2011) 'Assessment of the canopy urban heat island of a coastal arid tropical city: The case of Muscat, Oman', *Atmospheric Research*, 101(1–2), pp. 215–227. doi: 10.1016/j.atmosres.2011.02.010.

Chen, F. *et al.* (2011) 'The integrated WRF/urban modelling system: Development, evaluation, and applications to urban environmental problems', *International Journal of Climatology*, 31(2), pp. 273–288. doi: 10.1002/joc.2158.

Chen, Z. T. *et al.* (2022) 'Deep learning projects future warming-induced vegetation growth changes under SSP scenarios', *Advances in Climate Change Research*, 13(2), pp. 251–257. doi: 10.1016/j.accre.2022.01.007.

Cherchi, A. *et al.* (2019) 'Journal of Advances in Modeling Earth Systems Global Mean Climate and Main Patterns of Variability in the CMCC-CM2 Coupled Model Journal of Advances in Modeling Earth Systems', *Journal of Advances in Modeling Earth Systems*, 11, pp. 185–209. doi: 10.1029/2018MS001369.

Chin, H. N. S. *et al.* (2005) 'Evaluation of an urban canopy parameterization in a mesoscale model using VTMX and URBAN 2000 data', *Monthly Weather Review*, 133(7), pp. 2043–2068. doi: 10.1175/MWR2962.1.

Chow, W. T. L. and Roth, M. (2006) 'Temporal dynamics of the urban heat island of Singapore', *International Journal of Climatology*, 26(15), pp. 2243–2260. doi: 10.1002/joc.1364.

Christen, A. and Vogt, R. (2004) 'Energy and radiation balance of a central European city',

International Journal of Climatology, 24(11), pp. 1395–1421. doi: 10.1002/joc.1074.

Clinton, N. and Gong, P. (2013) 'MODIS detected surface urban heat islands and sinks: Global locations and controls', *Remote Sensing of Environment*, 134, pp. 294–304. doi: 10.1016/j.rse.2013.03.008.

Corbane, C. *et al.* (2020) 'The grey-green divide: multi-temporal analysis of greenness across 10,000 urban centres derived from the Global Human Settlement Layer (GHSL)', *International Journal of Digital Earth*, 13(1), pp. 101–118. doi: 10.1080/17538947.2018.1530311.

Cui, Y. Y. and de Foy, B. (2012) 'Seasonal Variations of the Urban Heat Island at the Surface and the Near-Surface and Reductions due to Urban Vegetation in Mexico City', *Journal of Applied Meteorology and Climatology*, 51(5), pp. 855–868. doi: 10.1175/JAMC-D-11-0104.1.

Daniel, M. *et al.* (2019) 'Benefits of explicit urban parameterization in regional climate modeling to study climate and city interactions', *Climate Dynamics*, 52(5–6), pp. 2745–2764. doi: 10.1007/s00382-018-4289-x.

Dash, P. *et al.* (2002) 'Land surface temperature and emissivity estimation from passive sensor data: Theory and practice-current trends', *International Journal of Remote Sensing*, 23(13), pp. 2563–2594. doi: 10.1080/01431160110115041.

Deilami, K., Kamruzzaman, M. and Liu, Y. (2018) 'Urban heat island effect: A systematic review of spatio-temporal factors, data, methods, and mitigation measures', *International Journal of Applied Earth Observation and Geoinformation*, pp. 30–42. doi: 10.1016/j.jag.2017.12.009.

Demuzere, M., De Ridder, K. and Van Lipzig, N. P. M. (2008) 'Modeling the energy balance in Marseille: Sensitivity to roughness length parameterizations and thermal admittance', *Journal of Geophysical Research*, 113(D16), p. D16120. doi: 10.1029/2007JD009113.

Deosthali, V. (2000) 'Impact of rapid urban growth on heat and moisture islands in Pune City, India', *Atmospheric Environment*, 34(17), pp. 2745–2754. doi: 10.1016/S1352-2310(99)00370-2.

Dewan, A. *et al.* (2021) 'Surface urban heat island intensity in five major cities of Bangladesh: Patterns, drivers and trends', *Sustainable Cities and Society*, 71, p. 102926. doi: 10.1016/J.SCS.2021.102926.

Didan, K. *et al.* (2015) 'MODIS Vegetation Index User 's Guide (Collection 6)', 2015(May), p. 31.

Domeisen, D. I. V. *et al.* (2023) 'Prediction and projection of heatwaves', *Nature Reviews Earth and Environment*, 4(1), pp. 36–50. doi: 10.1038/s43017-022-00371-z.

Dormann, C. F. *et al.* (2013) 'Collinearity: a review of methods to deal with it and a simulation study evaluating their performance', *Ecography*, 36(1), pp. 27–46. doi: 10.1111/J.1600-0587.2012.07348.X.

Döscher, R. *et al.* (2022) 'The EC-Earth3 Earth system model for the Coupled Model Intercomparison Project 6', *Geosci. Model Dev.*, 15(February 2021), pp. 2973–3020. doi: https://doi.org/10.5194/gmd-15-2973-2022.

Draper, N. . and Smith, H. (1998) *Applied regression analysis*.

Du, H. *et al.* (2021) 'Simultaneous investigation of surface and canopy urban heat islands over global cities', *ISPRS Journal of Photogrammetry and Remote Sensing*, 181(163), pp.

67–83. doi: 10.1016/j.isprsjprs.2021.09.003.

Dunne, J. P. *et al.* (2020) 'The GFDL Earth System Model Version 4.1 (GFDL-ESM 4.1) : Overall Coupled Model Description and Simulation Characteristics Journal of Advances in Modeling Earth Systems', *Journal of Advances in Modeling Earth Systems*, pp. 1–56. doi: https://doi.org/ 10.1029/2019MS002015.

Duvenaud, D. *et al.* (2013) 'Structure Discovery in Nonparametric Regression through Compositional Kernel Search'. Available at: http://arxiv.org/abs/1302.4922 (Accessed: 21 October 2021).

Eliasson, I. (1996) 'Urban nocturnal temperatures, street geometry and land use', in *Atmospheric Environment*, pp. 379–392. doi: 10.1016/1352-2310(95)00033-X.

Elson, P. *et al.* (2023) 'SciTools/cartopy'.

Equere, V., Mirzaei, P. A. and Riffat, S. (2020) 'Definition of a new morphological parameter to improve prediction of urban heat island', *Sustainable Cities and Society*, 56, p. 102021. doi: 10.1016/j.scs.2020.102021.

Erell, E. and Williamson, T. (2007) 'Intra-urban differences in canopy layer air temperature at a mid-latitude city', *International Journal of Climatology*, 27(9), pp. 1243–1255. doi: 10.1002/joc.1469.

Ermida, S. L. *et al.* (2019) 'Quantifying the Clear-Sky Bias of Satellite Land Surface Temperature Using Microwave-Based Estimates', *Journal of Geophysical Research: Atmospheres*, 124(2), pp. 844–857. doi: 10.1029/2018JD029354.

ESA Land Cover CCI project team; Defourny, P. (2019) *ESA Land Cover Climate Change Initiative (Land_Cover_cci): Global Land Cover Maps, Version 2.0.7, Centre for Environmental Data Analysis*.

Estoque, R. C., Murayama, Y. and Myint, S. W. (2017) 'Effects of landscape composition and pattern on land surface temperature: An urban heat island study in the megacities of Southeast Asia', *Science of the Total Environment*, 577, pp. 349–359. doi: 10.1016/j.scitotenv.2016.10.195.

Estournel, C. *et al.* (1983) 'Observations and Modeling of Downward Radiative Fluxes (Solar and Infrared) in Urban/Rural Areas', *Journal of Climate and Applied Meteorology*, 22(1), pp. 134–142. doi: 10.1175/1520-0450(1983)022<0134:OAMODR>2.0.CO;2.

Eyring, V. *et al.* (2016) 'Overview of the Coupled Model Intercomparison Project Phase 6 (CMIP6) experimental design and organization', *Geosci. Model Dev*, 9. doi: 10.5194/gmd-9-1937-2016.

Eyring, V. *et al.* (2019) 'Taking climate model evaluation to the next level', *Nature Climate Change*, 9(2), pp. 102–110. doi: 10.1038/s41558-018-0355-y.

Famiglietti, C. A. *et al.* (2018) 'Global Validation of MODIS Near-Surface Air and Dew Point Temperatures', *Geophysical Research Letters*, 45(15), pp. 7772–7780. doi: 10.1029/2018GL077813.

Fang, H. *et al.* (2019) 'An Overview of Global Leaf Area Index (LAI): Methods, Products, Validation, and Applications', *Reviews of Geophysics*, 57(3), pp. 739–799. doi: 10.1029/2018RG000608.

Feng, J. L., Cai, X. M. and Chapman, L. (2019) 'Impact of atmospheric conditions and levels of urbanization on the relationship between nocturnal surface and urban canopy heat islands', *Quarterly Journal of the Royal Meteorological Society*, 145(724), pp. 3284–3299. doi: 10.1002/qj.3619.

Figuerola, P. I. and Mazzeo, N. A. (1998) 'Urban-rural temperature differences in Buenos Aires', *International Journal of Climatology*, 18(15), pp. 1709–1723. doi: 10.1002/(SICI)1097-0088(199812)18:15<1709::AID-JOC338>3.0.CO;2-I.

Findlay, B. F. and Hirt, M. S. (1969) 'An urban-induced meso-circulation', *Atmospheric Environment (1967)*, 3(5), pp. 537–542. doi: 10.1016/0004-6981(69)90043-2.

Fischer, E. M., Oleson, K. W. and Lawrence, D. M. (2012) 'Contrasting urban and rural heat stress responses to climate change', *Geophysical Research Letters*, 39(3), p. n/a-n/a. doi: 10.1029/2011GL050576.

Flores R., J. L., Pereira Filho, A. J. and Karam, H. A. (2016) 'Estimation of long term low resolution surface urban heat island intensities for tropical cities using MODIS remote sensing data', *Urban Climate*, 17, pp. 32–66. doi: 10.1016/j.uclim.2016.04.002.

Fox, M., Long, D. and Magazzeni, D. (2017) 'Explainable Planning'. Available at: http://arxiv.org/abs/1709.10256.

Freitas, E. D. *et al.* (2007) 'Interactions of an urban heat island and sea-breeze circulations during winter over the metropolitan area of São Paulo, Brazil', *Boundary-Layer Meteorology*, 122(1), pp. 43–65. doi: 10.1007/s10546-006-9091-3.

Fu, P. and Weng, Q. (2018) 'Variability in annual temperature cycle in the urban areas of the United States as revealed by MODIS imagery', *ISPRS Journal of Photogrammetry and Remote Sensing*, 146, pp. 65–73. doi: 10.1016/j.isprsjprs.2018.09.003.

Gaffin, S. R. *et al.* (2008) 'Variations in New York city's urban heat island strength over time and space', *Theoretical and Applied Climatology*, 94(1–2), pp. 1–11. doi: 10.1007/s00704-007-0368-3.

Gagliano, A., Nocera, F. and Aneli, S. (2017) 'Computational Fluid Dynamics Analysis for Evaluating the Urban Heat Island Effects', *Energy Procedia*, 134, pp. 508–517. doi: 10.1016/J.EGYPRO.2017.09.557.

Garciá-Diéz, M. *et al.* (2016) 'Advantages of using a fast urban boundary layer model as compared to a full mesoscale model to simulate the urban heat island of Barcelona', *Geoscientific Model Development*, 9(12), pp. 4439–4450. doi: 10.5194/gmd-9-4439-2016.

Gasparrini, A. *et al.* (2017) 'Projections of temperature-related excess mortality under climate change scenarios', *The Lancet Planetary Health*, 1(9), pp. e360–e367. doi: 10.1016/S2542-5196(17)30156-0.

Gaur, A., Eichenbaum, M. K. and Simonovic, S. P. (2018) 'Analysis and modelling of surface Urban Heat Island in 20 Canadian cities under climate and land-cover change', *Journal of Environmental Management*, 206, pp. 145–157. doi: 10.1016/J.JENVMAN.2017.10.002.

Gawuc, L. *et al.* (2020) 'Statistical Modeling of Urban Heat Island Intensity in Warsaw, Poland Using Simultaneous Air and Surface Temperature Observations', *IEEE Journal of Selected Topics in Applied Earth Observations and Remote Sensing*, 13, pp. 2716–2728.

Gelaro, R. *et al.* (2017) 'The modern-era retrospective analysis for research and applications, version 2 (MERRA-2)', *Journal of Climate*, 30(14), pp. 5419–5454. doi: 10.1175/JCLI-D-16-0758.1.

Geletič, J. *et al.* (2019) 'Inter-/intra-zonal seasonal variability of the surface urban heat island based on local climate zones in three central European cities', *Building and Environment*, 156, pp. 21–32. doi: 10.1016/j.buildenv.2019.04.011.

Geletič, J., Lehnert, M. and Dobrovolný, P. (2016) 'Land Surface Temperature Differences

within Local Climate Zones, Based on Two Central European Cities', *Remote Sensing*, 8(10), p. 788. doi: 10.3390/rs8100788.

Georgescu, M. *et al.* (2011) 'An alternative explanation of the semiarid urban area "oasis effect"', *Journal of Geophysical Research: Atmospheres*, 116(D24), p. n/a-n/a. doi: 10.1029/2011JD016720.

Georgescu, M. *et al.* (2014) 'Urban adaptation can roll back warming of emerging megapolitan regions', *Proceedings of the National Academy of Sciences of the United States of America*, 111(8), pp. 2909–2914. doi: 10.1073/PNAS.1322280111/-/DCSUPPLEMENTAL.

Geron, A. (2017a) 'Chapter 7: Ensemble Learning and Random Forests', in *Hands-On Machine Learning with Scikit-Learn & TensorFlow*. 10th edn.

Geron, A. (2017b) *Hands-On Machine Learning with Scikit-Learn and TensorFlow*.

Gillies, S. and Others, & (2007) 'Shapely: manipulation and analysis of geometric objects, Available at: "https://github.com/Toblerity/Shapely"'.

Giroux, S. *et al.* (2021) 'Informal vendors and food systems planning in an emerging African city', *Food Policy*, 103(May 2020), p. 101997. doi: 10.1016/j.foodpol.2020.101997.

Gomis-Cebolla, J. *et al.* (2023) 'Evaluation of ERA5 and ERA5-Land reanalysis precipitation datasets over Spain (1951–2020)', *Atmospheric Research*, 284(December 2022). doi: 10.1016/j.atmosres.2023.106606.

Goodess, C. *et al.* (2021) 'Climate change projections for sustainable and healthy cities', 2(1), p. 812. doi: 10.5334/BC.111.

Goosse, H. *et al.* (2010) 'Chapter 3 . Modelling the climate system', in *Introduction to climate dynamics and climate modelling*, pp. 59–86.

Görtler, J., Kehlbeck, R. and Deussen, O. (2019) 'A Visual Exploration of Gaussian Processes', *Distill*, 4(4), p. e17. doi: 10.23915/DISTILL.00017.

Grady Dixon, P. and Mote, T. L. (2003) 'Patterns and causes of Atlanta's urban heat island-initiated precipitation', *Journal of Applied Meteorology*, 42(9), pp. 1273–1284. doi: 10.1175/1520-0450(2003)042<1273:PACOAU>2.0.CO;2.

Grimmond, C. S. B. *et al.* (2010) 'The international urban energy balance models comparison project: First results from phase 1', *Journal of Applied Meteorology and Climatology*, 49(6), pp. 1268–1292. doi: 10.1175/2010JAMC2354.1.

Grömping, U. (2012) 'Variable Importance Assessment in Regression: Linear Regression versus Random Forest'. doi: 10.1198/tast.2009.08199.

Gu, Y. and Li, D. (2018) 'A modeling study of the sensitivity of urban heat islands to precipitation at climate scales', *Urban Climate*, 24, pp. 982–993. doi: 10.1016/j.uclim.2017.12.001.

Gujarati, D. N. (2020) 'Linear Regression: A Mathematical Introduction', *Linear Regression: A Mathematical Introduction*. doi: 10.4135/9781071802571.

Hamdi, R. *et al.* (2014) 'Assessment of three dynamical urban climate downscaling methods: Brussels's future urban heat island under an A1B emission scenario', *International Journal of Climatology*, 34(4), pp. 978–999. doi: 10.1002/joc.3734.

Harris, C. R. *et al.* (2020) 'Array programming with NumPy', *Nature*, 585(7825), pp. 357–362. doi: 10.1038/s41586-020-2649-2.

Harris, L. and Rao Kotamarthi, V. (2005) 'The characteristics of the Chicago lake breeze and its effects on trace particle transport: Results from an episodic event simulation', *Journal of Applied Meteorology*, 44(11), pp. 1637–1654. doi: 10.1175/JAM2301.1.

Hart, M. A. and Sailor, D. J. (2009) 'Quantifying the influence of land-use and surface characteristics on spatial variability in the urban heat island', *Theoretical and Applied Climatology*, 95(3–4), pp. 397–406. doi: 10.1007/s00704-008-0017-5.

Hastie, T. and Tibshirani, R. (1986) 'Generalised Additive Models', *Statistical Science*, 1(3), pp. 297–318.

Hastings, D. A. *et al.* (1999) 'The Global Land One-kilometer Base Elevation (GLOBE) Digital Elevation Model, Version 1.0.' Available at: http://www.ngdc.noaa.gov/mgg/topo/globe.html.

He, B. *et al.* (2019) 'CAS FGOALS-f3-L Model Datasets for CMIP6 Historical Atmospheric Model Intercomparison Project Simulation', *Advances in Atmospheric Sciences*, 36(8), pp. 771–778. doi: 10.1007/s00376-019-9027-8.

Heal, G. and Park, J. (2013) 'Feeling the Heat: Temperature, Physiology and the Weath of Nations', *NBER Working Paper Series*, (19725). Available at: http://www.nber.org/papers/w19725.

Heaviside, C., Macintyre, H. and Vardoulakis, S. (2017) 'The Urban Heat Island: Implications for Health in a Changing Environment', *Current environmental health reports*, pp. 296–305. doi: 10.1007/s40572-017-0150-3.

Herrera, J. *et al.* (2012) *Informal Sector and Informal Employment : Overview of Data for 11 Cities in 10 Developing Countries, WIEGO Working Paper*. Available at: http://www.wiego.org/sites/wiego.org/files/publications/files/Herrera_WIEGO_WP9.pdf.

Hersbach, H. *et al.* (2020) 'The ERA5 global reanalysis', *Quarterly Journal of the Royal Meteorological Society*, 146(730), pp. 1999–2049. doi: 10.1002/qj.3803.

Hidalgo, J., Pigeon, G. and Masson, V. (2008) 'Urban-breeze circulation during the CAPITOUL experiment: observational data analysis approach', *Meteorol Atmos Phys*, 102, pp. 223–241. doi: 10.1007/s00703-008-0329-0.

Hinkel, K. M. *et al.* (2003) 'The urban heat island in winter at Barrow, Alaska', *International Journal of Climatology*, 23(15), pp. 1889–1905. doi: 10.1002/joc.971.

Hoerl, A. E. and Kennard, R. W. (1970) 'Ridge Regression: Biased Estimation for Nonorthogonal Problems', *Technometrics*, 12(1), pp. 55–67. doi: 10.1080/00401706.1970.10488634.

Horton, R. M. *et al.* (2016) 'A Review of Recent Advances in Research on Extreme Heat Events', *Current Climate Change Reports*, pp. 242–259. doi: 10.1007/s40641-016-0042-x.

Howard, L. (1833) *THE CLIMATE OF LONDON*.

Hoyer, S. and Hamman, J. (2017) 'xarray: N-D labeled Arrays and Datasets in Python', *Journal of Open Research Software*, 5(1), p. 10. doi: 10.5334/jors.148.

Hu, L. *et al.* (2014) 'How can we use MODIS land surface temperature to validate long-term urban model simulations?', *Journal of Geophysical Research: Atmospheres*, 119(6), pp. 3185–3201. doi: 10.1002/2013JD021101.

Hu, L. and Brunsell, N. A. (2013) 'The impact of temporal aggregation of land surface temperature data for surface urban heat island (SUHI) monitoring', *Remote Sensing of Environment*, 134, pp. 162–174. doi: 10.1016/j.rse.2013.02.022.

Hu, L. and Brunsell, N. A. (2015) 'A new perspective to assess the urban heat island through remotely sensed atmospheric profiles', *Remote Sensing of Environment*, 158, pp. 393–406. doi: 10.1016/j.rse.2014.10.022.

Hu, Y. *et al.* (2019) 'Comparison of surface and canopy urban heat islands within megacities of eastern China', *ISPRS Journal of Photogrammetry and Remote Sensing*, 156(March), pp. 160–168. doi: 10.1016/j.isprsjprs.2019.08.012.

Huang, F. *et al.* (2020) 'Satellite identification of atmospheric-surface-subsurface urban heat islands under clear sky', *Remote Sensing of Environment*, 250(November 2019), p. 112039. doi: 10.1016/j.rse.2020.112039.

Huang, K. *et al.* (2019) 'Projecting global urban land expansion and heat island intensification through 2050', *Environmental Research Letters*, 14(11). doi: 10.1088/1748-9326/ab4b71.

Huang, Q. *et al.* (2020) 'The roles of meteorological parameters in Shanghai's nocturnal urban heat island from 1979 to 2013', *Theoretical and Applied Climatology*, 141(1–2), pp. 285–297. doi: 10.1007/s00704-020-03214-3.

Huete, A. *et al.* (2002) 'Overview of the radiometric and biophysical performance of the MODIS vegetation indices', *Remote Sensing of Environment*, 83(1–2), pp. 195–213. doi: 10.1016/S0034-4257(02)00096-2.

Hung, T. K. and Wo, O. C. (2012) 'Development of a community weather information network (Co-WIN) in Hong Kong', *Weather*, 67(2), pp. 48–50. doi: 10.1002/wea.1883.

Hunter, J. D. (2007) 'Matplotlib: A 2D Graphics Environment', *Computing in Science & Engineering*, 9(3), pp. 90–95. doi: 10.1109/MCSE.2007.55.

Ichinose, T., Shimodozono, K. and Hanaki, K. (1999) 'Impact of anthropogenic heat on urban climate in Tokyo', in *Atmospheric Environment*, pp. 3897–3909. doi: 10.1016/S1352-2310(99)00132-6.

Imhoff, M. L. *et al.* (2010) 'Remote sensing of the urban heat island effect across biomes in the continental USA', *Remote Sensing of Environment*, 114(3), pp. 504–513. doi: 10.1016/j.rse.2009.10.008.

James, G. *et al.* (2021) *An Introduction to Statistical Learning*, *Springer texts*.

Jin, M. and Dickinson, R. E. (2010) 'Land surface skin temperature climatology: Benefitting from the strengths of satellite observations', *Environmental Research Letters*, 5(4). doi: 10.1088/1748-9326/5/4/044004.

Johnson, D. P. and Wilson, J. S. (2009) 'The socio-spatial dynamics of extreme urban heat events: The case of heat-related deaths in Philadelphia', *Applied Geography*, 29(3), pp. 419–434. doi: 10.1016/j.apgeog.2008.11.004.

Johnson, G. T. *et al.* (1991) 'Simulation of surface urban heat islands under "ideal" conditions at night part 1: Theory and tests against field data', *Boundary-Layer Meteorology*, 56(3), pp. 275–294. doi: 10.1007/BF00120424.

Jones, P. D. and Lister, D. H. (2009) 'The urban heat island in central London and urban-related warming trends in central London since 1900', *Weather*, 64(12), pp. 323–327. doi: 10.1002/wea.432.

Jones, P. D., Lister, D. H. and Li, Q. (2008) 'Urbanization effects in large-scale temperature records, with an emphasis on China', *Journal of Geophysical Research Atmospheres*, 113(16), pp. 1–12. doi: 10.1029/2008JD009916.

Jongtanom, Y., Kositanont, C. and Baulert, S. (2011) 'Temporal variations of urban heat

island intensity in three major cities, Thailand', *Modern Applied Science*, 5(5), pp. 105–110. doi: 10.5539/mas.v5n5p105.

Jonsson, P. (2004) 'Vegetation as an urban climate control in the subtropical city of Gaborone, Botswana', *International Journal of Climatology*, 24(10), pp. 1307–1322. doi: 10.1002/joc.1064.

Jordahl, K. *et al.* (2020) 'geopandas/geopandas: v0.8.1'. doi: 10.5281/zenodo.3946761.

Joseph, V. R. (2022) 'Optimal ratio for data splitting', *Statistical Analysis and Data Mining*, 15(4), pp. 531–538. doi: 10.1002/sam.11583.

Joshi, M. *et al.* (2011) 'Projections of when temperature change will exceed 2°C above pre-industrial levels', *Nature Climate Change*, 1(November), pp. 407–412. doi: 10.1038/nclimate1261.

Kabano, P., Lindley, S. and Harris, A. (2021) 'Evidence of urban heat island impacts on the vegetation growing season length in a tropical city', *Landscape and Urban Planning*, 206(October 2020), p. 103989. doi: 10.1016/j.landurbplan.2020.103989.

Karl, T. R., Diaz, H. F. and Kukla, G. (1988) 'Urbanization: Its Detection and Effect in the United States Climate Record', *Journal of Climate*, 1(11), pp. 1099–1123. doi: 10.1175/1520-0442(1988)001<1099:uidaei>2.0.co;2.

Katabatic wind - AMS Glossary (2012). Available at: http://glossary.ametsoc.org/wiki/Katabatic_wind (Accessed: 10 August 2020).

Katzav, J., Dijkstra, H. A. and de Laat, A. T. J. J. (2012) 'Assessing climate model projections: State of the art and philosophical reflections', *Studies in History and Philosophy of Science Part B: Studies in History and Philosophy of Modern Physics*, 43(4), pp. 258–276. doi: 10.1016/J.SHPSB.2012.07.002.

Keeratikasikorn, C. and Bonafoni, S. (2018) 'Satellite Images and Gaussian Parameterization for an Extensive Analysis of Urban Heat Islands in Thailand', *Remote Sensing*, 10(5), p. 665. doi: 10.3390/rs10050665.

Kelley, M. *et al.* (2020) 'GISS-E2.1: Configurations and Climatology', *Journal of Advances in Modeling Earth Systems*, 12, pp. 1–38. doi: 10.1029/2019MS002025.

Keppas, S. C. *et al.* (2021) 'Future climate change impact on urban heat island in two mediterranean cities based on high-resolution regional climate simulations', *Atmosphere*, 12(7). doi: 10.3390/atmos12070884.

Kidder, S. Q. and Essenwanger, O. M. (1995) 'The effect of clouds and wind on the difference in nocturnal cooling rates between urban and rural areas', *Journal of Applied Meteorology*, 34(1), pp. 2440–2448. doi: 10.1175/1520-0450(1995)034<2440:teocaw>2.0.co;2.

Kii, M. (2021) 'Projecting future populations of urban agglomerations around the world and through the 21st century', *npj Urban Sustainability*, 1(1). doi: 10.1038/s42949-020-00007-5.

Kim, J. J. and Baik, J. J. (2001) 'Urban street-canyon flows with bottom heating', *Atmospheric Environment*, 35(20), pp. 3395–3404. doi: 10.1016/S1352-2310(01)00135-2.

Kim, Y. *et al.* (2021) 'Spatial, Temporal, and Multivariate Bias in Regional Climate Model Simulations', *Geophysical Research Letters*, 48(11), pp. 1–9. doi: 10.1029/2020GL092058.

Kim, Y. and Baik, J. (2004) 'Daily maximum urban heat island intensity in large cities of Korea', *Theor. Appl. Climatol. 79*, 164, pp. 151–164. doi: 10.1007/s00704-004-0070-7.

Kim, Y. H. and Baik, J. J. (2002) 'Maximum urban heat island intensity in Seoul', *Journal*

of Applied Meteorology, 41(6), pp. 651–659. doi: 10.1175/1520-0450(2002)041<0651:MUHIII>2.0.CO;2.

Kobayashi, S. *et al.* (2015) 'The JRA-55 reanalysis: General specifications and basic characteristics', *Journal of the Meteorological Society of Japan*, 93(1), pp. 5–48. doi: 10.2151/jmsj.2015-001.

Kolokotroni, M. and Giridharan, R. (2008) 'Urban heat island intensity in London: An investigation of the impact of physical characteristics on changes in outdoor air temperature during summer', *Solar Energy*, 82(11), pp. 986–998. doi: 10.1016/j.solener.2008.05.004.

Konstantinov, P., Varentsov, M. and Esau, I. (2018) 'A high density urban temperature network deployed in several cities of Eurasian Arctic', *Environmental Research Letters*, 13(7). doi: 10.1088/1748-9326/aacb84.

Kottek, M. *et al.* (2006) 'World map of the Köppen-Geiger climate classification updated', *Meteorologische Zeitschrift*, 15(3), pp. 259–263. doi: 10.1127/0941-2948/2006/0130.

Kovats, R. S. and Hajat, S. (2008) 'Heat stress and public health: A critical review', *Annual Review of Public Health*, 29, pp. 41–55. doi: 10.1146/annurev.publhealth.29.020907.090843.

Kubilay, A. *et al.* (2020) 'Advancement in Urban Climate Modelling at Local Scale: Urban Heat Island Mitigation and Building Cooling Demand', *Atmosphere 2020, Vol. 11, Page 1313*, 11(12), p. 1313. doi: 10.3390/ATMOS11121313.

Kumar, A., Mukherjee, M. and Goswami, A. (2023) 'Inter-seasonal characterization and correlation of Surface Urban Heat Island (SUHI) and Canopy Urban Heat Island (CUHI) in the urbanized environment of Delhi', *Remote Sensing Applications: Society and Environment*, 30(December 2022), p. 100970. doi: 10.1016/j.rsase.2023.100970.

Kusaka, H. *et al.* (2001) 'A simple single-layer urban canopy model for atmospheric models: Comparison with multi-layer and slab models', *Boundary-Layer Meteorology*, 101(3), pp. 329–358. doi: 10.1023/A:1019207923078.

Kusaka, H. and Kimura, F. (2004) 'Thermal Effects of Urban Canyon Structure on the Nocturnal Heat Island: Numerical Experiment Using a Mesoscale Model Coupled with an Urban Canopy Model', *Journal of Applied Meteorology*, 43(12), pp. 1899–1910. doi: 10.1175/JAM2169.1.

Kusaka, H. and Takane, Y. (2012) 'Urban Climate Projection by the WRF Model at 3-km Horizontal Grid Increment: Dynamical Downscaling and Predicting Heat Stress in the 2070's August for Tokyo, Osaka, and Nagoya Metropolises', *Journal of the Meteorological Society of Japan*, 90, pp. 47–63. doi: 10.2151/jmsj.2012-B04.

Lai, J. *et al.* (2018) 'Does quality control matter? Surface urban heat island intensity variations estimated by satellite-derived land surface temperature products', *ISPRS Journal of Photogrammetry and Remote Sensing*, 139, pp. 212–227. doi: 10.1016/J.ISPRSJPRS.2018.03.012.

Lai, J. *et al.* (2021) 'Meteorological controls on daily variations of nighttime surface urban heat islands', *Remote Sensing of Environment*, 253, p. 112198. doi: 10.1016/j.rse.2020.112198.

Lamb, W. F. *et al.* (2019) 'Learning about urban climate solutions from case studies', *Nature Climate Change*, 9(4), pp. 279–287. doi: 10.1038/s41558-019-0440-x.

Lan, T. *et al.* (2023) 'The future of China's urban heat island effects: A machine learning based scenario analysis on climatic-socioeconomic policies', *Urban Climate*, 49(March), p. 101463. doi: 10.1016/j.uclim.2023.101463.

Lauwaet, D. *et al.* (2015) 'Detailed urban heat island projections for cities worldwide: Dynamical downscaling CMIP5 global climate models', *Climate*, 3(2), pp. 391–415. doi: 10.3390/cli3020391.

Lauwaet, D. *et al.* (2016) 'Assessing the current and future urban heat island of Brussels', *Urban Climate*, 15, pp. 1–15. doi: 10.1016/j.uclim.2015.11.008.

Lee, J.-Y. *et al.* (2021) 'Future Global Climate: Scenario-based Projections and Near-term Information', *Climate Change 2021: The Physical Science Basis. Contribution of Working Group I to the Sixth Assessment Report of the Intergovernmental Panel on Climate Change [Masson-Delmotte, V., P. Zhai, A. Pirani, S.L. Connors, C. Péan, S. Berger, N. Caud, Y. Chen*, pp. 553–672. doi: 10.1017/9781009157896.006.

Lee, K. *et al.* (2020) 'Trend analysis of urban heat island intensity according to urban area change in Asian mega cities', *40th Asian Conference on Remote Sensing, ACRS 2019: Progress of Remote Sensing Technology for Smart Future*.

Lee, S. H. and Baik, J. J. (2010) 'Statistical and dynamical characteristics of the urban heat island intensity in Seoul', *Theoretical and Applied Climatology*, 100(1), pp. 227–237. doi: 10.1007/s00704-009-0247-1.

Lente, G. and Ősz, K. (2020) 'Barometric formulas: various derivations and comparisons to environmentally relevant observations', *ChemTexts*, 6(2), pp. 1–14. doi: 10.1007/S40828-020-0111-6/FIGURES/6.

Lerch, M. (2017) 'International migration and city growth', *UN Population Division, Technical Paper No. 10. New York: United Nations*, (December 2017).

Leutwyler, D. *et al.* (2017) 'Evaluation of the convection-resolving climate modeling approach on continental scales', *Journal of Geophysical Research*, 122(10), pp. 5237–5258. doi: 10.1002/2016JD026013.

Levermore, G. *et al.* (2018) 'The increasing trend of the urban heat island intensity', *Urban Climate*, 24, pp. 360–368. doi: 10.1016/j.uclim.2017.02.004.

Li, D. *et al.* (2019) 'Urban heat island: Aerodynamics or imperviousness?', *Science Advances*, 5(4). doi: 10.1126/sciadv.aau4299.

Li, H. *et al.* (2018) 'Interaction between urban heat island and urban pollution island during summer in Berlin', *Science of the Total Environment*, 636, pp. 818–828. doi: 10.1016/j.scitotenv.2018.04.254.

Li, J. *et al.* (2011) 'Impacts of landscape structure on surface urban heat islands: A case study of Shanghai, China', *Remote Sensing of Environment*, 115(12), pp. 3249–3263. doi: 10.1016/j.rse.2011.07.008.

Li, K., Chen, Y. and Gao, S. (2022) 'Uncertainty of city-based urban heat island intensity across 1112 global cities: Background reference and cloud coverage', *Remote Sensing of Environment*, 271, p. 112898. doi: 10.1016/J.RSE.2022.112898.

Li, L., Zha, Y. and Wang, R. (2020) 'Relationship of surface urban heat island with air temperature and precipitation in global large cities', *Ecological Indicators*, 117(June), p. 106683. doi: 10.1016/j.ecolind.2020.106683.

Li, L., Zha, Y. and Zhang, J. (2020) 'Spatially non-stationary effect of underlying driving factors on surface urban heat islands in global major cities', *International Journal of Applied Earth Observation and Geoinformation*, 90, p. 102131. doi: 10.1016/j.jag.2020.102131.

Li, X. *et al.* (2021) 'Global urban growth between 1870 and 2100 from integrated high resolution mapped data and urban dynamic modeling', *Communications Earth and*

Environment, 2(1), pp. 1–10. doi: 10.1038/s43247-021-00273-w.

Li, Xiaoma *et al.* (2017) 'The surface urban heat island response to urban expansion: A panel analysis for the conterminous United States', *Science of The Total Environment*, 605–606, pp. 426–435. doi: 10.1016/J.SCITOTENV.2017.06.229.

Li, Y. *et al.* (2021) 'Context sensitivity of surface urban heat island at the local and regional scales', *Sustainable Cities and Society*, 74, p. 103146. doi: 10.1016/J.SCS.2021.103146.

Liang, S. and Wang, J. (2020) 'Chapter 6 - Broadband albedo', in *Advanced Remote Sensing*, pp. 193–250. doi: 10.1016/B978-0-12-815826-5.00006-4.

Lindén, J., Grimmond, C. S. B. and Esper, J. (2015) 'Urban warming in villages', *Adv. Sci. Res.*, 12, pp. 157–162. doi: 10.5194/asr-12-157-2015.

Lindley, S. *et al.* (2018) 'Rethinking urban green infrastructure and ecosystem services from the perspective of sub-Saharan African cities', *Landscape and Urban Planning*, 180(January), pp. 328–338. doi: 10.1016/j.landurbplan.2018.08.016.

Liu, H. *et al.* (2021) 'The influence of urban form on surface urban heat island and its planning implications: Evidence from 1288 urban clusters in China', *Sustainable Cities and Society*, 71. doi: 10.1016/J.SCS.2021.102987.

Liu, Y. *et al.* (2006) 'Verification of a Mesoscale Data-Assimilation and Forecasting System for the Oklahoma City Area during the Joint Urban 2003 Field Project', *Journal of Applied Meteorology and Climatology*, 45(7), pp. 912–929. doi: 10.1175/JAM2383.1.

Liu, Z. *et al.* (2022) 'Surface warming in global cities is substantially more rapid than in rural background areas', *Communications Earth and Environment*, 3(1). doi: 10.1038/s43247-022-00539-x.

Lowe, J. A. *et al.* (2019) 'UKCP18 Science Overview Report', *Met Office*, 2(March), pp. 1–73. Available at: https://www.metoffice.gov.uk/pub/data/weather/uk/ukcp18/science-reports/UKCP18-Overview-report.pdf.

Ma, L. *et al.* (2021) 'Changing Effect of Urban Form on the Seasonal and Diurnal Variations of Surface Urban Heat Island Intensities (SUHIIs) in More Than 3000 Cities in China', *Sustainability 2021, Vol. 13, Page 2877*, 13(5), p. 2877. doi: 10.3390/SU13052877.

Ma, W. *et al.* (2016) 'Air temperature field distribution estimations over a Chinese mega-city using MODIS land surface temperature data: the case of Shanghai', *Frontiers of Earth Science*, 10(1), pp. 38–48. doi: 10.1007/s11707-015-0510-y.

Magee, N., Curtis, J. and Wendler, G. (1999) 'The urban heat island effect at Fairbanks, Alaska', *Theoretical and Applied Climatology*, 64(1–2), pp. 39–47. doi: 10.1007/s007040050109.

Mahowald, N. *et al.* (2016) 'Projections of leaf area index in earth system models', *Earth System Dynamics*, 7(1), pp. 211–229. doi: 10.5194/esd-7-211-2016.

Maller, C. J. and Strengers, Y. (2011) 'Housing, heat stress and health in a changing climate: Promoting the adaptive capacity of vulnerable households, a suggested way forward', *Health Promotion International*, 26(4), pp. 492–498. doi: 10.1093/heapro/dar003.

Mallick, J., Rahman, A. and Singh, C. K. (2013) 'Modeling urban heat islands in heterogeneous land surface and its correlation with impervious surface area by using night-time ASTER satellite data in highly urbanizing city, Delhi-India', *Advances in Space Research*, 52(4), pp. 639–655. doi: 10.1016/j.asr.2013.04.025.

Manoli, G. *et al.* (2019) 'Magnitude of urban heat islands largely explained by climate and population', *Nature*, 573(7772), pp. 55–60. doi: 10.1038/s41586-019-1512-9.

Mao, K. *et al.* (2018) 'Retrieval of Land-surface Temperature from AMSR2 Data Using a Deep Dynamic Learning Neural Network', *Chinese Geographical Science*, 28(1), pp. 1–11. doi: 10.1007/s11769-018-0930-1.

Marquès, E. *et al.* (2022) 'Urban Heat Island Estimation from Crowdsensing Thermometers Embedded in Personal Cars', *Bulletin of the American Meteorological Society*, 103(4), pp. E1098–E1113. doi: 10.1175/bams-d-21-0174.1.

Martilli, A. (2003) 'A two-dimensional numerical study of the impact of a city on atmospheric circulation and pollutant dispersion in a coastal environment', *Boundary-Layer Meteorology*, 108(1), pp. 91–119. doi: 10.1023/A:1023044100064.

Martilli, A., Clappier, A. and Rotach, M. W. (2002) 'An urban surface exchange parameterisation for mesoscale models', *Boundary-Layer Meteorology*, 104(2), pp. 261–304. doi: 10.1023/A:1016099921195.

Martin-Vide, J. and Moreno-Garcia, M. C. (2020) 'Probability values for the intensity of Barcelona's urban heat island (Spain)', *Atmospheric Research*, 240, p. 104877. doi: 10.1016/j.atmosres.2020.104877.

Masson, V. (2000) 'A physically-based scheme for the urban energy budget in atmospheric models', *Boundary-Layer Meteorology*, 94(3), pp. 357–397. doi: 10.1023/A:1002463829265.

Mauritsen, T. *et al.* (2019) 'Developments in the MPI-M Earth System Model version 1.2 (MPI-ESM1.2) and Its Response to Increasing CO2', *Journal of Advances in Modeling Earth Systems*, 11, pp. 998–1038. doi: 10.1029/2018MS001400.

McCarthy, M. P. *et al.* (2011) 'Simulating climate change in UK cities using a regional climate model, HadRM3', *International Journal of Climatology*, 32(12), pp. 1875–1888. doi: 10.1002/joc.2402.

McCarthy, M. P., Best, M. J. and Betts, R. A. (2010) 'Climate change in cities due to global warming and urban effects', *Geophysical Research Letters*, 37(9). doi: 10.1029/2010GL042845.

Mentaschi, L. *et al.* (2022) 'Global long-term mapping of surface temperature shows intensified intra-city urban heat island extremes', *Global Environmental Change*, 72, p. 102441. doi: 10.1016/J.GLOENVCHA.2021.102441.

Miao, S. *et al.* (2009) 'An observational and modeling study of characteristics of urban heat island and boundary layer structures in Beijing', *Journal of Applied Meteorology and Climatology*, 48(3), pp. 484–501. doi: 10.1175/2008JAMC1909.1.

Mihalakakou, G. *et al.* (2002) 'Application of neural networks to the simulation of the heat island over Athens, Greece, using synoptic types as a predictor', *Journal of Applied Meteorology*, 41(5), pp. 519–527. doi: 10.1175/1520-0450(2002)041<0519:AONNTT>2.0.CO;2.

Mirzaei, P. A. (2015) 'Recent challenges in modeling of urban heat island', *Sustainable Cities and Society*, 19, pp. 200–206. doi: 10.1016/j.scs.2015.04.001.

Mirzaei, P. A. and Haghighat, F. (2010) 'Approaches to study Urban Heat Island - Abilities and limitations', *Building and Environment*, 45(10), pp. 2192–2201. doi: 10.1016/j.buildenv.2010.04.001.

Moda, H. M., Filho, W. L. and Minhas, A. (2019) 'Impacts of climate change on outdoor workers and their safety: Some research priorities', *International Journal of Environmental Research and Public Health*, 16(18). doi: 10.3390/ijerph16183458.

MODIS Web (2020). Available at: https://modis.gsfc.nasa.gov/about/ (Accessed: 4 December 2020).

Mohan, M. *et al.* (2012) 'Urban Heat Island Assessment for a Tropical Urban Airshed in India', *Atmospheric and Climate Sciences*, 02(02), pp. 127–138. doi: 10.4236/acs.2012.22014.

Molnar, C. (2022) *Interpretable Machine Learning: A Guide for Making Black Box Models Explainable (2nd ed.)*.

Mora, C. *et al.* (2017) 'Global risk of deadly heat', *Nature Climate Change*, 7(7), pp. 501–506. doi: 10.1038/nclimate3322.

Moreno-Garcia, M. C. (1994) 'Intensity and form of the urban heat island in barcelona', *International Journal of Climatology*, 14(6), pp. 705–710. doi: 10.1002/joc.3370140609.

Morris, C. J. G. and Simmonds, I. (2001) 'Quantification of the influence of wind and cloud on the nocturnal urban heat island of a large city', *Journal of Applied Meteorology*, 40(2), pp. 169–182. doi: 10.1175/1520-0450(2001)040<0169:QOTIOW>2.0.CO;2.

Mulcahy, J. P. *et al.* (2022) 'UKESM1.1 : Development and evaluation of an updated configuration of the UK Earth System Model', *Geosci. Model Dev.* doi: https://doi.org/10.5194/gmd-2022-113.

Müller, W. A. *et al.* (2018) 'A Higher-resolution Version of the Max Planck Institute Earth System Model (MPI-ESM1.2-HR)', *Journal of Advances in Modeling Earth Systems*, 10, pp. 1383–1413. doi: 10.1029/2017MS001217.

Muñoz Sabater, J. (2019) *ERA5-Land monthly averaged data from 1981 to present, Copernicus Climate Change Service (C3S) Climate Data Store (CDS)*. doi: 10.24381/cds.68d2bb30.

Murari, K. K. *et al.* (2015) 'Intensification of future severe heat waves in India and their effect on heat stress and mortality', *Regional Environmental Change*, 15(4), pp. 569–579. doi: 10.1007/s10113-014-0660-6.

Nakicenovic, N. *et al.* (2000) *IPCC Special Report on Emissions Scenarios*, *Cambridge University Press*. doi: 10.1017/CBO9781107415324.004.

National Aeronautics and Space Administration (2021a) 'MCD43A2 - MODIS/Terra+Aqua BRDF/Albedo Quality Daily L3 Global - 500m'.

National Aeronautics and Space Administration (2021b) 'MCD43A3 - MODIS/Terra+Aqua BRDF/Albedo Daily L3 Global - 500m'.

National Aeronautics and Space Administration (2021c) 'MOD13A2 - MODIS/Terra Vegetation Indices 16-Day L3 Global 1km SIN Grid'.

National Aeronautics and Space Administration (2021d) 'MYD13A2 - MODIS/Aqua Vegetation Indices 16-Day L3 Global 1km SIN Grid'.

Navarro-Racines, C. *et al.* (2020) 'High-resolution and bias-corrected CMIP5 projections for climate change impact assessments', *Scientific Data*, 7(1), pp. 1–14. doi: 10.1038/s41597-019-0343-8.

Nembrini, S., König, I. R. and Wright, M. N. (2018) 'The revival of the Gini importance?', *Bioinformatics*, 34(21), pp. 3711–3718. doi: 10.1093/bioinformatics/bty373.

Nichol, J. E. (1996) 'High-resolution surface temperature patterns related to urban morphology in a tropical city: A satellite-based study', *Journal of Applied Meteorology*, 35(1), pp. 135–146. doi: 10.1175/1520-0450(1996)035<0135:HRSTPR>2.0.CO;2.

Nie, W. *et al.* (2017) 'Impacts of Anthropogenic Heat on Summertime Rainfall in Beijing', *Journal of Hydrometeorology*, 18(3), pp. 693–712. doi: 10.1175/JHM-D-16-0173.1.

Nowack, P. *et al.* (2020) 'Causal networks for climate model evaluation and constrained projections', *Nature Communications*, 11(1), pp. 1–11. doi: 10.1038/s41467-020-15195-y.

Nowack, P. *et al.* (2021) 'Machine learning calibration of low-cost NO2 and PM10 sensors: Non-linear algorithms and their impact on site transferability', *Atmospheric Measurement Techniques*, 14(8), pp. 5637–5655. doi: 10.5194/amt-14-5637-2021.

O'Neill, B. C. *et al.* (2016) 'The Scenario Model Intercomparison Project (ScenarioMIP) for CMIP6', *Geoscientific Model Development*, 9(9), pp. 3461–3482. doi: 10.5194/GMD-9-3461-2016.

O'Neill, B. C. *et al.* (2017) 'The roads ahead: Narratives for shared socioeconomic pathways describing world futures in the 21st century', *Global Environmental Change*, 42, pp. 169–180. doi: 10.1016/J.GLOENVCHA.2015.01.004.

OECD (2020) 'Improving Transport Planning for Accessible Cities', *OECD Urban Studiess, OECD Publishing, Paris*. doi: 10.1787/fcb2eae0-en.

Ohashi, Y. and Kida, H. (2002) *Effects of Mountains and Urban Areas on Daytime Local-Circulations in the Osaka and Kyoto Regions, Journal of the Meteorological Society of Japan*.

Oke, T. R. (1973) 'City size and the urban heat island', *Atmospheric Environment*. doi: 10.1016/0004-6981(73)90140-6.

Oke, T. R. (1976) 'The distinction between canopy and boundary-layer urban heat Islands', *Atmosphere*, 14(4), pp. 268–277. doi: 10.1080/00046973.1976.9648422.

Oke, T. R. (1978) 'Boundary Layer Climates', in, pp. 273–294.

Oke, T. R. (1981) 'Canyon Geometry and the Urban Heat Island', *Journal of Climatology*, 1, pp. 237–254.

Oke, T. R. (1982) 'The energetic basis of the urban heat island', *Quarterly Journal of the Royal Meteorological Society*, 108(455), pp. 1–24. doi: 10.1002/qj.49710845502.

Oke, T. R. *et al.* (1991) *Simulation of surface urban heat islands under 'ideal' conditions at night part 2: Diagnosis of causation, Boundary-Layer Meteorology*. doi: 10.1007/BF00119211.

Oke, T. R. (1995) 'The heat island of the urban boundary layer: characteristics, causes and effects', *Wind Climate in Cities*, (January 1995). doi: 10.1007/978-94-017-3686-2.

Oke, T. R. *et al.* (1999) 'The energy balance of central Mexico City during the dry season', in *Atmospheric Environment*, pp. 3919–3930. doi: 10.1016/S1352-2310(99)00134-X.

Oke, T. R. (2004) 'Initial Guidance To Obtain Representative Meteological Observations at Urban Sites', *WMO IOM*, 81(1250).

Oke, T. R. (2006) 'Towards better scientific communication in urban climate', *Theor. Appl. Climatol*, 84, pp. 179–190. doi: 10.1007/s00704-005-0153-0.

Oke, T. R. *et al.* (2017) *Urban Climates, Urban Climates*. doi: 10.1017/9781139016476.

Oke, T. R., Zeuner, G. and Jauregui, E. (1992) *The surface energy balance in Mexico City, Atmospheric Environment*.

Oleson, K. (2012) 'Contrasts between Urban and rural climate in CCSM4 CMIP5 climate change scenarios', *Journal of Climate*, 25(5), pp. 1390–1412. doi: 10.1175/JCLI-D-11-

00098.1.

Oleson, K. W. *et al.* (2011) 'An examination of urban heat island characteristics in a global climate model', *International Journal of Climatology*, 31(12), pp. 1848–1865. doi: 10.1002/joc.2201.

Oudin Åström, D., Bertil, F. and Joacim, R. (2011) 'Heat wave impact on morbidity and mortality in the elderly population: A review of recent studies', *Maturitas*, pp. 99–105. doi: 10.1016/j.maturitas.2011.03.008.

Ouyang, W. *et al.* (2020) 'Vertical difference of climate change impacts on vegetation at temporal-spatial scales in the upper stream of the Mekong River Basin', *Science of the Total Environment*, 701, p. 134782. doi: 10.1016/j.scitotenv.2019.134782.

Park, H. and Jeong, S. (2021) 'Leaf area index in Earth system models: how the key variable of vegetation seasonality works in climate projections', *Environmental Research Letters*, 16(3), p. 034027. doi: 10.1088/1748-9326/ABE2CF.

Parker, W. S. (2016) 'Reanalyses and observations: What's the Difference?', *Bulletin of the American Meteorological Society*, pp. 1565–1572. doi: 10.1175/BAMS-D-14-00226.1.

Paschalis, A. *et al.* (2021) 'Urban Forests as Main Regulator of the Evaporative Cooling Effect in Cities', *AGU Advances*, 2(2). doi: 10.1029/2020av000303.

Pedregosa, F. *et al.* (2011) 'Scikit-learn: Machine Learning in Python', p. 2825−2830.

Peng, J. *et al.* (2018) 'Spatial-temporal change of land surface temperature across 285 cities in China: An urban-rural contrast perspective', *Science of the Total Environment*, 635, pp. 487–497. doi: 10.1016/j.scitotenv.2018.04.105.

Peng, J. *et al.* (2020) 'Quantifying spatial morphology and connectivity of urban heat islands in a megacity: A radius approach', *Science of the Total Environment*, 714, p. 136792. doi: 10.1016/j.scitotenv.2020.136792.

Peng, S. *et al.* (2012) 'Surface urban heat island across 419 global big cities', *Environmental Science and Technology*, 46(2), pp. 696–703. doi: 10.1021/es2030438.

Peng, W. *et al.* (2022) 'Urban Climate Surface and canopy urban heat islands : Does urban morphology result in the spatiotemporal differences?', *Urban Climate*, 42(February), p. 101136. doi: 10.1016/j.uclim.2022.101136.

Pichierri, M., Bonafoni, S. and Biondi, R. (2012) 'Satellite air temperature estimation for monitoring the canopy layer heat island of Milan', *Remote Sensing of Environment*, 127, pp. 130–138. doi: 10.1016/j.rse.2012.08.025.

Ploton, P. *et al.* (2020) 'Spatial validation reveals poor predictive performance of large-scale ecological mapping models', *Nature Communications 2020 11:1*, 11(1), pp. 1–11. doi: 10.1038/s41467-020-18321-y.

Potithep, S. *et al.* (2010) 'What is the actual relationship between LAI and VI in a deciduous broadleaf forest?', *International Archives of the Photogrammetry, Remote Sensing and Spatial Information Science*, XXXVIII(8), pp. 609–614.

Prakash, S. *et al.* (2018) 'Estimation of consistent global microwave land surface emissivity from AMSR-E and AMSR2 observations', *Journal of Applied Meteorology and Climatology*, 57(4), pp. 907–919. doi: 10.1175/JAMC-D-17-0213.1.

Puplampu, D. A. and Boafo, Y. A. (2021) 'Exploring the impacts of urban expansion on green spaces availability and delivery of ecosystem services in the Accra metropolis', *Environmental Challenges*, 5(July), p. 100283. doi: 10.1016/j.envc.2021.100283.

Quan, J. *et al.* (2013) 'Detecting changing trajectory of urban heat island using Gaussian model in Beijing, China', in *International Geoscience and Remote Sensing Symposium (IGARSS)*, pp. 3841–3844. doi: 10.1109/IGARSS.2013.6723669.

Quan, J. *et al.* (2014) 'Multi-temporal trajectory of the urban heat island centroid in Beijing, China based on a Gaussian volume model', *Remote Sensing of Environment*, 149, pp. 33–46. doi: 10.1016/j.rse.2014.03.037.

Rajasekar, U. and Weng, Q. (2009) 'Urban heat island monitoring and analysis using a non-parametric model: A case study of Indianapolis', *ISPRS Journal of Photogrammetry and Remote Sensing*, 64(1), pp. 86–96. doi: 10.1016/j.isprsjprs.2008.05.002.

Rasmussen, C. E. and Williams, C. K. I. (2006) *Gaussian Processes for Machine Learning*, *Journal fur Urologie und Urogynakologie*.

Rasul, A. *et al.* (2017) 'A Review on Remote Sensing of Urban Heat and Cool Islands', *Land*, 6(2), p. 38. doi: 10.3390/land6020038.

Rasul, A., Balzter, H. and Smith, C. (2015) 'Spatial variation of the daytime Surface Urban Cool Island during the dry season in Erbil, Iraqi Kurdistan, from Landsat 8', *Urban Climate*, 14, pp. 176–186. doi: 10.1016/j.uclim.2015.09.001.

Ren, G. Y. *et al.* (2007) 'Implications of temporal change in urban heat island intensity observed at Beijing and Wuhan stations', *Geophysical Research Letters*, 34(5). doi: 10.1029/2006GL027927.

Revi, A. *et al.* (2014) 'Urban areas', *Climate Change 2014: Impacts, Adaptation, and Vulnerability. Part A: Global and Sectoral Aspects. Contribution of Working Group II to the Fifth Assessment Report of the Intergovernmental Panel on Climate Change [Field, C.B., V.R. Barros, D.J. Dokken, K.J.*, pp. 535–612.

Richardson, A. D. *et al.* (2013) 'Climate change, phenology, and phenological control of vegetation feedbacks to the climate system', *Agricultural and Forest Meteorology*, 169, pp. 156–173. doi: 10.1016/j.agrformet.2012.09.012.

De Ridder, K. (2006) 'Testing Brutsaert's temperature roughness parameterization for representing urban surfaces in atmospheric models', *Geophysical Research Letters*, 33(13), p. L13403. doi: 10.1029/2006GL026572.

De Ridder, K., Lauwaet, D. and Maiheu, B. (2015) 'UrbClim - A fast urban boundary layer climate model', *Urban Climate*, 12, pp. 21–48. doi: 10.1016/j.uclim.2015.01.001.

Robinson, P. J. (2001) 'On the definition of a heat wave', *Journal of Applied Meteorology*, 40(4), pp. 762–775. doi: 10.1175/1520-0450(2001)040<0762:OTDOAH>2.0.CO;2.

Rohini, P., Rajeevan, M. and Mukhopadhay, P. (2019) 'Future projections of heat waves over India from CMIP5 models', *Climate Dynamics*, 53(1), pp. 975–988. doi: 10.1007/s00382-019-04700-9.

Romero-Lankao, P. and Dodman, D. (2011) 'Cities in transition: Transforming urban centers from hotbeds of GHG emissions and vulnerability to seedbeds of sustainability and resilience. Introduction and Editorial overview', *Current Opinion in Environmental Sustainability*, pp. 113–120. doi: 10.1016/j.cosust.2011.02.002.

Rotach, M. W. (1999) 'On the influence of the urban roughness sublayer on turbulence and dispersion', *Atmospheric Environment*, 33(24–25), pp. 4001–4008. doi: 10.1016/S1352-2310(99)00141-7.

Roth, M. (2000) 'Review of atmospheric turbulence over cities', *Quarterly Journal of the Royal Meteorological Society*, 126(564), pp. 941–990. doi: 10.1002/qj.49712656409.

Roth, M. (2007) 'Review of urban climate research in (sub)tropical regions', *INTERNATIONAL JOURNAL OF CLIMATOLOGY Int. J. Climatol*, 27, pp. 1859–1873. doi: 10.1002/joc.1591.

Roth, M. and Oke, T. R. (1989) 'Satellite-derived urban heat islands from three coastal cities and the utilization of such data in urban climatology', *International Journal of Remote Sensing*, 10(11), pp. 1699–1720.

Sailor, D. J. (2011) 'A review of methods for estimating anthropogenic heat and moisture emissions in the urban environment', *International Journal of Climatology*, 31(2), pp. 189–199. doi: 10.1002/joc.2106.

Sakakibara, Y. and Owa, K. (2005) 'Urban-rural temperature differences in coastal cities: influence of rural sites', *International Journal of Climatology*, 25(6), pp. 811–820. doi: 10.1002/joc.1180.

Salamanca, F. *et al.* (2011) 'A study of the urban boundary layer using different urban parameterizations and high-resolution urban canopy parameters with WRF', *Journal of Applied Meteorology and Climatology*, 50(5), pp. 1107–1128. doi: 10.1175/2010JAMC2538.1.

Salamanca, F. P. and Mahalov, A. (2019) 'Summer- and Wintertime Variations of the Surface and Near-Surface Urban Heat Island in a Semiarid Environment', *Weather and Forecasting*, 34(6), pp. 1849–1865. doi: 10.1175/WAF-D-19-0054.1.

Saleh, A. K. M. E., Arashi, M. and Kibria, B. M. G. (2019) 'Theory of ridge regression estimation with applications'. Available at: http://proquest.safaribooksonline.com/?fpi=9781118644614.

Sanderson, B. M., Knutti, R. and Caldwell, P. (2015) 'Addressing interdependency in a multimodel ensemble by interpolation of model properties', *Journal of Climate*, 28(13), pp. 5150–5170. doi: 10.1175/JCLI-D-14-00361.1.

Santamouris, M. (2015) 'Analyzing the heat island magnitude and characteristics in one hundred Asian and Australian cities and regions', *Science of the Total Environment*, 512–513, pp. 582–598. doi: 10.1016/j.scitotenv.2015.01.060.

dos Santos, R. S. (2020) 'Estimating spatio-temporal air temperature in London (UK) using machine learning and earth observation satellite data', *International Journal of Applied Earth Observation and Geoinformation*, 88(February), p. 102066. doi: 10.1016/j.jag.2020.102066.

Sarkar, A. and de Ridder, K. (2011) 'The Urban Heat Island Intensity of Paris: A Case Study Based on a Simple Urban Surface Parametrization', *Boundary-Layer Meteorology*, 138(3), pp. 511–520. doi: 10.1007/s10546-010-9568-y.

Schaaf, C. *et al.* (2015) 'MODIS MCD43 Product User Guide V005'. doi: 10.5067/MODIS/MCD43A3.006.

Schatz, J. and Kucharik, C. J. (2014) 'Seasonality of the urban heat island effect in Madison, Wisconsin', *Journal of Applied Meteorology and Climatology*, 53(10), pp. 2371–2386. doi: 10.1175/JAMC-D-14-0107.1.

van der Schriek, T. *et al.* (2020) 'Projected future temporal trends of two different urban heat islands in Athens (Greece) under three climate change scenarios: A statistical approach', *Atmosphere*, 11(6), pp. 1–25. doi: 10.3390/atmos11060637.

Schwarz, N., Lautenbach, S. and Seppelt, R. (2011) 'Exploring indicators for quantifying surface urban heat islands of European cities with MODIS land surface temperatures', *Remote Sensing of Environment*, 115(12), pp. 3175–3186. doi: 10.1016/j.rse.2011.07.003.

Schwarz, N. and Manceur, A. M. (2015) 'Analyzing the influence of urban forms on surface urban heat Islands in Europe', *Journal of Urban Planning and Development*, 141(3). doi: 10.1061/(ASCE)UP.1943-5444.0000263.

Segal, M. *et al.* (1997) 'Small Lake Daytime Breezes: Some Observational and Conceptual Evaluations', *Bulletin of the American Meteorological Society*, 78(6), pp. 1135–1147. doi: 10.1175/1520-0477(1997)078<1135:SLDBSO>2.0.CO;2.

Seland, Ø. *et al.* (2020) 'Overview of the Norwegian Earth System Model (NorESM2) and key climate response of CMIP6 DECK, historical, and scenario simulations', *Geosci. Model Dev.*, 13, pp. 6165–6200.

Servén, D. and Brummitt, C. (2018) 'pyGAM: Generalized Additive Models in Python'.

Shao, H. and Kim, G. (2022) 'A Comprehensive Review of Different Types of Green Infrastructure to Mitigate Urban Heat Islands: Progress, Functions, and Benefits', *Land 2022, Vol. 11, Page 1792*, 11(10), p. 1792. doi: 10.3390/LAND11101792.

Sharma, R. *et al.* (2016) 'Application of UrbClim for an Asian tropical city - The case of Delhi', in *European Space Agency, (Special Publication) ESA SP*. Available at: https://www.researchgate.net/publication/323113931 (Accessed: 2 May 2020).

Shashua-Bar, L. and Hoffman, M. E. (2000) 'Vegetation as a climatic component in the design of an urban street. An empirical model for predicting the cooling effect of urban green areas with trees', *Energy and Buildings*, 31(3), pp. 221–235. doi: 10.1016/S0378-7788(99)00018-3.

Shen, C. *et al.* (2022) 'Evaluation of global terrestrial near-surface wind speed simulated by CMIP6 models and their future projections', *Annals of the New York Academy of Sciences*, 1518(1), pp. 249–263. doi: 10.1111/nyas.14910.

Sherman, P., Lin, H. and McElroy, M. (2022) 'Projected global demand for air conditioning associated with extreme heat and implications for electricity grids in poorer countries', *Energy and Buildings*, 268, p. 112198. doi: 10.1016/j.enbuild.2022.112198.

Sidiqui, P., Huete, A. and Devadas, R. (2016) 'Heat Island Patterns over Sydney, Australia using MODIS and Landsat-8', *2016 Fourth International Workshop on Earth Observation and Remote Sensing Applications*.

Silber, I. *et al.* (2019) 'Cloud influence on ERA5 and AMPS surface downwelling longwave radiation biases in West Antarctica', *Journal of Climate*, 32(22), pp. 7935–7949. doi: 10.1175/JCLI-D-19-0149.1.

Silva, R. *et al.* (2022) 'Lisbon urban heat island in future urban and climate scenarios', *Urban Climate*, 44(May), p. 101218. doi: 10.1016/j.uclim.2022.101218.

Singh, P., Kikon, N. and Verma, P. (2017) 'Impact of land use change and urbanization on urban heat island in Lucknow city, Central India. A remote sensing based estimate', *Sustainable Cities and Society*, 32, pp. 100–114. doi: 10.1016/j.scs.2017.02.018.

Snow, A. D. *et al.* (2021) 'pyproj4/pyproj: 3.0.1rc0'. doi: 10.5281/zenodo.4571637.

Snyder, W. C. *et al.* (1998) 'Classification-based emissivity for land surface temperature measurement from space', *International Journal of Remote Sensing*, 19(14), pp. 2753–2774. doi: 10.1080/014311698214497.

Sofer, M. and Potchter, O. (2006) 'The urban heat island of a city in an arid zone: The case of Eilat, Israel', *Theoretical and Applied Climatology*, 85(1–2), pp. 81–88. doi: 10.1007/s00704-005-0181-9.

Stewart, I. D. (2007) 'Landscape representation and the urban-rural dichotomy in empirical

urban heat island literature, 1950–2006', *Acta Climatologica et Chorologica*, 40(41), pp. 111–121.

Stewart, I. D. and Oke, T. R. (2012) 'Local climate zones for urban temperature studies', *Bulletin of the American Meteorological Society*, 93(12), pp. 1879–1900. doi: 10.1175/BAMS-D-11-00019.1.

Stocker, T. F. *et al.* (2013) *IPCC, 2013: Climate Change 2013: The Physical Science Basis:Contribution of Working Group I to the Fifth Assessment Report of the Intergovernmental Panel on Climate Change, Cambridge University Press, Cambridge, United Kingdom and New York, NY, USA*. doi: 10.1017/CBO9781107415324.Summary.

Streutker, D. R. (2002) 'A remote sensing study of the urban heat island of Houston, Texas', *International Journal of Remote Sensing*, 23(13), pp. 2595–2608. doi: 10.1080/01431160110115023.

Stumpf, R. (2012) 'Distance to Nearest Coastline: 0.01-Degree Grid', *NASA Goddard Space Flight Center (GSFC) Ocean Color Group*. Available at: https://oceancolor.gsfc.nasa.gov/docs/distfromcoast/.

Sugawara, H. and Takamura, T. (2014) 'Surface Albedo in Cities: Case Study in Sapporo and Tokyo, Japan', *Boundary-Layer Meteorology*, 153(3), pp. 539–553. doi: 10.1007/s10546-014-9952-0.

Sun, T., Sun, R. and Chen, L. (2020) 'The trend inconsistency between land surface temperature and near surface air temperature in assessing Urban heat island effects', *Remote Sensing*, 12(8). doi: 10.3390/RS12081271.

Sundborg, Å. (1950) 'Local Climatological Studies of the Temperature Conditions in an Urban Area', *Tellus*, 2(3), pp. 222–232. doi: 10.3402/tellusa.v2i3.8544.

Suter, I. *et al.* (2022) 'UDALES 1.0: A large-eddy simulation model for urban environments', *Geoscientific Model Development*, 15(13), pp. 5309–5335. doi: 10.5194/gmd-15-5309-2022.

Swart, N. C. *et al.* (2019) 'The Canadian Earth System Model version 5 (CanESM5.0.3)', 5, pp. 4823–4873. doi: https://doi.org/10.5194/gmd-12-4823-2019.

Tan, M. and Li, X. (2015) 'Quantifying the effects of settlement size on urban heat islands in fairly uniform geographic areas', *Habitat International*, 49, pp. 100–106. doi: 10.1016/j.habitatint.2015.05.013.

Tatebe, H. *et al.* (2019) 'Description and basic evaluation of simulated mean state, internal variability, and climate sensitivity in MIROC6 Hiroaki', *Geosci. Model Dev.*, 12, pp. 2727–2765. doi: https://doi.org/10.5194/gmd-12-2727-2019.

Taylor, J. *et al.* (2015) 'Mapping the effects of urban heat island, housing, and age on excess heat-related mortality in London', *Urban Climate*, 14, pp. 517–528. doi: 10.1016/j.uclim.2015.08.001.

Tebaldi, C. *et al.* (2021) 'Climate model projections from the Scenario Model Intercomparison Project (ScenarioMIP) of CMIP6', *Earth System Dynamics*, 12(1), pp. 253–293. doi: 10.5194/esd-12-253-2021.

Tempfli, K. *et al.* (2009) *Principles of Remote Sensing: An Introductory Textbook*. Volume 2 o.

Teng, H. *et al.* (2023) 'Future changes and driving factors of global peak vegetation growth based on CMIP6 simulations', *Ecological Informatics*, 75(November 2022), p. 102031. doi: 10.1016/j.ecoinf.2023.102031.

Tewari, M. *et al.* (2017) 'Impacts of projected urban expansion and global warming on cooling energy demand over a semiarid region', *Atmospheric Science Letters*, 18(11), pp. 419–426. doi: 10.1002/asl.784.

The pandas development team (2023) 'Pandas (v2.1.1)'. doi: https://doi.org/10.5281/zenodo.8364959.

Theeuwes, N. E. *et al.* (2019) 'Persistent cloud cover over mega-cities linked to surface heat release', *npj Climate and Atmospheric Science*, 2(1), pp. 1–6. doi: 10.1038/s41612-019-0072-x.

Thiis, T. K. *et al.* (2017) 'Monitoring and Simulation of Diurnal Surface Conditions of a Wooden Façade', *Procedia Environmental Sciences*, 38(1878), pp. 331–339. doi: 10.1016/j.proenv.2017.03.088.

Tian, B. and Dong, X. (2020) 'The Double-ITCZ Bias in CMIP3, CMIP5, and CMIP6 Models Based on Annual Mean Precipitation', *Geophysical Research Letters*, 47(8), pp. 1–11. doi: 10.1029/2020GL087232.

Tiangco, M., Lagmay, A. M. F. and Argete, J. (2008) 'ASTER-based study of the night-time urban heat island effect in Metro Manila', *International Journal of Remote Sensing*, 29(10), pp. 2799–2818. doi: 10.1080/01431160701408360.

Tomlinson, C. J. *et al.* (2011) 'Remote sensing land surface temperature for meteorology and climatology: A review', *Meteorological Applications*, pp. 296–306. doi: 10.1002/met.287.

Tomlinson, C. J. *et al.* (2012) 'Derivation of Birmingham's summer surface urban heat island from MODIS satellite images', *International Journal of Climatology*, 32(2), pp. 214–224. doi: 10.1002/joc.2261.

Toparlar, Y. *et al.* (2017) 'A review on the CFD analysis of urban microclimate', *Renewable and Sustainable Energy Reviews*, 80, pp. 1613–1640. doi: 10.1016/J.RSER.2017.05.248.

Tran, H. *et al.* (2006) 'Assessment with satellite data of the urban heat island effects in Asian mega cities', *International Journal of Applied Earth Observation and Geoinformation*, 8(1), pp. 34–48. doi: 10.1016/j.jag.2005.05.003.

Uehara, K. *et al.* (2000) 'Wind tunnel experiments on how thermal stratification affects flow in and above urban street canyons', *Atmospheric Environment*, 34(10), pp. 1553–1562. doi: 10.1016/S1352-2310(99)00410-0.

Unger, J. *et al.* (2010) 'Modeling of the urban heat island pattern based on the relationship between surface and air temperatures', *Idojaras*, 114(4), pp. 287–302.

United Nations, Department of Economic and Social Affairs, Population Division (2018) 'World Urbanisation Prospects: The 2018 Revision, Online Edition'.

United Nations, Department of Economic and Social Affairs, P. D. (2019) *World Urbanization Prospects: The 2018 Revision (ST/ESA/SER.A/420), New York: United Nations*. doi: 10.4054/DemRes.2005.12.9.

Unwin, D. J. (1980) 'The Synoptic Climatology of Birmingham's Urban Heat Island, 1965–74', *Weather*, pp. 43–50. doi: 10.1002/j.1477-8696.1980.tb03484.x.

Upmanis, H., Eliasson, I. and Lindqvist, S. (1998) 'The influence of green areas on nocturnal temperatures in a high latitude city (Goteborg, Sweden)', *International Journal of Climatology*, 18(6), pp. 681–700. doi: 10.1002/(SICI)1097-0088(199805)18:6<681::AID-JOC289>3.0.CO;2-L.

Venter, Z. S., Chakraborty, T. and Lee, X. (2021) 'Crowdsourced air temperatures contrast

satellite measures of the urban heat island and its mechanisms', *Science Advances*, 7(22), pp. 1–10. doi: 10.1126/sciadv.abb9569.

Virtanen, P. *et al.* (2020) 'SciPy 1.0: fundamental algorithms for scientific computing in Python', *Nature Methods*, 17(3), pp. 261–272. doi: 10.1038/S41592-019-0686-2.

Voldoire, A. *et al.* (2019) 'Evaluation of CMIP6 DECK Experiments Journal of Advances in Modeling Earth Systems', *Journal ofAdvances in Modeling Earth Systems*, 11, pp. 2177–2213. doi: 10.1029/2019MS001683.

Volodin, E., Mortikov, E. V and Kostrykin, S. (2018) 'Simulation of the modern climate using the INM-CM48 climate model', *Russ. J. Numer. Anal. Math. Modelling*, 33(6), pp. 367–374. doi: 10.1515/rnam-2018-0032.

Voogt, J. A. and Oke, T. R. (2003) 'Thermal remote sensing of urban climates', *Remote Sensing of Environment*, 86(3), pp. 370–384. doi: 10.1016/S0034-4257(03)00079-8.

Vukovich, F. M. (1971) 'Theoretical analysis of the effect of mean wind and stability on a heat island circulation characteristic of an urban complex', *Monthly Weather Review*, 99(12), pp. 919–926. doi: 10.1175/1520-0493(1971)099<0919:taoteo>2.3.co;2.

van Vuuren, D. P. *et al.* (2011) 'The representative concentration pathways: An overview', *Climatic Change*, 109(1), pp. 5–31. doi: 10.1007/s10584-011-0148-z.

Wan, Z. (2008) 'New refinements and validation of the MODIS Land-Surface Temperature/Emissivity products', *Remote Sensing of Environment*, 112(1), pp. 59–74. doi: 10.1016/j.rse.2006.06.026.

Wan, Z. (2013) *Collection-6 MODIS Land Surface Temperature Products Users' Guide*.

Wan, Z. and Dozier, J. (1996) 'A generalized split-window algorithm for retrieving land-surface temperature from space', *IEEE Transactions on Geoscience and Remote Sensing*, 34(4), pp. 892–905. doi: 10.1109/36.508406.

Wan, Z., Hook, S. and Hulley, G. (2015) *MYD11A2 MODIS/Aqua Land Surface Temperature/Emissivity 8-Day L3 Global 1km SIN Grid V006 [Data set]*, *NASA EOSDIS Land Processes DAAC*. doi: https://doi.org/10.5067/MODIS/MYD11A2.006.

Wang, H. *et al.* (2023) 'Machine learning applications on air temperature prediction in the urban canopy layer: A critical review of 2011–2022', *Urban Climate*, 49(July 2022), p. 101499. doi: 10.1016/j.uclim.2023.101499.

Wang, J. *et al.* (2015) 'Spatiotemporal Variation in Surface Urban Heat Island Intensity and Associated Determinants across Major Chinese Cities', *Remote Sensing 2015, Vol. 7, Pages 3670-3689*, 7(4), pp. 3670–3689. doi: 10.3390/RS70403670.

Wang, S. *et al.* (2019) 'Urban−rural gradients reveal joint control of elevated CO2 and temperature on extended photosynthetic seasons', *Nature Ecology and Evolution*, 3(7), pp. 1076–1085. doi: 10.1038/s41559-019-0931-1.

Wang, W., Yao, X. and Shu, J. (2020) 'Air advection induced differences between canopy and surface heat islands', *Science of the Total Environment*, 725, p. 138120. doi: 10.1016/j.scitotenv.2020.138120.

Ward, K. *et al.* (2016) 'Heat waves and urban heat islands in Europe: A review of relevant drivers', *Science of the Total Environment*, 569–570, pp. 527–539. doi: 10.1016/j.scitotenv.2016.06.119.

Waskom, M. (2021) 'seaborn: statistical data visualization', *Journal of Open Source Software*, 6(60), p. 3021. doi: 10.21105/joss.03021.

Wasser, L. *et al.* (2019) 'EarthPy: A Python package that makes it easier to explore and plot raster and vector data using open source Python tools.', *Journal of Open Source Software*, 4(43), p. 1886. doi: 10.21105/joss.01886.

Weng, Q., Lu, D. and Schubring, J. (2004) 'Estimation of land surface temperature-vegetation abundance relationship for urban heat island studies', *Remote Sensing of Environment*, 89(4), pp. 467–483. doi: 10.1016/j.rse.2003.11.005.

Wienert, U. and Kuttler, W. (2005) 'The dependence of the urban heat island intensity on latitude - A statistical approach', *Meteorologische Zeitschrift*, 14(5), pp. 677–686. doi: 10.1127/0941-2948/2005/0069.

Wong, N. H. and Yu, C. (2005) 'Study of green areas and urban heat island in a tropical city', *Habitat International*, 29(3), pp. 547–558. doi: 10.1016/j.habitatint.2004.04.008.

Wood, S. N. (2006) *Generalized additive models : an introduction with R*. doi: 10.1201/9781315370279/GENERALIZED-ADDITIVE-MODELS-SIMON-WOOD.

Wood, S. N. (2017) *Generalized additive models: An introduction with R, second edition*, *Generalized Additive Models: An Introduction with R, Second Edition*. doi: 10.1201/9781315370279/GENERALIZED-ADDITIVE-MODELS-SIMON-WOOD.

Wouters, H. *et al.* (2013) 'The diurnal evolution of the urban heat island of Paris: A model-based case study during Summer 2006', *Atmospheric Chemistry and Physics*, 13(17), pp. 8525–8541. doi: 10.5194/acp-13-8525-2013.

Wu, X. *et al.* (2019) 'Investigating surface urban heat islands in South America based on MODIS data from 2003-2016', *Remote Sensing*, 11(10). doi: 10.3390/rs11101212.

Xiong, Y. *et al.* (2012) 'The Impacts of Rapid Urbanization on the Thermal Environment: A Remote Sensing Study of Guangzhou, South China', *Remote Sensing*, 4(7), pp. 2033–2056. doi: 10.3390/rs4072033.

Yague, C., Zurita, E. and Martinez, A. (1991) 'Statistical Analysis of the Madrid Urban Heat Island', 25(3), pp. 327–332.

Yang, J. *et al.* (2022) 'Contributions of sea – land breeze and local climate zones to daytime and nighttime heat island intensity', *npj Urban Sustainability*, 2(12). doi: 10.1038/s42949-022-00055-z.

Yang, Q., Huang, X. and Li, J. (2017) 'Assessing the relationship between surface urban heat islands and landscape patterns across climatic zones in China', *Scientific Reports 2017 7:1*, 7(1), pp. 1–11. doi: 10.1038/s41598-017-09628-w.

Yang, Q., Huang, X. and Tang, Q. (2019) 'The footprint of urban heat island effect in 302 Chinese cities: Temporal trends and associated factors', *Science of the Total Environment*, 655, pp. 652–662. doi: 10.1016/j.scitotenv.2018.11.171.

Yang, W. *et al.* (2022) 'Climate, CO2, and Anthropogenic Drivers of Accelerated Vegetation Greening in the Haihe River Basin', *Remote Sensing*, 14(2). doi: 10.3390/rs14020268.

Yao, R. *et al.* (2018) 'Less sensitive of urban surface to climate variability than rural in Northern China', *Science of the Total Environment*, 628–629, pp. 650–660. doi: 10.1016/j.scitotenv.2018.02.087.

Yao, R. *et al.* (2021) 'Long-term trends of surface and canopy layer urban heat island intensity in 272 cities in the mainland of China', *Science of the Total Environment*, 772, p. 145607. doi: 10.1016/j.scitotenv.2021.145607.

Yoshikado, H. (1994) 'Interaction of the sea breeze with urban heat islands of different sizes

and locations', *Journal of the Meteorological Society of Japan*, pp. 139–143. doi: 10.2151/jmsj1965.72.1_139.

Yuan, W. *et al.* (2021) 'Projecting Future Vegetation Change for Northeast China Using CMIP6 Model', *Remote Sensing 2021, Vol. 13, Page 3531*, 13(17), p. 3531. doi: 10.3390/RS13173531.

Zhang, H., Nettleton, D. and Zhu, Z. (2019) 'Regression-Enhanced Random Forests', *JSM Proceedings*, (1). doi: https://doi.org/10.48550/arXiv.1904.10416.

Zhang, X. *et al.* (2004) 'The footprint of urban climates on vegetation phenology', *Geophysical Research Letters*, 31(12), pp. 10–13. doi: 10.1029/2004GL020137.

Zhao, L. *et al.* (2014) 'Strong contributions of local background climate to urban heat islands', *Nature*, 511(7508), pp. 216–219. doi: 10.1038/nature13462.

Zhao, Q. *et al.* (2020) 'Future greening of the Earth may not be as large as previously predicted', *Agricultural and Forest Meteorology*, 292–293, p. 108111. doi: 10.1016/J.AGRFORMET.2020.108111.

Zhao, S., Zhou, D. and Liu, S. (2016) 'Data concurrency is required for estimating urban heat island intensity', *Environmental Pollution*, 208, pp. 118–124. doi: 10.1016/j.envpol.2015.07.037.

Zheng, G. and Moskal, L. M. (2009) 'Retrieving Leaf Area Index (LAI) Using Remote Sensing: Theories, Methods and Sensors', *Sensors (Basel, Switzerland)*, 9(4), p. 2719. doi: 10.3390/S90402719.

Zhou, B. *et al.* (2016) 'Assessing seasonality in the surface urban heat island of London', *Journal of Applied Meteorology and Climatology*, 55(3), pp. 493–505. doi: 10.1175/JAMC-D-15-0041.1.

Zhou, B. *et al.* (2019) '"Surface," "satellite" or "simulation": Mapping intra-urban microclimate variability in a desert city', *International Journal of Climatology*, p. joc.6385. doi: 10.1002/joc.6385.

Zhou, B., Rybski, D. and Kropp, J. P. (2013) 'On the statistics of urban heat island intensity', *Geophysical Research Letters*, 40(20), pp. 5486–5491. doi: 10.1002/2013GL057320.

Zhou, B., Rybski, D. and Kropp, J. P. (2017) 'The role of city size and urban form in the surface urban heat island', *Scientific Reports*, 7(1). doi: 10.1038/s41598-017-04242-2.

Zhou, D. *et al.* (2014) 'Surface urban heat island in China's 32 major cities: Spatial patterns and drivers', *Remote Sensing of Environment*, 152, pp. 51–61. doi: 10.1016/j.rse.2014.05.017.

Zhou, D. *et al.* (2016) 'Climate-vegetation control on the diurnal and seasonal variations of surface urban heat islands in China', *Environmental Research Letters*, 11(7), p. 74009. doi: 10.1088/1748-9326/11/7/074009.

Zhou, D. *et al.* (2019) 'Satellite remote sensing of surface urban heat islands: Progress, challenges, and perspectives', *Remote Sensing*, 11(1), pp. 1–36. doi: 10.3390/rs11010048.

Zhou, J. *et al.* (2011) 'Maximum Nighttime Urban Heat Island (UHI) Intensity Simulation by Integrating Remotely Sensed Data and Meteorological Observations', *IEEE Journal of Selected Topics in Applied Earth Observations and Remote Sensing*, 4(1), pp. 138–146. doi: 10.1109/JSTARS.2010.2070871.

Zhou, Y. *et al.* (2019) 'Sea breeze cooling capacity and its influencing factors in a coastal city', *Building and Environment*, 166, p. 106408. doi: 10.1016/j.buildenv.2019.106408.

Zhu, D. *et al.* (2021) 'Non-optimum temperature-related mortality burden in China: Addressing the dual influences of climate change and urban heat islands', *Science of the Total Environment*, 782, p. 146760. doi: 10.1016/j.scitotenv.2021.146760.

Zhu, X. *et al.* (2017) 'An idealized LES study of urban modification of moist convection', *Quarterly Journal of the Royal Meteorological Society*, 143(709), pp. 3228–3243. doi: 10.1002/QJ.3176.

Zhuang, J. *et al.* (2021) 'pangeo-data/xESMF: v0.5.3'. doi: https://doi.org/10.5281/zenodo.4294774.

Ziehn, T. *et al.* (2020) 'The Australian Earth System Model: ACCESS-ESM1.5', *Journal ofSouthern Hemisphere Earth Systems Science*, 70, pp. 193–214. doi: https://doi.org/10.1071/ES19035.

Software

Thanks to the Centre for Environmental Data Analysis (CEDA) for the data accessed via the CEDA catalogue (EVI, Albedo, Landcover_cci) and use of the JASMIN supercomputer.

Some of the work in this thesis was also carried out on the High-Performance Computing Cluster supported by the Research and Specialist Computing Support service at the University of East Anglia.

Python packages used in the undertaking of this thesis are listed in Table A.5.18.

A. APPENDIX

A.1. LITERATURE REVIEW SUPPLEMENTARY MATERIAL

Table A.1.1 Studies which compare the CUHI and SUHI and the findings relevant to the comparison.

Reference	Cities Studied	Method	Findings
(Unger *et al.*, 2010)	Szeged (Hungary)	• LST data collected by airborne thermal infrared sensor. • 1.5m air temperature data collected using a car-based temperature sensor. • Both collected simultaneously. • 2 days in August	• Air and surface temperature measurements have a strong relationship, with air temperature being strongly influenced by the temperatures of the surrounding surfaces.
(Azevedo *et al.*, 2016)	Birmingham (UK)	• LST data from MODIS aqua satellite sensor (13:30, 01:30 overpasses). • Air temperature data from high resolution meteorological network of temperature sensors and weather station interpolated using kriging. • Weather station (surrounding pixel for LST) used as rural reference area. • Daytime 06:00-17:59 air temperature, 13:30 overpass for LST, Night-time 18:00-05:59 for air temperature, 01:30 overpass for LST. Day/ nights then averaged based on weather condition stability classes. • June, July, August 2013.	• During the day there is a clear SUHI for all weather conditions, but for the CUHI, only the city centre is warmer than the reference. • The hottest areas of the CUHI and SUHI are both the urban core, but the CUHI thermal core extends in a different direction to the SUHI, influenced by the wind direction. The SUHI is influenced by land use. • Daytime CUHI-SUHI intensity differences (at overpass time) vary with land use. • Night-time SUHI and CUHI spatial patterns are similar to daytime. • The SUHI is consistently greater than the CUHI (day and night).
(Ma *et al.*, 2016)	Shanghai (China)	• LST data from MODIS satellite sensor (10:30 overpass used) • Air temperature data from weather stations, at 08:00 and 14:00, linearly interpolated to estimate satellite overpass time.	• Pearson's correlation between MODIS LST and air temperature is 0.836. Split into months, correlations were highest in Autumn (October, 0.828) and lowest in Summer (July, 0.131). Differences in summer could be due to vegetation. • SUHI is consistently larger than the CUHI.

		• January, April, July, October 2007 and 2008.	
(Hu *et al.*, 2019)	Beijing, Shanghai, Guangzhou (China)	• LST data from MODIS satellite sensor, 8-day composite (10:30. 13:30, 22:30 and 01:30 overpasses used). • Air temperature data from 19 urban and rural weather stations. • 2003 to 2016, grouped into seasons	• Annual mean SUHIs generally larger than CUHIs. • The largest differences between SUHI and CUHI magnitude occur in summer. • The SUHI is largest in the summer and the CUHI is largest in winter.
(Feng *et al.*, 2019)	Birmingham (UK)	• LST data from MODIS aqua satellite sensor (22:30 and 01:30 overpasses). • Air temperature data from high resolution meteorological network of temperature sensors (20) and weather stations (2) • Simultaneous temperatures compared. • Weather station (surrounding pixel for LST) used as rural reference area. • June 2013 to August 2014	• The SUHI-CUHI relationship weakens as wind speed increases and seasonally is weakest in winter (colder weather). • A CUHI is found to exist in cases when the SUHI is zero. • The CUHI and SUHI are more correlated in the urban areas versus the suburban, but a relationship between the two exists for both. • CUHI is impacted more than SUHI by wind speed.
(Wang *et al.*, 2020)	Shanghai, Beijing, Taipei (China), Birmingham (UK)	• LST data from MODIS satellite sensor (10:30, 13:30, 22:30, 01:30 overpasses). • 1.5m air temperature data from weather stations interpolated using kriging. • Simultaneous temperatures compared. • Rural reference area used. For the air temperature, stations warmer than the rest due to air plume from city removed. • WRF-UCM simulation run to examine mechanisms.	• 9% (201 out of 2232) CUHI-SUHI pairs were significantly different, with correlation coefficients of less than 0.2. • Beijing and Shanghai had greater differences in the CUHI-SUHI then Taipai and Birmingham which may be attributed to the mountain-valley breeze in Beijing and sea-land breeze in Shanghai. • SUHI intensity is consistently greater than the CUHI, and differences are greatest during the day (mean 1.88°C) than at night (0.63°C). Differences attributed to air advection. • Static estimations of the CUHI (i.e., weather station pairs) are not appropriate for CUHI studies as downwind rural areas are impacted by the CUHI.

		• Multiple images over 2014-2016 for Birmingham, 2012-2014 for other cities.	
(Sun *et al.*, 2020)	Baoding, Beijing, Cangzhou, Chengde, Handan, Hengshui, Langfang, Qinhuangdao, Shijiazhuang, Tangshan, Tianjin, Xingtai, Zhangjiakou (China)	• LST data from MODIS satellite sensor (10:30 and 22:30 overpasses) • 2m air temperature data from weather stations (16 urban, 158 rural) • Mean, maximum and minimum LST calculated using both overpasses, and extracted from weather station data for air temperature. • Rural reference area locations of rural weather stations. • 2001 to 2015.	• SUHI and CUHI calculated using mean temperatures were correlated, with a regression of SUHI on UHI giving R-squared valued of 0.794. Correlations not strong using minimum and maximum temperatures. • Both CUHI and SUHI show increasing trends, in line with increasing urbanisation of the cities.
(Gawuc *et al.*, 2020)	Warsaw (Poland)	• LST data from MODIS satellite sensor (22:30 and 01:30 overpasses) • Air temperature data from weather stations (21 total). • Simultaneous temperatures compared. • Rural reference area locations of rural weather stations. • 2008 to 2017, night-time only.	• Linear relationship between night-time CUHI and SUHI, with the strongest correlations where the station pairs have the highest CUHI intensity.
(Amorim *et al.*, 2021)	Presidente Prudente (Brazil),	• LST data from Landsat 8 satellite (daytime and night-time).	• Stronger SUHIs exist during the day (SUHI is recorded when not CUHI is shown), and CUHIs are greater than SUHIs during the night

	Rennes (France)	• Air temperature measurements taken at fixed urban and rural points (taken for 30 days). • Simultaneous temperature records. • 2019, images for President Prudente, October at 13:22, November at 01:50. Rennes November at 10:59, 21:33.	
(Yao *et al.*, 2021)	272 cities in China	• LST data from MODIS satellite sensor (10:30 and 22:30 overpasses) • Air temperature data from weather stations (697 total), mapped to a 1km resolution grid using satellite data. • Rural reference for the SUHI was a 'buffer' ring of area around outside of the city perimeter. • Seasonal mean temperatures used. • 2001-2018	• Trends in night-time SUHI and CUHI strongly related, but daytime the relationship is weak. • For the period studied, the CUHI increased. The SUHI increased apart from daytime winter.
(Venter *et al.*, 2021)	342 cities in Europe	• LST data from MODIS satellite sensor (10:30, 13:30, 22:30, 01:30 overpasses) • Air temperature data from crowdsourced citizen weather stations • Simultaneous temperature records. • July 2019 (month with heatwave)	• SUHI greater than the CUHI for 96% of cities during the day and 80% during the night. • Mean SUHI for all cities is 1.45°C versus CUHI of 0.26°C.
(Du *et al.*, 2021)	366 global cities	• LST data from MODIS satellite sensor (13:30 and 01:30 overpasses) • Air temperature data from urban-rural weather station pairs (monthly mean and minimum values).	• Annual mean SUHI is greater than CUHI by 1.1°C during the day and 0.3°C at night. • In equatorial, warm temperate, and snow climates SUHI is greater then CUHI, but in arid climates the SUHI is lower than CUHI (by 0.8°C) during the day.

		• Rural reference for the SUHI was a 'buffer' ring of area around outside of the city perimeter. • Monthly mean temperatures used. • 2012	
(Cao *et al.*, 2021)	Shenzhen (China)	• LST data from MODIS satellite sensor (13:30 and 22:30 overpasses). • Air temperature data from network of 117 weather stations. • 8-day composite used for LST but times simultaneous to air temperature (hourly measurements were taken). • 2017.	• Urban LST is significantly correlated with air temperature (daytime and night-time), but the locations of the cool and hot spots were not always the same.
(Berg and Kucharik, 2022)	Madison (USA)	• LST data from Landsat 7 and 8 satellite (11:30 and 23:30 overpasses) • 3.5m air temperature data from network of 146 temperature sensors, interpolated to 400m grid using kriging. • Simultaneous temperature records. • June, July, August 2012-2019	• Differences between LST and air temperature greatest during the day. • LST exhibits a greater temperature range than air temperature measured in the same location. • Rural temperatures vary dependent on rural reference point chosen.
(Amani-Beni *et al.*, 2022)	Beijing (China)	• LST data from Landsat 8 satellite (14:53 overpass) • Air temperature data from bicycle mounted sensors • Rural reference taken as centre of large park in the city (680 hectares in size). • Simultaneous temperature records. • 10 July 2017	• SUHI is larger than the CUHI. • LST and air temperature positively correlated, but cool and warm spots differ spatially.

(Peng *et al.*, 2022)	Kitakyushu (Japan)	• LST data from MODIS satellite sensor (10:30, 13:30, 22:30 and 01:30 overpasses). • Air temperature data from a gridded 1km dataset (from Japan Ministry of Land, Infrastructure, Transport and Tourism). • Rural reference area taken as a 10km 'buffer' ring around the perimeter of the city. • 2010	• Daytime SUHI and CUHI had similar spatial patterns but different spatial patterns at night. • Both CUHI and SUHI highest during summer daytime and weakest during winter night-time.
(Kumar *et al.*, 2023)	Delhi (India)	• LST data from MODIS satellite sensor (10:30 and 22:30 overpasses). • Air temperature data from 39 monitoring stations. • Seasonal means used. • Rural reference area taken as the non-urban pixels in the 39x39km study area. • 2019 to 2021	• The mean CUHI is greater than the mean SUHI in all 4 seasons (note this is both overpasses). • In winter, the hottest areas for the CUHI and SUHI are the same, but during spring • Both CUHI and SUHI show increasing trends in spatial extent for the study period.

Table A.1.2 Statistical models predicting the SUHI of cities based on input variables. Not all the studies have input variables related to climate, and climate variables can be seen highlighted in bold in the table.

Paper Reference	Cities studied	Models used	Input Variables	Test/Training split	Findings
(Schwarz and Manceur, 2015)	274 cities in Europe	Multiple Linear Regression	Land composition (size of each landcover type), elevation, population, distance to next city, **rainfall**, **temperature of coldest/ warmest month**, albedo, distance to coast, **sunshine hours,** latitude	Data split into 5. Resulting patterns did not change considerably between them, so results presented show one randomly chosen.	Explanatory power of the model is lower for the night-time SUHI. Population/city size variables most significant.
(Y. Li *et al.*, 2021)	5000 cities in Europe	Multiple Linear Regression Geographically Weighted Regression (GWR) Nonlinear Regression (Multiple Linear Regression model with variables transformed using sin, ln and functions of variables)	Summer average EVI, **precipitation, maximum 2m air temperature and 10m wind speed,** elevation, **solar radiation**, latitude	No split (all data included in model)	GWR captures the relationship better than linear regression. Nonlinear regression performance is better than linear and comparable to GWR. Colder, wetter, winder cities with more vegetated rural areas experience strongest SUHI.

(Li, Zha and Wang, 2020)	145 Global Cities (population over 1 mil and contain a weather station)	Linear Regression (separately for each variable)	**Air temperature**, **precipitation**	All data used as training/test	Stronger correlation of the SUHI intensity and precipitation than with air temperature. Positive correlation during the day and negative at night. Cities with greater urban rural vegetation differences enhance the SUHI.
(Zhou *et al.*, 2014)	32 cities in China	Multiple Linear Regression	Vegetation index, albedo, night-time lights, elevation, built-up intensity, urban size, **total precipitation, mean temperature**	Non-parametric bootstrapping, 1000 randomisations	Summer daytime SUHI primarily explained by night-time lights, and winter by temperature and precipitation
(Manoli *et al.*, 2019)	30,000 Global cities	Nonlinear physics modelling	**Precipitation**, population, albedo	n/a	Mean annual precipitation and population size are the strongest predictors, and have nonlinear relationships with the SUHI magnitude
(Ma *et al.*, 2021)	Over 3000 cities in China	Random Forest Regression	Anthropogenic heat flux, night light intensity, population density, morphological continuity, morphological fractal dimension, area size, elevation, **precipitation rate, solar radiation, air temperature, specific humidity, wind speed**	3-fold cross validation, split by time	Area size was the most influential in summer, urban development important winter. During the night, urban morphology was more important in predicting SUHI magnitude, but in the day natural factors were more important (climate variables and elevation)

(Liu *et al.*, 2021)	1288 cities in China	Multiple Linear Regression	urban size, shape, centrality	All data used as training/test	Stronger relationships observed in the daytime than night-time.
(Imhoff *et al.*, 2010)	38 cities in USA	Linear Regression (separately for each variable)	Impervious surface area (ISA), size grouped by biome (landcover type)	All data used as training/test	ISA good predictor of the LST for all biomes expect desert and xeric shrublands. A positive relationship between SUHI magnitude and city area is found.
(Peng *et al.*, 2018)	285 cities in China	Linear Regression	LST change over time	All data used as training/test	The SUHI is largest in summer daytime, and SUHI magnitude varies dependent on location of cities.
(Zhou *et al.*, 2017)	5000 cities in Europe	Multiple Linear Regression	City size, anisometry and fractal dimension	All data used as training/test	UHI intensity increases with log city size and fractal dimension, decreases with log anisometry.
(Clinton and Gong, 2013)	28,327 Global cities	Random Forest Regression (plus wrapped regression trees for variable selection) Cluster analysis	Latitude, longitude, population, nightlights, urban area, EVI, urban structure height	All data used as training/test	Development intensity, vegetation amount, size of urban metropolis were found to be the most important variables to predict SUHI intensity.
(Wang *et al.*, 2015)	67 cities in China	Random Forest Regression	Human-induced heat discharge factors, land surface, urban form, NDVI, albedo	Split by years (2003-2008 training, 2009-2010 test)	In Southern China the daytime SUHI was more intense, with annual electricity consumption & number public buses had greatest effect. The night-time SUHI was more intense in Northern China, where vegetation had greatest effect.

Methods of studying the UHI: Modelling

Parameterisations

There is a large body of research into the parameterisations of the urban surface scheme, with varying levels of complexity. Parameterisations of the urban surface in GCMs and RCMs can be split into 3 groups: bulk parameterisation, single level urban canopy models (UCMs) and multi-level UCMs. In bulk parameterisation, the urban surface is represented by bare soil or a flat plate with modified roughness length and thermal properties. There is reduced moisture availability to ensure sensible heat fluxes are favoured over latent (Masson, 2000; Martilli *et al.*, 2002; Best, 2005; Liu *et al.*, 2006). Single layer UCMs add more complexity. They represent the general characteristics of urban morphology, but do not take into account microscale aspects such as individual buildings or parks (Masson, 2000; Martilli *et al.*, 2002; Liu *et al.*, 2006). Kusaka (2001) developed a single layer UCM commonly used in WRF model simulations (see Table A.1.3). This UCM considers 3 surfaces (roofs, roads and walls) and the influence of shadowing and reflection of radiation due to canyon geometry. The most complex models are multi-level UCMs. These provide a more detailed representation of the urban form, dividing surfaces into a number of horizontal patches with their own energy balances (Grimmond *et al.*, 2010).

The parametrisation used depends on the goal of the study; multilevel UCMs are computationally expensive and require detailed input values, but are useful for studying complex urban interactions (Best, 2005; Chen *et al.*, 2011). More simple approaches can be useful for looking at the evolution of the CUHI over a number of months or years, with some schemes no more complex to implement than the traditional modelling methods used previously (Best, 2005). In an international comparison project, simple parameterisations were found to perform just as well as those more complex (Grimmond *et al.*, 2010) and represent the seasonal cycle of the CUHI even better (Best and Grimmond, 2013).

An additional note, which concerns parameterisations, but not those of the urban surface, is that improving on the horizontal grid resolution in RCMs has been shown by sensitivity experiments to be as important as improving the representation of the urban surface (Chin *et al.*, 2005). This can be done by using very high-resolution RCMs known as convection-permitting models (Argüeso *et al.*, 2014; Hamdi *et al.*, 2014). These models have small enough grid spaces to resolve convection processes, meaning parameterisations of convection, known to be very difficult and complex, are no longer required, therefore giving a more accurate depiction of the atmosphere (Leutwyler *et al.*, 2017). Finer resolution models also improve simulation of topography and coastlines of importance, as CUHIs are impacted by coastal locations, discussed in section 2.4 (Lowe *et al.*, 2019). Consequently, the ongoing research

into the improvement in resolutions of RCMs will lead to better prediction and projection of the UHI.

Table A.1.3 Some examples of regional climate models used in UHI studies.

Regional Climate Model	UHI studies using RCM	Cities	Spatial Resolution in studies	Temporal span in studies	Urban surface parameterisation used in studies
Hadley Centre Regional Climate Model (HadRM3)	(McCarthy *et al.*, 2011)	London (UK)	25km (Not convection resolving but latest model is)	Simulates 2060 scenario	Bulk (Best, 2005)
Weather Research and Forecast (WRF)	(Miao *et al.*, 2009; Chen *et al.*, 2011; Georgescu *et al.*, 2011; Argüeso *et al.*, 2014; Tewari *et al.*, 2017; Salamanca and Mahalov, 2019)	Tokyo, Osaka, Nagoya (Japan) Phoenix, Tuscan (USA) Sydney (Australia)	1 to 3km (Convection resolving (Chen *et al.*, 2011))	Used for present CUHI only in some studies Simulates to 2070 scenario	Single layer UCM (Kusaka *et al.*, 2001; Kusaka and Kimura, 2004) Multilayer UCM (Salamanca *et al.*, 2011)
Advanced Regional Prediction Systems (ARPS)	(Demuzere *et al.*, 2008; Sarkar and de Ridder, 2011; Wouters *et al.*, 2013)	Paris, Marseille (France)	1km (Convection resolving)	Only used to model present CUHI	Bulk (De Ridder, 2006)
ALARO, ARPEGE-IFS system	(Hamdi *et al.*, 2014)	Brussels (Belgium)	4km (Convection resolving)	Simulates 2100 scenario	Single layer UCM (Masson, 2000)

Computational Fluid Dynamics

Computational Fluid Dynamics (CFD) are a computational method of examining small scale UHI features. CFD models are used to capture complex physical processes to investigate their interactions with urban morphology, water bodies, vegetation and urban materials (Kubilay *et al.*, 2020). The models allow for the most detailed understanding of the local scale, and this not only is useful for understanding local processes, but also can contribute to parameterisation schemes in lower resolution circulation models (GCMs and RCMs). The downside of these

models is that detailed knowledge of urban geometry and boundary conditions is needed, and they are computationally expensive (Toparlar *et al.*, 2017). Often CFD models are coupled with building energy simulations to give measurements of the impact of aspects such as building height (Allegrini and Carmeliet, 2018) or CUHI mitigation methods (Kubilay *et al.*, 2020). A review of CFD studies finds two families of these models commonly employed, Reynolds-averaged Navier Stokes (RANS) equations or Large Eddy Simulations (LES). These refer to the representation of turbulence in the model. LES are considered more accurate, but have a higher computational expense then RANS (Toparlar *et al.*, 2017). A LES model specifically for urban environments, uDALES, has been developed by Suter et al (2022).

Lab-based scale modelling

Lab based models, aiming to emulate the structure of an urban area, are used in experiments to examine the effect of geometry and urban roughness. These typically scrutinise processes in the microscale (Figure 2.2), looking at behaviours within urban canyons but can also be used to investigate local (Figure 2.2) scale processes in less detail (Oke *et al.*, 1991; Uehara *et al.*, 2000; Kim and Baik, 2001). For example, Oke (1981) uses 50 plywood blocks in a heating chamber to represent a city and the same volume of flat wood as a rural representation, in order to investigate the effect of geometry at a local scale. Uehara (2000) examines the wind speed and temperatures of a street canyon model in a wind tunnel, looking at processes on a microscale. This type of modelling is useful to verify and calibrate mathematical models but has drawbacks in terms of the ability to simulate certain processes, such as radiation, and is also expensive (Mirzaei and Haghighat, 2010).

Influence of weather and climate

Meteorological influence of the UHI

Despite urban areas being known to reduce the wind flow due to urban roughness, they also create air flow in the form of country breezes, also known as urban breezes (Findlay and Hirt, 1969). Analogous to this sea breeze, the country breeze gradient forms from cooler country air and relatively warmer urban air (Vukovich, 1971; Hidalgo *et al.*, 2008). These country breezes supply cooler air to the urban area and are positively correlated with CUHI intensity; nocturnal hours where the CUHI intensity is greatest is when the country breeze occurs most frequently (Barlag and Kuttler, 1990).

Alongside the country breeze effect, the UHI may be responsible for other changes in the local scale weather, with observational (Grady Dixon and Mote, 2003) and modelling (Nie *et al.*, 2017; Zhu *et al.*, 2017) studies finding precipitation patterns are altered by the presence of a city. It is worth mentioning however, that there is still uncertainty as to whether this triggered

by the UHI. Zhu et al (2017) attribute the modifications to the urban comparative dryness to a rural area rather than the increased temperature. UHIs have also been linked to increased cloud cover over urban areas, attributed the warm rising air above urban surfaces feed moisture to the clouds. The authors attribute this persistence of cloud cover to the UHI rather than the increase in aerosols (due to pollution over cities) because of the cloud type. The type of cloud seen to persist is low and non-precipitating, which does not have its lifetime increased by aerosols (Theeuwes *et al.*, 2019).

Table A.1.4 Studies examining the future SUHI based on climate change scenarios. Many studies use RCMs and focus on one or two cities. Findings noted on the table are related to the impacts of climate change on the CUHI magnitude.

Reference	Cities Studied	Model used	Model Resolution	Climate Scenario	Urban Expansion	Findings
(Oleson *et al.*, 2011)	Global Model	Urban parameterisation couple to community land model (CLM)	(1.9 ° lat x 2.5° lon)	AR4 A2 (high emissions)	None	Slight decrease in the CUHI. Primarily due to different responses to increased long wave radiation due to atmospheric warming.
(McCarthy *et al.*, 2011)	UK cities	RCM (HadRM3 used to downscale HadCM3 (GCM))	25 km	SRES A1B (medium emissions)	None	The magnitude of the CUHI remains the same with 110 climate change.
(Hamdi *et al.*, 2014)	Brussels (Belgium)	Urban parameterisation (SURFEX and TEB) with limited area model (ARPEGE-IFS) and atmospheric model (ALARO)	1 km	SRES A1B (medium emissions)	None	Decreases found in the daytime CUHI and either no change or a decrease in the nocturnal CUHI in the period 2017- 2100.
(Argüeso *et al.*, 2014)	Sydney (Australia)	RCM (WRF) with GCM (CSIRO)	2 km	SRES A2 (high emissions)	Accounted for	Future urbanization will have strong effect on minimum urban temperatures (little on maximum), in the period 2040-2059.
(Lauwaet *et al.*, 2016)	Brussels (Belgium)	UrbClim (downscaled from COSMO-CLM)	250 m	RCP4.5 and RCP8.5 (medium and high emissions	None	The CUHI decreases slightly in 2060-2069 period for both emissions pathways. Only the

						summer months are investigated.
(Tewari *et al.*, 2017)	Arizona and Tucson (USA)	RCM (WRF)	1 km	RCP8.5 (high emissions)	Accounted for	Increase in temperature in both cities due to urban expansion and climate change.
(van der Schriek *et al.*, 2020)	Athens (Greece)	RCM (EURO-CORDEX)	12 km	RCP2.6, RCP4.5, and RCP8.5(low, medium, and high emissions)	None	Slight increase in summer CUHI in all RCP scenarios. The CUHI pushes the city temperatures to above heatwaves conditions, resulting in higher frequency of night-time heatwaves in city only.
(Allaga-Zsebeházi, 2021)	Budapest (Hungary)	RCM (HMS-ALADIN), SURFEX	1 km	RCP8.5 (high emissions)	None	Decrease in the CUHI intensity (most in Spring and Summer) by 2071 to 2100.
(Keppas *et al.*, 2021)	Rome (Italy) and Thessaloniki (Greece)	RCM (WRF)	2 km	RCP 8.5 (high emissions)	None	No significant changes in CUHI magnitude in the periods 2016-2050 or 2096-2100
(Silva *et al.*, 2022)	Lisbon (Portugal)	RCM (WRF)	1km	RCP 8.5 (high emissions)	Accounted for	Largest increase in the CUHI intensity by period 2081- 2100 during the night due to more urban landcover and less greenspace
(Andrade *et al.*, 2023)	Lisbon and Porto (Portugal)	RCMs from EURO-CORDEX without urban representations compared to UrbClim	0.11 °x 0.11 ° (UrbClim 100m)	RCP 8.5 (high emissions)	None	Summer daytime trends increase the most in to by period 2021-2050.

Table A.1.5 Studies which carry out SUHI analyses including large numbers of cities. The highest number of studies is in China, with seven studies in total.

Reference	Study area	Aim
(Tran *et al.*, 2006)	18 Asian megacities	Comparative assessment of SHI in temperate and tropical regions.
(Imhoff *et al.*, 2010)	38 most populous USA cities	Assess the SUHI and its relationship with development intensity, size and ecological setting.
(Schwarz *et al.*, 2011)	263 European cities	Examine the different indicators used to quantify the SUHI.
(Peng *et al.*, 2012)	419 Global cities	Assessment of the diurnal and seasonal variation of the SUHI.
(Clinton and Gong, 2013)	Global	Aims to identify the key factors that contribute to the SUHI.
(Zhou *et al.*, 2013)	All cities in Europe	Investigate relationships of SUHII with cluster size and temperature of the surroundings.
(Zhou *et al.*, 2014)	32 Chinese cities	Aims to quantify diurnal and seasonal SUHI, spatial patterns and drivers.
(Schwarz and Manceur, 2015)	Europe	Analysis of the urban form and its impact on SUHI.
(Wang *et al.*, 2015)	67 Chinese cities	Assessment of seasonal and diurnal variations of the SUHI and relationships with social, economic and natural factors.
(D. Zhou *et al.*, 2016)	China	Examine diurnal and seasonal cycles of SUHI intensity.
(Ward *et al.*, 2016)	70 European cities	Investigate the causes of SUHIs and its change during heat waves.
(Yang *et al.*, 2017)	332 Chinese cities	Assessment of the different landcover types on the SUHI.
(Zhou *et al.*, 2017)	Europe	Examine role of city size and urban form in the SUHI.
(Fu and Weng, 2018)	US cities (~2000)	Exploration of annual temperature cycles.
(Peng *et al.*, 2018)	285 Chinese cities	Analyse the spatial temporal change of LST .
(Li *et al.*, 2019)	60 North American cities	Analyses whether SUHI spatial variability is due to aerodynamics or imperviousness.

(Manoli *et al.*, 2019)	Global	Investigate relationships between SUHI and population and background climate.
(Chakraborty and Lee, 2019)	Global	Developed algorithm to categorise SUHIs on global scale and examine vegetation control.
(Wu *et al.*, 2019)	44 South American cities	Examination between SUHI intensity and influencing factors.
(Chakraborty and Lee, 2019)	9500 Global cities	Development and testing of a new method of SUHI quantification.
(Liu *et al.*, 2021)	1288 Chinese cities	Examination of how urban morphology impacts the SUHI intensity.
(Ma *et al.*, 2021)	3000 Chinese cities	Investigation of the SUHI seasonal and diurnal variations and how various human and natural factors influence its intensity.
(Mentaschi *et al.*, 2022)	9028 Global cities	Investigation into the extreme values of SUHI – both spatially within the city and in the study time period.

A.2. DATA SUMMARY TABLES

Table A.2.6 Datasets used for the city selection.

Dataset	Resolution	Temporal characteristics	Usage	Reference
United Nations population of urban Agglomerations	Nearest thousand population	Every 5 years from 1950 – 2035	To find cities across the globe with populations of between 300,000 and 1,000,000	(United Nations, Department of Economic and Social Affairs, Population Division, 2018)
NASA Goddard Space Flight centre Ocean Color Group distance to nearest coastline	0.01 degrees	-	To identify coastal cities	(Stumpf, 2012)
GloboLakes: high- resolution global limnology dataset v1	300m	Static waterbodies between 2005 and 2010	To identify cities near lakes	(Laura Carrea *et al.*, 2015)
Global Land One-kilometer Base Elevation (GLOBE) Digital Elevation Model dataset	1000m	-	To distinguish cities in hilly areas versus those on a plateau	(Hastings *et al.*, 1999)

Table A.2.7 Datasets used for the SUHI quantification.

Dataset	Resolution	Temporal characteristics	Usage	Reference
Terra Land Surface Temperature/ Emissivity 8-Day Global (MOD11A2)	1000m	Every 8 days from 2000-2020	Providing LST to calculate the Gaussian surface approximation	(Wan *et al.*, 2015)
Aqua Land Surface Temperature/ Emissivity 8-Day Global (MYD11A2)	1000m	Every 8 days from 2002-2020	Providing LST to calculate the Gaussian surface approximation	(Wan *et al.*, 2015)
ESA Land Cover Climate Change Initiative: Global Land Cover Maps, Version 2.0.7	300m	Each year between 1992 and 2015	Providing information on the land cover type to identify urban area	(ESA Land Cover CCI project team; Defourny, 2019)

Table A.2.8 Datasets used for quantification of the model predictor variables.

Dataset	Resolution	Temporal characteristics	Usage	Reference
Climate Data: ERA-5	9km	Monthly from 1981 to present	Climate predictor variables	(Muñoz Sabater, 2019)
MODIS EVI: MYD13A2, MOD13A2	1000m	Every 16 days from 2002 to 2020	Vegetation predictor variables	(National Aeronautics and Space Administration, 2021c, 2021d)
MODIS Albedo: MCD43A3, MCD43A2	500m	Daily from 2002 to 2020	Albedo predictor variables	(National Aeronautics and Space Administration, 2021b, 2021a)
CMIP6 ScenarioMIP Projections	2.8°x 2.8°	Monthly from 1850 to 2015 (historical) and 2015 to 2100 (ssp370)	Climate and vegetation projections	See Table A.2.10 and Table A.11

Table A.2.9 Global reanalysis datasets considered for this study.

Reanalysis Dataset	Horizontal resolution	Temporal	Reference
ERA-5	0.1°x0.1° (Native resolution 9km)	Coverage: 1981 to present Resolution: Monthly (also hourly product)	(Muñoz Sabater, 2019)
MERRA-2	0.625°×0.5°	Coverage: 1980 to present Resolution: Hourly	(Gelaro *et al.*, 2017)
JRA-55	1.25° × 1.25°	Coverage: 1958 to present Resolution: 3 hours	(Kobayashi *et al.*, 2015)

Table A.2.10 Information on the GCMs used to generate the changes in climate variables.

Institution	Country	Model Centre ID	Model	Variant used	Horizontal Resolution (lon x lat)	Reference
Chinese Academy of Sciences	China	CAS	FGOALS-f3-L	r1i1p1f1	1.3° x 1°	(He *et al.*, 2019)
Canadian Centre for Climate Modelling and Analysis	Canada	CCCma	CanESM5	r1i1p1f1	2.8° x 2.8°	(Swart *et al.*, 2019)
Fondazione Centro Euro-Mediterraneo sui Cambiamenti Climatici	Italy	CMCC	CMCC-CM2-SR5	r1i1p1f1	1.3° x 1°	(Cherchi *et al.*, 2019)
CSIRO (Commonwealth Scientific and Industrial Research Organisation), ARCCSS (Australian Research Council Centre of Excellence for Climate System Science)	Australia	CSIRO-ARCCSS	ACCESS-CM2	r1i1p1f1	1.9° x 1.3°	(Bi *et al.*, 2020)
Deutsches Klimarechenzentrum	Germany	DKRZ	MPI-ESM1-2-LR	r1i1p1f1	1.9° x 1.9°	(Müller *et al.*, 2018; Mauritsen *et al.*, 2019)
EC-Earth-Consortium – Multiple Institutions (AEMET, BSC, CNR-ISAC, DMI, ENEA, FMI, Geomar, ICHC, ICTP, IDL, IMAU, IPMA, KIT, KNMI, Lund University, Met Eireann, NLeSC, NTNU, Oxford University, surfSARA,	Europe	EC-Earth-Consortium	EC-Earth3	r1i1p1f1	0.7° x 0.7°	(Döscher *et al.*, 2022)

SMHI, Stockholm University, Unite ASTR, University College Dublin University of Bergen, University of Copenhagen, University of Helsinki, University of Santiago de Compostela, Uppsala University, Utrecht University, Vrije Universiteit Amsterdam, Wageningen University)						
Institute for Numerical Mathematics	Russia	INM	INM-CM5-0	r1i1p1f1	2° x 1.5°	(Volodin *et al.*, 2018)
Institut Pierre Simon Laplace	France	IPSL	IPSL-CM6A-LR	r1i1p1f1	2.5° x 1.3°	(Boucher *et al.*, 2020)
JAMSTEC (Japan Agency for Marine-Earth Science and Technology), AORI (Atmosphere and Ocean Research Institute, The University of Tokyo), NIES (National Institute for Environmental Studies), R-CCS (RIKEN Center for Computational Science)	Japan	MIROC	MIROC6	r1i1p1f1	1.4° x 1.4°	(Tatebe *et al.*, 2019)
NorESM Climate modelling Consortium (CICERO (Center for International Climate and Environmental Research), MET-Norway, NERSC (Nansen Environmental and Remote Sensing Center), NILU (Norwegian Institute	Norway	NCC	NorESM2-MM	r1i1p1f1	1.3° x 1°	(Seland *et al.*, 2020)

for Air Research), University of Bergen, University of Oslo, UNI (Uni Research))						
National Oceanic and Atmospheric Administration	USA	NOAA-GFDL	GFDL-ESM4	r1i1p1f1	1.3° x 1°	(Dunne *et al.*, 2020)
CNRM (Centre National de Recherches Meteorologiques), CERFACS (Centre Europeen de Recherche et de Formation Avancee en Calcul Scientifique)	France	CNRM-CERFACS	CNRM-CM6-1	r1i1p1f2*	1.4° x 1.4°	(Voldoire *et al.*, 2019)
Met Office Hadley Centre	UK	MOHC	UKESM1-1-LL	r1i1p1f2*	1.9° x 1.3°	(Mulcahy *et al.*, 2022)
Goddard Institute for Space Studies	USA	NASA-GISS	GISS-E2-1-G	r1i1p1f2*	2.5° x 2°	(Kelley *et al.*, 2020)

Table A.2.11 Information on the ESMs used to generate the changes in LAI.

Institution	Country	Model Centre ID	Model	Variant used	Horizontal Resolution (lon x lat)	Reference
Canadian Centre for Climate Modelling and Analysis	Canada	CCCma	CanESM5	r1i1p1f1	2.8° x 2.8°	(Swart *et al.*, 2019)
CNRM (Centre National de Recherches Meteorologiques), CERFACS (Centre Europeen de Recherche et de Formation Avancee en Calcul Scientifique)	France	CNRM-CERFACS	CNRM-CM6-1	r1i1p1f2*	1.4° x 1.4°	(Voldoire *et al.*, 2019)
CSIRO (Commonwealth Scientific and Industrial Research Organisation), ARCCSS (Australian Research Council Centre of Excellence for Climate System Science)	Australia	CSIRO-ARCCSS	ACCESS-ESM1-5	r1i1p1f1	1.9° x 1.3°	(Ziehn *et al.*, 2020)
Institut Pierre Simon Laplace	France	IPSL	IPSL-CM6A-LR	r1i1p1f1	2.5° x 1.3°	(Boucher *et al.*, 2020)
Met Office Hadley Centre	UK	MOHC	UKESM1-1-LL	r1i1p1f2*	1.9° x 1.3°	(Mulcahy *et al.*, 2022)

*Note: Some GCMs/ESMs in the table do not have the 'r1i1p1f1' variant. UKESM1-1-LL and GISS-E2-1-G only have one variant available (r1i1p1f2) so this was used, and the same was chosen for CNRM-CM6-1. The variant ID is used by the modelling centres to distinguish between ensembles of model runs and having a different forcing index (the f1 or f2 at the end of the variant ID) does not necessarily mean the forcing versions are different. In UKESM1 for example, the f1 index is not used at all in the CMIP6 experiments. An essential aspect relating to variant ID however, is that the historical simulation used alongside the ScenarioMIP model outputs is the same variant.

A.3. ALTERNATIVE STATISTICAL MODELS EXAMINED

This section outlines the additional statistical models which were fitted, but not selected as the final model.

Generalised Additive Model (GAM)

Linear Generalised Additive Models (GAMs) are the middle ground between MLR and more complex machine learning models, such as neural networks. They can model nonlinear relationships, capturing behaviour with smooth nonparametric functions which means no knowledge of the data distribution is required (Hastie and Tibshirani, 1986). These functions are weighted with a coefficient in the model, similarly to MLR, as shown in equation (1.1). As the model fits a function, it does not face the same issues as RFRs with regards to extrapolation. As long as the underlying relationship between input and output variables remain the same after for new datapoints, extrapolation is possible.

$$y = \beta_0 + s_1(x_1) + s_2(x_2) + \cdots + s_k(x_k) \qquad (1.1)$$

where y is the target variable, x_1, x_2, … x_k are the predictor variables, and $s_1(.)$, $s_2(.)$ … $s_k(.)$ are smooth functions (Hastie and Tibshirani, 1986).

The most common basis function used is cubic splines (Buja *et al.*, 1989). This is a curve, continuous in value and first and second derivatives, made up of sections of cubic polynomials joined together. The continuous nature of the functions renders them useful for interpolation (they have been proved to be the smoothest interpolator), and choosing a cubic function gives flexibility, but not so much the model will overfit (Wood, 2006).

As with the RR model, the main disadvantage of the GAM in this case is that it is sensitive to multicollinearity, so can become unstable if there are predictor variables that can be represented by some function of others. Another disadvantage of GAMs is the risk of overfitting, and to prevent this the models can be regularised using a smoothing parameter, similarly to RR (section 3.5). Each spline term has the regularisation parameter (λ) applied to its 2nd derivative to penalise 'wiggliness' and make the function smoother. Each linear term has the parameter applied as a ridge penalty (as with RR) (Wood, 2017; Servén and Brummitt, 2018). The nonlinear relationships fitted by the GAM also make it difficult to know whether or not the model will perform well under extrapolation cases. Cubic functions can lead to large changes in y for small changes in x, which is problematic if the behaviour of the function is to do so for the values towards the start or end of the data value range.

The model is fitted with cubic splines as the basis function, with each spline able to have a different choice for its value of λ, the smoothing parameter, which is calculated using the hyperparameter selection process as other models, outlined in section 3.5.

Gaussian Process Regression (GPR)

Gaussian Process Regression (GPR) is a modelling technique similar to RFR and GAM in that they are do not make any assumptions about the underlying relationships of the data (RR in contrast assumes the relationships are linear). GPR uses the current observations and interpolates from them in order to make a prediction, essentially determining the behaviour of a point based on how similar it is to other known points. Figure A.3.1 shows this difference in approach for a simple one-dimensional example.

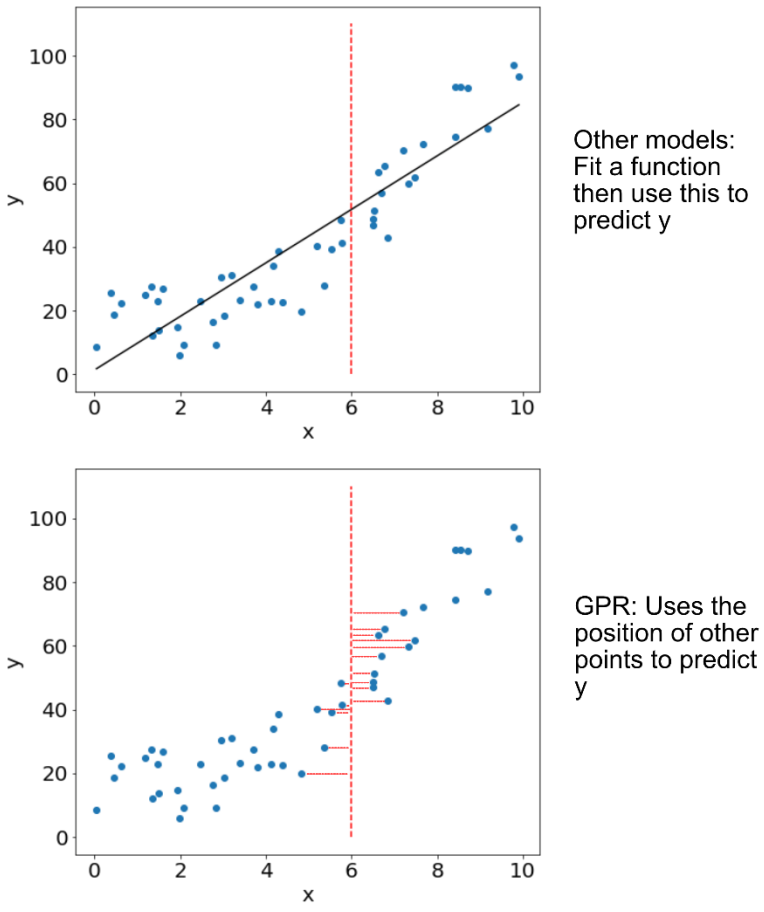

Figure A.3.1 The differences between a linear model and GPR. Here we want to predict y for x = 6, marked by the red dotted line on the plots. For a linear model, a function is drawn through the points, and using this function, a prediction for y can be made. GPR instead examines the nearby points, and makes a prediction based on how similar they are to points where the y- value in known. For example, the points with red lines drawn to them are similar to x = 6, so a predict of x can be generated from them. The further away in space (or less similar) a point is, the less influential it is in the value of the prediction.

The intuition behind this is that the behaviour of a point is likely to be more similar to those of its neighbours, and less so to those far away from it. A prediction made from GPR is a combination of all the points in the training dataset, but with each giving a weighting based on similarity to the new point for which y is to be predicted. GPR assumes the distribution of each point is gaussian (normally) distributed, with a mean value (the most likely position of the point – the mean function) and a variance (the noise).

As mentioned previously the functions must be smooth, with similar input points giving similar predictions. The equation for covariance of points x and y is shown in equation (1.2). If points x and y have a positive covariance, x will increase as y increases. If the covariance is 0, then there is no relationship between the variables; knowing if x is increasing or decreasing tells us nothing about y.

$$cov(x,y) = \frac{\sum(x_i - \bar{x})(y_i - \bar{y})}{N} \qquad (1.2)$$

An essential step of the GPR is quantifying how similar a point is to another, and this is done by generating a function for covariance, known as a kernel. So, the kernel works by taking a pair of input points and returning a measure of how similar they are (Görtler *et al.*, 2019).

Specifying a suitable kernel requires both a combination of expertise and trial and error (Duvenaud *et al.*, 2013). A suitable approach for finding a kernel is to select a few commonly used kernels and compare their marginal likelihood, choosing the kernel that optimises this. Expressions for some commonly used kernels can be seen in Table A.3.12.

Table A.3.12 Table of common covariance functions, from (Rasmussen and Williams, 2006)

Covariance function	Expression
Constant	$\sigma_0{}^2$
Linear	$\sum_{d=1}^{D} \sigma_d^2 x_d x'_d$
Polynomial / Dot Product -	$(\boldsymbol{x} \cdot \boldsymbol{x}' + \sigma_0^2)^p$
Squared Exponential (also known as Radial Basis Function)	$\exp\left(-\frac{r^2}{2l^2}\right)$
Matérn	$\frac{1}{2^{v-1}\Gamma(v)}\left(\frac{\sqrt{2v}}{l}r\right)^v K_v\left(\frac{\sqrt{2v}}{l}r\right)$
Exponential	$\exp\left(-\frac{r}{l}\right)$
γ-exponential (family including the Exponential and Squared Exponential)	$\exp\left(-\left(\frac{r}{l}\right)^\gamma\right)$

Difference covariance functions can be related to different aspects of the data to be modelled. A common choice for kernels shown in the table is squared exponential kernels, also known as radial basis functions (RBFs). These are functions of r =|**x** – **x**'|, where x and x' are the points for which the kernel is to be calculated. An example of where this kernel function could be useful is when modelling data with a smooth increasing trend. The Matérn kernel is related to this in that when the ν in its function (see Table A.3.12) tends to infinity, it becomes the squared exponential covariance function. This parameter (ν) limits the number of times the function can be differentiable (Rasmussen and Williams, 2006).

Another well-known kernel is a dot product, also shown in Table A.3.12, by which are functions dependent on **x**·**x**'. When the variance term, σ_0^2, of the kernel is set to zero, this kernel is also known as the linear kernel. These kernel functions are invariant to rotation of the two coordinates but not translation, with the variance term determining the offset of the kernel function (Rasmussen and Williams, 2006).

A more complex covariance function can be created by combining these simpler covariance functions to provide a model with a superior fit. For example, the squared exponential kernel function can be differentiated infinite times, which gives the kernel the property of being very smooth. When using the model to predict real life processes, this smoothness may not be realistic, and the use of another kernel (for example Matérn) is required. An additional kernel function which can aid the modelling of non-idealised situations is the white noise kernel. This adds noise with constant variance to the kernel function, independently and normally distributed (Rasmussen and Williams, 2006). As with RR, a regularisation parameter, λ, is also added to the diagonal of the kernel matrix to prevent overfitting.

Like GAMs, GPR is a machine learning technique that can handle non-linear relationships and aims to fit a smooth curve between points. It has the advantage of assigning uncertainty to its predictions, which becomes larger when the predicted output is far away from the sample dataset (this is its main advantage over using neural networks). GPR also has the benefit of being more suitable for smaller datasets, as methods such as neural networks require large datasets for training. As with the RFR model, the method is nonparametric, so does not assume the sample data has any particular distribution. The main disadvantage of GPR is that it is computationally intense for large datasets and it loses efficiency in high dimensional spaces. This means if too many variables are used in the model, it will take a very long time to run. The requirement of a kernel also adds in complexity, as a poor choice of this will make the function slow to converge. The ability of GPR to extrapolate is good if the covariance relationship described in the kernel function continues to hold for the new datapoint. However,

the further away the new point from the training data, the wider the confidence interval will be (Rasmussen and Williams, 2006).

The main decision to be made with GPR model is the choice if the kernel. In order to take advantage of the properties of the different kernels, a sum kernel functions is used. These consist of the RBF (or squared exponential), Matèrn, dot product (polynomial) and white noise kernels.

The kernel hyperparameter choices are optimised during the fitting process in scikit learn by maximising the log-marginal-likelihood (a measure of goodness of fit of the model to the training data), but the hyperparameter defining the number of different initial conditions investigated to find these hyperparameters is manually set before, known as the number of optimiser restarts. Therefore, the regularisation the regularisation parameter (λ) and number of optimiser restarts are determined using 5-fold cross validation.

Feature Importances

Feature importances are mentioned in section 3.5 as a useful interpretation methodology for the RFR model. As they are not used in the main body of this thesis, the mechanisms behind them are outlined below.

Feature importances are generated using a measure called average impurity reduction. When the data is split at a node by a variable, there will be a decrease in the sum of squared residuals. The impact of each variable in reducing the sum of squared residuals is calculated for each node, giving a value for each individual variable in a tree. This is then averaged across the entire forest, and scaled so the sum of importances is one (Nembrini *et al.*, 2018). The higher the feature importance score, the higher its contribution to the predictive power of the model. Similarly with other variable comparison methodologies, care must be taken when using this approach with correlated variables. If two variables are closely related, they might be used interchangeably to reduce the sum of squared residuals and have a relatively low importance each when used in the model together. However, if only one was used as a single uncorrelated variable, its overall importance would rank higher. Additionally, the methodology is biased towards variables which have many points at which they split the data (for example, splitting the data via five nodes rather than just one), so should be used in complement with other model interpretation metrics to ensure a fair interpretation (Nembrini *et al.*, 2018).

Modelling the 13:30 SUHI

This part of the section details the fitting, performance, and the inference that can be made from the additional statistical models.

For the RR model only, an extra variable selection step is applied. The model is given additional variables by means of taking squares and products of pairs of variables (section 3.5). The result means while there are 8 ‘core’ variables identified in the variable selection process, there are 44 variables utilised in the model. To ensure the model contains the optimum number of variables, a stepwise selection process is used. This consists of fitting the model for all variables, removing the variable with the smallest coefficient value, and repeating until only one variable remains. The point where the adding additional variables into the model does not create a large amount of improvement in its performance statistics is used to determine the final variables included in the model. These can be seen in Table A.3.14.

Table A.3.13 shows the performance statistics for the additional models, alongside the chosen model, REFR, for comparison. In terms of performance statistics, all models do a good job predicting the SUHI_MEAN. Despite RR having the lowest R-squared and RMSE, the model performs equally as well on the train and test datasets, indicating the model is capturing the relationships between predictors and target and not overfitting. Other models give an impressive performance on the training data, with a slightly worse (but still very good) performance on test data. This could indicate there is some overfitting, so using these models to extrapolate is done with caution. In terms of performance on test data, GPR and RERF are the best candidates. With consideration into the mechanisms behind the model, and given RERF has been shown to perform well in extrapolation circumstances (Zhang *et al.*, 2019), this model was determined the best choice.

Table A.3.13 Summary of SUHI_MEAN performance statistics (R-squared and RMSE) for all models investigated. Training data is from odd years and test data even years. Hyperparameters selected using cross validation are shown, see section 3.5 and the current section for descriptions of these.

Model	Train R-squared	Test R-squared	Train RMSE	Test RMSE	Hyperparameters	Fit/ Cross Validation Time
RR	0.79	0.79	1.10	1.10	$\lambda = 50$	~ 1 second
RFR	0.90	0.85	0.77	0.85	Maximum Tree Depth = 90 Number of Trees = 200 Minimum number of samples per leaf = 12 Minimum number of samples to split a node = 15 Number of features considered to split a node = 6	8 hours
REFR	0.90	0.87	0.77	0.86	$\lambda = 1000$ Maximum Tree Depth = 30 Number of Trees = 100 Minimum number of samples per leaf = 20 Minimum number of samples to split a node = 8 Number of features considered to split a node = 6	3 days 22 hours
GAM	0.81	0.80	1.05	1.06	$\lambda_{EVI\_U} = 10$ $\lambda_{EVI\_D} = 100$ $\lambda_{LOG\_AREA} = 0.6$ $\lambda_{WSA\_D} = 0.6$ $\lambda_{ELEVATION\_D} = 0.6$ $\lambda_{RH} = 100$ $\lambda_{TP} = 0.6$ $\lambda_{STD\_ELEVATION\_U} = 0.6$	25 mins
GPR	0.96	0.88	0.48	0.82	$\lambda = 0.01$ Number of optimiser restarts = 0	3 days 15 hours

ALE plots (section 3.5) are used to examine the behaviour of the models, and to ensure this is as expected, based on the known behaviours of SUHIs. RR ALE plots in this case are hard to interpret due to the interaction terms, so are not shown in this thesis. ALE plots for RFR, REFR, GAM and GPR are all plotted together as they use the same variables and can be seen in Figure 4.36. The REFR is included again in order to examine the differences between model predictions.

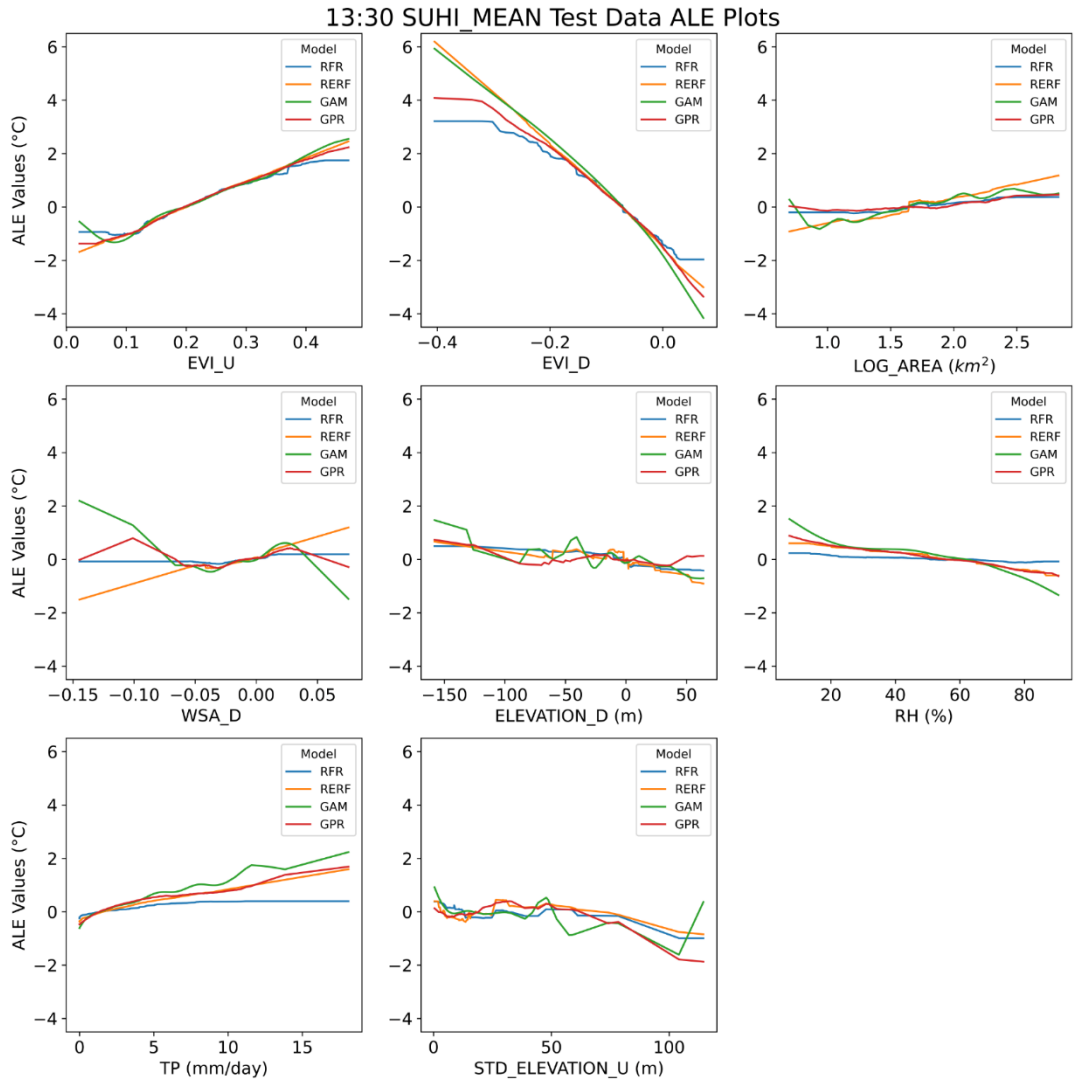

Figure A.3.2 13:30 SUHI_MEAN ALE plots for the RFR (blue), REFR (orange), GAM (green) and GPR (red). Details of ALE plots are given in section 3.5. The ALE plots were fit using test data. Training data ALE plots show the same relationships.

Mostly the models agree about the impact of the predictor variables on the SUHI_MEAN, but some additional inference can be made. For example, the ALE plots for RFR and GPR for EVI_U and EVI_D suggest there could be some saturation for the variables, where EVI_U is so low, decreasing it further has little impact on the SUHI_MEAN. Both these models use the training data directly to make the prediction, rather than fitting a function or relationship, and this behaviour is therefore synonymous with the underlying mechanisms behind the models.

WSA_D (urban – rural) impact on the models is where the highest discrepancies between models appears. The relationship is the same for the mid-range, where urban and rural albedo are similar, but when there is a larger difference, the impact of albedo is different based on the choice of model. The ALE plots for GAM show there are issues from using this model to extrapolate if variables fall outside of the training data range. For example, the plots for

EVI_U, LOG_AREA, WSA_D and STD_ELEVATION_U at the extreme ends have concerning behaviour for extrapolation, where a small change in the variable would produce a large change in the prediction of SUHI_MEAN.

Although the RR model cannot be directly compared by the use of ALE plots, inference can be made using the coefficients. This is a benefit of the model fitting a function to the points rather than using the training data to make the predictions (done by RFR and GPR, and partially RERF). Table A.3.14 shows the coefficients for the RR model. As the model is linear, all the relationships here are linear. EVI_D (EVI_U – EVI_R) has the largest magnitude coefficient and is negative, so as the difference between EVI_U and EVI_U decreases, or EVI_U becomes larger than EVI_R, the SUHI becomes smaller or becomes more negative. Another thing to highlight from the table is the interactions. There are two coefficients involving RH, these are EVI_D x RH with coefficient 0.62 and EVI_U x RH with coefficient -0.28. So here the overall effect of RH on the RR prediction depends on the vegetation conditions of the city. If the city is in area with high EVI_R, so EVI_D (EVI_U – EVI_R) is below the mean (note the predictor variables are normalised before they are used in the model), an increase in RH will translate as a decrease on the RR SUHI_MEAN prediction. If the area has little vegetation (an arid desert environment), so EVI_R and EVI_U are both small, but EVI_U is larger than EVI_R, an increase in RH increases the RR SUHI_MEAN prediction.

Table A.3.14 The predictor variables in the RR model and their coefficients for prediction of the SUHI_MEAN. A positive coefficient refers to the predictor variable have an increasing effect on the SUHI magnitude prediction as it increases, and a negative coefficient a decreasing effect as the predictor variable increases.

RR Predictor Variable	RR Coefficient
EVI_D	-1.24
EVI_U	0.80
EVI_D x RH	0.62
EVI_D x LOG_AREA	-0.76
TP	0.32
EVI_U x TP	-0.31
LOG_AREA x TP	0.33
EVI_U x LOG_AREA	0.32
STD_ELEVATION_U^2	-0.20
WSA_D x STD_ELEVATION_U	0.29
EVI_U x RH	-0.28
ELEVATION_D x STD_ELEVATION_U	-0.26

One of the benefits of using RFR is that feature importances can be used to make inference about the relationships between predictor and target variables. Figure A.3.3 shows the RFR feature importances for the 13:30 MEAN_SUHI as target variable. Here it can be seen that the highest ranked variable is EVI_D, which has a feature importance of 0.68.

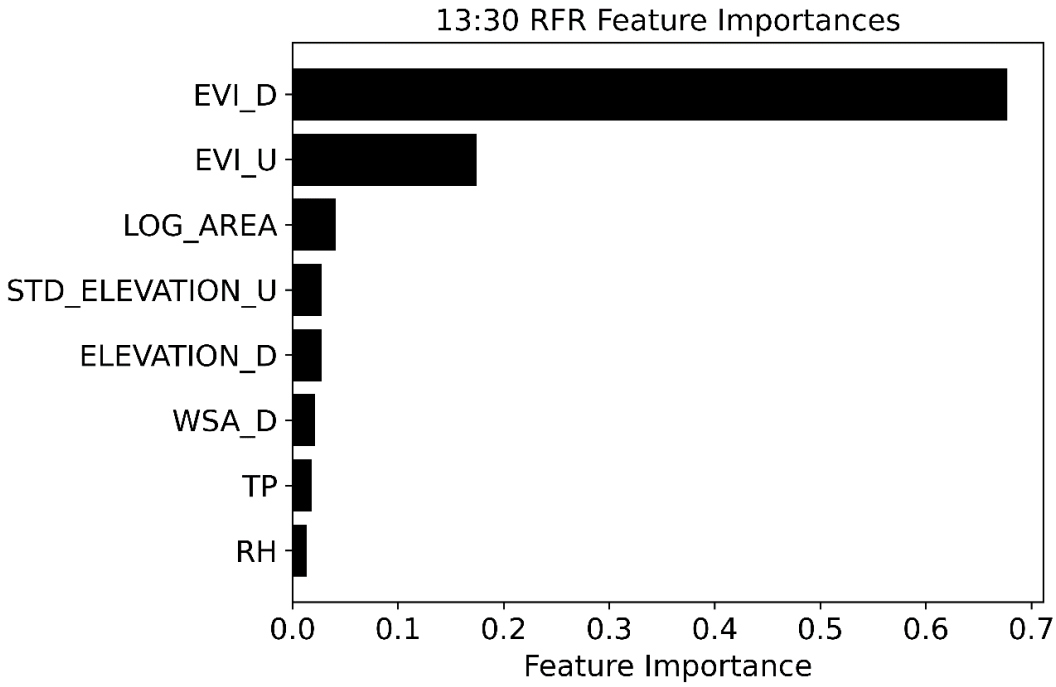

Figure A.3.3 RFR Feature Importances with target variable 13:30 Mean SUHI. The total feature importance is scaled so it sums to one.

Modelling the 01:30 SUHI

Model fittings were carried out via the same methodologies as for the 13:30 MEAN_SUHI but using the 01:30 MEAN_SUHI as the target variable. Table A.3.15 shows the performance statistics and model details.

Table A.3.15 Summary of 01:30 SUHI_MEAN performance statistics (R-squared and RMSE) for all models investigated. Training data is from odd years and test data even years. Hyperparameters selected using cross validation are shown, see section 3.5 for descriptions of these.

Model	Train R-squared	Test R-squared	Train RMSE	Test RMSE	Hyperparameters	Fit/ Cross Validation Time
RR	0.47	0.45	0.60	0.62	$\lambda = 1$	~ 1 second
RFR	0.63	0.58	0.50	0.54	Maximum Tree Depth = 50 Number of Trees = 100 Minimum number of samples per leaf = 50 Minimum number of samples to split a node = 50 Number of features considered to split a node = 9	8 hours
REFR	0.73	0.67	0.43	0.48	$\lambda = 10$ Maximum Tree Depth = 10 Number of Trees = 100 Minimum number of samples per leaf = 8 Minimum number of samples to split a node = 20 Number of features considered to split a node = 9	2 days 22 hours
GAM	0.57	0.55	0.54	0.56	$\lambda_{SSR\_NO\_SEASON} = 100$ $\lambda_{EVI\_U} = 0.6$ $\lambda_{EVI\_D} = 100$ $\lambda_{LOG\_AREA} = 0.6$ $\lambda_{WSA\_U} = 0.6$ $\lambda_{WSA\_D} = 0.6$ $\lambda_{ELEVATION\_D} = 0.6$ $\lambda_{RH} = 100$ $\lambda_{TP} = 100$ $\lambda_{STD\_ELEVATION\_R} = 0.6$	18 hours
GPR	0.7	0.65	0.45	0.49	$\lambda = 1$ Number of optimiser restarts = 20	3 days 15 hours

ALE plots for the models are shown in Figure A.3.4. For the majority of the predictor variables, the models agree on their impact on the MEAN_SUHI.

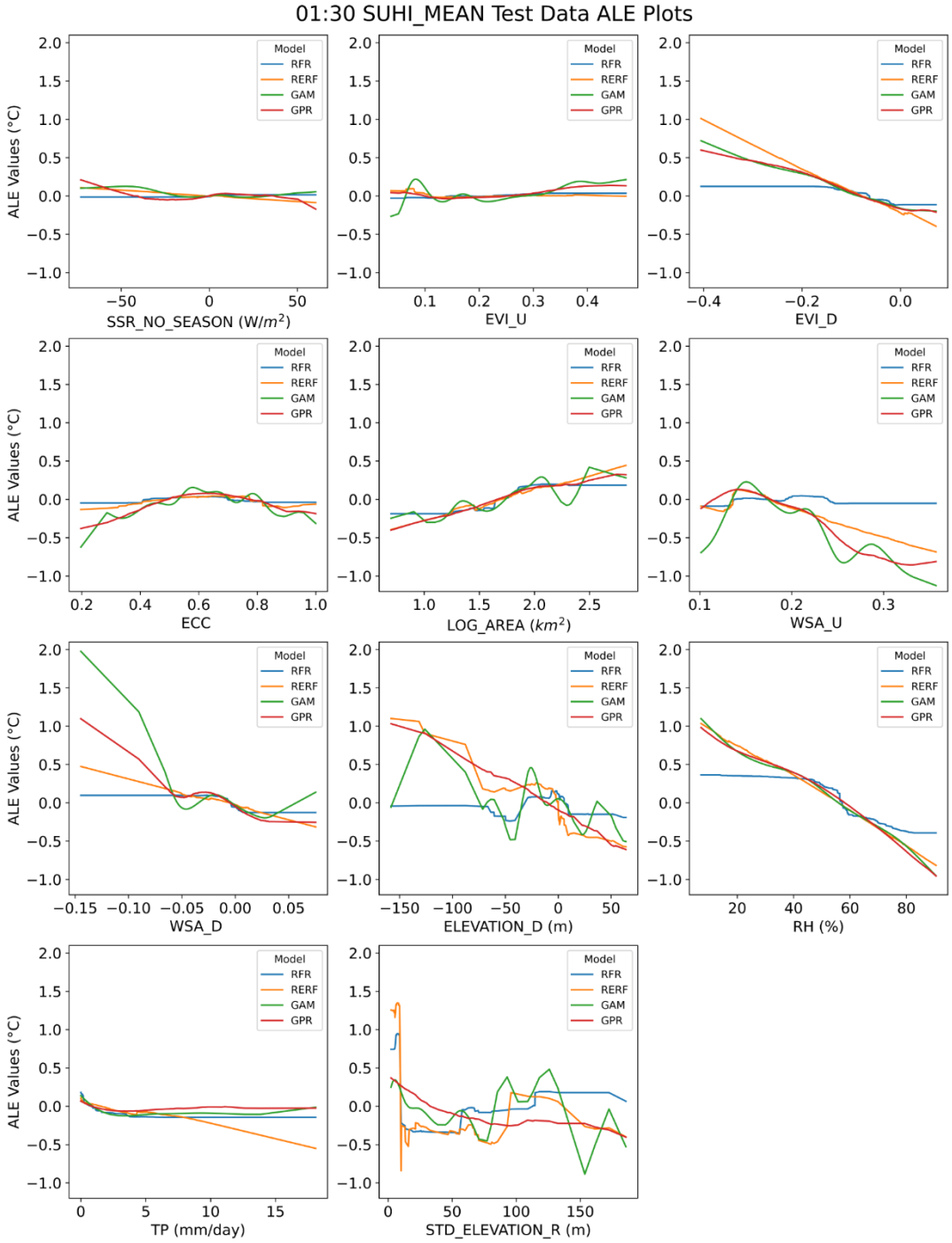

Figure A.3.4 01:30 SUHI_MEAN ALE plots for the RFR (blue), REFR (orange), GAM (green) and GPR (red). Details of ALE plots are given in section 3.5. The ALE plots were fit using test data. Training data ALE plots show the same relationships.

Figure A.3.5 shows the feature importances for the model with the SUHI_MEAN as the target variable. The variable deemed to contribute most to the prediction is RH, with a feature importance of 0.37. In comparison to the 13:30 SUHI_MEAN, which was found to have EVI_R as the highest ranked variable with importance of 0.68, the variable importance for the 01:30 SUHI has more of a shared importance of variables than dominance of one.

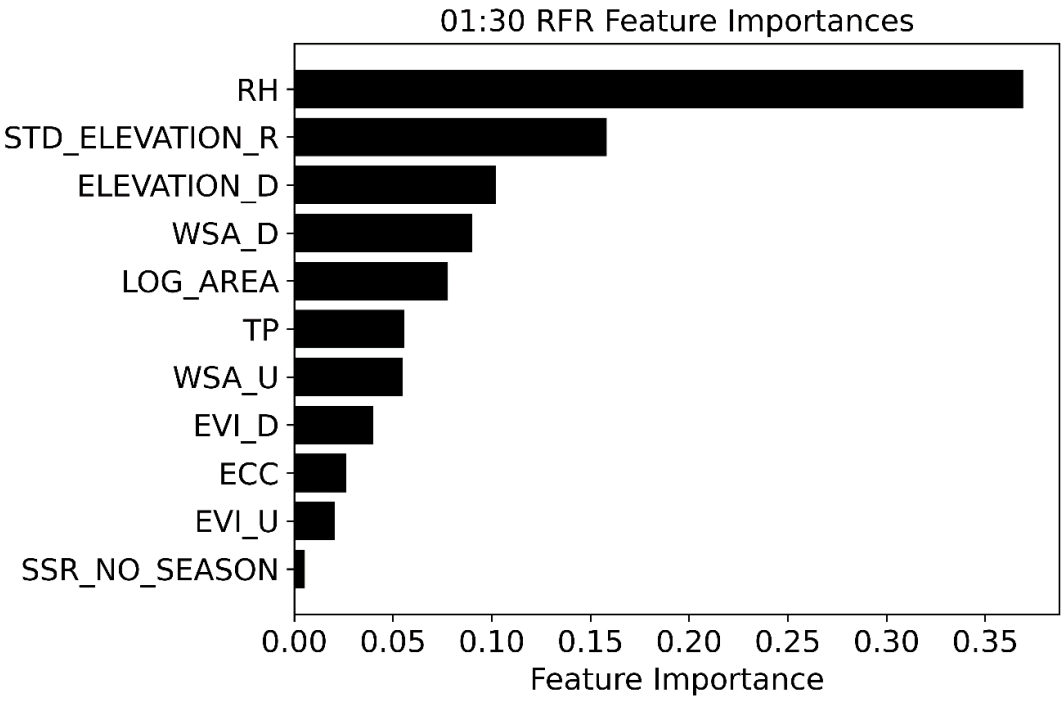

Figure A.3.5 RFR Feature Importances with target variable 01:30 Mean SUHI. The total feature importance is scaled so it sums to one.

The RR model has the weakest performance in terms of R-squared and RMSE, with R-squared of 0.45 and RMSE of 0.62 for the test data. RERF here shows good performance, with performance statistics for the test data (R-squared 0.67 and RMSE 0.48K).

A.4. ALTERNATIVE SUHI QUANTIFICATION MEASURES EXAMINED

Gaussian Surface Approximation SUHI (SUHI_PEAK_GSA)

One of the methods of quantifying the SUHI is by means of a Gaussian surface approximation (GSA), modelling the SUHI as a smoothed Gaussian surface (Streutker, 2002). A schematic outlining the overall process can be seen in Figure A.4.6 and is outlined below, with numbers corresponding to those on the schematic.

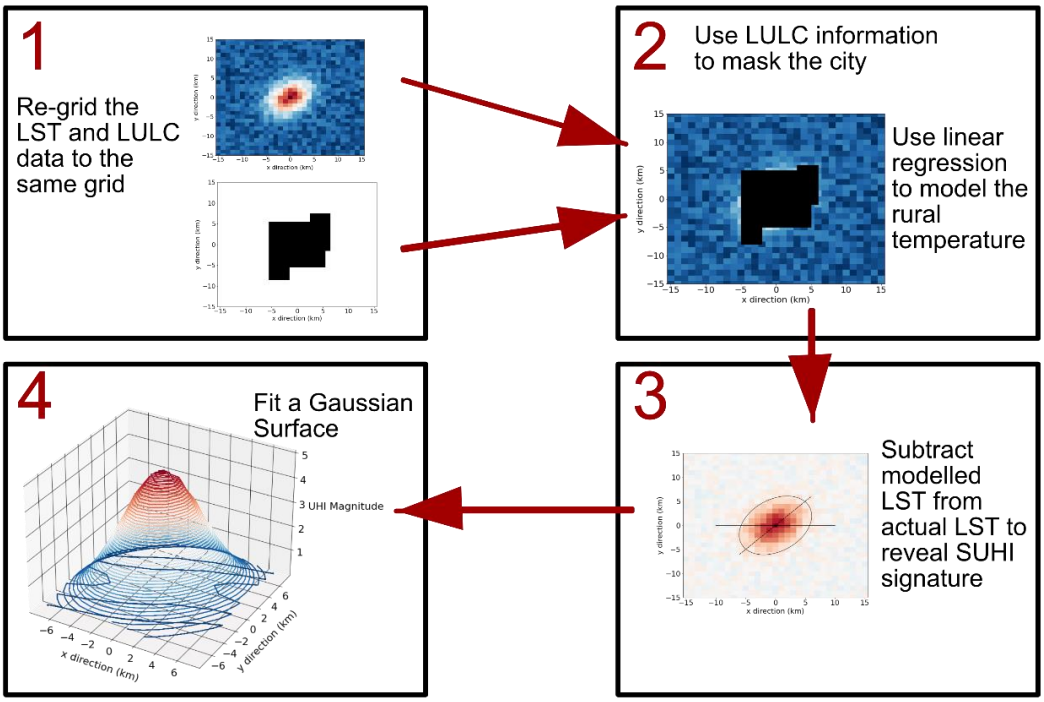

Figure A.4.6 An overview of the steps taken to fit a Gaussian Surface Approximation of a SUHI

The parameters of the Gaussian Surface are calculated by the following (Anniballe and Bonafoni, 2015).

1. Urban or rural classification is given to each pixel on the LST image, using the LULC dataset. The area of the city is then identified. Figure A.4.7 shows the layout of the city of Sao Jose Do Rio Preto, Brazil. The origin marks the city centre, identified using the coordinates of the city (United Nations, Department of Economic and Social Affairs, 2019) and units are in meters. The red box represents the area where urban pixels are classed as being part of the city.

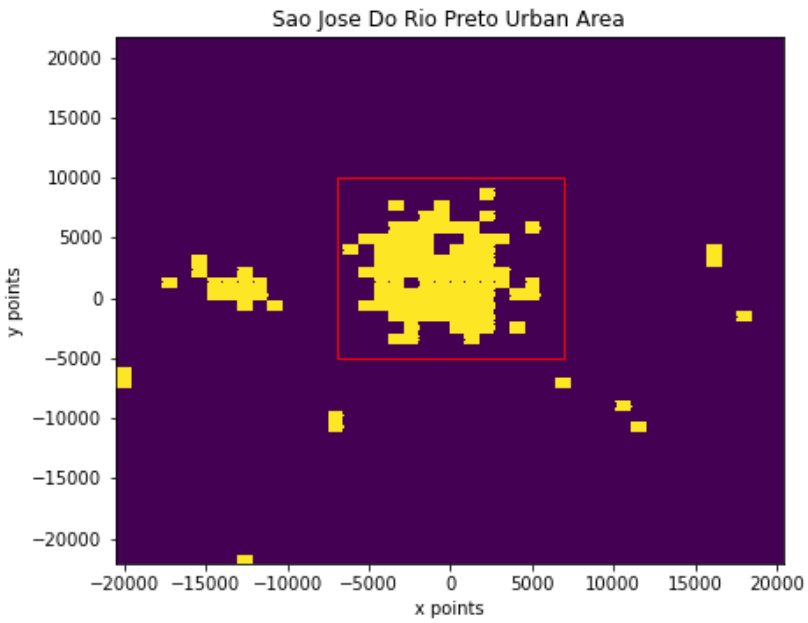

Figure A.4.7 Sao Jose Do Rio Preto, Brazil Urban Areas. Yellow pixels represent the urban area, purple the rural area. The red box encloses urban pixels belonging to the city.

2. The urban land (yellow pixels) outside of the city is then removed from the analysis. This is because the interest is in the SUHI; the difference between the city's urban land and the rural land surrounding it, not in considering the influence any villages surrounding a city. In the example of Sao Jose Do Rio Preto, Figure A.4.7, these are the yellow pixels outside of the red box surrounding the city.

   A linear regression of LST, based on the distance from the city centre in the x and y directions is carried out in order to estimate the temperature of the area in the absence of the city. This involves fitting the rural LSTs to the form of equation (1.3).

$$T_{rural}(x, y) = T_0 + a_1 x + a_2 y \qquad (1.3)$$

   where T_0, a_1, a_2 are coefficients to be determined.

3. This relationship is then used to estimate a rural 'baseline' temperature for the entirety of the area, giving the estimated temperature in absence of a city. The difference between this and the actual LST gives a value for the SUHI at each point, as outlined in equation (1.4).

$$SUHI = LST - T_{rural} \tag{1.4}$$

The benefit of modelling the rural baseline as this planar surface, rather than taking a single mean and using this as the rural baseline, is that it accounts for different pixels in the city area having different temperatures if the influence of the city were removed. For example, if a rural area looked like that shown in Figure A.4.8. Examining the centre of this image, the left top of the central area would have a warmer temperature and the right bottom a lower one.

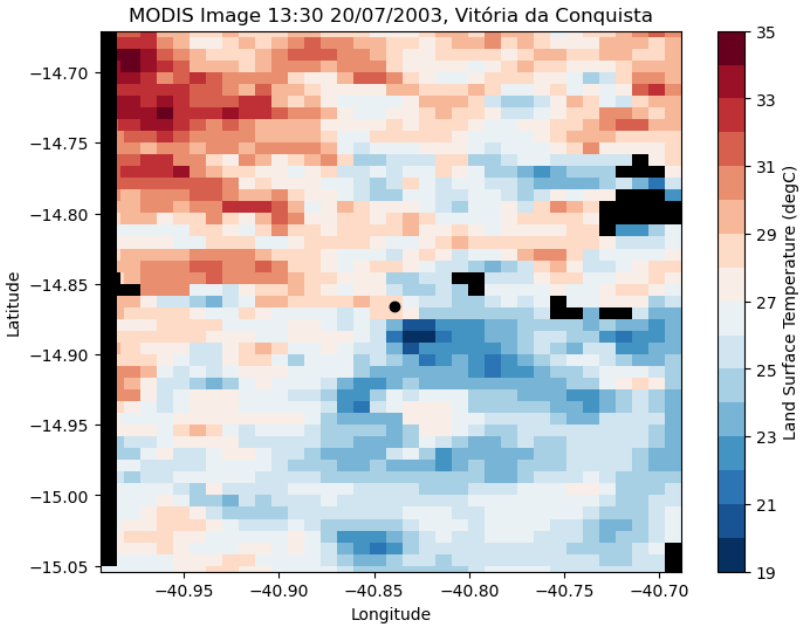

Figure A.4.8 MODIS LST image of Vitoria da Conquista, Brazil. The dot in the middle of the plot marks the city centre. This LST heatmap demonstrates how there can be a temperature gradient in an area, which will be captured by a modelled baseline, but not by taking the mean of the rural area.

4. The Gaussian surface approximation is then generated by fitting the surface to the curve in equation (1.5). The fit is constrained on x_0 and y_0 so it does not go outside of the city bounds. Initial guesses are set for (x_0, y_0) as the city centre (0,0), a_0 as half the maximum SUHI, (a_x, a_y) as extent of the city bounds and ϕ as 0°.

$$SUHI(x,y) = a_0 \times \exp[-\frac{((x-x_0)\cos\varphi + (y-y_0)\sin\varphi)^2}{0.5a_x^2} - \frac{((y-y_0)\cos\varphi - (x-x_0)\sin\varphi)^2}{0.5a_y^2}] \quad (1.5)$$

where, (x,y) represent the location of a pixel, (x_0,y_0) represent the location of the centre of the SUHI, a_0 represents the SUHI peak magnitude, a_x and a_y represent the spatial extent, and ϕ represents the angle of orientation.

The peak magnitude, a_0, will be referred to from now on as *SUHI_PEAK_GSA*.

The GSA is advantageous when examining the SUHI as it allows more than simply the SUHI magnitude to examined. By fitting urban temperatures to a simplified spatial distribution, the approximation generates six parameters that can be used to characterise the SUHI of a particular city, which are seen in equation (1.5). Their benefits are described in Table A.4.16.

Table A.4.16 Description and uses of the parameters generated by fitting a GSA.

GSA Parameter	
Peak SUHI magnitude (a_0) (referred to as SUHI_PEAK_GSA)	The peak intensity, where the SUHI magnitude is the greatest, unaffected by extreme values of temperature within the city. This gives more information than purely using the average throughout the entire city, as it differentiates between a city with an intense SUHI in one place and lower temperatures on the outskirts, versus a city with an overall even SUHI throughout. This is an important consideration in terms of the impact of the SUHI on city inhabitants, as it gives the SUHI magnitude in the areas of the city where it is felt the most. Peak magnitude also can be calculated by looking at quantiles (Flores R. *et al.*, 2016).
Spatial Extent of the SUHI (a_x, a_y)	The spatial extents give an idea of the footprint of the SUHI, with a_x showing the extent in the x direction, and a_y the y direction. Yang et al (2019) notes a focus on magnitude in UHI research but little attention given to its spatial extent, an important aspect of the UHI. This aspect of the UHI gives an idea of the influence of the SUHI outside of the city, or if the SUHI is concentrated within the main area of a city. This can be particularly useful for examining the diurnal cycle, as the SUHI tends to be more spread out during the day and the night-time SUHI shows a more concentrated heating at the urban core (Tran *et al.*, 2006).
Centre of SUHI magnitude (x_0, y_0)	These coordinates show where the most intense SUHI is located. This is useful to understand as to whether this is at the city core, or offset in a different area, perhaps the most build up or industrial region of the city. In terms of application of mitigation measures, knowing where the SUHI is at is peak is valuable, as it translates as knowledge of where cooling measures (for a strong positive heat island) such as green or blue spaces could be concentrated to keep the warmest areas cooler.
Angle of orientation (φ)	The angle of orientation gives the direction in which the SUHI extends the furthest. From this the eccentricity, a measure of how elliptical the city shape is, can be generated.

Alongside the advantages of the parameter generation, using an approximation to examine the SUHI surface has an additional benefit of being more resilient to gaps in the data due to cloud contamination. On cloudy days where an image has a lower number of good quality pixels, gaps in the data will result in less bias (Lai *et al.*, 2021). This is due to the fit of a smooth temperature surface to the city, rather than taking the mean of all pixels.

A drawback of using the GSA is that it requires the shape of the SUHI signature to be elliptical, meaning if the shape of a city is irregular, its characteristics will be misrepresented by the approximation. However, it is worth noting an ellipse can provide a better representation of an irregular surface in comparison to assuming a single uniform temperature (i.e., the SUHI_MEAN) or circular-only Gaussian surface. Another consideration is that the rural LST also may not be correctly represented by a plane, the consequence of which would mean the SUHI signature being modelled is distorted (Flores R. *et al.*, 2016). The errors in fitting are screened to ensure goodness of fit using Pearson's linear correlation (r) and root mean squared error (RMSE). Pearson correlation values range from -1 to 1, with 0 indicating no correlation and 1 a strong positive correlation. Therefore, values above 0.5 will show a moderate to good correlation or better. Based on this, for GSA fit made the correlation was calculated and if the correlation between the GSA prediction and observations was less than 0.5, the fit was deemed invalid. This approach is used in other studies, with the same threshold of under 0.5 indicating an unacceptable fit (Quan *et al.*, 2014; Yang *et al.*, 2019). RMSE (section 0) is used to ensure accuracy of the GSA by flagging fits with a RMSE above some threshold to be invalid. Some caution must be taken when choosing the threshold value in this scenario as RMSE is not a scaled value, meaning choosing a threshold value too low would tend to bias the successfully fitted images towards smaller SUHI magnitudes. Cities with higher SUHI magnitudes will have greater variations in the SUHI and therefore likely higher RMSE values. Examination of the results showed that this was indeed the case. Lai et al (2021) uses RMSE to assess GSA fit, with a 1.5K RMSE threshold, but due to the aforementioned justification, fits with RMSE greater than 2.5K were removed. The mean percentage of GSA fits that meet this criterion are 76% for daytime images and 94% of night-time.

SUHI_MEAN also is used to improve the results of the SUHI_PEAK_GSA. In the case that a SUHI does not exist, i.e., the LST of the urban and rural areas are the same, it is not possible to fit a GSA. In order to identify these situations, the SUHI_MEAN was consulted. Section 3.2, outlining the LST data product used states the product was found to have an accuracy of greater 1K in in situ studies. Therefore, if mean SUHI is between -0.5K and 0.5K it is taken as confirmation the SUHI does not exist or is extremely weak, and the SUHI_PEAK_GSA was taken to be zero. Reasons for certain cities being more difficult to fit include being

bisected by a river (so there is a cooling effect through the middle), being a long stringlike shape, or containing large suburban areas and roads throughout the rural reference.

Quantile Peak SUHI

The quantile method, as with the GSA, aims to examine the peak SUHI intensity. This is useful to include as another method to confirm the validity of the SUHI_PEAK_GSA. Flores R. (2016) recommends this method as one complementary to using the SUHI_PEAK_GSA, useful for cities with more than one area of peak intensity and with a non-ellipsoidal shape. For the case of the cities investigated in this research, it is most likely there will only be one area of peak intensity however, as they are limited to small and medium sized cities.

The quantile peak intensity was calculated by taking the 75th percent quantile LST pixel within the city area and subtracting the median LST pixel in the rural area, see equation (1.6). Flores R. (2016) proposes use of the 95th percent quantile, however taking into account the smaller size of some of the cities in this analysis (5km^2 at the smallest) the lower threshold of 75th was used.

$$SUHI_{quantile} = LST_{urban\ 75} - LST_{rural\ median} \quad (1.6)$$

This method is used as an additional check to ensure validity of the SUHI_PEAK_GSA and SUHI_MEAN.

Comparison of SUHI_MEAN and SUHI_PEAK_GSA

The daytime SUHI for both metrics has greater magnitude and more variation during the day than during the night. The SUHI_PEAK_GSA is greater in magnitude than the SUHI_MEAN, as would be expected, and has more variation. The magnitude of the negative SUHIs is generally smaller than the positive SUHI magnitudes for both SUHI_MEAN and SUHI_PEAK_GSA. Table A.4.17 gives a comparison of the means and standard deviations of the two metrics.

Table A.4.17 Summary of the mean and standard deviations of city SUHI metrics (averaged from cities not across entire dataset). Cities with a mean positive SUHI make up the positive SUHI columns and cities with a mean negative SUHI the negative SUHI. The groupings are done separately for day and night.

	Positive SUHI		Negative SUHI	
Metric	13:30	01:30	13:30	01:30
SUHI_MEAN	2.2 ± 1.3 K	1.5 ± 0.6 K	-1.1 ± 0.9 K	-
SUHI_PEAK_GSA	3.5 ± 1.9 K	2.7 ± 0.8 K	-2.0 ± 1.7 K	-

Figure A.4.9 shows correlations between the day, night and two SUHI metrics. The SUHI_MEAN and SUHI_PEAK_GSA are highly correlated with a Pearson's correlation coefficient of 0.9. During the daytime, when there exists a negative SUHI, a jump can be seen where the SUHI_PEAK_GSA becomes more negative than the SUHI_MEAN. This cannot be seen during the night as it is uncommon for there to be a negative SUHI. From this it can be induced that while the daytime mean SUHI can give a magnitude of close to zero, the SUHI_PEAK_GSA shows the SUHI does occur in certain parts of the city at higher intensity. This differentiates between cities with evenly spread weak urban heating versus cities with more intense central hotspots and cooler outskirts. For both SUHI_MEAN and SUHI_PEAK_GSA, the 13:30 and 01:30 SUHIs are not highly correlated, which is discussed for the SUHI_MEAN in section 4.2.

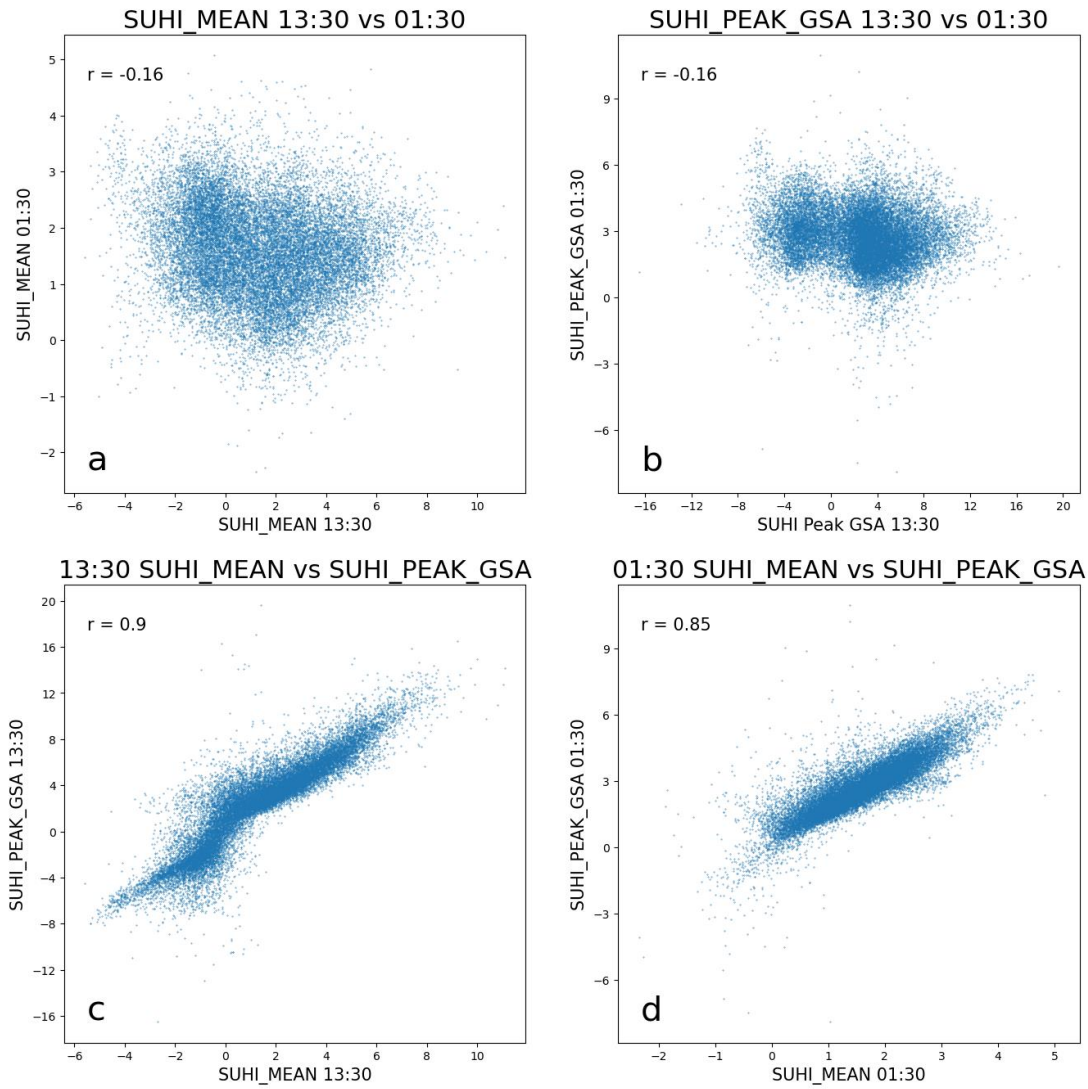

Figure A.4.9 Scatter plots showing correlations with Pearson correlation coefficient, r for a) SUHI_MEAN 13:30 vs 01:30 overpasses b) SUHI_PEAK_GSA 13:30 vs 01:30 overpasses c) 13:30 SUHI_MEAN vs SUHI_PEAK_GSA d) 13:30 SUHI_MEAN vs SUHI_PEAK_GSA. Each point represents one month from the period 2002-2020 with all cities included.

Figure A.4.10 and Figure A.4.11 show maps of SUHI_MEAN and SUHI_PEAK_GSA at 13:30 and 01:30, respectively. Here, it can be seen at 13:30, SUHIs both show more variation and larger magnitudes then they do at 01:30. Across cities and locations, the 01:30 SUHI is more similar in both its magnitude and its sign (being positive). This could be an indication that the properties that impact the SUHI during the day can fluctuate from city to city and by season, whereas the factors at night are less varied, as theorised in section 2.5.1.

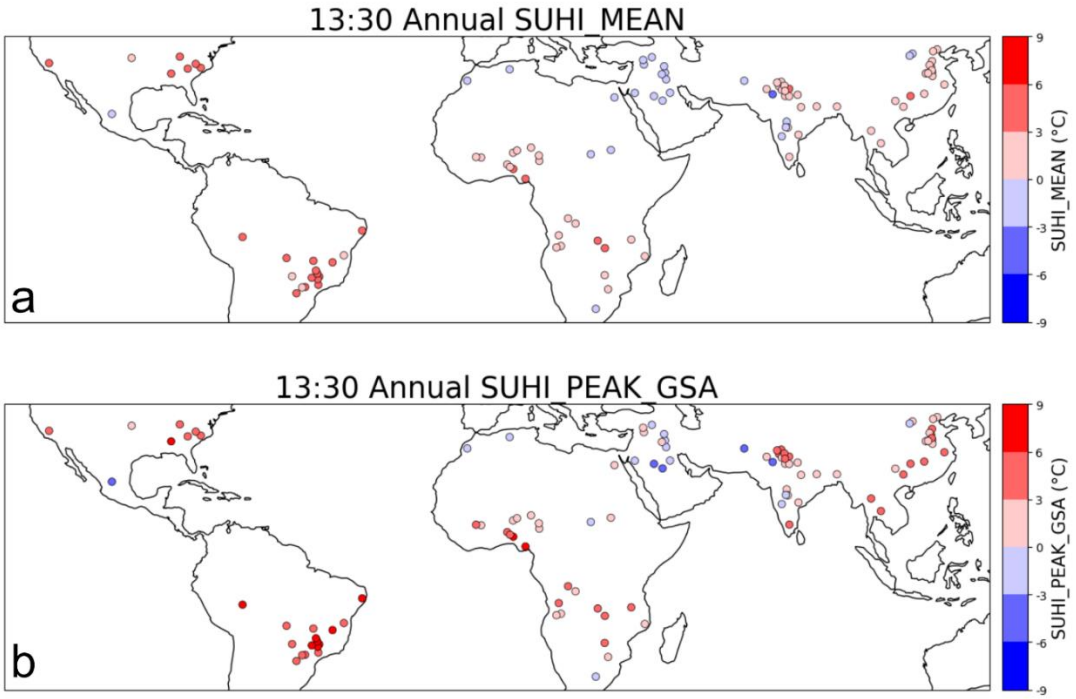

Figure A.4.10 A comparison of the mean Annual SUHI magnitudes for the different quantification methods at 13:30. The SUHI_PEAK_GSA has larger absolute magnitudes, and in some cases is positive whilst the SUHI_MEAN is negative.

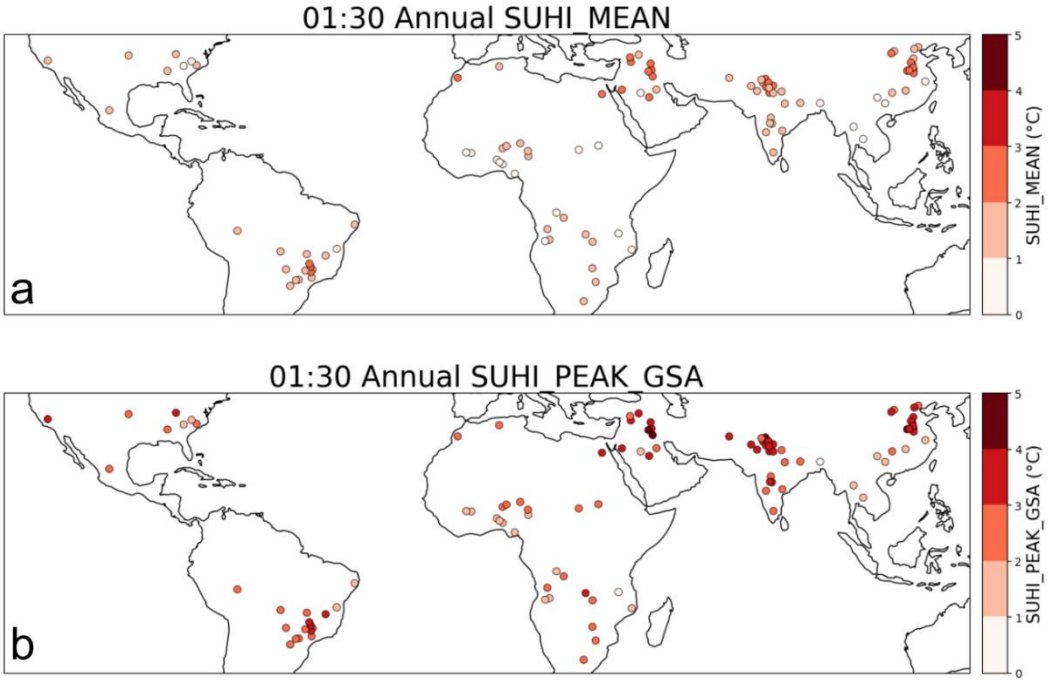

Figure A.4.11 A comparison of the mean Annual SUHI magnitudes for the different quantification methods at 01:30. Both methods give only positive SUHIs during the night, with the SUHI_PEAK_GSA showing larger magnitudes.

Statistical Model Performance Predicting SUHI_PEAK_GSA

Using the same methodology as for the MEAN_SUHI outlined in section 4.4, the optimum number of variables for the SUHI_PEAK_GSA as target variable was 9, show in Figure A.4.12.

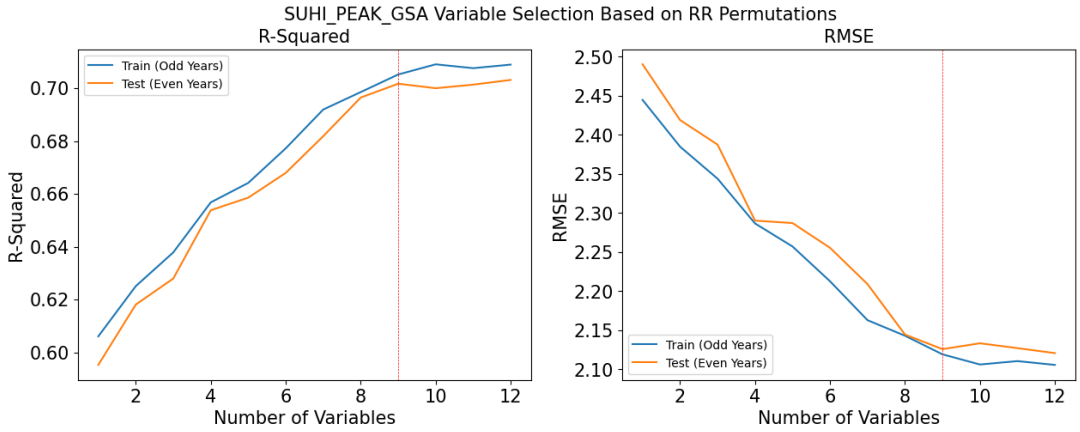

Figure A.4.12 Performance statistics (R-squared and RMSE) for the best performing models for each number of predictor variables, with SUHI_PEAK_GSA as target variable. The red line marks the 'elbow' of the plot, taken to be where the addition of further variables will not improve model performance.

The variables selected as giving the best predictive performance for the SUHI_GSA_PEAK differ slightly from the SUHI_MEAN, which includes LOG_AREA, whereas SUHI_GSA_PEAK does not include LOG_AREA but has STD_ELEVATION_D and WSA_U instead. The plots also show how, for all the combinations of variables run, the performance statistics with SUHI_GSA_PEAK as the target variable show the model is less able to capture the behaviour of the SUHI quantified with this measure in comparison to the SUHI_MEAN.

A.5. ADDITIONAL CLIMATE PROJECTION PLOTS

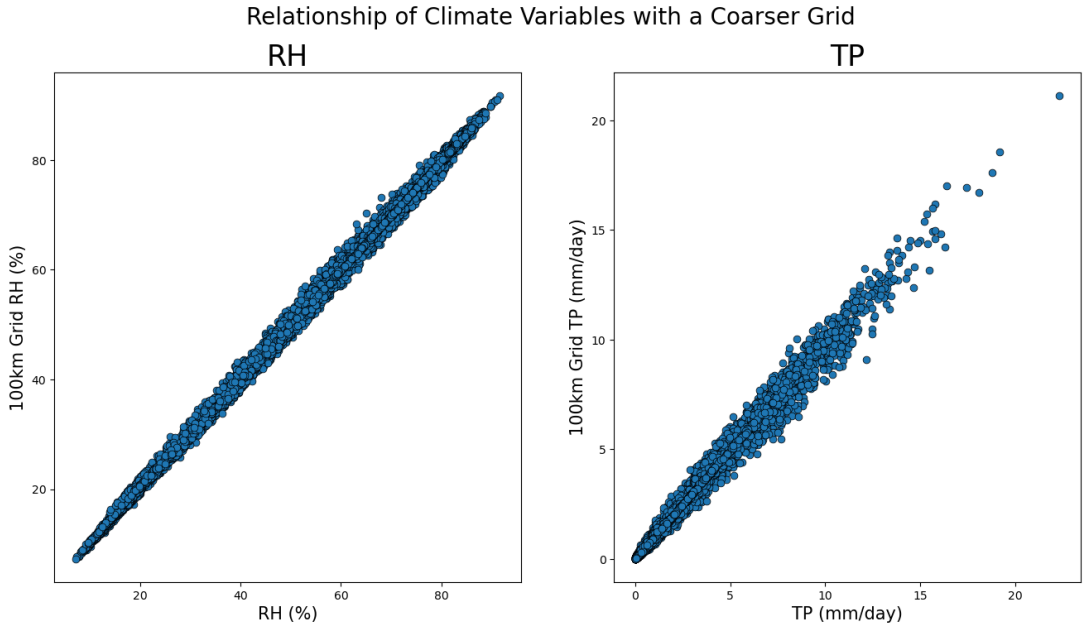

Figure A.5.13 Scatter plots to show the potential effects of coarser resolution RH and TP. For each city, the resolution was increased to the 100km area around the city and compared with the resolution used in the ML models.

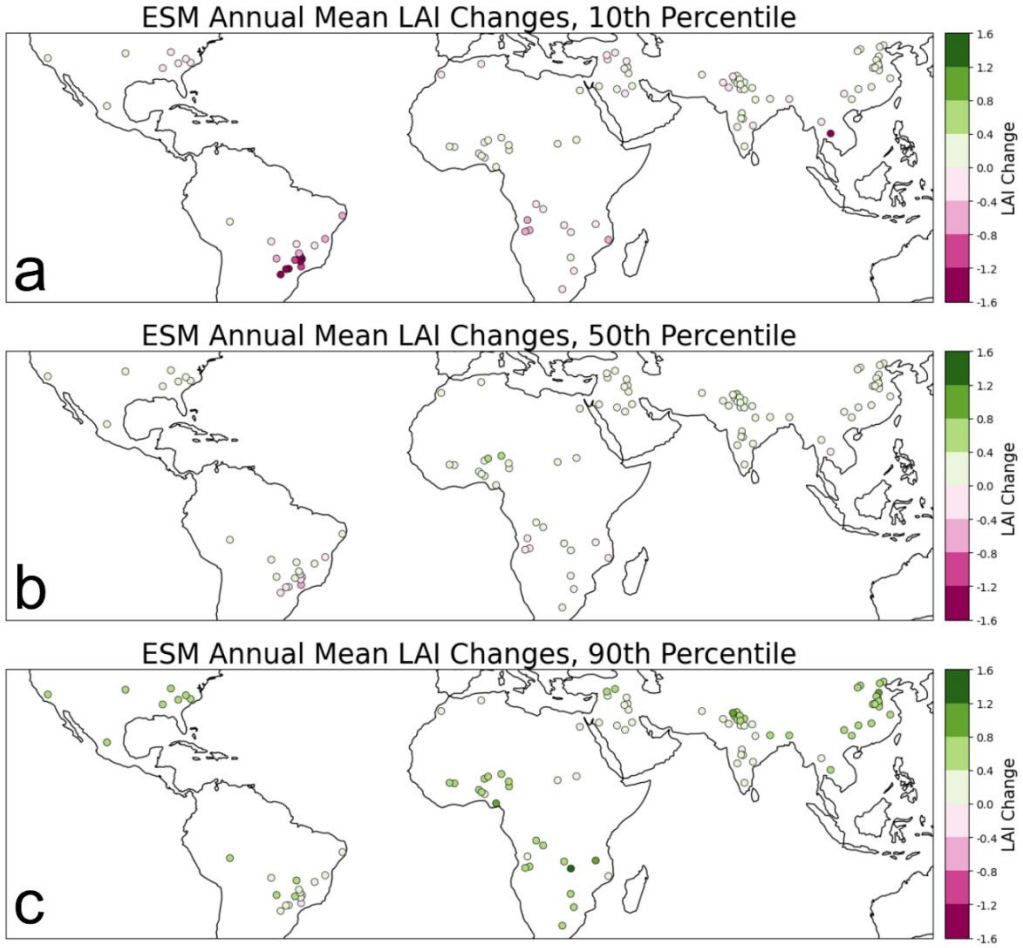

Figure A.5.14 ESM absolute value of LAI change from historical pre-industrial LAI to 2°C mean global temperature projected LAI. The spread of the ESM projected changes is shown by a) the 10th Percentile, b) the 50th Percentile (Median), c) the 90th Percentile.

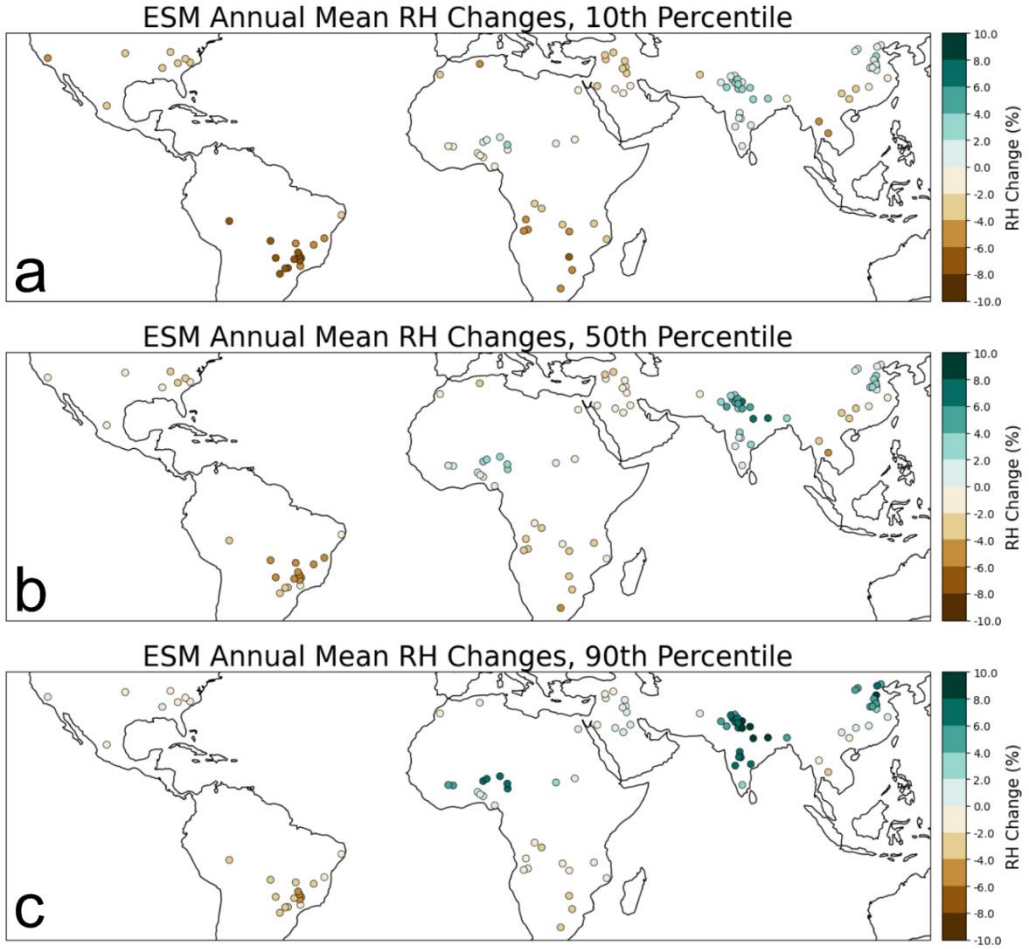

Figure A.5.15 ESM RH change from historical pre-industrial RH to 2°C mean global temperature projected RH. The spread of the ESM projected changes is shown by a) the 10th Percentile, b) the 50th Percentile (Median), c) the 90th Percentile.

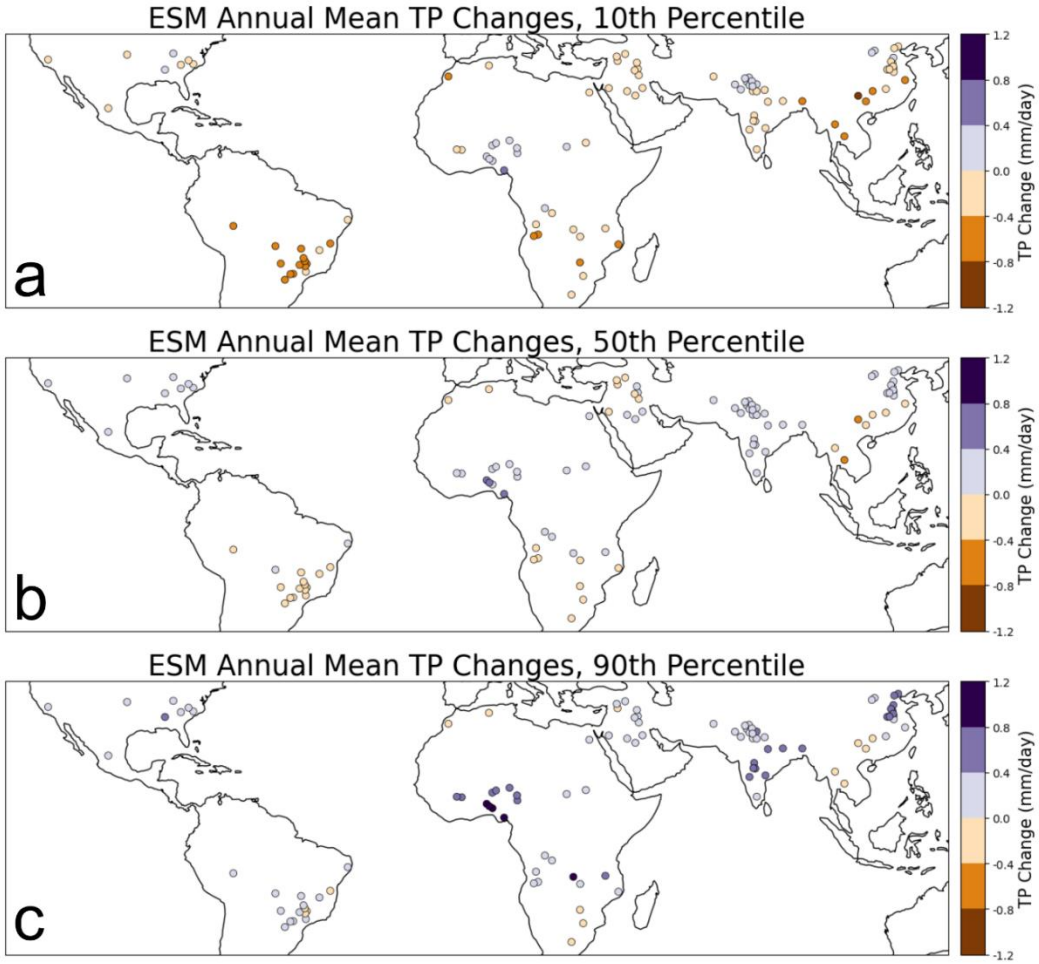

Figure A.5.16 ESM TP change from historical pre-industrial TP to 2°C mean global temperature projected TP. The spread of the ESM projected changes is shown by a) the 10th Percentile, b) the 50th Percentile (Median), c) the 90th Percentile.

Table A.5.18 Python Packages used.

Application	Function/ Package	Reference
Cross Validation, RR, RFR, GPR, Analysis	Scikit-Learn	(Pedregosa *et al.*, 2011)
RERF	linear-tree	https://github.com/cerlymarco/linear-tree/tree/main
Data Visualisation and Analysis	Pandas	(The pandas development team, 2023)
Data Visualisation and Analysis	Geopandas	(Jordahl *et al.*, 2020)
Data Visualisation	Matplotlib	(Hunter, 2007)
Data Visualisation	Seaborn	(Waskom, 2021)
Data manipulation and analysis	Scipy	(Virtanen *et al.*, 2020)
Loading data and analysis	xarray	(Hoyer and Hamman, 2017)
Data manipulation	Rasterio	https://github.com/rasterio/rasterio
Data Analysis	Numpy	(Harris *et al.*, 2020)
Data Analysis	Earthpy	(Wasser *et al.*, 2019)
Data Analysis	Shapely	(Gillies and Others, 2007)
Data Visualisation and Analysis	Cartopy	(Elson *et al.*, 2023)
Re-gridding	xESMF	(Zhuang *et al.*, 2021)
Re-projecting	Pyproj	(Snow *et al.*, 2021)